



POLITECNICO
MILANO 1863

School of Civil, Environmental and Land Management Engineering

M.Sc. in Civil Engineering for Risk Mitigation

**EXPERIMENTAL AND NUMERICAL ANALYSIS OF
OVERLOADED CHANNEL IN SUPERCRITICAL CONDITION**

Supervisor: Dr. Alessio Radice

Master of Science Thesis by:

Hasan Eslami (915797)

Mohsen Yavary Nia (914981)

Hooshyar Yousefyani (915638)

Academic Year 2020-2021

ACKNOWLEDGMENTS

We would like to thank everyone who supported us in completing this master thesis.

Special thanks to our supervisor, Professor Alessio Radice, for his time, support, and guidance throughout this journey.

We are also grateful to all staff and professors of the Politecnico di Milano for showing us the way during this master's degree program.

Finally, we would like to express our deepest appreciation to our friends and families for supporting and encouraging us during these years, and also thanks to dear Saeideh for all her help.

CONTENTS

ACKNOWLEDGMENTS	I
CONTENTS.....	III
LIST OF FIGURES	VII
LIST OF TABLES	XIII
ABSTRACT (ENGLISH).....	XVI
SOMMARIO (ITALIANO)	XVII
ABSTRACT (PERSIAN).....	XVIII
CHAPTER 1 INTRODUCTION.....	1
1.1. Context, objectives, and structure of the work.....	2
1.2. Sediment characteristics.....	5
1.2.1. Size	5
1.2.1.1. Nominal diameter (d_n)	5
1.2.1.2. Area diameter (d_a)	5
1.2.1.3. Triaxial diameter (d_t).....	6
1.2.1.4. Sieve diameter	6
1.2.1.5. Sedimentation diameter (d_w).....	6
1.2.2. Shape.....	6
1.2.2.1. Shape factor (SF).....	6
1.2.2.2. Roundness.....	6
1.2.2.3. Sphericity (S_c)	7
1.2.3. Density	8
1.2.3.1. Particle density (ρ_s).....	8
1.2.3.2. Bulk density (ρ_b)	8
1.2.4. Porosity (p).....	8
1.2.5. Void ratio (e)	9
1.3. Sediment transport.....	9
1.3.1. Bedload	10
1.3.2. Suspended Load	11
1.4. Factors that Influence Sediment Transport.....	11
1.4.1. Sediment and Geology.....	12

1.4.2. Sediment and Geomorphology.....	12
1.4.3. Sediment and Organic Factors.....	12
1.4.4. Water Flow.....	12
1.4.5. Weather Events and Water Level	13
1.4.6. Human Influence.....	13
1.5. The threshold of motion	13
1.5.1. Stress balance	14
1.5.2. Critical shear stress	15
1.5.3. Shields diagram.....	16
1.6. Predictions of bedload transport.....	17
1.7. Bed layers.....	19
1.7.1. Two-layer model	21
1.8. Morphological evolution.....	21
1.8.1. Analytical model	22
1.8.1.1. Eigenvalue analysis and approximation	24
1.9. Experimental studies.....	27
CHAPTER 2 EXPERIMENTAL SET-UP AND METHODS OF DATA ACQUISITION.....	29
2.1. Experimental set-up.....	30
2.1.1. Experimental channel	30
2.1.2. Water feeding and recirculation system	32
2.1.3. Sediment material.....	33
2.2. Measurements	34
2.2.1. Sediment inflow discharge.....	35
2.2.1.1. Image processing: PIV (Particles Image Velocimetry)	35
2.2.1.2. Calibration process	40
2.2.2. Riverbed elevation detection.....	44
2.2.2.1. Image processing: Bed detection using Sobel Operator	45
2.2.2.2. Image processing: Bed detection using Motion detection.....	45
2.2.2.3. Comparison between both methods for detection of the bed	50
2.2.3. Water surface elevation detection	51
2.2.3.1. Image processing: monitoring the piezometers' data.....	52
2.2.3.2. Image processing: water surface detection using Motion detection.....	52
2.2.4. Calculation of sediment amount inside the collector.....	53
2.3. Evolution of the main system from parent thesis work	54
2.4. Experimental procedure	55
2.4.1. Pre-experiment phase.....	55
2.4.2. Experiment phase	55
2.4.3. Post-experiment phase.....	56

CHAPTER 3 INITIAL SEDIMENT TRANSPORT CAPACITY AND INCIPIENT MOTION	57
3.1. Introduction	58
3.2. Estimation of the initial sediment transport capacity	59
3.2.1. Meyer-Peter and Müller formula (MPM formula)	59
3.2.2. SC experiments	62
3.2.3. Collector method	65
3.2.4. Monitoring method	68
3.2.5. Comparison of the estimations.....	72
3.3. Incipient motion, estimation of the critical water discharge	76
CHAPTER 4 RESULTS OF AGGRADATION EXPERIMENTS	85
4.1. Aggradation experiments, parameters.....	86
4.2. Experimental results	87
4.2.1. Spatial and temporal evolution of the bed and water	87
4.2.2. Spatial and temporal evolution of the Froude number.....	96
4.2.3. Analysis of the aggradation wave celerity	99
4.2.4. Analysis of mass conservation	102
4.3. Summary	103
CHAPTER 5 NUMERICAL SIMULATION	106
5.1. Introduction	107
5.2. Hydro-morphologic model and numerical solver used	107
5.2.1. Model parameterization	108
5.2.1.1. Geometry	108
5.2.1.2. Hydraulics.....	109
5.2.1.3. Morphology.....	110
5.3. Comparison between numerical and experimental results	113
5.4. Calibration of the model	118
5.4.1. Modification of the bedload factor	118
5.4.2. Modification of the Manning's coefficient	122
5.4.3. Final calibration of the model.....	122
5.5. Discussion on the roughness of the channel	129
CHAPTER 6 SUMMARY AND CONCLUSIONS.....	131
BIBLIOGRAPHY.....	138
APPENDIX	142

LIST OF FIGURES

Figure 1.1. Two-dimensional particle images showing definitions for radii of individual corner ($r_1, r_2 \dots r_n$) and the maximum inscribed circle (R)	7
Figure 1.2. Bedload particles travel with water flow by rolling, sliding, or bouncing along the bottom (Fondriest Environmental 2014).	10
Figure 1.3. The lighter particles travel by flow as suspended load (Fondriest Environmental 2014).	11
Figure 1.4. Schema of a particle subjected to an instantaneous hydrodynamic force (Dey 2014)	14
Figure 1.5. Shields diagram depicts critical Shields number (τ_c^*) as a function of shear Reynolds number (Re^*) (Dey 2014)	17
Figure 1.6. Comparison between the bedload transport rate according to Meyer-Peter formula, Einstein's calculation, and laboratory data (Chanson 2004)	19
Figure 1.7. A gravity bed of loose sediment grains (Southard 2019)	19
Figure 1.8. The schema of the layers in bedload transport.....	20
Figure 1.9. The flow velocity distribution when dealing with bedload layer.	20
Figure 1.10. Two-layer model scheme.....	21
Figure 1.11. Comparison of exact and approximate eigenvalues: (a) in region outside $Fr = 1$; (b) close to $Fr = 1$. Circles mark exact values, dashed lines are used for approximation by Lyn and Altinakar 2002, and continuous lines are used for the proposed approximation equation 1.45 (Goutière et al. 2008)	26
Figure 2.1. schematic presentation of the experimental facility (Unigarro Villota, 2017).....	30
Figure 2.2. Artificial channel.	30
Figure 2.3. Laser distance meter fixed to the channel.	31
Figure 2.4. The relationship between the laser reading and the channel slope (Unigarro Villota, 2017).	31
Figure 2.5. Upstream tank.	32
Figure 2.6. Monitored collector located at the downstream of the channel.....	32
Figure 2.7. Guillotine valve and flow meter.	33
Figure 2.8. PVC grains are used as sediment particles.	33
Figure 2.9. (a) Hopper. (b) Selector vibration intensity level.	35

Figure 2.10. Camera positioned above the vibrating channel.....	36
Figure 2.11. (a) Frame extracted from the video. (b) Extracted frame after the correction of the distortion.....	36
Figure 2.12. (a) First photo selected ($F1$). (b) second photo selected ($F2$).	37
Figure 2.13. Graphical explanation of the jump and step parameters, where the values are selected as an example and equal to 5 and 1, respectively.	37
Figure 2.14. Selected working area.....	38
Figure 2.15. Working area and its x and y directions.	39
Figure 2.16. The width of the vibrating channel.....	39
Figure 2.17. An example of the temporal evolution of the velocity.....	40
Figure 2.18. (a) curves for showing the effect of vibration level and opening height on $Qsin$. (b) the corresponding error bars.....	41
Figure 2.19. (a) curves for showing the effect of vibration level and opening height on $Qsin$. (b) the corresponding error bars (Heydari, 2020).....	42
Figure 2.20. (a) curves for showing the effect of vibration level and opening height on $Qsin$. (b) the corresponding error bars (Unigarro Villota, 2017).....	43
Figure 2.21. The transfer function and its curve fitted to the white points which are related to the experiments of the preliminary campaign for the calibration process.	43
Figure 2.22. An example of the temporal evolution of the velocity.....	44
Figure 2.23. Cameras positioned in front of the channel.....	44
Figure 2.24. (a) photo of the channel before applying the Sobel operator. (b) photo of the channel after applying the Sobel operator.....	45
Figure 2.25. (a) Frame extracted from video. (b) Extracted frame after the correction of the distortion.....	46
Figure 2.26. (a) First photo selected ($F1$). (b) second photo selected ($F2$).	46
Figure 2.27. The processed photo showing the motion with black color (threshold value=0.04).	46
Figure 2.28. Schematic representation of the moving window from its initial position.....	47
Figure 2.29. (a) The selected column is shown in red for showing its related signal. (b) The signal along the selected column with a red dot on it representing the location of the center of the moving window when the moving window leaves the black layer completely.	48
Figure 2.30. The produced bed profile shown in red.	48

Figure 2.31. Error sources related to (a) the noises, (b) the lack of visibility, and (c) the motion of other objects.....	49
Figure 2.32 The detected bed profile after correction of the outliers.	49
Figure 2.33. The blue line shows the profile before smoothing, and the red line shows the profile after smoothing.	50
Figure 2.34. (a) Spatial evolution of the bed in a specific time. The blue line is produced by using motion detection, and the red line is produced by using the Sobel operator. (b) Temporal evolution of the bed in a specific section of the channel. The blue line is produced by using motion detection, and the red line is produced by using the Sobel operator.	50
Figure 2.35. The green line shows the bed profile detected by using motion detection, and the red line shows the bed profile detected by using the Sobel operator.	51
Figure 2.36. Piezometers pipes.....	51
Figure 2.37. (a) Image of the piezometer. (b) Negative image. (c) Binary image (Zanchi, 2018).	52
Figure 2.38. (a) The selected column, shown in red, for showing its related signal. (b) The signal along the selected column with a red dot on it representing the location of the center of the moving window when the moving window enters the black layer. (c) The produced water surface profile, shown in blue. (d) The detected water surface profile after correction of the outliers.....	53
Figure 2.39. The polygon created with the selected points to represent the shape of sediments inside the collector.....	54
Figure 3.1. Temporal evolution of sediment inflow discharge for experiment SC3, obtained from PIV process.....	63
Figure 3.2. Temporal evolution of the bed for experiment SC3, obtained from the bed detection process.	64
Figure 3.3. The sediment volume inside the collector at different times for experiment AE6....	66
Figure 3.4. The sediment transport capacity for experiment AE6, calculated with the collector method.....	66
Figure 3.5. Turbulent flow inside the monitored collector	67
Figure 3.6. The monitored bed profile is shown in blue, and the constantly extended part is shown in red. Experiment: AE6, time: 100 sec. The area under the whole profile is considered as the $A(t = 100 \text{ sec})_{bed}$	68

Figure 3.7. The monitored bed profile is shown in blue, and the linearly extended part is shown in red. Experiment: AE6, time: 100 sec. The area under the whole profile is considered as the $A(t = 100 \text{ sec})_{bed}$	69
Figure 3.8. Measured volume of the sediment deposited in the bed with respect to the reference using two scenarios for experiment AE6. The calculations of the $V(t)_{measured \text{ bed}}$ is done at every 5-sec time interval.....	69
Figure 3.9. The linear line fitted to the measured volume of sediment deposited in the bed, experiment AE6, Case CU1, $t_1 = 0$ and $t_2 = 55 \text{ sec}$	70
Figure 3.10. The linear line fitted to the measured volume of sediment deposited in the bed, experiment AE6, Case CU2, $t_1 = 30 \text{ sec}$ and $t_2 = 55 \text{ sec}$	71
Figure 3.11. The linear line fitted to the measured volume of sediment deposited in the bed, experiment AE6, Case IU1, $t_1 = 0$ and $t_2 = 55 \text{ sec}$	71
Figure 3.12. The linear line fitted to the measured volume of sediment deposited in the bed, experiment AE6, Case IU2, $t_1 = 30 \text{ sec}$ and $t_2 = 55 \text{ sec}$	71
Figure 3.13. Comparison between the initial sediment transport capacities obtained from the different methods.....	73
Figure 3.14. Comparison between the results of SC, monitoring_CU1, and collector methods .	75
Figure 3.15. Positions of the three metallic plates along the channel (Zucchi 2018)	79
Figure 3.16. Flowmeter is not able to measure very low water discharge and shows zero value (Heydari 2020).	80
Figure 3.17. The erosion phenomenon at the lateral sides of the channel during a trial incipient motion experiment with a low water discharge (Heydari 2020).....	81
Figure 3.18. Experimental results from previous studies, performed in the Politecnico di Milano.	81
Figure 3.19. Extrapolation from previous data to estimate Q_c , using a polynomial of order 2 (trial 1).	82
Figure 3.20. Extrapolation from previous data to estimate Q_c , using a polynomial of order 3 (trial 2).	83
Figure 4.1. Spatial evolution of bed and water at the selected times for experiment AE5 with overloading ratio equal to 2.92 and water discharge equal to 5 l/s.....	88
Figure 4.2. Temporal evolution of bed and water at the selected sections for experiment AE5 with overloading ratio equal to 2.92 and water discharge equal to 5 l/s.....	89
Figure 4.3. Spatial evolution of bed and water at the selected times for experiment AE7 with overloading ratio equal to 1.075 and water discharge equal to 7 l/s.	90

Figure 4.4. Temporal evolution of bed and water at the selected sections for experiment AE7 with overloading ratio equal to 1.075 and water discharge equal to 7 l/s.	91
Figure 4.5. Degradation phenomenon at the downstream of the channel. Experiments AE1-8, time: end of the experiments	92
Figure 4.6. The sketch of the degradation procedure in the downstream part of the channel ..	93
Figure 4.7. Color gradient graphs for experiment AE5. (a) bed evolution in space and time (b) water evolution in space and time	94
Figure 4.8. Color gradient graphs for experiment AE7. (a) bed evolution in space and time (b) water evolution in space and time	95
Figure 4.9. Color gradient graph for Froude number, experiment AE1.	97
Figure 4.10. Color gradient graph for Froude number, experiment AE5.	97
Figure 4.11. Color gradient graph for Froude number, experiment AE8.	98
Figure 4.12. Schematic representation of the two types of sediment front: a) dispersive type, b) translating type (Zanchi 2018).	99
Figure 4.13. Lines fitted to the borders between the colors of the color gradient graphs in the upstream part, experiment AE8.	100
Figure 4.14. The plot of the x-coordinate of aggradation heights and their corresponding time and the fitted linear lines, experiment EA8.....	100
Figure 4.15. The plot of aggradation wave celerity for different aggradation heights in different experiments.	101
Figure 4.16. The plot of normalized aggradation wave celerity for different normalized aggradation heights in different experiments.	102
Figure 5.1. Characteristics of the channel section.....	108
Figure 5.2. The scheme of the experimental and simulated channel	109
Figure 5.3. The sediment graph corresponding to the experiment AE2, used as the upstream boundary condition in the simulated channel.....	111
Figure 5.4. Spatial evolution of bed and water at the selected times for experiment AE5 with overloading ratio equal to 2.92. The experimental results are compared to the numerical ones.....	114
Figure 5.5. Temporal evolution of bed and water at the selected points for experiment AE5 with overloading ratio equal to 2.92. The experimental results are compared to the numerical ones.....	115

Figure 5.6. Spatial evolution of bed and water at the selected times for experiment AE7 with overloading ratio equal to 1.075. The experimental results are compared to the numerical ones..... 116

Figure 5.7. Temporal evolution of bed and water at the selected points for experiment AE7 with overloading ratio equal to 1.075. The experimental results are compared to the numerical ones..... 117

Figure 5.8. Spatial evolution of bed and water at the selected times for experiment AE5. The experimental results are compared to the numerical ones obtained by applying the new modified bedload factor. 120

Figure 5.9. Spatial evolution of bed and water at the selected times for experiment AE7. The experimental results are compared to the numerical ones obtained by applying the new modified bedload factor. 121

Figure 5.10. Spatial evolution of bed and water at the selected times for experiment AE5. The experimental results are compared to the numerical ones obtained by applying the final calibration parameters..... 124

Figure 5.11. Temporal evolution of bed and water at the selected points for experiment AE5. The experimental results are compared to the numerical ones obtained by applying the final calibration parameters..... 125

Figure 5.12. Spatial evolution of bed and water at the selected times for experiment AE7. The experimental results are compared to the numerical ones obtained by applying the final calibration parameters..... 126

Figure 5.13. Temporal evolution of bed and water at the selected points for experiment AE7. The experimental results are compared to the numerical ones obtained by applying the final calibration parameters..... 127

Figure 5.14. Spatial evolution of bed and water at the downstream part for experiment AE7. 128

Figure 5.15. Temporal evolution of bed and water at the point 4.9 m far from the upstream, for experiment AE7..... 128

LIST OF TABLES

Table 1.1. The empirical and semi-empirical formulation for bedload transport (Chanson 2004)	18
Table 2.1. The type and number of cameras used for each type of measurement for each experiment.....	34
Table 2.2. The type and number of cameras used for each type of measurement for each experiment.....	34
Table 2.3. Detail of the vibration level and the opening height for the preliminary campaign...	41
Table 2.4. The evolution of data acquisition procedure.....	55
Table 3.1. The results of the estimation of the initial sediment transport capacity for experiment series with $Q = 7 \text{ l/s}$, using Brownlie and Van Rijn approaches and applying MPM formula.....	61
Table 3.2. The results of experiment SC3, obtained from the PIV process.....	63
Table 3.3. The estimation of initial sediment transport capacity of the channel derived from the experiment AE6 (with $Q = 7 \text{ l/s}$) and using the collector method.	66
Table 3.4. The initial sediment transport capacity of the channel obtained with different scenarios in the monitoring method, derived from experiment AE6.....	72
Table 3.5. The initial sediment transport capacity of the channel obtained using different methods.....	73
Table 3.6. The final value of Qs_0 for the experiments with $Q = 5 \text{ l/s}$. The results of the SC, monitoring_CU1, and collector methods are averaged.	75
Table 3.7. The final value of Qs_0 for the experiments with $Q = 7 \text{ l/s}$. The results of the SC, monitoring_CU1, and collector methods are averaged.	75
Table 3.8. Estimation of the critical water discharge using Brownlie (1981) and Van Rijn (1984) formulae.....	77
Table 3.9. Estimation of the modified critical Shields parameter using Armanini and Scotton formula.....	78
Table 3.10. The critical water discharge obtained experimentally by Zucchi (2018).....	80
Table 3.11. The dimensionless sediment transport capacity of the channel per unit width	82
Table 3.12. The critical water discharge is obtained from an extrapolation operation (trial 1). .	83
Table 3.13. The critical water discharge is obtained from an extrapolation operation (trial 3)..	83

Table 3.14. All values related to the critical water discharge, estimated by different methods.	83
Table 4.1. The parameters of experiments AE1 -AE8.	86
Table 4.2. Celerity of aggradation wave for different aggradation heights in different experiments.	101
Table 4.3. Results of mass conservation analysis.	103
Table 5.1. Material properties used in the experimental and numerical models.	110
Table 5.2. The required boundary conditions according to the theory to solve the SVE and Exner equations.	112
Table 5.3. Numerical parameters corresponding to each experiment.	113
Table 5.4. Modified bedload factor for different experiments, obtained from making equality between the experimental Q_{s0} and the numerical one.....	119
Table 5.5. Selected calibration parameters for each experiment.	123

ABSTRACT (ENGLISH)

Floods are among the adverse natural events with the possibility of turning into a disaster, causing economic losses and casualties. Flood events can become even more dangerous with the presence of intense sediment transport since the morphologic response of a river can determine erosion and deposition in different areas. In-bed structures can be undermined in erosional reaches, while the riverbed elevation increases in a depositional reach and, consequently, the conveyance of the river decreases. The dynamics of the morphologic processes may be different in lowland and upland reaches due to different sediment, slopes, and flow properties.

The aim of the thesis is to study, experimentally and numerically, the bed aggradation process in an overloaded channel with a supercritical flow regime. The aggradation experiments of the study are executed in the Mountain Hydraulics Laboratory of the Politecnico di Milano, located in the Lecco campus. These experiments are characterized by an inflow discharge of sediment material that is larger than the sediment transport capacity, resulting in the deposition of sediment in the studied channel. A series of aggradation experiments are realized varying the water discharge and the inflow sediment discharge. Beyond the observation of the phenomenon in progress, the experiments provide quantitative information. For the purpose of experimental data acquisition, different parts of the experimental system are monitored with different cameras, and measurements are done through some image processing methods, appropriately devised. The experimental campaign is completed by experiments specifically devoted to determining the sediment transport capacity of the flow at the initial condition.

The time scales of a considered scenario are of great importance for the goal of emergency planning. For the present experiments, this consideration stimulates a study of the propagation of a sediment aggradation wave, for which a front can be identified, and its celerity can be determined. The runs performed in this thesis enable preliminary considerations to be made on how a front celerity may depend on the control parameters of the system.

The aggradation process studied by the experimental tests is also reproduced with a numerical simulation. The software used to implement the numerical model is BASEMENT, provided by ETH Zurich. In order to obtain a good correspondence between numerical and experimental results, two parameters are calibrated: the Manning coefficient and a bedload factor for the computation of the sediment transport capacity. Depending on the water discharge, different values for calibration factors are obtained.

Keywords: aggradation, sediment transport capacity, inflow sediment discharge, sediment propagation, sediment front celerity, experimental model, numerical model, calibration factors.

SOMMARIO (ITALIANO)

Le alluvioni sono tra gli eventi naturali avversi con la possibilità di trasformarsi in un disastro, causando perdite economiche e vittime. Gli eventi alluvionali possono diventare ancora più pericolosi con la presenza di un intenso trasporto di sedimenti poiché la risposta morfologica di un fiume può determinare erosione e deposizione in diverse aree. Nei tratti in erosione le fondazioni delle strutture in alveo possono essere instabilizzate, mentre in un tratto deposizionale l'aumento della quota del fondo riduce la capacità di portata dell'alveo. La dinamica dei processi morfologici può essere diversa nei corsi d'acqua di pianura e di montagna, a causa delle differenti proprietà dei sedimenti, pendenze e flussi.

Obiettivo della tesi è studiare, sperimentalmente e numericamente, il processo di sovralluvionamento del letto in un canale con flusso supercritico. Gli esperimenti morfologici dello studio sono eseguiti nel Laboratorio di Idraulica Montana del Politecnico di Milano, situato nel campus di Lecco. Questi esperimenti sono caratterizzati da un apporto di materiale solido maggiore della capacità di trasporto del flusso idrico, con conseguente deposito di sedimento nel canale studiato. Viene realizzata una serie di esperimenti di sovralluvionamento variando la portata idrica e l'apporto dei sedimenti in ingresso. Oltre all'osservazione del fenomeno, gli esperimenti forniscono informazioni quantitative. Ai fini dell'acquisizione dei dati sperimentali, diverse parti del sistema sperimentale vengono monitorate con alcune telecamere e le misurazioni vengono effettuate attraverso metodi di elaborazione delle immagini, opportunamente ideati. La campagna sperimentale è completata da prove specificatamente dedicate alla determinazione della capacità di trasporto dei sedimenti per il flusso nelle condizioni iniziali.

Le scale temporali di uno scenario considerato sono di grande importanza per la gestione dell'emergenza. Per i processi qui considerati, questo stimola lo studio della propagazione di un'onda di deposizione dei sedimenti, per la quale è possibile identificare un fronte e determinarne la celerità. Le prove svolte in questa tesi consentono di fare considerazioni preliminari su come una celerità del fronte di deposizione possa dipendere dai parametri di controllo del sistema.

Il processo morfologico studiato nelle prove sperimentali viene inoltre riprodotto con una simulazione numerica. Il software utilizzato per implementare il modello numerico è BASEMENT, fornito dall'ETH di Zurigo. Al fine di ottenere una buona corrispondenza tra risultati numerici e sperimentali, vengono calibrati due parametri: il coefficiente di Manning e un coefficiente da applicare a una formula per il calcolo della capacità di trasporto dei sedimenti. A seconda della portata idrica, si ottengono valori diversi per i fattori di calibrazione.

Parole chiave: sovralluvionamento, capacità di trasporto dei sedimenti, apporto solido, propagazione dei sedimenti, celerità del fronte dei sedimenti, modello sperimentale, modello numerico, fattori di calibrazione.

ABSTRACT (PERSIAN)

سیلاب ها از جمله حوادث طبیعی زیان آور هستند که احتمال تبدیل شدن به یک فاجعه با خسارات اقتصادی و تلفات جانی را دارند. شرایط می تواند حتی خطرناک تر شود، زمانی که حجم زیادی از رسوبات و سنگدانه ها در مسیر جریان آب حرکت کنند. وجود حجم زیادی از این ذرات و ته نشینی آنها در مسیر رودخانه می تواند باعث کاهش ظرفیت رودخانه و در نتیجه افزایش سطح آب رودخانه شود؛ بنابراین، خطر وقوع سیلاب در این حالت به مقدار قابل توجهی می تواند افزایش یابد .

هدف این پایان نامه، مطالعه ی پروسه ی ته نشینی و رسوب گذاری در بستر کانال، هم به صورت آزمایشگاهی و هم به صورت شبیه سازی عددی، در جریان های فوق بحرانی است. آزمایش های مربوط به ته نشینی و رسوب گذاری ذرات در کانال، در آزمایشگاه هیدرولیک دانشگاه پلی تکنیک میلان (واحد لکو) انجام می شوند. آنچه این آزمایش ها را از هم تفکیک می کند، مقدار دبی ذرات ورودی به کانال و همچنین دبی آب ورودی به کانال می باشد. دبی ذرات ورودی به کانال به گونه ای انتخاب می شوند که از مقدار ظرفیت انتقال ذرات کانال بیشتر باشد، که در نتیجه منجر به ته نشینی و رسوب ذرات در بستر کانال می شود. علاوه بر مشاهده ی پدیده ی رسوب گذاری در بستر کانال در طول یک آزمایش، یک سری نتایج کمی هم از آزمایشات حاصل می شوند. این نتایج با اعمال تکنیک های مختلف از جمله، فیلم گرفتن از قسمت های مختلف کانال در طول آزمایش، انجام اندازه گیری های مربوطه با استفاده از پردازش تصویرهای استخراج شده از فیلم ها و استخراج پروفایل های آب و بستر بدست می آیند. علاوه بر آزمایش های مربوط به رسوب و ته نشینی ذرات در کانال، یک سری آزمایش های دیگر هم برای تعیین ظرفیت انتقال ذرات کانال انجام می شوند.

بخشی از ذرات ورودی به کانال در بستر کانال ته نشین می شوند و بخشی از آن به انتهای کانال انتقال می یابند. حال، از دیدگاه برنامه ریزی اظطراری، زمان رسیدن موج رسوبات به انتهای کانال از اهمیت ویژه ای برخوردار است. در این خصوص، در این مطالعه، تحقیقی در خصوص سرعت حرکت جبهه ی موج ذرات در امتداد کانال انجام می شود.

آزمایشات انجام شده برای مطالعه پروسه ی رسوب گذاری در کانال، با یک مدل عددی هم شبیه سازی می شوند. نرم افزار مورد استفاده برای ساخت مدل عددی، BASEMENT می باشد. برای اینکه مطابقت مناسبی بین نتایج عددی و نتایج آزمایشگاهی حاصل شود، دو پارامتر کالیبره می شود: یکی ضریب مانینگ و دیگری ضریب استفاده شده در محاسبه ی ظرفیت انتقال ذرات کانال. مقدار پارامترهای کالیبراسیون به دبی آب ورودی به کانال بستگی دارد.

کلید واژه ها:

رسوب گذاری، جریان فوق بحرانی، ظرفیت انتقال ذرات کانال، سرعت جبهه ی موج ذرات، دبی ذرات ورودی به کانال، مدل آزمایشگاهی، مدل عددی، پارامترهای کالیبراسیون.

CHAPTER 1

INTRODUCTION

1.1. Context, objectives, and structure of the work

In general, nature tends to maintain equilibrium, so it responds to any situation that disturbs the balance in order to return to a stable state. As a natural system is in equilibrium, the river network is controlled by some parameters such as path slope, flow discharge, sediment characteristics, and sediment discharge. Any natural disturbances such as heavy rains, floods, and landslides or artificial disturbances such as hydraulic structures (dams, dike) in aquatic systems cause disruption of the hydraulic regime and changes in the sediment transport rate. The change in sediment load rate depends mainly on the fluid flow conditions, which may cause aggradation or degradation in the bed of the flow path. The flowing in the natural aquatic bodies has essential roles, it is responsible for scouring the rivers' bed, transporting the sediments, and grains' deposition, eventually the river morphology would be changed (Chanson 2004). In the mountainous area, many rivers can be found with a supercritical flow regime because of the high slope of the riverbed. Another example of having a supercritical flow regime is the alluvial rivers that are often subcritical; however, in the event of flooding or severe changes in river morphology, it can cause changes in flow rate and water level, resulting in a supercritical flow.

Furthermore, the presence of changes in the bed's slope due to erosion and sediment deposition can cause changes in the flow regime (Bellal 2012). These water bodies' changes have critical economic effects such as reservoir reduction of the dam, scouring the bridge's piles, weirs' wall, and channel banks. Some adverse effects in water bodies like scouring the foundation of hydraulic infrastructure, filling shipping lanes with sediments, and reducing dam tank capacity are because of engineers' incapability to estimate the amount of sediment transportation (Chanson 2004).

The characteristics of flowing streams in mountainous areas are different from those of lowland rivers. Some of the mountain rivers' characteristics are their steep and non-monotonic slopes and small catchments. As mentioned before, the mountain rivers often have a supercritical flow regime, which causes mountain-born sediments to enter the riverbed and be transported downstream. Because of favorable mountain living conditions, many residential areas are situated along mountainous rivers. Life in these areas is not without danger because an erosional reach can undermine the structures, and a depositional reach can raise the flood water levels; as a result, it increases the flood hazard. Therefore, the existence of warning systems, protection measures, and risk mitigation actions is essential. Some critical factors for introducing hazard warning systems and introducing protection methods in these areas are identifying the amount of precipitation and the quantity of sediment transferred downstream. For this context, the extent of the aggradation and degradation in supercritical and subcritical streams, as well as in the transition from one regime to another, should be recognized. In addition, it is worth mentioning that in hazard studies, the time scales of any process are important to design mitigation measures in emergencies. In a sediment transport process, the relevant time scale is

determined by how fast the morphologic process propagates, so it is essential to study the celerity of the sediment front propagation.

A research line has already been active for studying the aggradation process in the Mountain Hydraulics Lab of the Politecnico di Milano University, located in the Lecco campus. Several experimental campaigns had been conducted before to study the aggradation process in the subcritical flows. Some methods for performing the experiments and analyzing the experimental results had been developed through these campaigns (Unigarro Villota 2017; Zanchi 2018; Zucchi 2018). The main goal of these campaigns was to analyze the aggradation process by studying the sediment front characteristics, such as the sediment front propagation celerity and its corresponding height. After finishing the subcritical campaigns, a new campaign has been run to study this process in the supercritical regime. The campaign was started by Heydari (2020), and the idea was to use the methods developed for previous campaigns to study the properties of the sediment front wave in supercritical flows. Because of high uncertainties in the results, Heydari concluded that the problem is related to the low number of the experiments and the incapability of the previous methods for studying the aggradation process in supercritical flows.

The current study aims to estimate the hydro-morphologic evolution of an experimental channel in the supercritical regime, dealing with an aggradation phenomenon, where the inflow sediment discharge is higher than the initial sediment transport capacity of the channel. This study is performed in two complementary approaches: physical laboratory experimentation and numerical simulation.

Series of experimental tests are carried out for the purposes of this thesis. These experiments are divided into two categories:

- **SC experiments:** These experiments are performed to find a range for the initial sediment transport capacity (Q_{s0}) of the initial channel's bed. Since in this study, the channel's properties (bed slope, channel's cross-section, and channel's length) and sediment properties remained constant, the sediment transport capacity theoretically changes only with water discharge. As a result, an SC experiment must be performed for each water discharge to estimate the corresponding sediment transport capacity.
- **AE experiments:** In these experiments, the bed and water's temporal and spatial evolution are studied for further analyses of the aggradation process. The procedure is to set a water discharge (Q); then, for each water discharge, different experiments are performed with different sediment inflow discharges (Q_{sin}). These sediment inflow discharges are chosen in a way that the loading ratio (Lr) be greater than one to have aggradation ($Lr = Q_{sin}/Q_{s0} > 1$).

It should be mentioned that in the presented work, two series of experiments in terms of water discharge are performed, the experiments with water discharge equal to 5 l/s and the ones with water discharge equal to 7 l/s.

INTRODUCTION

At the end of the experimental parts, the results are compared and analyzed to investigate the possible correlation between the obtained outcomes and the boundary conditions.

The final part of this study is devoted to comparing the obtained results from the experimental part and numerical simulation to calibrate and validate the numerical model; moreover, each method's advantages and disadvantages are discussed.

For the reasons mentioned in the previous thesis conclusion (Heydari 2020), the experimental methods have been updated in the present thesis to analyze the aggradation process in the supercritical flows. Therefore, some of the data acquisition methods are updated, and the cameras for the bed detection part are changed to increase the quality of recordings in terms of distortion and noise. Also, a new type of experiments (SC) is introduced for the estimation of the initial sediment transport capacity (Q_{s0}), and a new method is introduced for the recognition of the sediment front.

The present dissertation composes of six chapters:

Chapter 1

General introduction of the work and introduce the concept of the sediment transport phenomenon.

Chapter 2

The description of the laboratory equipment used in the experiments, the methods for data acquisition, and a brief description of the experimental procedures are presented.

Chapter 3

Some analytical and experimental (SC Experiments) approaches to obtain the sediment transport capacity are introduced, the sediment transport capacity for each approach is calculated, and the comparison among them is presented. Also, the incipient motion condition and estimation of the critical water discharge are discussed.

Chapter 4

The obtained results of the morphologic experiments (AE experiments) are analyzed and discussed.

Chapter 5

The results for the numerical simulation of the experiments and their calibrations with respect to the experimental results are presented.

Chapter 6

The summary and conclusion of the study and some suggestions for future studies are presented.

1.2. Sediment characteristics

A wide range of materials can be classified as sediment consisting of minerals, organic and inorganic, transmitted by water, wind, or ice. In addition to soil-based materials often referred to as sediment, such as clay, silt, and sand, decomposed organic matter and inorganic biogenic material are also known as sediment. Weathering and erosion are considered a source of mineral sediment, whereas organic sediment generally comes from detritus and decomposing material such as algae (Fondriest Environmental 2014). The word sediment in natural science referred to the loose particulate material found on Earth's surface from land weathering and carried away by the wind, water, or ice. In engineering terms, the particulate materials conveyed by the flow system or just possibly transferable, regardless of their origin, besides the natural sediment, are considered sediment (Southard 2019). According to this fact, weathering is a prevalent phenomenon on the Earth, and also the Earth is covered by airstream and water network; therefore, it can be possible to find the sediment across the world. Sediments play an essential role not only in the establishment of downstream deltas but also in the preservation of aquatic habitats like wetlands, pools, river channels, flood plain soils, and so on (Ziegler et al. 2014).

The sediments are characterized according to their size, shape, and density as one particle and porosity, void ratio.

1.2.1. Size

One of the essential features of the sediment particle is the size. There are several ways to describe the size property of the sediment mentioned below:

1.2.1.1. Nominal diameter (d_n)

The nominal diameter equals the diameter of a sphere having equivalent volume with the sediment:

$$d_n = \left(\frac{6V}{\pi}\right)^{1/3} \quad 1.1$$

In the equation, V shows the sediment volume.

1.2.1.2. Area diameter (d_a)

Area diameter represents the diameter of a sphere with a surface equal to the sediment:

$$d_a = \left(\frac{S}{\pi}\right)^{0.5} \quad 1.2$$

where S represents the total surface area of sediment, the flat-shaped particles are usually characterized by area diameter (Dey 2014).

1.2.1.3. Triaxial diameter (d_t)

This diameter is equal to:

$$d_t = \frac{(d_1 + d_2 + d_3)}{3} \quad 1.3$$

where d_1 , d_2 , and d_3 shows the maximum, intermediate, and minimum lengths of three axes of the particle, respectively.

1.2.1.4. Sieve diameter

The sieve diameter can be expressed in two ways. First, it is equal to the smallest size of the sieve that particle passes (d_{pass}). Second, the largest sieve size particles remain on the sieve and cannot pass (d_{ret}). As the number of sieves increases, the number of size divisions and the relative level of analytical details increase (Switzer 2013). By weighing each sieve's remaining sediment, one can obtain such information like the sieve mesh sizes, raw weights, weight percentages, and cumulative percentages, finer or coarser than the specific sieve (Switzer 2013).

1.2.1.5. Sedimentation diameter (d_w)

Sedimentation diameter is the sphere's diameter with equivalent terminal fall velocity and relative density with the sediment particle in the same sedimentation fluid under the same atmospheric pressure and temperature (Dey 2014).

1.2.2. Shape

Another physical feature of sediment grain is the particle shape. The particle shape may provide some information about the sedimentary history of the particle and its hydrodynamic behavior in the transmission environment. Sediment particles have different shapes, so several logical methods are used to classify the shape of the sediment:

1.2.2.1. Shape factor (SF)

It can be described as below:

$$SF = \frac{d_3}{\sqrt{d_1 \times d_2}} \quad 1.4$$

where d_1 , d_2 , and d_3 are the maximum, intermediate, and minimum lengths of three axes of the particle, respectively.

1.2.2.2. Roundness

Roundness is an indicator comparing the outline of the two-dimensional projection of the particle to a circle. Wadell (1932) introduced this index as below:

$$\text{Roundness} = \frac{\sum_{i=1}^n \left(\frac{r_i}{R}\right)}{n} \quad 1.5$$

where r_i shows the radius of curvature of particle corners, R is the radius of the largest surrounded sphere, and n is the number of particle corners measured. Figure 1.1 shows the schematic of the particle corners.

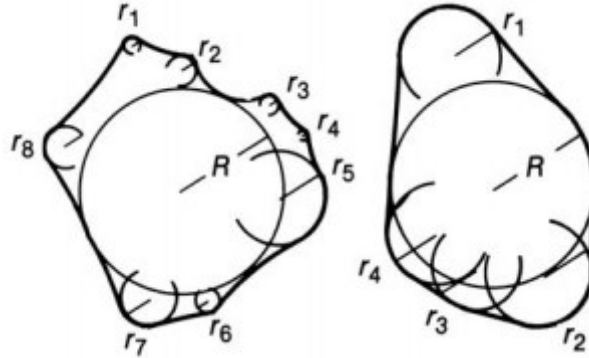


Figure 1.1. Two-dimensional particle images showing definitions for radii of individual corner ($r_1, r_2 \dots r_n$) and the maximum inscribed circle (R).

The average of the radius of the particle edges curvature to the radius of the largest circle represented by the particle is considered to be roundness (Dey 2014).

1.2.2.3. Sphericity (S_c)

Sphericity is considered as another shape parameter in the sediment analysis. Actually, the motion of a settling particle relative to a liquid is described as sphericity. Wadell (1932) describes it as a ratio of the surface of the sphere that has a volume equal to the sediment particle to the actual surface of the sediment particle. Since it is almost difficult to obtain small particles' actual surface, Wadell redefined sphericity in another way (Dey 2014).

$$S_c = \left(\frac{V}{V_c}\right)^{1/3} \quad 1.6$$

where V is the particle sediment volume, and V_c is the volume of the confined sphere. Nonetheless, the sphericity can also be estimated as:

$$S_c \approx \frac{d_n}{d_1} \quad 1.7$$

where d_n and d_1 are the nominal and maximum axes length of the particle, respectively.

Another way to calculate the sphericity is presented by Krumbein (1941) as:

$$S_c = \left(\frac{d_2 \times d_3}{d_1^2}\right)^{1/3} \quad 1.8$$

INTRODUCTION

where d_1 , d_2 , and d_3 are the maximum, intermediate, and minimum lengths of three axes of the particle, respectively. The sphericity indicator has a value ranging from 0 (nonspherical) to 1 (perfect sphere), that the most sedimentary particles falling has a value between 0.3 to 0.9.

1.2.3. Density

Density describes the mass of a unit volume of a substance. There are two basic ways to express sediment density.

1.2.3.1. Particle density (ρ_s)

The particle density describes the mass of a unit volume of sediment solids. For instance, when the particle density equals 2.65 gr/cm^3 , it means that the mass of 1 cm^3 of solid material is equal to 2.65 gr . Mineral particles have particle density between 2.60 to 2.75 gr/cm^3 , while in an equal volume, the mass of organic particles is less than mineral particles, so the particle density of organic matter is often 1.2 to 1.4 gr/cm^3 (Haan, Barfield, and Hayes 1994). Equation 1.9 shows the relationship between the particle density (ρ_s) and the specific particle weight (γ_s).

$$\rho_s = \frac{m_s}{V_s} = \frac{\gamma_s}{g} \quad 1.9$$

where m_s is the mass of the solid, V_s is the solid volume and γ_s shows the unit weight of the solid.

1.2.3.2. Bulk density (ρ_b)

The difference between bulk density and particle density is that in particle density, the mass of a unit solid volume is considered, whereas to calculate the bulk density, the mass of a total volume of the substance is used. The total volume consists of the solids and pores volume (Haan, Barfield, and Hayes 1994). The relation between the bulk density (ρ_b) and unit weight of the material (γ) is presented below:

$$\rho_b = \frac{m_s}{V_t} = \frac{\gamma}{g} \quad 1.10$$

where m_s is the mass of the solid, V_t shows the total volume, including the solid and pores volume, and γ represents the unit weight of the material.

1.2.4. Porosity (p)

The porosity is the ratio of the void volume to the total volume. It is a volume ratio, so it is dimensionless, and it is usually reported as a fraction or percentage. It can be shown as below:

$$p = \frac{V_v}{V_v + V_s} \quad 1.11$$

where V_v is the void volume, and V_s shows the solid volume.

1.2.5. Void ratio (e)

This parameter shows the volume of the void per unit volume of the solid so that it has a relationship with the porosity that can be seen as follow:

$$e = \frac{V_v}{V_s} = \frac{p}{1 - p} \quad 1.12$$

1.3. Sediment transport

The concept of sediment transport comes from applied engineering, which is used for flood management, erosional control, and watershed management, as well as economic purposes like oil and mineral extraction. Sediment can move by means of water, wind, and gravity (Chaudhry 2007). The movement of mineral and organic particles in the environment by wind or water is called sediment transport. River networks are one of the most critical aquatic environments for sediment transport so that rivers can transfer sediments from high altitudes such as mountainous areas to low heights such as plateaus and coasts, which changes the morphology of the terrain. The fluvial process consists of sediment transport that causes aggradation or degradation of the river's bed surface (Dey 2014). By employing the water discharge and sediment concentration data, the sediment load of a river can be calculated, and this value shows the amount of sediment flux carried by the stream and is usually expressed in terms of mass per unit time like tone per year (*tons/year*) (Czuba et al. 2011). Depending on the water flow intensity, the particles in the water column can be suspended when moving downstream or simply push particles along the bottom of the stream (Fondriest Environmental 2014).

By assuming the erodible, coarse, and nonadhesive particles as a bed flow channel, the weathered and abraded materials, electrostatic and electrolytic effects seen in the clay transportation are excluded (Gyr and Hoyer 2006).

There are four different ways to transport the bed materials: first, the light materials that can be raised and suspended in the water body, then in a still environment get deposited and settle again on the bed. Second, the heavier particle can be rolled on the bed when the flow is strong enough. Third, the grains with moderate weight are moved by the fluid as a two-phase flow and act like fluidized materials; and fourth, very light materials transported during the whole transportation as suspended particles. In reality, distinguish these four categories is challenging, so the materials are classified into two branches. One branch is a suspended load in which particles spend most of their transfer time as suspended particles in the flow. Another branch is the particles move near the bed surface that is called bedload. According to the sediment concentration by volume, there is sediment transport for low and high concentrations that the second one is known as two-phase flow (Gyr and Hoyer 2006).

One essential aspect of analyzing the fluvial process in the stream network is the amount of the total sediment transport rate; besides the water discharge, this value can control the river bed's dynamic stability or instability like aggradations and degradations. The total load can be

INTRODUCTION

introduced as an amount of sediment passed through a specific cross-section per unit time and width for a given flow. The total load is the summation of the bedload, suspended load, and wash load based on the particle feature. Despite the wash load basically exists in nature and is often significant, it cannot be recognized in experimental studies because determining the border of the wash load and suspended load is problematic (Dey 2014). The sediment may change its position between bedload and suspended load during the travel of the particle in the river network, according to the grain size and water discharge (Ziegler et al. 2014).

The flow mechanism over a fixed bed and a movable bed is entirely different because of the sediments' interplay with fluid and bed. The fluid causes acceleration of the particles while the bed gives deceleration to particles. A significant portion of the particle motion goes to the bed, and the flow can only recover part of the motion; therefore, most of the fluid energy transferred to particles is dissipated by the bed (Dey et al. 2012). The estimation of the bedload and suspended load represents the essential part of the sediment budgets in the watershed. This information can be employed not only to manage river systems, flood control, water quality, and water storage but also to estimate the dam reservoir filling rate and its lifetimes (Ziegler et al. 2014).

1.3.1. Bedload

The sediment portion in the river network transported by rolling, bouncing, and sliding along the stream bed is called bedload (Ziegler et al. 2014). These particles remain in contact with the river bed during transportation (Fondriest Environmental 2014). Particles do not have a uniform and continuous movement on the bed so that a particle can impact the group of the particles on the bed (Dey et al. 2012). Once the fluid's energy overcomes the resisting force arising from sediment weight and its cohesion, the bedload will happen (Fondriest Environmental 2014). As long as the flow rate is not strong enough to suspend the particles, the particles' velocity is less than the speed of the fluid around them (Dey et al. 2012). The bedload transport can be seen during the low flow rate for smaller particles and high flow rate for larger particles, and The bedload is about 5 to 20 % of the total load (Czuba et al. 2011). [Figure 1.2](#) depicts the schematic of the bedload.

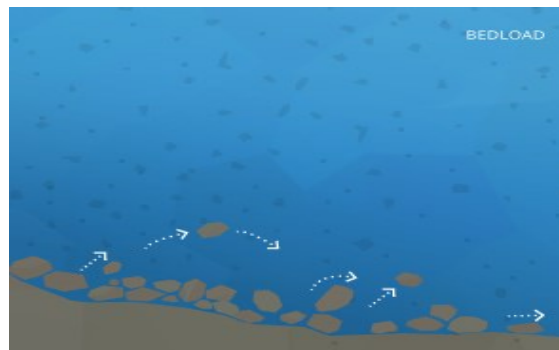


Figure 1.2. Bedload particles travel with water flow by rolling, sliding, or bouncing along the bottom (Fondriest Environmental 2014).

1.3.2. Suspended Load

The suspended load can occur when the flow rate is strong enough to raise the smaller particles of the bedload in the water column (Fondriest Environmental 2014). It should be noticed that suspended sediment is entirely different from the suspended load. Any particle suspended in the water column, regardless of whether the water is flowing or not, is called suspended sediment. On the other hand, any suspended particle in the column of water carried downstream by a stream of water is called a suspended load (Dey 2014). Since water flow causes small upward currents and turbulence, which causes smaller particles to rise in the water column, the moving water is required to create a suspended load (Ziegler et al. 2014). Water flow determines what particle size can be suspended in moving water (Dey 2014). Whenever the water flow rate is augmented, the larger particles can be more likely to be suspended in the upward current; the suspended load will also fall to the bottom and move as bedload if the flow rate subsides (Fondriest Environmental 2014). The schematic of the suspended load can be seen in [Figure 1.3](#).

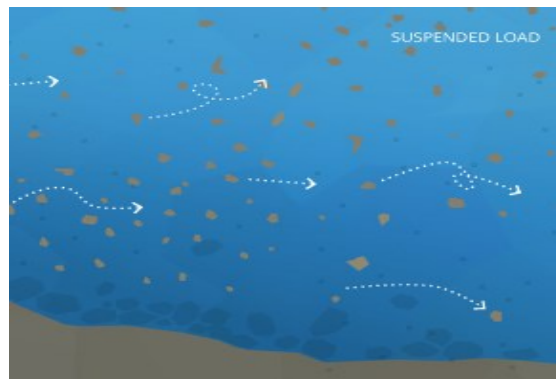


Figure 1.3. The lighter particles travel by flow as suspended load (Fondriest Environmental 2014).

It should be noticed that there is no clear border between bedload and suspended load. It means that a particle can be moved as bedload or suspended load at different moments and also can be motionless at another moment. Therefore, there is a significant overlap based on the size distribution between bedload and suspended load, even though it is evident that the suspended load particles' size is smaller than the bed load grains (Dey et al. 2012).

1.4. Factors that Influence Sediment Transport

Sediment transport can be affected by different factors. The geology, geomorphology, and organic elements are the sediment's origin and continuously change the sediment load; therefore, the sediment transport will change. These factors affect the amount, size, and material of the transported particles in the specific water network. Besides the mentioned items, some external factors like changing the water flow, water level, precipitation, and human effect influence the sediment transport (Fondriest Environmental 2014).

1.4.1. Sediment and Geology

The nature of the mineral-based sediment is the fundamental issue that directly relates to the surrounding environment. It means that the location and the geology of the ground show the exact nature of the sediment. For instance, the mountain ranges produce the glacial type of sediment, while the soil-based sediment can be found in the low-lying rivers, and the high-flow streams are prone to convey the local gravel, pebbles, and small stones. The soft stones can easily erode and carry through water networks, but the harder rocks are less likely to erode and move by the river. So the geology of the environment can show the arrangement of sediments to some extent.

1.4.2. Sediment and Geomorphology

The quantity of sediment entering the water and its transporting distance is related to the terrain whereby rivers flow. The bedrock and most human-made channels are resistant to be rapidly eroded, so they are less likely to increase the sediment load. These kinds of channels that do not add the sediment are called non-alluvial channels, but most streams are known as alluvial rivers that can open their path by washing the Earth's surface (Fondriest Environmental 2014). The waterway's depth and width in an alluvial stream depend on its strength and the material that forms the channel's borders. Since some part of the sediment load is taken from the sides and bottom of the channel, rivers flowing through soft soil generally have a higher sediment transport load than the rivers passing through bedrock.

On the other hand, sediment transport can change the shape of the terrain. It can move some materials from steep upstream and deposits them in mild downstream. Therefore, sediment transport and geomorphology interact with each other.

1.4.3. Sediment and Organic Factors

Another source of sediment besides mineral-based sediment is organic sediment. Organic sediments are derived from algae, plants, and other organic matters falling in the flow. In addition to the location, the season influences the amount of organic sediments. A study reported that the organic part of the suspended sediment is higher in February than in November (McNally and Mehta 2009).

1.4.4. Water Flow

One of the most critical factors in sediment transport is water discharge. In order to initiate the sediment motion, flow discharge is required (Fondriest Environmental 2014). The sediments are lifted by the water flow, transferred, and finally deposited downstream, where the flow in this location does not have enough strength to carry the particles. The high water discharge can convey more and heavier particles than the small water flow because the more increased flow

has greater erosional energy. Water discharge can be described based on two ways. It can be calculated as a cross-section's area multiplied by the flow velocity, or it can be described as water volume passed from a specific cross-section in unit time.

1.4.5. Weather Events and Water Level

As mentioned before, sediment transport is affected by the water flow. The Earth's features (like the slope of the terrain) and the water level in the channel change the water flow. Also, the water level depends on the weather event like rainfall. The slight or heavy precipitation can change the stream's water level, and it causes to rise in the water flow, so the sediment transport is increased (Fondriest Environmental 2014).

1.4.6. Human Influence

Sediment loading and sediment transport will be affected by anthropogenic factors such as dams and changed land use. Human land utilization, such as urban areas, farming, and building plants, affects sediment load but does not affect the transport rate. These consequences are indirect because heavy rainfall or flooding is necessary to transport produced sediment into the waterway. Therefore, the anthropogenic use of soil is a significant contributor to over-sedimentation caused by erosion and runoff. This enhancement happens due to disturbed lands like logging, mining, building, and agricultural sites that usually reveal and weaken the soil's surface by removing the natural land cover. This loose land can then be easily transported by rainfall and runoff into a nearby river or stream.

1.5. The threshold of motion

Over the past decades, practical experiments and theoretical measures have been performed to determine the threshold bed shear stress at the particle's incipient motion. In order to predict the sediment transport rates, surplus shear stress has played a vital role (Simões 2014).

In the sediment transport concept, the hydrodynamic force exerted to sediment by the flow and the resistance force due to the submerged weight are used to formulate the non-dimensional threshold bed shear stress known as threshold shields parameter. The constants and coefficients in this formulation are determined experimentally, so all analytical models related to the threshold bed shear stress are semi theoretical models. Also, there are some experimental formulas introduced by different researchers (Dey 2014).

Shields (1936) proposed a semi theoretical method to estimate the threshold incipient motion for homogeneous particles, noncohesive materials, and horizontal bed (Zucchi 2018). He noticed that there is no particle movement when the velocity is too low. The sediments start to move when the destabilizing force on the particles overpass the stabilizing force once the flow velocity exceeds a particular value. The threshold of sediment motion can be measured by balancing the

INTRODUCTION

destabilizing force (in this case, it is drag force) and the stabilizing resistance (in this case, it is exerted by neighboring particles on the particle under consideration) (Langmaak 2013; Dey 2014). The schema of forces exerted on the particle has been shown in [Figure 1.4](#).

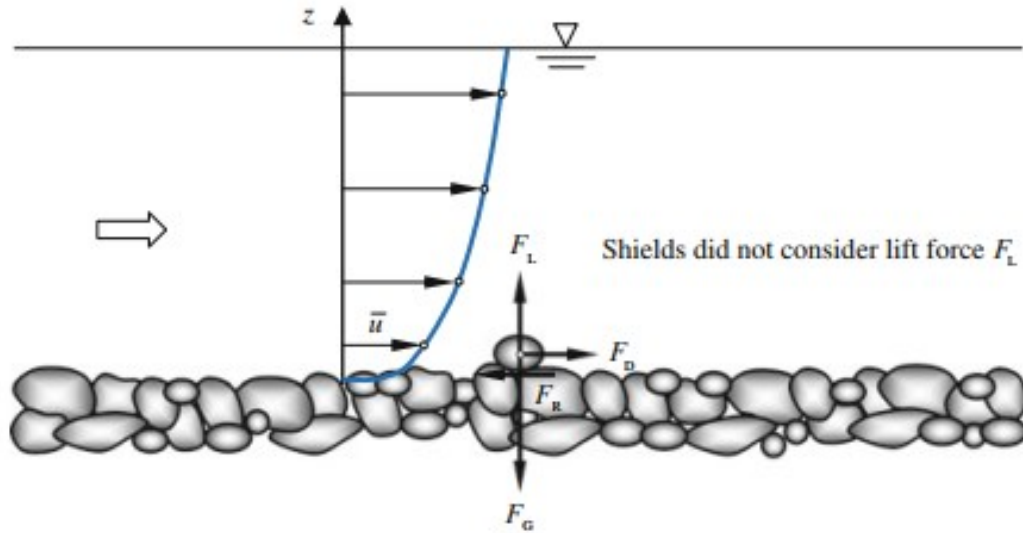


Figure 1.4. Schema of a particle subjected to an instantaneous hydrodynamic force (Dey 2014).

The force system consists of drag force (F_D), submerged weight (F_G), frictional resistance (F_R), and lift force (F_L). Shields neglected the lift force (F_L) in his calculation. \bar{u} is the local flow velocity.

1.5.1. Stress balance

A particle that is currently in stable condition on the bed's surface will start to move due to the fluid flow when the bed shear stress (τ) applied by flow overpasses the critical shear stress (τ_c). Therefore, the incipient movement happens when:

$$\tau = \tau_c \quad 1.13$$

Typically, the dimensionless numbers are used to represent this criterion:

$$\tau^* = \tau_c^* \quad 1.14$$

where τ^* and τ_c^* are dimensionless shear stress and dimensionless critical shear stress, respectively. The dimensionless shear stress (τ^*) is known as Shield stress and given by:

$$\tau^* = \frac{\tau}{(\rho_s - \rho)gd} \quad 1.15$$

where ρ_s represents the solid density, ρ represents the fluid density g is the gravitational acceleration, d shows the sediment diameter.

These equations are used for granular sediment, and they do not work for clays and muds because these sediments do not match the geometric simplification in equations. Also, the electrostatic force that can be found in the clay sediments is not considered in these equations.

The equations are designed for riverine sediment transport carried along with the fluid flow like streams, canals, or other open channels.

1.5.2. Critical shear stress

The drag force applies to the particles on the bed, and it causes initiating sediment motion. Sediment motion will start whenever the drag force exceeds the resistance force (Chaudhry 2007). The drag force (F_D) and the submerged weight (F_G) are obtained by:

$$F_D = \frac{1}{2} \pi \left(\frac{d}{2}\right)^2 \rho C_D \bar{u}^2 \quad 1.16$$

$$F_G = \frac{4}{3} \pi \left(\frac{d}{2}\right)^3 \rho R g \quad 1.17$$

where ρ represents the fluid density, g is the gravitational acceleration, d shows the sediment diameter, \bar{u} denotes the fluid velocity at the grain level, R is the submerged specific gravity of the sediment particle, and it equals:

$$R = (\rho_s - \rho) / \rho \quad 1.18$$

C_D shows the drag coefficient that is related to the Reynolds number:

$$R_e = \frac{\bar{u} \times d}{\nu} \quad 1.19$$

where ν is the kinematic viscosity, it can be calculated by the dynamic viscosity (μ) divided by the fluid density (ρ).

$$\nu = \frac{\mu}{\rho} \quad 1.20$$

The frictional resistance (F_R) is given by:

$$F_R = \mu_c F_G \quad 1.21$$

where μ_c denotes the frictional coefficient.

By establishing the following conditions, the sediment is on the threshold of the motion.

$$F_D = F_R \quad 1.22$$

$$\frac{\bar{u}^2}{R g d} = \frac{4 \mu_c}{3 C_D} \quad 1.23$$

In the situation of the hydraulically rough turbulent flow, the logarithmic profile or the law of the wall can be written as:

$$\frac{\bar{u}}{u_*} = \frac{1}{\kappa} \ln \left(\frac{z}{K_S} \right) + 8.5 \quad 1.24$$

INTRODUCTION

where:

\bar{u} = the velocity at the level of the z from the bed,

u_* = the shear velocity that is defined as ($u_* = \sqrt{\tau_b/\rho}$),

κ = von Kármán constant that equals 0.41.

K_s = the roughness height ($K_s = n_k d$ that n_k is dimensionless)

z = the height from the bed.

Consider an exposed grain that the distance of its centroid from the mean level of the bed equals $z = n_e d$ that n_e is a dimensionless number. For the exposed grain shown in [Figure 1.4](#), the equation [1.24](#) is written as below:

$$\frac{\bar{u}}{u_*} = \frac{1}{\kappa} \ln \left(\frac{n_e}{n_k} \right) + 8.5 \quad 1.25$$

By mixing the equation [1.23](#) and [1.25](#), it can be shown that:

$$\frac{u_*^2}{R g d} = \tau_c^* = \frac{4 \mu_c}{3 C_D} \left[\kappa \ln \left(\frac{n_e}{n_k} \right) + 8.5 \right]^{-2} \quad 1.26$$

The term τ_c^* in equation [1.26](#) is introduced as the critical Shields stress. If the particle on the bed surface wants to start motion because of the fluid flow, the non-dimensional bed shear stress (Shield stress τ^*) must surpass the critical Shields stress (τ_c^*).

1.5.3. Shields diagram

Shields (1936) worked on the incipient motion of granular sediment in the fluvial stream and bedload transportation. He ran many experiments and drew their results in a graph known as a Shields diagram. This diagram illustrates the relationship between the non-dimensional critical shear stress (τ_c^*) and the shear Reynolds number ($R_e^* = u_* d/\nu$) (Chaudhry 2007). [Figure 1.5](#) shows the Shields diagram. The relationship between τ_c^* and R_e^* was determined experimentally (Dey 2014).

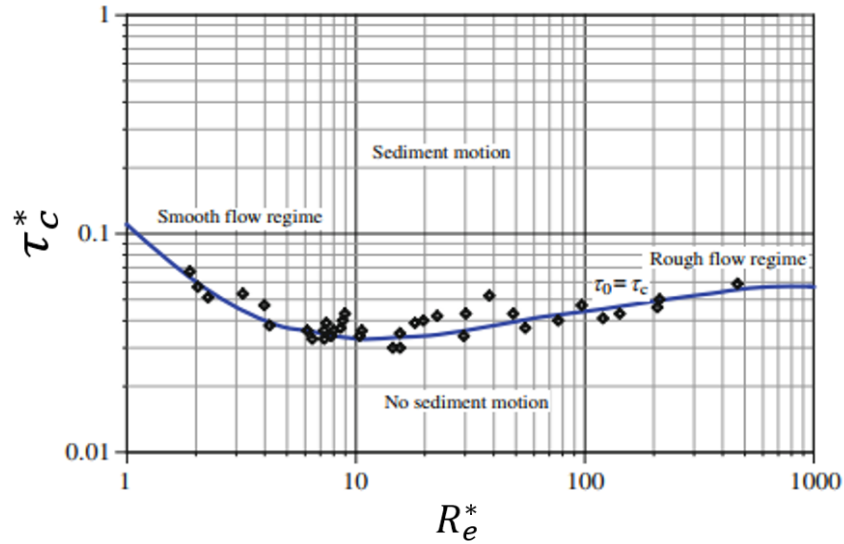


Figure 1.5. Shields diagram depicts critical Shields number (τ_c^*) as a function of shear Reynolds number (R_e^*) (Dey 2014).

According to the graph, for a specific sediment size, the zone above the curve corresponds to the motion condition, and the area below the curve represents no sediment motion. This figure illustrates three distinguished flow regions:

- 1) hydraulically smooth flow ($R_e^* \leq 2$)
- 2) hydraulically rough flow ($R_e^* \geq 500$)
- 3) hydraulically transitional flow ($2 < R_e^* < 500$)

The original Shields graph has no information for a smooth flow regime ($R_e^* \leq 2$). The linear relationship of the $\tau_c^*(R_e^*)$ curve is an extrapolation (Dey 2014).

1.6. Predictions of bedload transport

Several equations are proposed to predict the bedload transport rate by several researchers during the past decades. B.F.D du Boys (1879), a French hydraulic engineer, was the first researcher to present the successful development of this concept. He assumed that particles transfer in a sliding layer. After Boys, several researchers proposed empirical and semi-empirical equations (Chanson 2004). Although Einstein's (1942) equation for solid transport rate is obtained theoretically, other formulas have been acquired empirically (Zucchi 2018). [Table 1.1](#) presents the list of the formulas for bedload transport.

INTRODUCTION

Table 1.1. The empirical and semi-empirical formulation for bedload transport (Chanson 2004).

Reference	Formulation	Range	Remarks
Boys (1879)	$q_s = \lambda \tau_0 (\tau_0 - (\tau_0)_c)$ $\lambda = \frac{0.54}{(\rho_s - \rho)g} \text{ Schoklitsch(1914)}$ $\lambda \sim d_s^{-3/4} \text{ Sraub (1935)}$	$0.125 < d_s < 4 \text{ mm}$	λ was called the characteristic sediment coefficient Laboratory experiments with uniform grains of various kinds of sand and porcelain Based upon laboratory data
Schoklitsch (1930)	$q_s = \lambda' (\sin \theta)^k (q - q_c)$ $q_c = 1.944 \times 10^{-2} d_s (\sin \theta)^{-4/3}$	$0.305 < d_s < 7.02 \text{ mm}$	Based upon laboratory experiments
Shields (1936)	$\frac{q_s}{q} = 10 \frac{\sin \theta}{s} \frac{\tau_0 - (\tau_0)_c}{\rho g (S - 1) d_s}$	$1.06 < S < 4.25$ $1.56 < d_s < 2.47 \text{ mm}$	
Einstein (1942)	$\frac{q_s}{\sqrt{(S - 1) g d_s^3}} = 2.15 \exp \left(-0.391 \frac{\rho (S - 1) g d_s}{\tau_0} \right)$	$\frac{q_s}{\sqrt{(S - 1) g d_s^3}} < 0.4$ $1.25 < S < 4.25$ $0.315 < d_s < 28.6 \text{ mm}$	Laboratory experiments. Weak sediment transport formula for sand mixtures. Note: $d_s \approx d_{35}$ to d_{45}
Meyer-Peter (1949, 1951)	$\frac{\dot{m}^{2/3} \sin \theta}{d_s} - 9.57 (\rho g (S - 1))^{10/9} = 0.462 (S - 1) \frac{(\rho g (\dot{m}_s)^2)^{2/3}}{d_s}$ $\frac{q_s}{\sqrt{(S - 1) g d_s^3}} = \left(\frac{4 \tau_0}{\rho (S - 1) g d_s} - 0.188 \right)^{3/2}$	$1.25 < S < 4.2$	Laboratory experiments. Uniform grain size distribution. Laboratory experiments. Particle mixtures. Note: $d_s \approx d_{50}$
Einstein (1950)	Design chart $\frac{q_s}{\sqrt{(S - 1) g d_s^3}} = f \left(\frac{\rho (S - 1) g d_s}{\tau_0} \right)$	$\frac{q_s}{\sqrt{(S - 1) g d_s^3}} < 10$ $1.25 < S < 4.25$ $0.315 < d_s < 28.6 \text{ mm}$	Laboratory experiments. For sand mixtures. Note: $d_s \approx d_{35}$ to d_{45}
Schoklitsch (1950)	$\dot{m}_s = 2500 (\sin \theta)^{3/2} (q - q_c)$ $q_c = 0.26 (S - 1)^{5/3} d_{40}^{3/2} (\sin \theta)^{-7/6}$		Based upon laboratory experiments and field measurements (Danube and Aare rivers).
Nielsen (1992)	$\frac{q_s}{\sqrt{(S - 1) g d_s^3}} = \left(\frac{12 \tau_0}{\rho (S - 1) g d_s} - 0.05 \right) \sqrt{\frac{\tau_0}{\rho (S - 1) g d_s}}$	$1.25 < S < 4.22$ $0.69 < d_s < 28.7 \text{ mm}$	Re-analysis of laboratory data

Note: \dot{m} = mass water flow rate per unit width; \dot{m}_s = mass sediment flow rate per unit width; q = volumetric water discharge; q_s = volumetric sediment discharge per unit width; $(\tau_0)_c$ = critical bed shear for initiation of bed load

Among different formulations, it can be realized that the Mayer-Peter (1949, 1951) and Einstein's (1942) equations are the most notorious ones. The Mayer-Peter's equation is more prevalent in Europe, and it is more suitable for wide channels (large width to depth ratio) and coarse particles, while Einstein's formula is widely used in America and it results from physical models of particle movement (Chanson 2004). [Figure 1.6](#) shows the comparison between these two correlations.

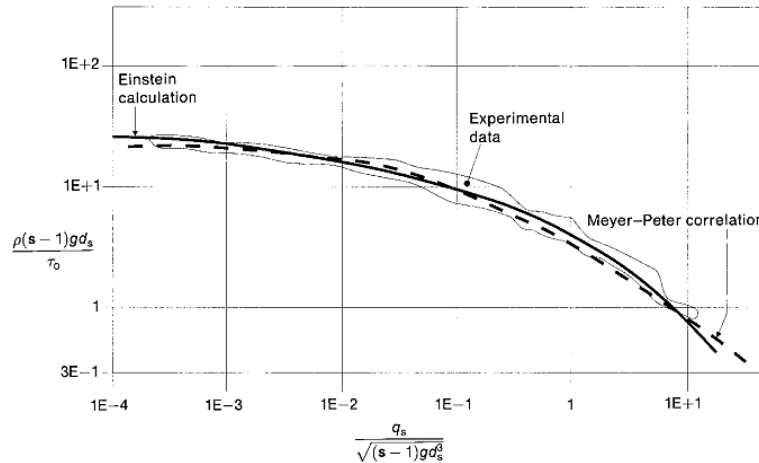


Figure 1.6. Comparison between the bedload transport rate according to Meyer-Peter formula, Einstein's calculation, and laboratory data (Chanson 2004).

1.7. Bed layers

The bottom part of a riverbed composes of loose particles. They lie over each other and produce an intertwined layer that is stable against the pull of gravity. This part is known as the gravity bed that there is a dense layer forming a bottom boundary of the fluid flow (Figure 1.7).

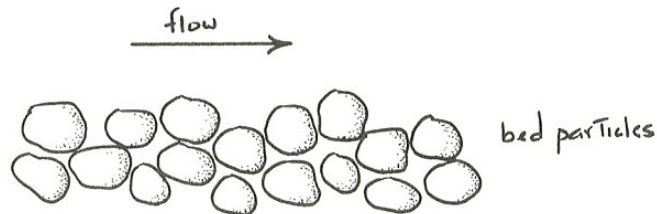


Figure 1.7. A gravity bed of loose sediment grains (Southard 2019).

In the sediment transport concept, the uppermost part of the gravity bed layer is considered where the particles have interaction with flow. This part can be moved or not; it depends on the strength of the flow. These potentially moveable particles are called the active layer (Southard 2019). All sediments in this layer can be transported, whereas the particles below this layer are stable and immobile (Pfeiffer et al. 2020). The water flow plus an intense bedload is known as sheet flow that can be observed in nature and industrial systems. In the natural environment, this occurs during river floods, in the steep mountain streams, and in debris flow (Bareš et al. 2016). The sheet flow feature has high bed shear stress that triggers the particles in the active layer to start motion. The particles in the ripples and dunes bedform are washed out with strong water flow, and the sheet layer with a high concentration of sediment is produced (Y. H. Wang and Yu 2007). The vertical stratification of the bedload flow consists of the transport layer, the fluid layer, and the free surface region. The upper part of the flow is considered the free surface region that is free of transported particles. The transport layer with a high concentration of the

INTRODUCTION

particles is located above the bed plane. This layer can be introduced as a sheet-flow layer or, in general term is known as a bedload layer. The middle layer between the free surface and the top of the bedload layer is noticed as a fluid layer (Bareš et al. 2016). The bedload transport happens in the thin layer of fluid close to the bed. The schema of the layers in bedload transport is illustrated in Figure 1.8.

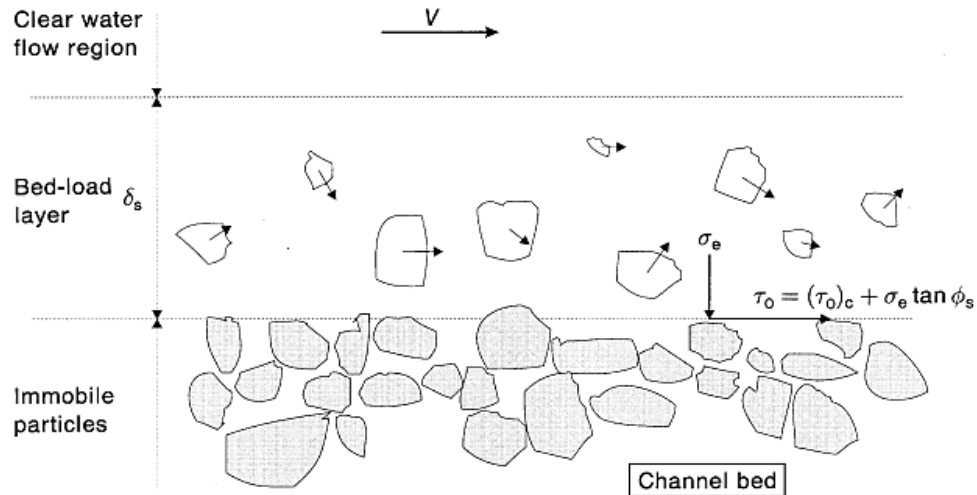


Figure 1.8. The schema of the layers in bedload transport.

When dealing with the sediment transport phenomenon, the border between the bed and the flow is not clear because of the presence of the bedload layer. In the previous works (Zanchi 2018; Zucchi 2018; Heydari 2020), the bedload surface is considered as the bed surface, while in this work, the surface of the immobile particles; in other words, the surface of the stationary bed is considered as the bed surface. The reason for choosing this surface as the bed surface is the fact that based on the law of the wall, the flow velocity is zero at the bed surface (Figure 1.9).

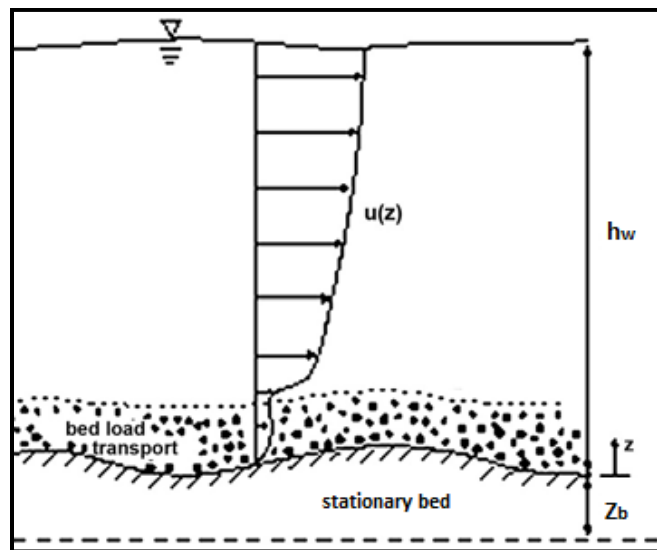


Figure 1.9. The flow velocity distribution when dealing with bedload layer (Wu, Rodi, and Wenka 2000).

It should be mentioned that in this work, because of the porous medium inside the bed, the flow velocity at the stationary bed's surface is not zero but very close to zero since almost no movement is observed on this surface.

1.7.1. Two-layer model

The moving part of the flow is divided into two layers that consist of the clear water and the transported layer. The main features of moving layers are the thickness of the water layer (h_w) and the transported layer (h_s), their velocities (u_w and u_s), and the level of the interface between the immobile layer and transported layer z_b . The velocity in the water layer (u_w) is more than the transported layer (u_s) and both of them are assumed to be uniform in their layer. There is a mixture of water and sediment with sediment concentrations in the transported layer (C_s) and fixed layer (C_b) that are assumed constant in time and space. The volumetric density of the transported layer (ρ'_s) is introduced as below:

$$\rho'_s = (1 - C_s)\rho_w + C_s\rho_s \quad 1.27$$

where ρ_w and ρ_s denote the water and grain density, respectively (Bellal 2012). Figure 1.10 illustrates the two-layer scheme.

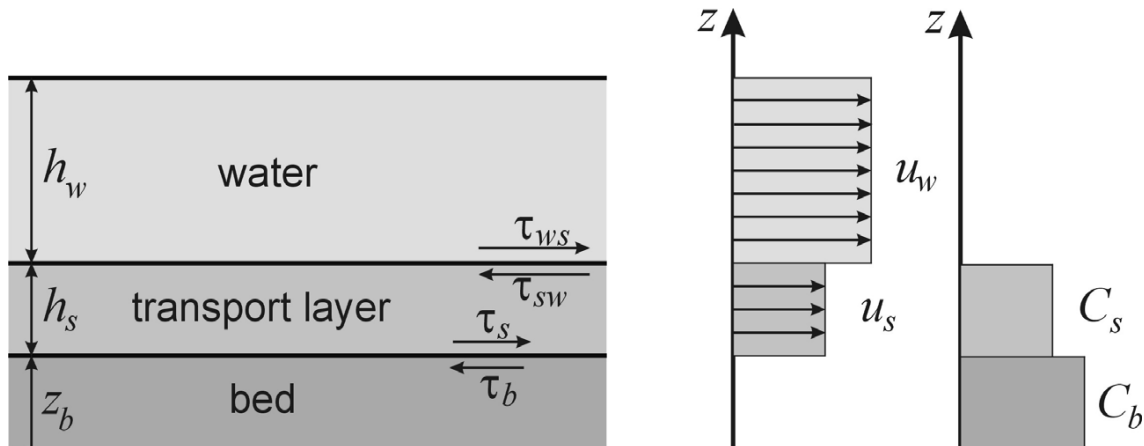


Figure 1.10. Two-layer model scheme.

1.8. Morphological evolution

Sediment transport is an integral part of river systems, so the effect of sediment transport must be considered to estimate the evolution of the riverbed. It is challenging to predict sediment transport and morphological changes of the river due to its dynamics. Over the past years, researchers have sought to know the mechanism of sediment transport and morphological changes under different conditions in aquatic environments. In order to achieve this goal, laboratory and numerical methods have been developed.

1.8.1. Analytical model

Some parameters like the particles' properties, the sediment transport capacity, the inflow sediment discharge, and the inflow water discharge can influence the morphological evolution of a mobile river's bed (Exner, 1925). The global bed material conservation equation known as the Exner equation is acquired by adding up the masses of all sediment material layers between the bed surface and a reference level. The Exner equation is used for sediment mass conservation in the fluvial system like a stream; It presents the mass conservation between sediment in the channel bed and transported sediment. In the case of the rectangular channel, erodible bed, homogenous material, and by neglecting the suspended load, the conservation of mass for sediment is presented as below:

$$(1 - p) \frac{\partial z_b}{\partial t} + \frac{\partial q_s}{\partial x} = 0 \quad 1.28$$

where:

p = the porosity of the sediment material,

z_b = the bed elevation,

$q_s = Q_s/B$ represents the unit sediment discharge, and B shows the channel width.

The Exner equation represents the mass conservation law for the sediment particles.

There is degradation when $\frac{\partial q_s}{\partial x} > 0$, $\frac{\partial z_b}{\partial t} < 0$

There is aggradation when $\frac{\partial q_s}{\partial x} < 0$, $\frac{\partial z_b}{\partial t} > 0$

Besides the Exner equation, in order to express the one-dimensional morphological evolution of the riverbed, two Saint-Venant equations are also used, which represent the mass balance and momentum conservation:

$$\frac{\partial h}{\partial t} + \frac{\partial q}{\partial x} = 0 \quad 1.29$$

$$\frac{\partial q}{\partial t} + \frac{\partial}{\partial x} \left(\frac{q^2}{h} \right) + gh \frac{\partial h}{\partial x} = gh(S_0 - S_f) \quad 1.30$$

where $q = u \times h$ is unit flow discharge, h shows the water depth, u is the depth-averaged velocity, and S_0, S_f are bottom and friction slope, respectively.

To simulate the aggradation and degradation of particles on the bed river, one can assume that equations 1.29 and 1.30 are valid in the presence of the sediment. If the bottom slope expresses as $S_0 = -\partial z_b / \partial x$, the equation 1.30 can be rewritten as below:

$$\frac{\partial q}{\partial t} + \frac{\partial}{\partial x} \left(\frac{q^2}{h} \right) + gh \left(\frac{\partial h}{\partial x} + \frac{\partial z_b}{\partial x} \right) = -ghS_f \quad 1.31$$

The governing equations consist of three equations, 1.28, 1.29, and 1.31, with five unknowns (h, q, z_b, q_s , and S_f); then two additional relations are needed to calculate q_s and S_f in order to use the system. The friction slope (S_f) can be calculated by the Manning formula:

$$S_f = \frac{n^2 \times U^2}{R_H^{4/3}} \quad 1.32$$

where n is the Manning's coefficient, R_H shows the hydraulic radius, and U is the local velocity of the flow.

The sediment discharge (q_s) is estimated from general formulae like Meyer-Peter and Müller (1948) as below:

$$q_s(q, h) = 8 \sqrt{g(s-1)d_{50}^3} \left(\frac{n^2 q^2}{(s-1)d_{50} h^{7/3}} - 0.047 \right)^{3/2} \quad 1.33$$

where n is the Manning's coefficient, $s = \rho_s/\rho_w$ shows the relative sediment density, and d_{50} denotes the median grain diameter.

The mathematically model of the bed evolution for one-dimensional flow consists of three equations, two Saint-Venant equations that describe mass balance and momentum conservation with the shallow-water assumption, one Exner equation that expresses the sediment continuity (equation's system 1.34). In addition, two other equations are used, one for the estimation of the solid discharge and the other for obtaining the friction slope.

$$\begin{cases} \frac{\partial h}{\partial t} + \frac{\partial q}{\partial x} = 0 \\ \frac{\partial q}{\partial t} + \frac{\partial}{\partial x} \left(\frac{q^2}{h} \right) + gh \left(\frac{\partial h}{\partial x} + \frac{\partial z_b}{\partial x} \right) = -ghS_f \\ (1-p) \frac{\partial z_b}{\partial t} + \frac{\partial q_s}{\partial x} = 0 \end{cases} \quad 1.34$$

This PDE system presents the bed and water level evolution in a one-dimensional case and uses only the bedload for sediment motion. The system was solved by Goutière et al. (2008) in a novel, simple, but rather accurate approximation of the eigenvalues of the system composes of Saint-Venant-Exner equations. The system of the equations can be rewritten in vector form as:

$$\frac{\partial \mathbf{U}}{\partial t} + \frac{\partial \mathbf{F}(\mathbf{U})}{\partial x} + \mathbf{H}(\mathbf{U}) \frac{\partial \mathbf{U}}{\partial x} = \mathbf{S}(\mathbf{U}) \quad 1.35$$

where:

$$\mathbf{U} = \begin{bmatrix} h \\ q \\ z_b \end{bmatrix} \quad \mathbf{F}(\mathbf{U}) = \begin{bmatrix} q \\ \frac{q^2}{h} + g \frac{h^2}{2} \\ \frac{q_s}{(1-p)} \end{bmatrix} = \begin{bmatrix} q \\ \sigma \\ \psi \end{bmatrix}$$

$$\mathbf{H}(\mathbf{U}) = \begin{bmatrix} 0 & 0 & 0 \\ 0 & 0 & gh \\ 0 & 0 & 0 \end{bmatrix} \quad \mathbf{S}(\mathbf{U}) = \begin{bmatrix} 0 \\ -ghS_f \\ 0 \end{bmatrix}$$

Equation 1.35 can be formulated as below:

$$\begin{aligned} & \frac{\partial \mathbf{U}}{\partial t} + \frac{\partial \mathbf{F}(\mathbf{U})}{\partial x} + \mathbf{H}(\mathbf{U}) \frac{\partial \mathbf{U}}{\partial x} \\ &= \frac{\partial \mathbf{U}}{\partial t} + \mathbf{A}(\mathbf{U}) \frac{\partial \mathbf{U}}{\partial x} + \mathbf{H}(\mathbf{U}) \frac{\partial \mathbf{U}}{\partial x} \\ &= \frac{\partial \mathbf{U}}{\partial t} + \mathbf{A}'(\mathbf{U}) \frac{\partial \mathbf{U}}{\partial x} \\ &= \mathbf{S}(\mathbf{U}) \end{aligned} \tag{1.36}$$

where $\mathbf{A}(\mathbf{U}) = \partial \mathbf{F}(\mathbf{U}) / \partial \mathbf{U}$ is Jacobian matrix; and $\mathbf{A}'(\mathbf{U}) = \mathbf{A}(\mathbf{U}) + \mathbf{H}(\mathbf{U})$ is a kind of pseudo-Jacobian, which is:

$$\mathbf{A}'(\mathbf{U}) = \frac{\partial \mathbf{F}(\mathbf{U})}{\partial \mathbf{U}} + \mathbf{H}(\mathbf{U}) = \begin{bmatrix} 0 & 1 & 0 \\ -\frac{q^2}{h^2} + gh & 2\frac{q}{h} & gh \\ \frac{1}{1-p} \frac{\partial q_s}{\partial h} & \frac{1}{1-p} \frac{\partial q_s}{\partial q} & 0 \end{bmatrix} \tag{1.37}$$

1.8.1.1. Eigenvalue analysis and approximation

The characteristic polynomial related to matrix $\mathbf{A}'(\mathbf{U})$ (equation 1.37) can be written as follow:

$$|\mathbf{A}' - \lambda \mathbf{I}| = \lambda^3 + a_1 \lambda^2 + a_2 \lambda + a_3 = 0 \tag{1.38}$$

with

$$a_1 = -2\frac{q}{h} \tag{a}$$

$$a_2 = \frac{q^2}{h^2} - gh - \frac{gh}{1-p} \frac{\partial q_s}{\partial q} \tag{b} \tag{1.39}$$

$$a_3 = -\frac{gh}{1-p} \frac{\partial q_s}{\partial h} \tag{c}$$

where $\partial q_s / \partial q$ and $\partial q_s / \partial h$ are calculated from equation 1.33. The three eigenvalues $\lambda_{1,2,3}$ of the matrix A' , which are related to the respective celerity dx / dt of the three characteristics are the roots of the polynomial of the equation 1.38. The theoretical calculation of these roots is possible, but the analytical computation is so complicated that it is not used practically (Lyn 1987; Lyn and Altinakar 2002; Goutière et al. 2008).

A new approximation of analytical computation is derived by using the properties of cubic polynomial $\alpha x^3 + \beta x^2 + \gamma x + \delta = 0$ that its roots x_1, x_2, x_3 are connected according to the below expressions:

$$\begin{aligned} x_1 + x_2 + x_3 &= -\frac{\beta}{\alpha} & (a) \\ x_1x_2 + x_2x_3 + x_3x_1 &= \frac{\gamma}{\alpha} & (b) \\ x_1x_2x_3 &= -\frac{\delta}{\alpha} & (c) \end{aligned} \quad 1.40$$

By applying the equation 1.40 (a) to the characteristic polynomial equation 1.38 and using the coefficients of equations 1.39 (a), one can write the below equation:

$$\lambda_1 + \lambda_2 + \lambda_3 = -a_1 = 2\frac{q}{h} = 2u \quad 1.41$$

As the impact of sediments on the characteristic equations is assumed to be a slight perturbation, It can be assumed that the presence of sediments does not affect the largest eigenvalue (Lyn and Altinakar 2002; Goutière et al. 2008).

$$\lambda_1 = \lambda_{H1} = u + c \quad 1.42$$

where $c = \sqrt{gh}$ shows hydrodynamic wave celerity, and the subscript H uses for hydrodynamic value. By using the assumption of the equation 1.42, the equation 1.41 can be rewritten as:

$$\lambda_2 + \lambda_3 = (\lambda_1 + \lambda_2 + \lambda_3) - \lambda_1 = 2u - (u + c) = u - c \quad 1.43$$

Because λ_1 does not account for sediment effects; therefore, this effect is only applied to λ_2 and λ_3 in the form of symmetrical deviation from $\lambda_{H2} = u - c$.

The equation 1.40 (c) can be rewritten by applying equation 1.43:

$$\lambda_1\lambda_2\lambda_3 = \lambda_{H1}\lambda_2(\lambda_{H2} - \lambda_2) = (u + c)\lambda_2(u - c - \lambda_2) = -a_3 = \frac{gh}{1-p} \frac{\partial q_s}{\partial h} \quad 1.44$$

that creates a quadratic polynomial in λ_2 , whose roots give λ_2 and hence also λ_3 in such a way that the three eigenvalues can be written in a non-dimensional form as follows:

$$\frac{\lambda_1}{u} \cong \left(1 + \frac{1}{Fr}\right) \quad (a)$$

$$\frac{\lambda_{2,3}}{u} \cong \frac{1}{2} \left[\left(1 - \frac{1}{Fr}\right) \mp \sqrt{\left(1 - \frac{1}{Fr}\right)^2 - \frac{4}{(Fr^2 + Fr)}\chi} \right] \quad (b) \quad 1.45$$

where $Fr = u/\sqrt{gh}$ is the Froud number, and χ is the non-dimensional factor that is related to the sediment discharge and can be described as follow:

$$\chi = \frac{1}{(1-p)u} \frac{\partial q_s}{\partial h} \quad 1.46$$

The comparison among the non-dimensional eigenvalues acquired by the approximate analytical formula (equation 1.45), the exact value is taken by a numerical eigenvalue solver, and the approximation proposed by Lyn and Altinakar (2002) is illustrated in Figure 1.11.

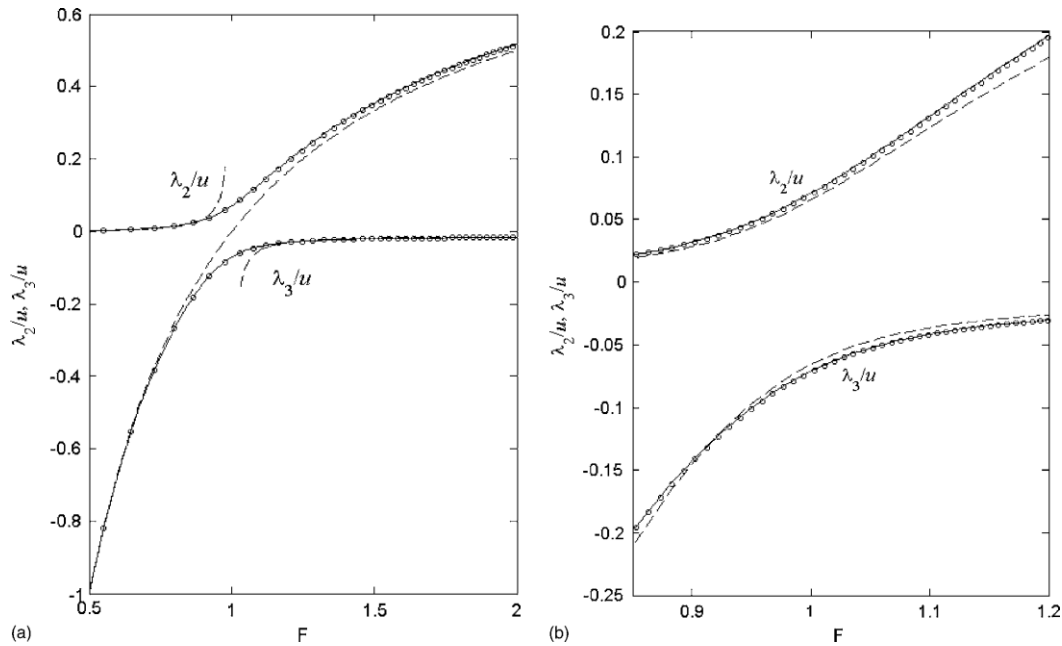


Figure 1.11. Comparison of exact and approximate eigenvalues: (a) in the region outside $Fr = 1$; (b) close to $Fr = 1$. Circles mark exact values, dashed lines are used for approximation by Lyn and Altinakar 2002, and continuous lines are used for the proposed approximation equation 1.45 (Goutière et al. 2008).

In order to acquire a unique solution for the partial differential equations, it is necessary to impose the initial and boundary conditions. According to the obtained results for eigenvalues (equation 1.45), two of them will be positive, while the remaining one is negative. In order to solve the system of equations 1.34, two boundary conditions must be introduced upstream, and a boundary condition must be imposed downstream.

1.9. Experimental studies

In addition to the proposed analytical models to predict morphological changes in riverbeds due to sediment transport under different flow regimes, laboratory research is underway to validate and calibrate these methods. Many researchers have tried to have a view and an understanding of this mechanism by simulating and at the same time simplifying aquatic environments such as rivers in the laboratory environment so that they can use it to bring analytical and numerical methods closer to reality. In the 70s and 80s, pioneering experimental work was carried out by Soni (1975) and Mehta (1980) (Alves and Cardoso 1999).

Soni (1975) worked on the stream's aggradation due to an increase in sediment load as his Ph.D. thesis at the University of Roorkee in India. He studied the phenomenon of aggradation, integrating the experimental findings with an analytical model, simulating the constant feeding rate of the sediment supply in a given section located along the river course. Concerning the injection point, the disturbance caused by the incoming sediment causes both upstream and downstream aggradation, changing the equilibrium bed slope S_0 . The initial bed elevation z_b and the water level h along the channel. He used the experimental results to calibrate the analytical model. In order to calibrate the analytical model, he used the experimental findings, specifically in the calibration of a and b coefficients that are used in the modeling of the sediment transport law equation ($Q_s = aU^b$) and also for aggradation coefficient K , found in the simplified differential equation for bed evolution ($\partial z/\partial t = K \partial^2 z/\partial x^2$ where z is the aggradation depth).

Jain (1981) suggested his approach, considering the problem formulation used by Soni (1975), applying a more suitable boundary condition that takes into account the balance between the volume of sediment added and the volume of deposition in the channel. The analytically obtained aggradation results demonstrate that it is not necessary to calibrate the aggradation coefficient K , proposed by Soni (1975), and the findings of the analytical model are in line with the experimental ones.

Yen, Chang, and Lee (1992) experimentally studied the riverbed evolution in the case of non-uniform sediment under the condition of overloading followed by underloading. In this essay, after a disturbance (in terms of sediment over or underloading) in the balanced system, a response time is defined as the time required to reach a new equilibrium state. The non-uniform granulometry of the sediment causes the armoring phenomenon in the degradation process in these studies, demonstrating that a complete recovery ($R = 100\%$) is only feasible in the case of uniform sediment content.

Alves and Cardoso (1999), based on the increasing Manning's coefficient, the influence of dune formation in the aggradation phase, and the celerity of the front of the sediment observed, conducted an experimental campaign of six experiments on aggradation phenomena. The analytical findings are then established and compared to the experimental ones in terms of

INTRODUCTION

aggradation height along the channel bed. For the solution of the linear parabolic model, the mathematical model used is the one proposed by Jain (1981).

Miglio, Gaudio, and Calomino (2009) derived their findings from multiple morphological empirical simulations conducted in a narrow semi-ovoid laboratory channel, handling both aggradation and degradation scenarios. There were two materials used in the experiments: sand and gravel. These data are compared to their numerical simulations (DORA model) that use the Ackers formula (1984), the Meyer-Peter and Müller formula (1948), and their calibrated sediment transport discharge empirical power-law formula. Compared to the measured sediment transport values for the equilibrium state, the calibration formula results show a good correspondence, while the equation of Meyer-Peter and Müller and Ackers's formula tend to overestimate this amount in general.

Campisano, Cutore, and Modica (2013) carried out an experimental project in the laboratory, adapting the channel's width for the various tests. In the two different series, the sediment material has also been altered. The comparison is then carried out with the numerical model, demonstrating a good matching of their results.

An et al. (2017) investigated the hydrograph boundary layer (HBL), which is the region directly downstream of the sediment input field. The mathematical model (Saint-Venant and Exner equations) is introduced and validated with regard to flume experiments. Simulations were subsequently carried out concerning the field size, simplifying the rectangular cross-section, and in the case of uniform and non-uniform sediment mixtures. The HBL occurs by looking at the diffusive nature of the morphological evolution problem's governing equations, and the numerical simulation results demonstrate this.

Zucchi (2018) performed his master thesis at the Mountain Hydraulics Lab of the Politecnico di Milano, located in the Lecco campus. It aims at deepening knowledge of aggradation phenomena caused by overloading through both numerical and experimental approaches. The experiments were performed with different sediment discharges, which were higher than the channel's sediment transport capacity, resulting in aggradation in the studied channel. In this study, 17 aggradation experiments are performed with different water discharge and inflow sediment discharge, besides the imposed water depth in the channel downstream. The numerical study was performed by using the BASEMENT software, which solves the PDEs system. The numerical results are calibrated according to the outcome of the experimental tests.

Heydari (2020) carried out his master thesis and conducted a series of experiments analysis in the overloading channel in the supercritical regime. He did the tests on the channel with an initial bed slope of 1.2 %. He used the Browline (1981) formula in order to estimate the threshold flow rate. The aggradation happened with the highest height close to the inlet point and decreased along the channel, resulting in the lowest height in the downstream part. Also, he studied the celerity propagation along the channel.

CHAPTER 2

EXPERIMENTAL SET-UP AND METHODS OF DATA ACQUISITION

2.1. Experimental set-up

All the experiments of this experimental campaign are performed at Mountain Hydraulics Laboratory of the Politecnico di Milano University, located in the Lecco campus. The experimental system to simulate a mountainous river is composed of different parts working together, and the main parts are going to be explained in this chapter. The whole system configuration can be seen in [Figure 2.1](#).

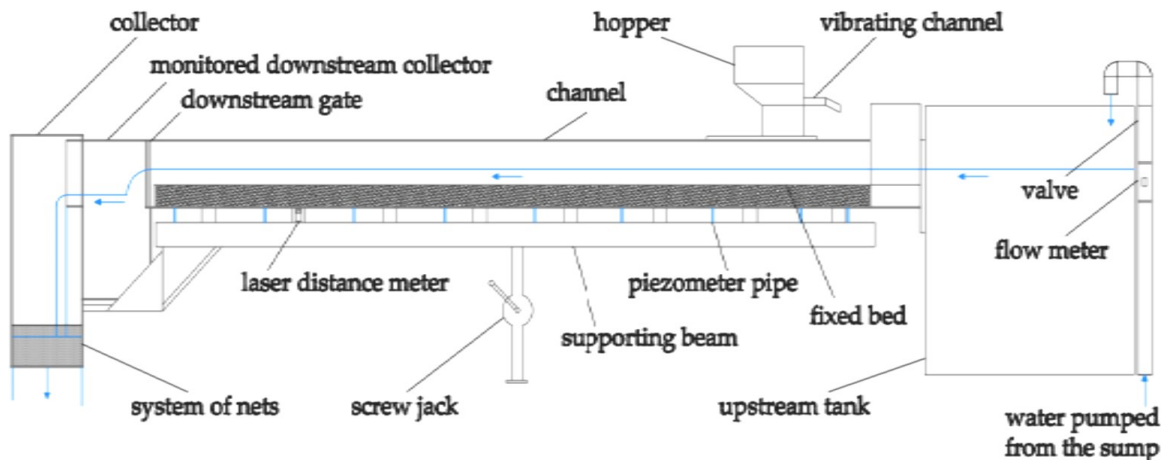


Figure 2.1. schematic presentation of the experimental facility (Unigarro Villota 2017).

2.1.1. Experimental channel

The experimental campaign is done through an artificial channel ([Figure 2.2](#)) with characteristics mentioned below:

length: 5.2 m width: 0.3 m bank height: 0.45 m

The bank is made with plexiglass, which is transparent, to help with data acquisition through cameras positioned along the channel.



Figure 2.2. Artificial channel.

The slope of the channel can be adjusted through a screw jack. For setting the channel slope, a laser distance meter (Figure 2.3) fixed to the channel is used to read the distance between the bottom of the channel and the ground. This number can be translated into a slope through a function (Figure 2.4) derived previously by Fazzini and Mottini (2015).



Figure 2.3. Laser distance meter fixed to the channel.

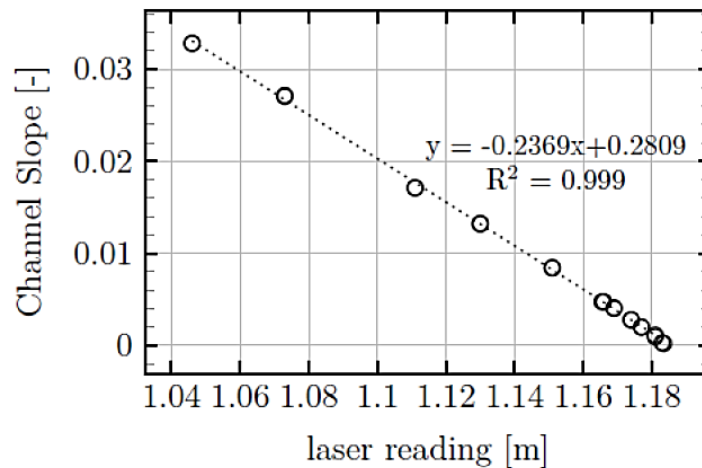


Figure 2.4. The relationship between the laser reading and the channel slope (Unigarro Villota 2017).

In order to simulate the erodible channel bed, the channel is filled with a 15 cm layer of PVC sediment particles (will be described in chapter 2.1.3) except for the first 0.75 m at the upstream of the channel where the bed is fixed. The fixed part is made by three plastic plates on which the sediment particles are glued to produce a similar roughness of the channel. The reason for using a fixed bed at the upstream part is to prevent the local scour caused by the sediment feeding system and the proximity to the water inlet.

2.1.2. Water feeding and recirculation system

The water is pumped from an underground container into the upstream tank (Figure 2.5) to fill the tank; when the water level inside the tank reaches the channel, water starts to flow inside the channel from upstream to downstream.



Figure 2.5. Upstream tank.

There are two collectors at the downstream, the first one is to monitor the amount of sediments transported through the channel (will be explained in chapter 2.2.4) (Figure 2.6), and the second one is for preventing the sediment particles from entering the underground container. After water entering into the underground container, it is pumped again into the upstream tank.



Figure 2.6. Monitored collector located at the downstream of the channel.

The water discharge can be regulated by using a guillotine valve, and the water discharge is measured by a flowmeter (Figure 2.7).



Figure 2.7. Guillotine valve and flow meter.

2.1.3. Sediment material

The sediment particles used to simulate the erodible channel bed are cylindrical PVC grains with various colors (Figure 2.8).



Figure 2.8. PVC grains are used as sediment particles.

The percentage of each color is mentioned below:

Black: 18 % Blue: 36 % white: 46 % Orange: very small amount

The equivalent mean diameter (d) is 3.8 mm with a standard deviation of the granulometric distribution of 1.04, the material density (ρ_s) is 1443 kg/m³, and the porosity (p) is 0.45. The particle characteristics are derived by Unigarro Villota (2017).

2.2. Measurements

In this campaign, there are some experimental data which are needed to be measured continuously; the data may change during the experiment’s duration because of the dynamic nature of aggradation experiments. As a result, they need to be measured at different times and locations for further analyses. Since it is almost impossible to measure the data manually in such a dynamic process, some data acquisition methods are performed for the purpose of this thesis.

Before getting into the details of data acquisition methods, it should be mentioned that there are four types of data that are measured through special techniques in these experiments:

- 1) Sediments inflow discharge
- 2) Bed surface elevation
- 3) Water surface elevation
- 4) Sediment inside the collector

The type and number of cameras used for recording different parts of the experiments are mentioned in [Table 2.1](#), and their specifications are mentioned in [Table 2.2](#):

Table 2.1. The type and number of cameras used for each type of measurement for each experiment.

<i>Experiment</i>	<i>Sediment inflow discharge</i>	<i>Bed and Water level</i>	<i>Sediment inside the collector</i>	<i>Piezometer</i>
AE1 to AE4	1 Gopro hero 4	3 SportCam XPRO 215	1 Gopro hero 4	1 SportCam XPRO 215
AE5	1 Gopro hero 4	1 Gopro hero 4 and 2 SportCam XPRO 215	1 SportCam XPRO 215	-
AE6 to AE8	1 Gopro hero 4	2 Gopro hero 7	1 Gopro hero 4	-
SC1 and SC2	1 Gopro hero 4	3 SportCam XPRO 215	1 Gopro hero 4	-
SC3	1 Gopro hero 4	1 Gopro hero 4 and 2 SportCam XPRO 215	1 SportCam XPRO 215	-

Table 2.2. The type and number of cameras used for each type of measurement for each experiment.

<i>Camera</i>	<i>SportCam XPRO 215</i>	<i>Gopro hero 4</i>	<i>Gopro hero 7</i>
Frame Rate	30 fps	30 fps	30 fps
Resolution	1920x1080	1920x1080	3840x2160

2.2.1. Sediment inflow discharge

There is a hopper (Figure 2.9 (a)) positioned upstream, which consists of a sediment container and a vibrating channel with an adjustable vibration level (Figure 2.9 (b)). There is a gate with an adjustable height between the container and the vibrating channel. Adjusting the vibration level and the gate height are two means of changing the sediment inflow discharge. One should know that the increase in the vibration level and the gate height leads to the increase in the sediment inflow discharge.

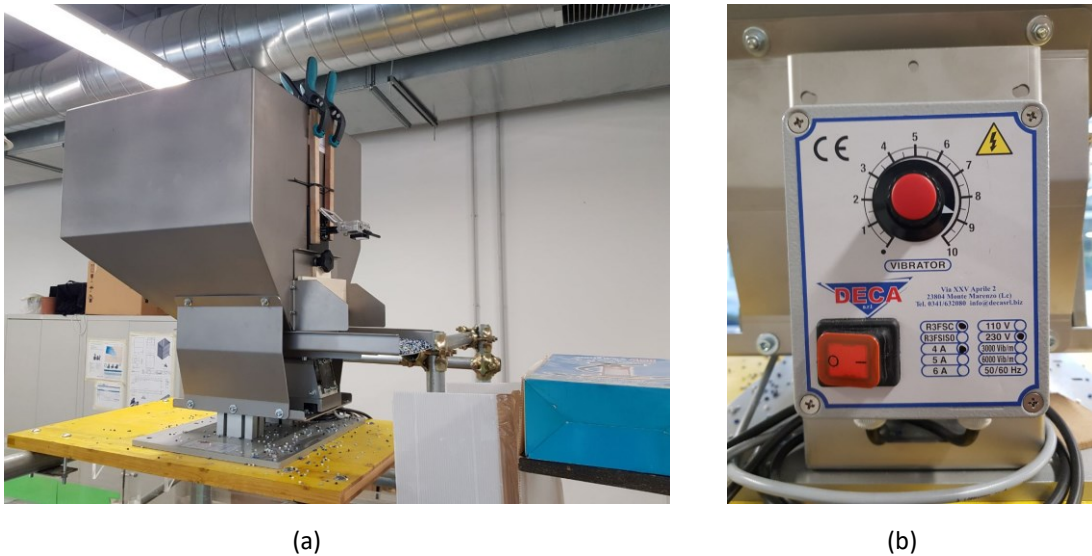


Figure 2.9. (a) Hopper. (b) Selector vibration intensity level.

2.2.1.1. Image processing: PIV (Particles Image Velocimetry) (Zanchi 2018)

The PIV algorithm allows computing the velocity of a moving object in a small duration of time (dt). This algorithm is only applicable when the surface geometry of the moving object remains constant; since the surface geometry of the moving sediments inside the vibrating channel seems to remain almost constant for a small duration of time, this method can be used to measure their average velocity.

In order to apply the method, a camera (Its type and specification are mentioned in Table 2.1 and Table 2.2) is used to record the motion of the sediments inside the vibrating channel. The camera is positioned right above the vibrating channel, and it is inclined such that the acquired video is looking perpendicularly to the vibrating channel (Figure 2.10).



Figure 2.10. Camera positioned above the vibrating channel.

After extracting the frames of the experiments' videos, the photos are changed from RGB to the grayscale color to be able to work with only one color channel instead of three color channels.

Since the lens of these types of cameras (action cameras) has a small focal distance, the photographs are affected by an angular distortion (Figure 2.11 (a)) which increases from the center to the borders. After extracting the frames of the videos, distorted photos should be corrected by applying the radial transformation:

$$\frac{r}{1 + k \times r^2} \quad 2.1$$

where r is the radial distance with respect to the center, and k is a calibration factor obtained with trial and error.

The undistorted frame is shown in Figure 2.11 (b).

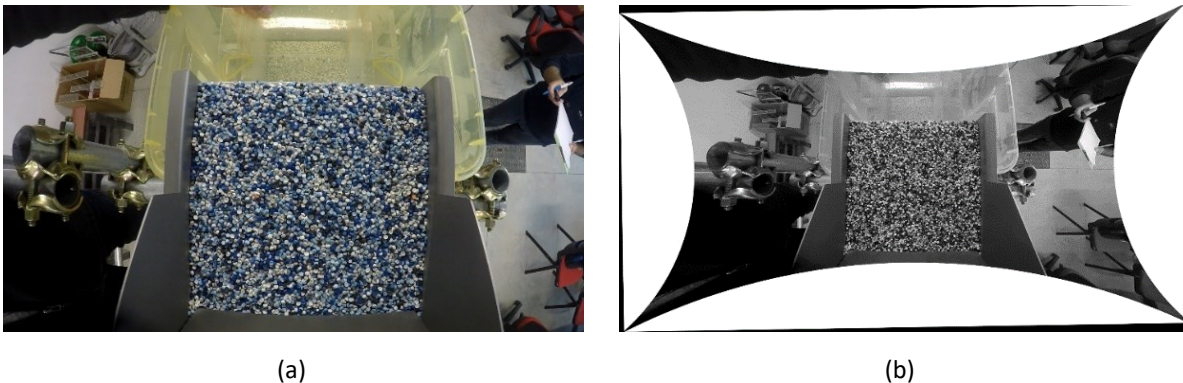


Figure 2.11. (a) Frame extracted from the video. (b) Extracted frame after the correction of the distortion.

For applying the PIV algorithm, a MATLAB code mainly developed by Radice et al. (2006) and modified by Zanchi (2018) is used. For running this code, there are some parameters that should be defined as input values. These parameters are explained through the algorithm explanation mentioned below.

The algorithm consists of several iterations, and each iteration has different steps as below:

1. Two subsequent photos (F_1 and F_2) are selected (Figure 2.12), each photo is a frame of the particles in motion along the vibrating channel captured at a specific time, the first photo (F_1) is captured at the time t_1 and the second one (F_2) is captured at the time t_2 ($t_1 < t_2$).

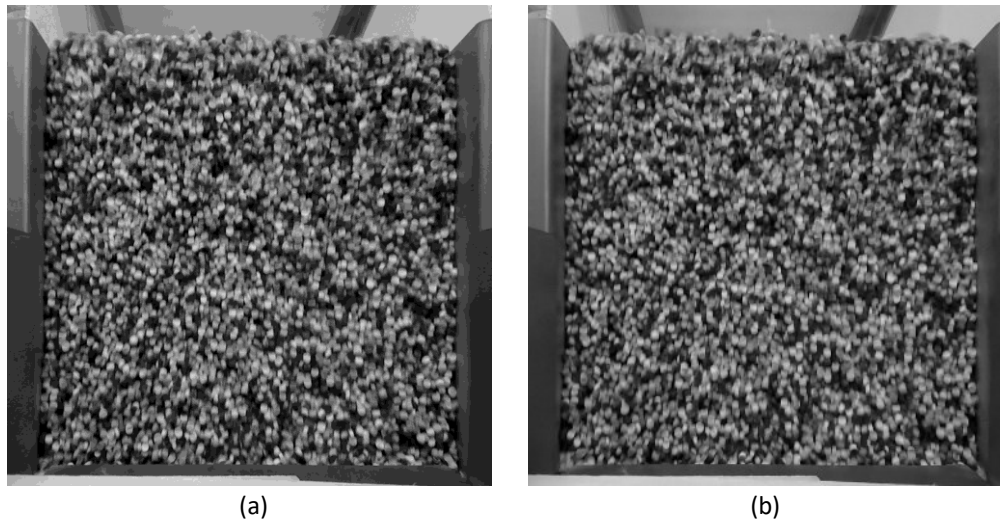


Figure 2.12. (a) First photo selected (F_1). (b) second photo selected (F_2).

The photos are selected as a function of the jump and step parameters. Jump is the distance between two photographs for successive iteration, while the step is the distance of two photographs in the current iteration (Figure 2.13).

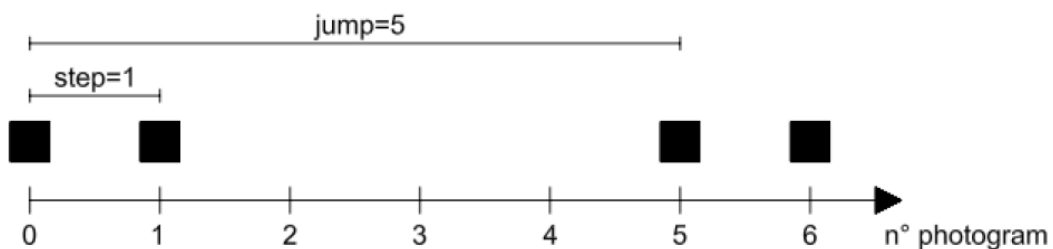


Figure 2.13. Graphical explanation of the jump and step parameters, where the values are selected as an example and equal to 5 and 1, respectively.

In this thesis, the jump is chosen equal to 1 to avoid the loss of data while the step value is changed in different experiments.

2. A working area is selected on F_1 (Figure 2.14) and the pixels' intensity inside this area is saved as a matrix (A_1).

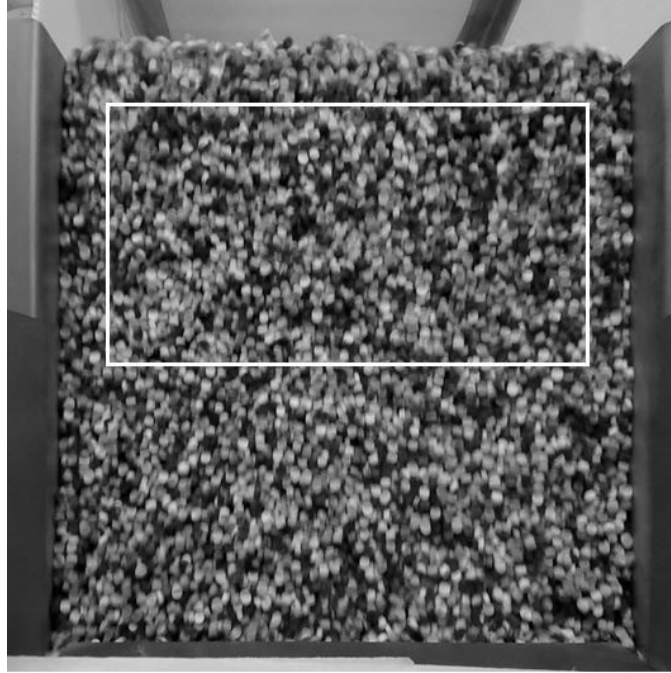


Figure 2.14. Selected working area.

It should be mentioned that the only difference between the application of the algorithm with previous theses (Zanchi 2018; Zucchi 2018; Heydari 2020) is the position of the working area. They chose a working area that covered almost the whole vibrating channel, while in this thesis, the working area should be selected at the downstream part of the vibrating channel (the upper part in the picture). The reason for choosing this area is the fact that the movement of sediments in the downstream part of the vibrating channel is different from the ones in the upstream part.

3. in the second photo (F_2), a searching window with the same size and the same position of the working area starts moving pixel by pixel; each time it moves, it saves the pixels' intensity inside the area as another matrix (A_2), and calculates the parameter (S) from the formula:

$$S = \frac{N_x \times N_y}{\sum_{i=1}^{N_x} \sum_{j=1}^{N_y} |(A_1(i,j) - A_2(i,j))|} \quad 2.2$$

where, N_x and N_y are the dimensions of the working area in pixels along x and y directions.

Because of the particles' movements, the pixels inside the working area in F_1 is displaced in F_2 in two orthogonal directions of x and y (Figure 2.15).

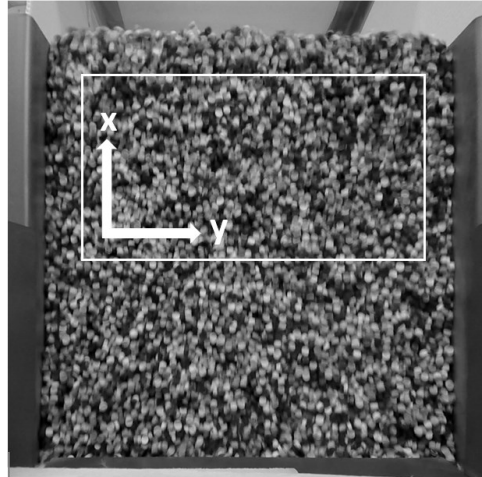


Figure 2.15. Working area and its x and y directions.

In this work, since the main direction of the movement is x direction, the dx is essential. The most probable dx coincides with the minimum value of S . The searching area can move along the whole pixels, which causes a high computational cost. Therefore, one should set a limit for the searching area in both directions to avoid the higher computational cost; these limits are U_{max} and V_{max} which are two other parameters for the functioning of the code. U_{max} is the maximum velocity in the main motion direction (x) and V_{max} is the maximum velocity in the orthogonal direction (y). In this work, since the velocity in the y direction is very low, V_{max} is chosen equal to 0.5 cm/s and U_{max} is chosen equal to 18 cm/s . Pay attention that the real velocity of the particles in both directions must be lower than these parameters.

4. In the previous step, the dx was obtained in pixel scale; now, it should be converted into a metric scale (cm) through a conversion factor. The conversion factor can be obtained by dividing the width of the vibrating channel in pixel to the measured width in centimeters (22 cm) (Figure 2.16).

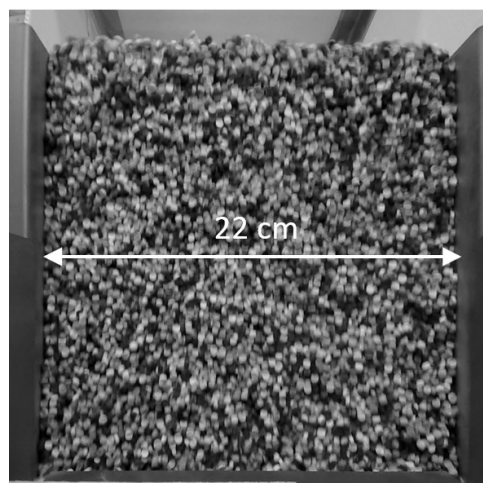


Figure 2.16. The width of the vibrating channel.

5. The velocity in x direction (u) for a single iteration can be calculated through the formula:

$$u = \frac{dx \times fps}{conv \times step} \quad 2.3$$

where fps is the frame rate of the videos recorded, and $conv$ is the conversion factor.

6. After finding the velocity for this time instant, another pair of photos are chosen based on jump and step parameters, and the code repeats all the steps mentioned above; at the end, it gives the temporal evolution of the velocity as the output (Figure 2.17).

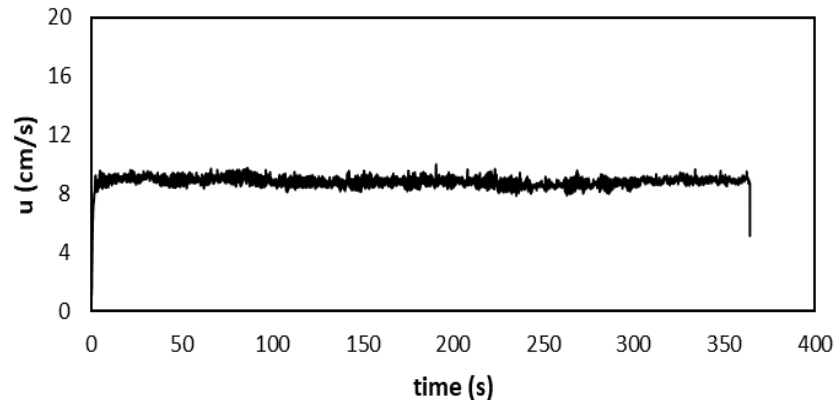


Figure 2.17. An example of the temporal evolution of the velocity.

The temporal velocity evolution is needed to be converted into the sediment inflow discharge (Q_{sin}) for the purpose of this thesis; this conversion is done through an experimental relationship which is derived through a calibration process explained below.

2.2.1.2. Calibration process

Before starting the SC and AE experiments, a preliminary campaign was carried out to link the average velocity of moving sediments on the vibrating channel (u_{mean}) to the sediment inflow discharge (Q_{sin}). The preliminary campaign consists of three sets of experiments based on different opening heights:

1. Opening height = 1 *cm*
2. Opening height = 2 *cm*
3. Opening height = 3 *cm*

The procedure for the opening height equal to 1 *cm* is explained below, and the same procedure is done for other opening heights.

First, the opening height is set on 1 *cm*, and the vibration level is set on 8. The cameras start to record, and the hopper is turned on for a specific duration. The sediments coming out from the hopper are collected by a bucket, then the weight of the sediments inside the bucket is measured and recorded. This procedure is repeated ten times with the same vibration level, but different

durations and their videos are recorded separately. Then the same procedure is repeated for other vibration levels. The details of the preliminary campaign are shown in [Table 2.3](#).

Table 2.3. Detail of the vibration level and the opening height for the preliminary campaign.

<i>Opening height (cm)</i>	<i>Vibration levels</i>
1	8 – 8.5 – 9 – 9.5 – 10
2	6.5 – 7.5 – 8.5 – 9 – 10
3	7 – 8 – 9 – 10

For every experiment, the sediment inflow discharge is obtained with the formula:

$$Q_{sin} = \frac{W_S / \rho_s}{t} \tag{2.4}$$

where, W_S is the weight of the sediment inside the bucket, ρ_s is the sediment density, and t is the duration of the experiment.

It should be mentioned that the value of Q_{sin} for each vibration level is obtained from the average of ten repetitions. Here in [Figure 2.18](#), the Q_{sin} for each experiment, and the related error bars are shown.

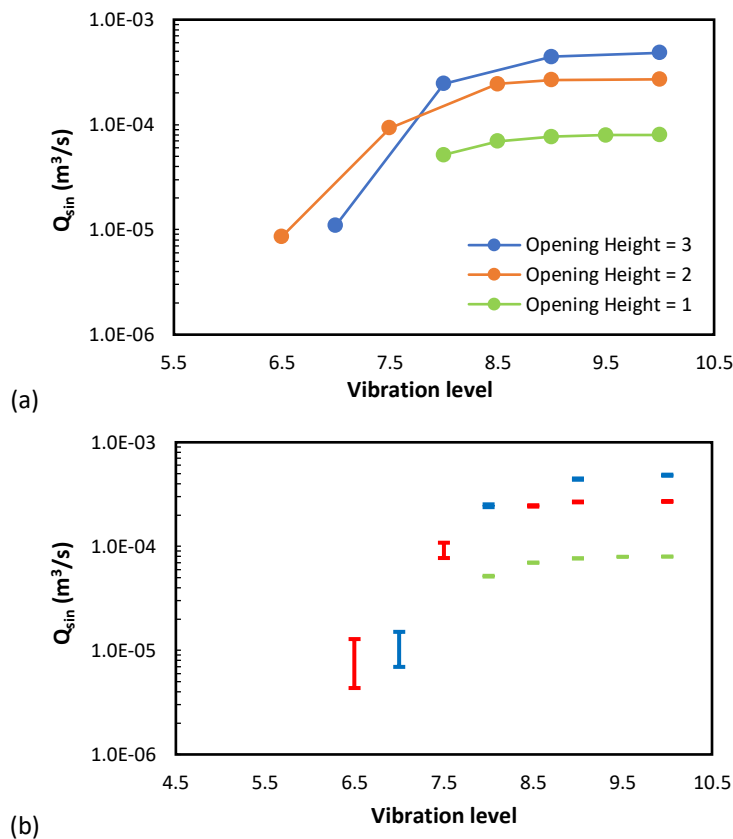


Figure 2.18. (a) curves for showing the effect of vibration level and opening height on Q_{sin} .
(b) the corresponding error bars.

EXPERIMENTAL SET-UP AND METHODS OF DATA ACQUISITION

As it is expected, the higher opening height results in more sediment inflow discharge. However, there is an inconsistency in the opening height 3 where, in vibration level 7, the graph passes through the graph of opening height 2. Also, it can be seen in [Figure 2.18 \(b\)](#), the error bars are very small after the vibration level 7.5.

The results derived by Heydari (2020) and Unigarro Villota (2017) are represented in [Figures 2.19](#) and [2.20](#), respectively.

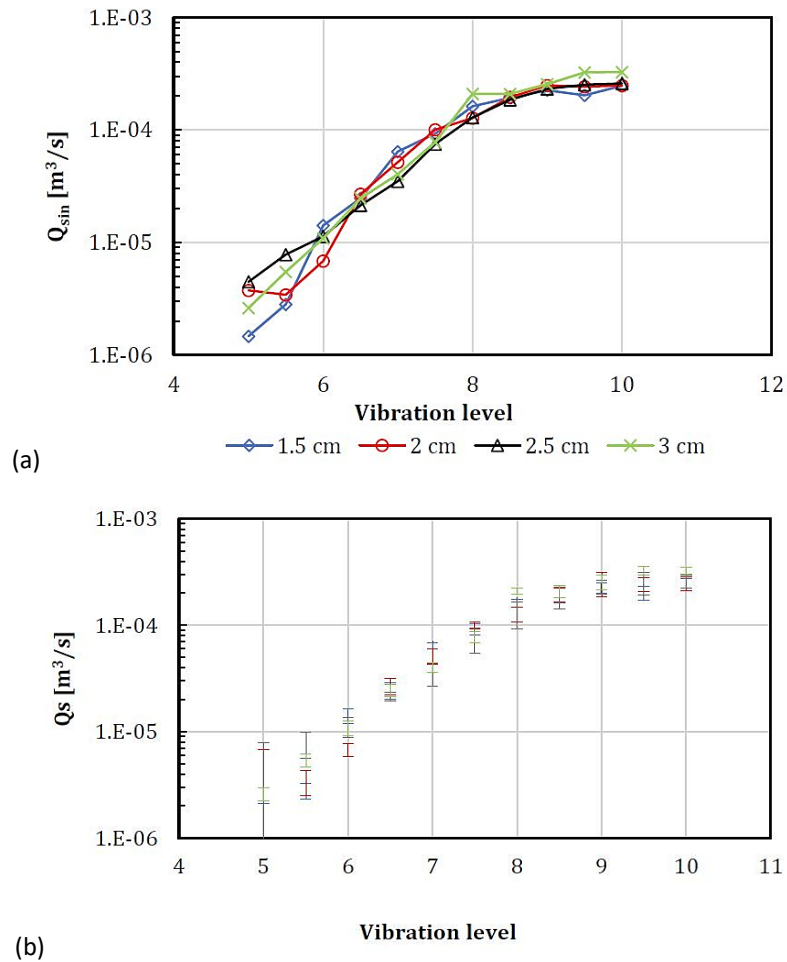


Figure 2.19. (a) curves for showing the effect of vibration level and opening height on Q_{sin} .
(b) the corresponding error bars (Heydari 2020).

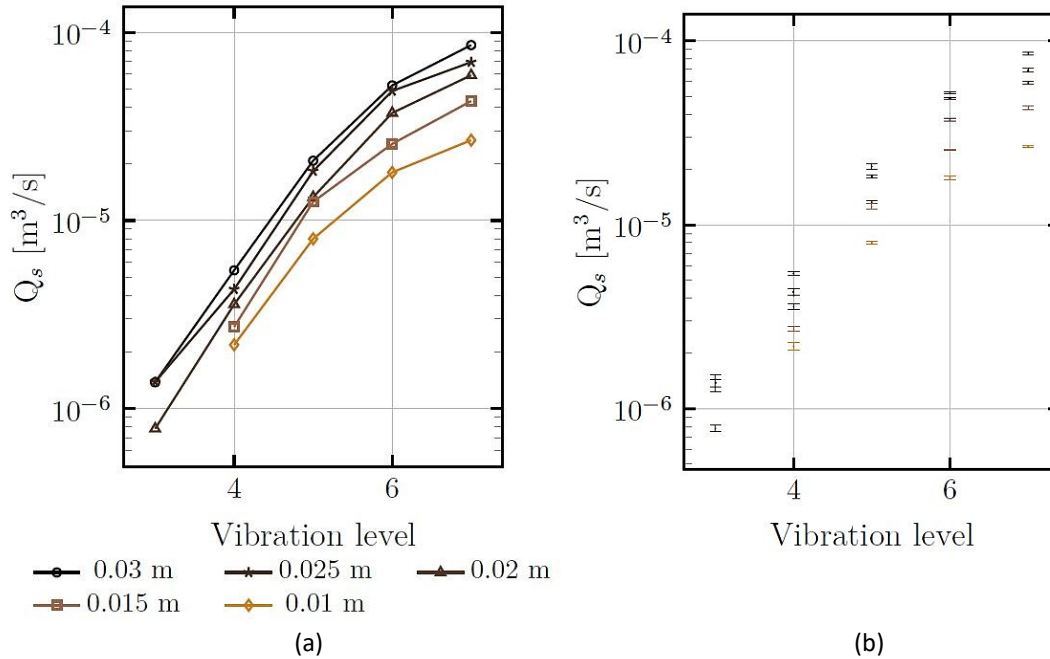


Figure 2.20. (a) curves for showing the effect of vibration level and opening height on Q_{sin} .
 (b) the corresponding error bars (Unigarro Villota 2017).

After finding the sediment inflow discharge for all experiments, the average velocity of the vibrating channel (u_{mean}) is obtained through the PIV algorithm. Now each experiment has a Q_{sin} and a u_{mean} and these data can be mapped on a graph with x -axis of u_{mean} and y -axis of Q_{sin} (Figure 2.21). A relationship between these two parameters can be found through fitting a second-degree polynomial of $y = ax^2 + bx + c$ and imposing c equal to zero; this is because when the velocity becomes zero, the inflow sediment discharge must be equal to zero, and this happens when c is equal to zero.

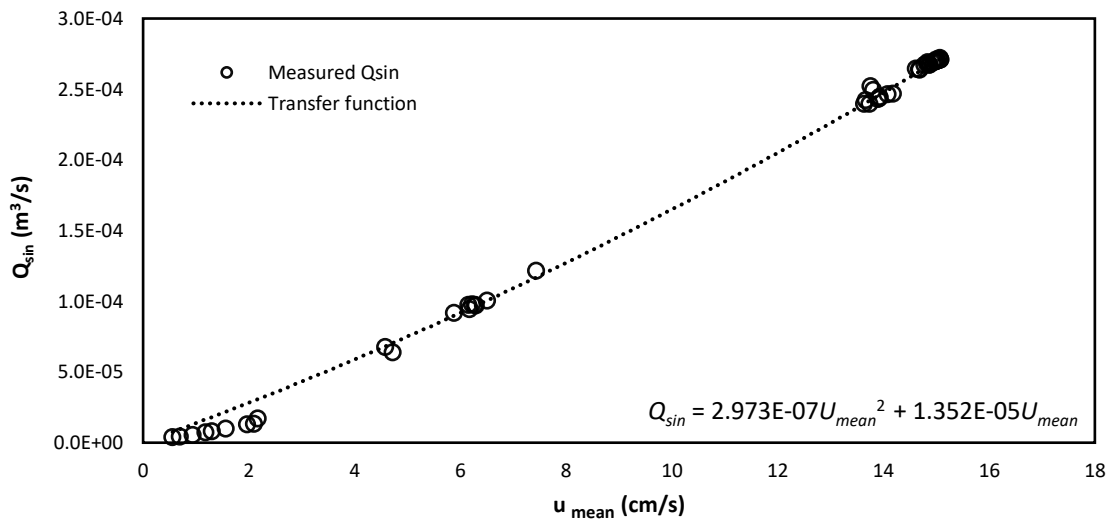


Figure 2.21. The transfer function and its curve fitted to the white points which are related to the experiments of the preliminary campaign for the calibration process.

EXPERIMENTAL SET-UP AND METHODS OF DATA ACQUISITION

As it can be seen in [Figure 2.21](#), the data related to the lower values of Q_{sin} (lower vibration levels) are not reliable since they deviate a lot from the fitted curve. This deviation is due to the hopper's non-uniform behavior in the lower vibration levels. For this reason, the vibration levels used in all the experiments are not lower than 7.3.

By having the transfer function, the temporal evolution of the sediment inflow discharge can be obtained in [Figure 2.22](#).

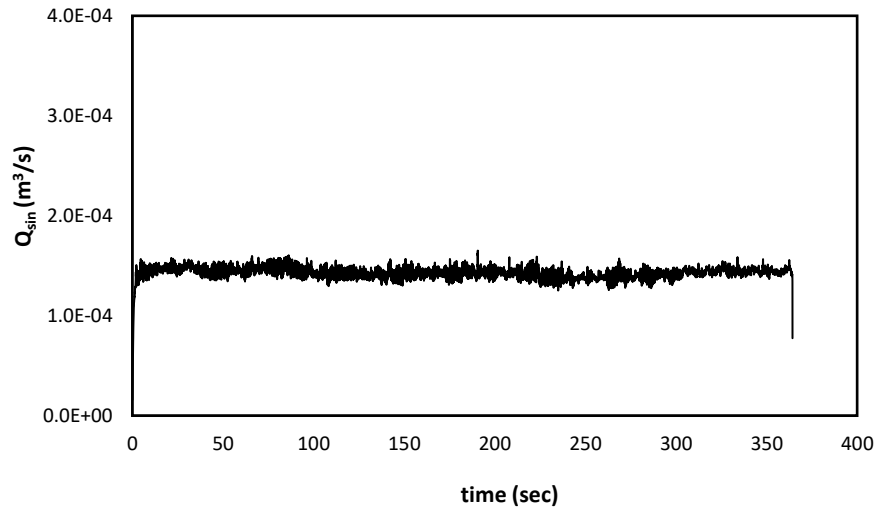


Figure 2.22. An example of the temporal evolution of the velocity.

2.2.2. Riverbed elevation detection

The channel is monitored from one side with action cameras (Their types and specifications are mentioned in [Table 2.1](#) and [2.2](#)) looking perpendicularly to the channel ([Figure 2.23](#)).



Figure 2.23. Cameras positioned in front of the channel.

In the previous works (Zanchi 2018; Zucchi 2018; Heydari 2020), the method used for the detection of the riverbed was an edge detection technique using the Sobel operator, while in this work, a new technique has been implemented for the reasons that will be mentioned in the [chapter 2.2.2.1](#).

2.2.2.1. Image processing: Bed detection using Sobel Operator

This technique uses the gradient of the image matrix in two orthogonal directions to find the amount of the changes of the intensities of the pixels which happen at the edges of the objects. The result of this processing is a binary image which is mainly black with some white pixels representing the edges of the objects in the photographs (Figure 2.24).

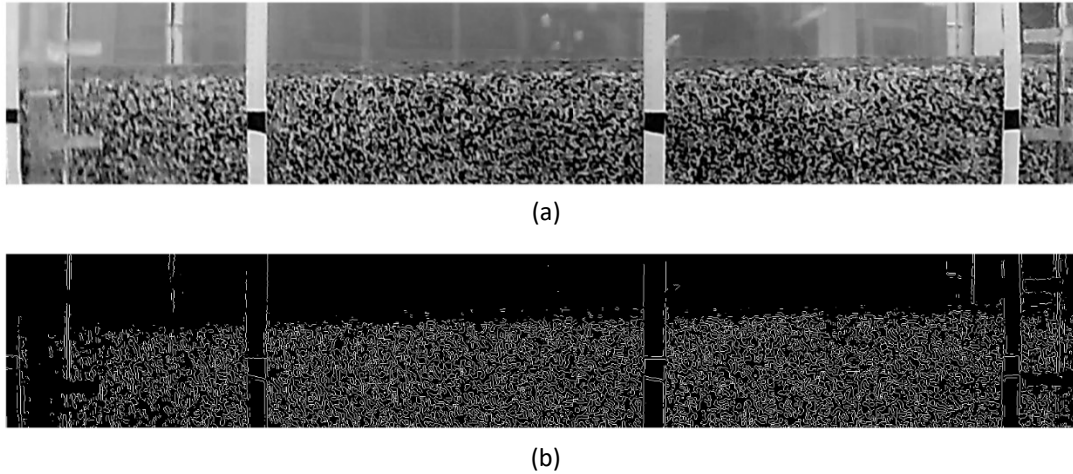


Figure 2.24. (a) photo of the channel before applying the Sobel operator. (b) photo of the channel after applying the Sobel operator.

After processing the photo with the Sobel operator, the border between the sediments and water can be clearly detected, and one can use it to find the bed profile.

Since this method only uses one photo per each instant of time, the sediments' motion is not taken into account; as a result, it leads to detect the surface of the moving sediments as the bed surface. Mainly for this reason, a different method is implemented for the detection of the stationary bed surface, which is explained in the following section.

2.2.2.2. Image processing: Bed detection using Motion detection

The algorithm consists of several iterations, and each iteration has different steps, as explained below:

1. After extracting the frames of the experiments' videos, converting them into grayscale, and removing their distortions (Figure 2.25), two subsequent photos (F_1 and F_2) are selected (Figure 2.26), each photo is a frame of the channel through the experiment, captured at a specific time. The photos are selected as the function of the jump and step parameters, the same as what is mentioned in chapter 2.2.1.1. For this work, the jump value is equal to 30 (1 sec), and the step value is equal to 1. The pixels intensity of F_1 are saved as a matrix (A_1) and the ones for F_2 are saved as another matrix (A_2).

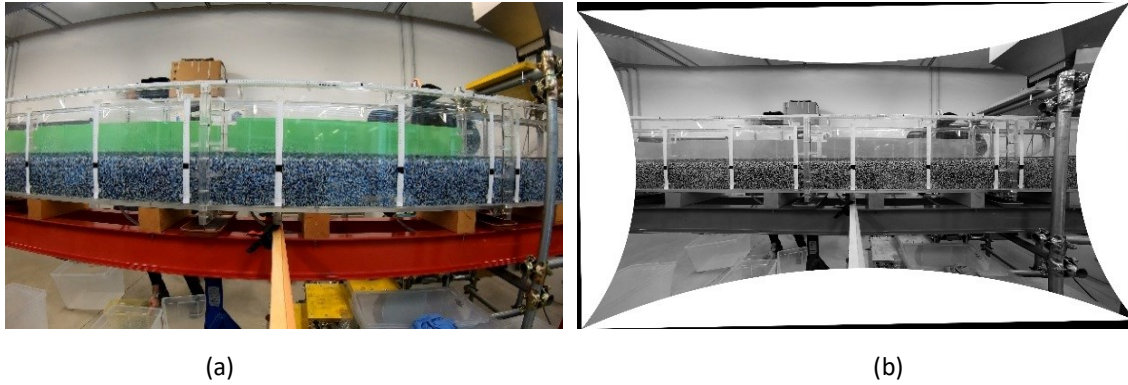


Figure 2.25. (a) Frame extracted from the video. (b) Extracted frame after the correction of the distortion.

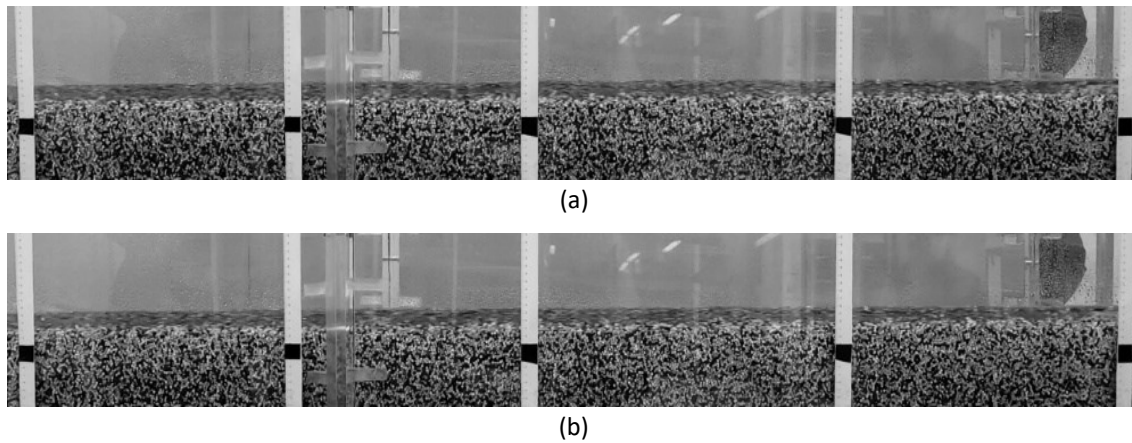


Figure 2.26. (a) First photo selected (F_1). (b) second photo selected (F_2).

2. A Gaussian filter is applied to the photos to remove the noises to avoid detecting them as motion.
3. The absolute value of subtraction of the two matrices (A_1 and A_2) is calculated, and a threshold is set; if the difference is bigger than the threshold, then it is detected as motion, and the pixel intensity is set to zero; else, it is set to one. The result of this stage is a binary image, which its black pixels (*pixel intensity* = 0) represent the areas where a motion is detected, and the white pixels (*pixel intensity* = 1) represent the areas where no motion is detected (Figure 2.27). It should be mentioned that the threshold value is chosen by trial and error. In this thesis work, the threshold ranges from 0.02 to 0.08.

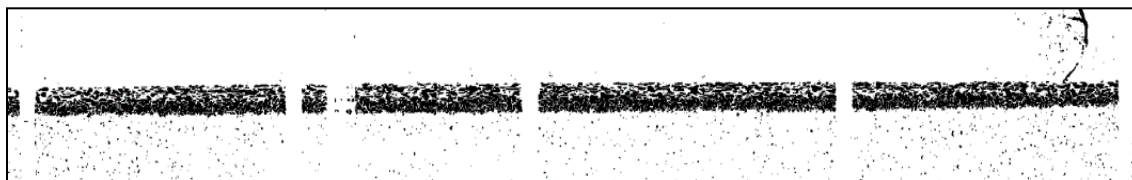


Figure 2.27. The processed photo is showing the motion with black color (threshold value=0.04).

4. The black layer seen in [Figure 2.27](#) is representative of the water and the moving layer, the lower side of this layer is the border between the stationary bed and the moving sediments, so by tracing it, one can find the edge of the bed. In order to do so, a moving window with a specific size is chosen, and it starts to move pixel by pixel from the top left corner to the down left corner ([Figure 2.28](#)) then it shifts a pixel to the right side, and again it starts moving from up to down. It should be mentioned that the size of the moving window is changeable; in this thesis work, it is chosen equal to 4×10 pixels.

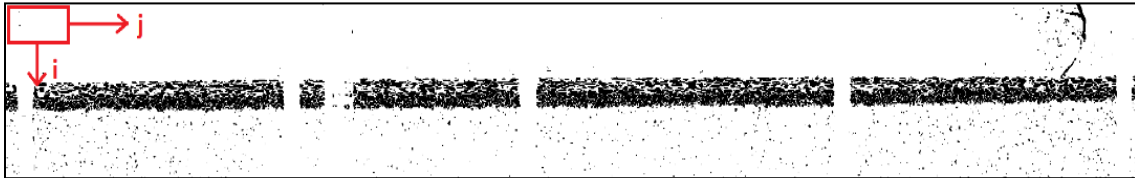


Figure 2.28. Schematic representation of the moving window from its initial position.

For each step it moves along a column, it calculates the average intensity of the pixels $P(i)$ fitted inside of it. By doing this, a signal is produced for each column; this signal shows the amount of the average intensity for each row of the column ([Figure 2.29](#)). The black layer in the processed photo is between two white areas, so when moving from up to down, the signal value significantly drops when entering the black layer and significantly rises when exiting from the black layer. As a result, there are two significant changes in the signal, the first one (upper one) is related to the water surface and the second one is related to the border between the moving layer and the stationary bed. For detection of the location of these changes, a MATLAB function (`findchangepts`) is used; since this function does not give the exact location of the changes in the signal, some modifications of the results are necessary to find the exact location of the bed ([Figure 2.29](#)). These modifications are:

- a. Going forward from the location of the changes reported by the MATLAB function and check if the slope of the signal shown in [Figure 2.29](#) is close to zero (almost horizontal). This is because the signal intensity remains almost constant (around one) after getting out from the black layer; as a result, the slope of the signal tends to be zero. The first point that matches with this condition is considered as the location of the center of the moving window when this window gets out from the black layer completely.
- b. Subtracting half of the window size from the location found in the previous step to find the exact location of the bed.

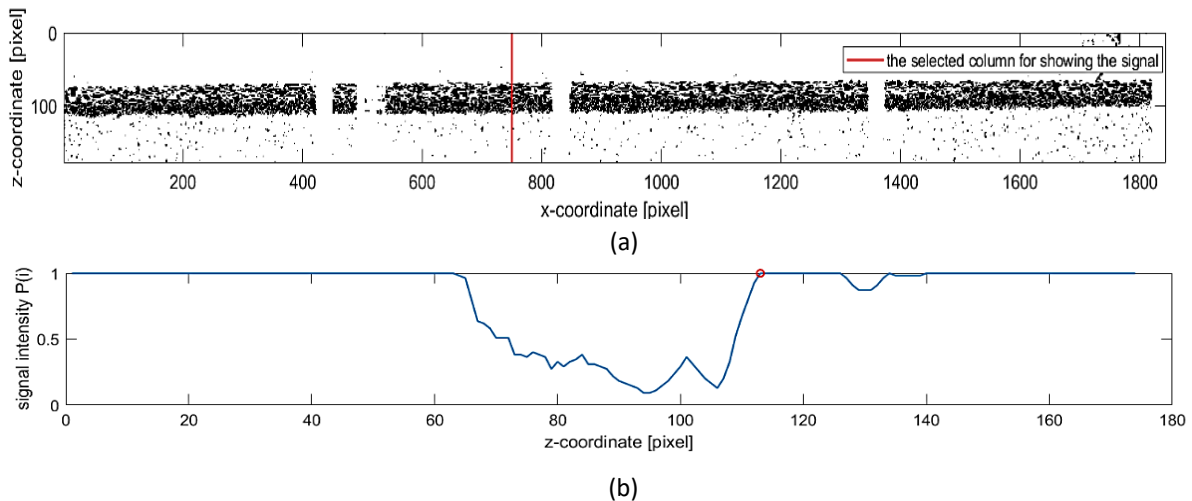


Figure 2.29. (a) The selected column is shown in red for showing its related signal. (b) The signal along the selected column with a red dot on it representing the location of the center of the moving window when the moving window leaves the black layer completely.

Up to this step, the location of the bed for each column of the photo is detected, so for each column, there is a point that represents the location of the bed; by putting these points together, the bed profile can be produced (Figure 2.30).

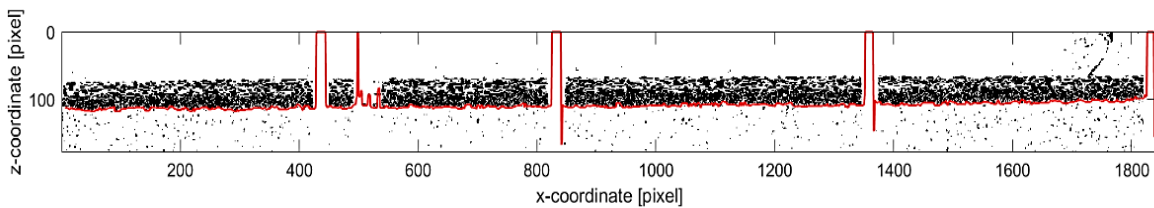


Figure 2.30. The produced bed profile is shown in red.

5. The bed profile produced until the previous step contains some errors; the main sources of these errors are:
 - a. The remaining noises are detected as motion. Apart from applying the gaussian filter to reduce the noise, using high-quality cameras and having a good lighting condition during the experiments can improve the situation.
 - b. The sections of the channel where the sediment motion is not visible.
 - c. The motion of other objects rather than sediments and water; basically, these motions are caused by the movement of people in the laboratory behind the channel or caused by the reflection of the people in front of the channel. To reduce the errors caused by people moving behind the channel, that side of the channel is covered with some green papers (Figure 2.2) to avoid detecting their motion, but still, nothing has been done to reduce the error caused by reflection.

The error sources mentioned above are shown in Figure 2.31.

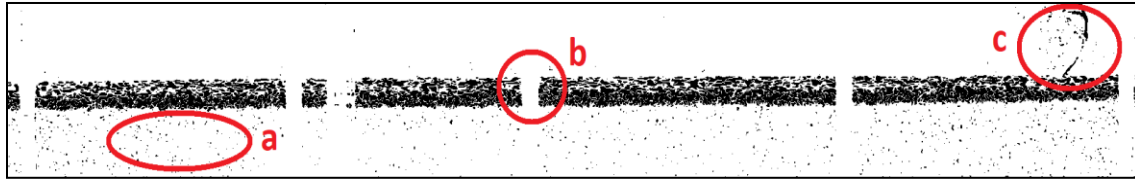


Figure 2.31. Error sources related to (a) the noises, (b) the lack of visibility, and (c) the motion of other objects.

6. To handle the remaining errors caused by reasons mentioned above, a MATLAB function (`filloutliers`) is used to find the outliers in the profile data and to replace them with appropriate data. This function considers each datum as an outlier if it deviates more than N times of standard deviation from the mean of the data in the neighborhood. N and the size of the neighborhood are two inputs of this function, and one should find them by trial and error. The final modified bed is represented in [Figure 2.32](#).

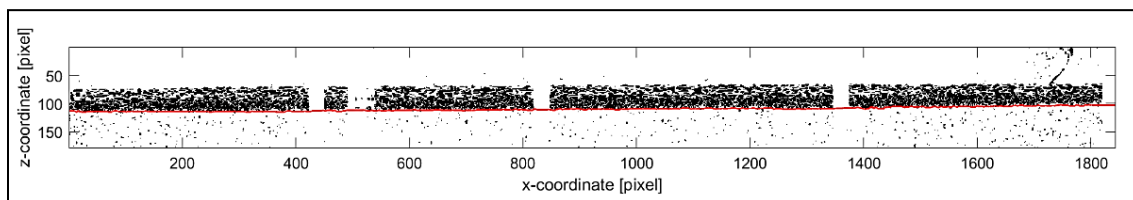


Figure 2.32. The detected bed profile after correction of the outliers.

7. The coordinates of the profile data are in the pixel scale; they should be converted into a metric scale through a conversion factor. The conversion factor can be obtained by dividing the monitored length of the channel in pixel to the monitored measured length in centimeters. The coordinates should be referenced in x -direction with respect to the origin located in upstream (the x -coordinate increases when moving from upstream to downstream) and in z -direction with respect to the position of black tapes which are located 15 cm above the bottom of the channel (the z -coordinate increases when moving from down to up).

A problem related to the referencing is the distortion of the photos. As mentioned before, a radial transformation is used for removing the distortions, but it is not able to remove them completely; as a result, it causes errors in referencing the coordinate system. Using cameras for bed detection with less distortion can improve the situation.

8. After finding the profile for this time instant, another pair of photos are chosen based on the jump and step parameters, and the code repeats all the steps mentioned above; at the end, one has the bed profile for each time instant (in this case, it is for every second).

The above-mentioned algorithm is applied to the frames captured by each camera separately since these cameras only capture a portion of the channel; as a result, the bed profile for each portion is obtained separately, and one should put them together to create the bed profile for the whole channel. After regrouping the data, the whole profile is smoothed by applying the Savitzky-Golay filter. This filter smooths data by fitting successive subsets of adjacent data

with a low degree polynomial by using the linear least-squares method. The comparison between the bed profile before and after smoothing is shown in [Figure 2.33](#).

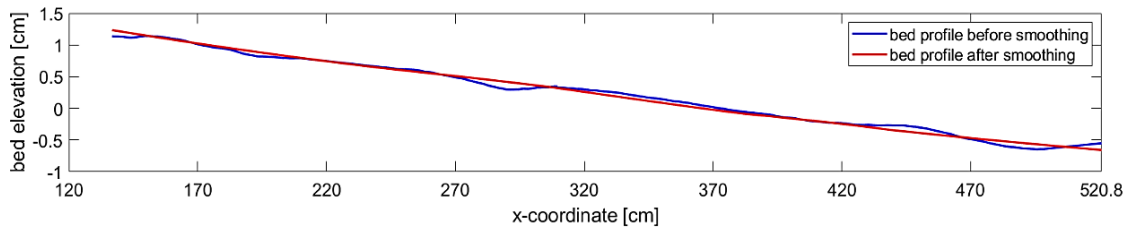


Figure 2.33. The blue line shows the profile before smoothing, and the red line shows the profile after smoothing.

2.2.2.3. Comparison between both methods for detection of the bed

The first difference made by applying the new method (motion detection) is the fact that it is less user-demanding and time-consuming compared to the previous one. This is because, in the previous algorithm, the process of correction of the errors (removing the outliers) was manual, while in the new one, this process is automatized.

The second difference is the improvement of temporal resolution. As mentioned above, the previous algorithm was more user-demanding and time-consuming. Therefore, with the previous algorithm, the bed profiles were produced with the temporal resolution of 10 seconds, whereas with the new one, the bed profiles can be produced easily with the temporal resolution of 1 second.

The other difference is the quality of the results. With the new method, the detected bed profiles are smoother than the ones detected with the previous method. This can be seen in [Figure 2.34](#).

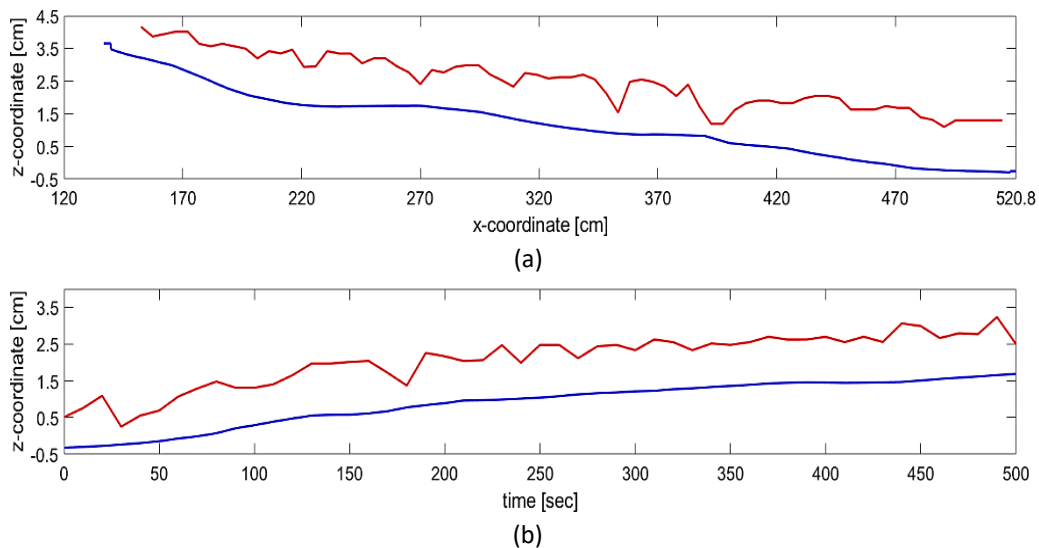


Figure 2.34. (a) Spatial evolution of the bed in a specific time. The blue line is produced by using motion detection, and the red line is produced by using the Sobel operator. (b) Temporal evolution of the bed in a specific section of the channel. The blue line is produced by using motion detection, and the red line is produced by using the Sobel operator.

The last difference of the new method is the fact that it detects the surface of the stationary bed as the bed surface, while the previous method detects the surface of the moving sediments as the bed surface. Since in this thesis it is assumed that the bed surface is the border between the stationary bed and the bedload layer, the motion detection algorithm is developed and used for detection of the bed surface.

The bed profiles derived with both methods (motion detection and Sobel operator) are shown in [Figure 2.35](#).

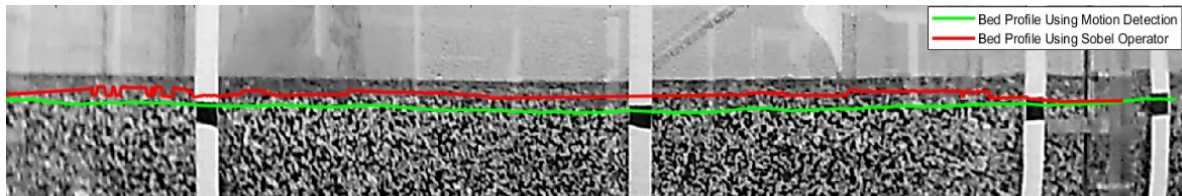


Figure 2.35. The green line shows the bed profile detected by using motion detection, and the red line shows the bed profile detected by using the Sobel operator.

2.2.3. Water surface elevation detection

There are nine piezometers positioned in 9 locations along the channel for the measurement of the water surface in each location ([Figure 2.36](#)).



Figure 2.36. Piezometers pipes.

In the previous works, these piezometers were used in order to obtain the water surface elevation through an image processing method, explained in the next section, while in this work, another method is used, which is the same as what used for the bed detection.

2.2.3.1. Image processing: monitoring the piezometers' data (Zanchi 2018)

Each piezometer contains a black plastic ball that stays on the water surface inside the pipe; since the plastic ball's color is in contrast with the background color, one can easily detect the ball's location to obtain the water surface, to do so, the piezometers were monitored with an action camera (Its type and specification are mentioned in [Table 2.1](#) and [2.2](#)). After changing the color scale of the picture into grayscale and removing the distortion, a negative picture is produced from the grayscale picture; therefore, the color of the ball changes from almost black into almost white and the background changes from almost white into almost black. Now with an appropriate threshold, a binary picture is produced so that the ball's color is completely white, and the background is completely black; as a result, one can easily find the location of the ball with detection of the white area, so the water surface related to each piezometer can easily be obtained. The processes done on the pictures are shown in [Figure 2.37](#).

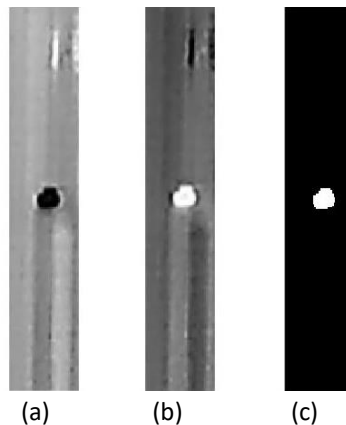


Figure 2.37. (a) Image of the piezometer. (b) Negative image. (c) Binary image (Zanchi 2018).

As mentioned in the previous section, the channel's water surface is only monitored with nine piezometers, so one can obtain the water surface in nine locations along the channel. This is while with the same method used for the bed detection (explained in [chapter 2.2.2.2](#)), the water surface can be obtained in every point along the channel. Another reason to use this new method instead of monitoring the piezometers is the fact that the processed data needed for obtaining the water surface level is obtained through the bed detection algorithm, so there is no need to spend more time for processing data to obtain the water surface level. The algorithm for this new method is explained in the following section.

2.2.3.2. Image processing: water surface detection using Motion detection

All the steps of the algorithm for detection of the water surface are the same as what mentioned in [chapter 2.2.2.2](#) except for step number 4, in which the lower edge of the black layer was used, while for detection of the water surface, the upper side of the black layer is used because this side represents the water surface. The procedure is shown in [Figure 2.38](#).

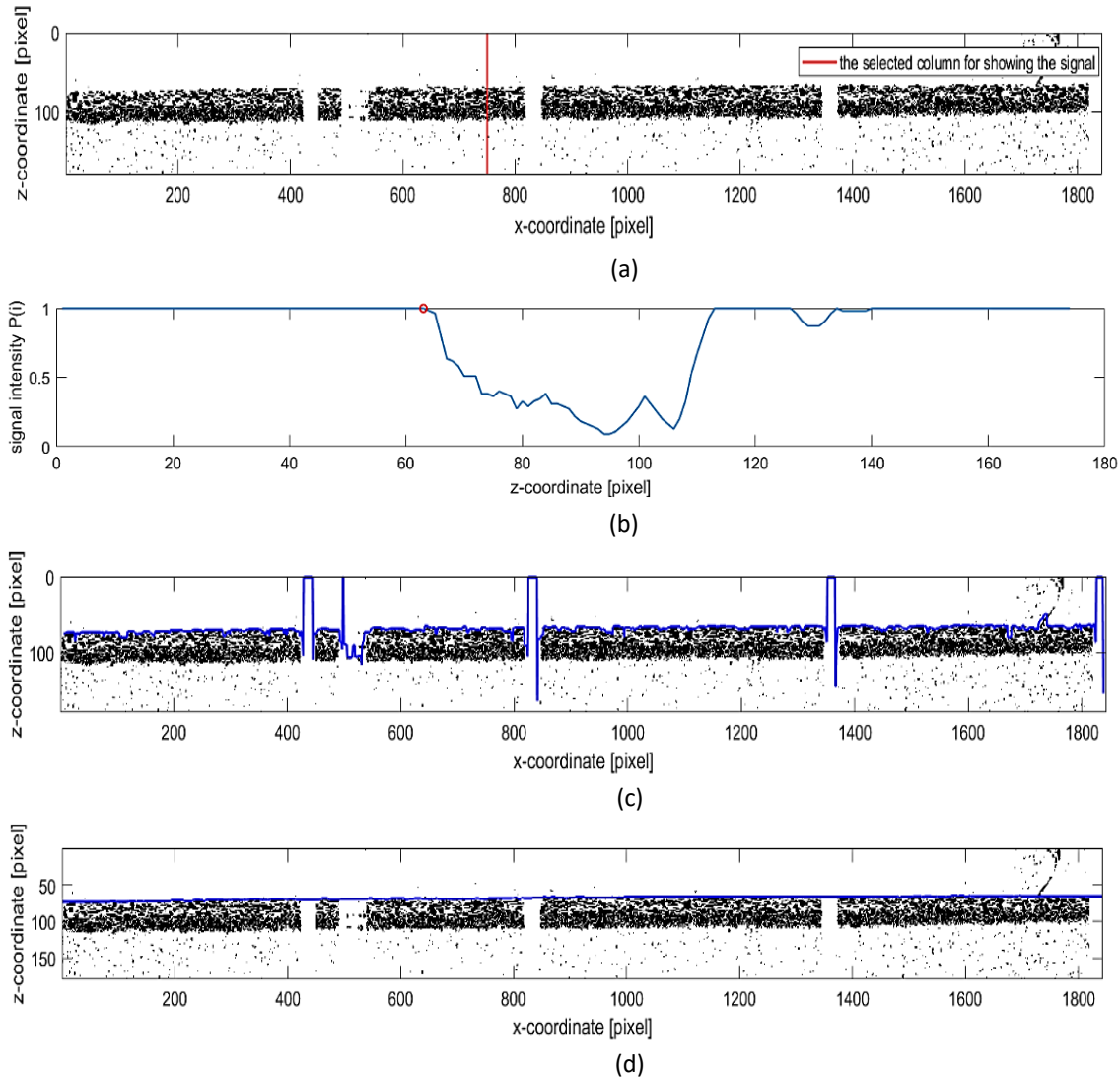


Figure 2.38. (a) The selected column, shown in red, for showing its related signal. (b) The signal along the selected column with a red dot on it representing the location of the center of the moving window when the moving window enters the black layer. (c) The produced water surface profile, shown in blue. (d) The detected water surface profile after correction of the outliers.

2.2.4. Calculation of sediment amount inside the collector (Zucchi 2018)

The sediments transported through the channel are trapped inside the collector; for further analyses, it is needed to calculate the amount of these sediments at different times. The method used to measure the sediment amount is almost manual. After extracting the frames, changing the color scale into grayscale, and removing the distortion, different points on the edge of the sediment are selected to extract their coordinates in pixel scale (Figure 2.39).

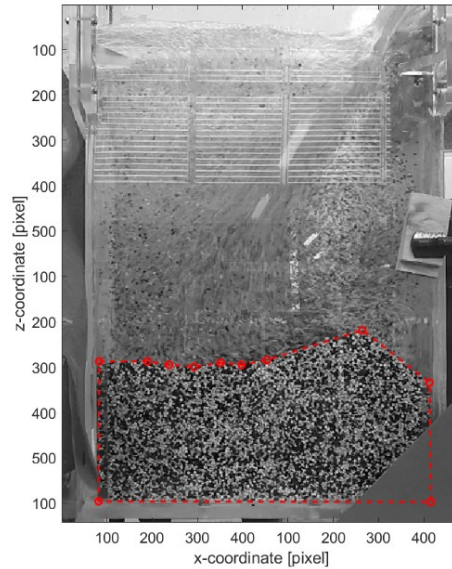


Figure 2.39. The polygon is created with the selected points to represent the shape of sediments inside the collector.

One should pay attention that these points should be selected in a way that the polygon created by these points should almost represent the shape of sediments accumulated inside the collector. After extracting the coordinates of the points, the area of the above-mentioned polygon can be calculated through the following formula:

$$A = \frac{(x_1 \times y_2 - x_2 \times y_1) + (x_2 \times y_3 - x_3 \times y_2) + \dots + (x_n \times y_1 - x_1 \times y_n)}{2} \quad 2.5$$

where x_n and y_n are the x -coordinate and y -coordinate of the point number n and A is the area of the polygon.

The obtained area is in pixel scale, so it has to be converted into a metric scale through a conversion factor. Now that the area of the sediments seen in the picture is available, one can find the apparent volume by multiplying this area into the width of the collector (0.3 m).

2.3. Evolution of the main system from parent thesis work

The methods of data acquisition for some parts of the experiments are changed to have more precise data with less time consumption, and the process for data acquisition is more automatized to make them less user-dependent. Another difference compared to the parent thesis is introducing a new type of experiments which are SC experiments; these experiments are designed to have an estimation of the sediment transport capacity of the channel (will be explained in [chapter 3.2.2](#)). The experiments are subdivided into three main categories:

- AE1 - AE3 (Heydari 2020)
- AE1 - AE8
- SC1 - SC3

It should be mentioned that the experimental data related to the parent thesis (AE1 - AE3) were processed again with the new methods; that is why the second category also includes AE1 - AE3. In [Table 2.4](#), the methods of data acquisition for each category are mentioned.

Table 2.4. The evolution of data acquisition procedure.

<i>Experiment</i>	<i>AE1 - AE3 (Heydari 2020)</i>	<i>AE1 - AE8</i>	<i>SC1 - SC3</i>
<i>Sediment inflow discharge</i>	measured by Particle Image Velocimetry (PIV) algorithm	measured by Particle Image Velocimetry (PIV) algorithm	measured by Particle Image Velocimetry (PIV) algorithm
<i>Bed profiles</i>	Bed detection using Sobel operator	Bed detection using motion detection	Bed detection using motion detection
<i>Water profiles</i>	Processing the images of piezometers	Water surface detection using motion detection	Water surface detection using motion detection
<i>Sediment inside the collector</i>	Manual	Manual	Manual

2.4. Experimental procedure

2.4.1. Pre-experiment phase

In this phase, everything needed to perform an experiment is done. First, the slope of the channel is set to the desired value (1.2 %). The water level inside the underground container is checked, and if it is too low, it must be restored for the proper functioning of the pumping system. The hopper must be filled with the sediment particles, and its opening height and vibration level are set to the desired values. The sediment particles inside the channel are smoothed with a fixed height of 15 *cm* with respect to the bottom of the channel. The bed surface should be sprayed with nebulized water to avoid their movement with the initial inflow of water; this is because when the water flow reaches dry particles on the surface, they start to move due to the surface tension of water. The cameras are positioned in their proper places for monitoring different parts of the experiment for the goal of data acquisition.

2.4.2. Experiment phase

The pumping system is turned on, and the water inflow discharge is set to a high value at the beginning to quickly fill the upstream tank; when the water enters the channel, the discharge is decreased to a lower value to avoid disturbance on the mobile bed; when the bed is completely saturated, and the water surface reached the bed surface, the cameras are turned on and their turn-on time is recorded, then the water discharge is set to the desired discharge almost gradually and when reaches it, the hopper is turned on and the time is recorded, this recorded

time is the time of the beginning of the experiment, and it is used for synching other cameras together. During the experiment, the water discharge is checked to regulate it if necessary. The hopper is filled constantly to avoid the hopper tank being empty until the end of the experiment, when the available sediment particles are finished. The hopper and the pump are turned off, and the finishing time is recorded to have the duration of the experiment.

2.4.3. Post-experiment phase

In this phase, the videos are downloaded from the cameras for the further process of the data. The sediments gathered inside the collectors and the extra sediments accumulated inside the channel are spread on several nets to let them dry in few days; these sediments are used for evaluation of the mass conservation to check if the experiment is performed correctly.

CHAPTER 3

INITIAL SEDIMENT TRANSPORT CAPACITY AND INCIPIENT MOTION

3.1. Introduction

The maximum amount of sediment that can be conveyed through a specific river section is called sediment transport capacity. This parameter has an important role in the description of the aggradation and degradation processes in a riverbed. Aggradation happens if the sediment inflow discharge in a specific section is more than its sediment transport capacity; on the other hand, degradation occurs when the sediment transport capacity is less than the sediment inflow discharge. Also, the equilibrium condition happens if the sediment inflow discharge is equal to the sediment transport capacity. The ratio between the sediment inflow discharge and the sediment transport capacity is called the loading ratio, Lr (equation 3.1).

$$Lr = \frac{Q_{sin}}{Q_s} \quad 3.1$$

where Q_{sin} is the sediment inflow discharge and Q_s is the sediment transport capacity.

Since the aim of this thesis work is to study the aggradation processes under the overloading conditions, the estimation of the sediment inflow discharge and the sediment transport capacity is required to evaluate Lr . The former one (Q_{sin}), which is an experimental control, was explained in [chapter 2.2.1](#). One of the aims of this chapter is to estimate the sediment transport capacity (Q_s) of the channel.

Sediment transport capacity depends on many factors; the most important ones are:

- Water discharge
- Slope
- Roughness
- Velocity of water
- Sediment size

Some of these parameters are dependent on the others, and a link exists between them. For example, the flow velocity depends on the water discharge, roughness, and slope.

It is important to note that in this chapter, it is needed to obtain the sediment transport capacity of the experimental channel in the initial condition (Q_{s0}) where the bed is not affected yet by the aggradation phenomenon. Indeed, the aggradation process is a dynamic one, in the sense that during this process, the channel increases its slope by time to reach the equilibrium condition. This increase in the slope causes the channel's sediment transport capacity to increase as well; thus, this quantity also changes with time. For reporting the channel's sediment transport capacity, one should consider the initial values of this quantity because, in the beginning, the bed has not been affected that much by the aggradation process.

It is worth restating that in the performed experiments, the channel's properties (e.g., bed slope, channel's cross-section, and sediment properties) remained constant. Therefore, theoretically,

the initial sediment transport capacity of the channel would change only with the water discharge. Since two series of experiments in terms of water discharge have been performed, it is expected to obtain two values for Q_{s0} , one for the experiments with $Q = 5 \text{ l/s}$ and another for the experiments with $Q = 7 \text{ l/s}$.

Also, at the end of the chapter, the incipient motion condition and estimation of the critical water discharge would be discussed.

3.2. Estimation of the initial sediment transport capacity

In the presented thesis work, four methods are applied to estimate the initial sediment transport capacity of the artificial channel:

- Meyer-Peter and Müller formula (MPM formula)
- SC experiments
- Collector method
- Monitoring method

In the following parts, these methods will be explained.

3.2.1. Meyer-Peter and Müller formula (MPM formula)

One of the most common formulae to estimate the sediment transport capacity is the one presented by Meyer-Peter and Müller in 1948 (equation 3.2).

$$\Phi = 8(\tau^* - \tau_c^*)^{1.5} \quad 3.2$$

where:

Φ = non-dimensional solid discharge per unit width

τ^* = Shields parameter

τ_c^* = critical Shields parameter

The critical Shields parameter can be determined either directly from the Shields diagram as a function of the shear Reynolds number (Figure 1.5) or from a transformed Shields diagram as a function of the dimensionless grain diameter D^* ($\tau_c^* = f(D^*)$); there are different formulae to transform the Shields diagram and estimate τ_c^* as a function of D^* . In the presented work, two formulae are used to calculate τ_c^* , the Brownlie (1981) formula, and the Van Rijn (1984) formula.

Brownlie approach to estimate the critical Shields parameter

In this approach, the following formula is used to calculate the critical Shields parameter, τ_c^* :

$$\tau_c^* = 0.22D^{*-1} + 0.06e^{-17.77D^{*-1}} \quad 3.3$$

$$D^* = d \left(\frac{(\rho_s - \rho)g}{\rho v^2} \right)^{1/3} \quad 3.4$$

where:

D^* = the dimensionless grain diameter

d = the diameter of the sediment material which in this work is equal to 0.0038 m

ρ_s = the material density which is equal to 1443 kg/m³

ρ = the water density which is 1000 kg/m³

ν = the water kinematic viscosity, equal to 1×10^{-6} m²/s

By using the above values, the dimensionless grain diameter is calculated equal to 62, and consequently, the critical Shields parameter is obtained equal to:

$$\tau_c^* = 0.0486$$

Van Rijn approach to estimate the critical Shields parameter

In this approach, in order to estimate the critical Shields parameter, depending on the value of the dimensionless grain diameter, different equations have been proposed (equations 3.5).

$$\begin{aligned}\tau_c^* &= 0.24D^{*-1} \quad \text{for } 1 \leq D^* \leq 4 \\ \tau_c^* &= 0.14D^{*-0.64} \quad \text{for } 4 < D^* \leq 10 \\ \tau_c^* &= 0.04D^{*-0.1} \quad \text{for } 10 < D^* \leq 20 \\ \tau_c^* &= 0.013D^{*0.29} \quad \text{for } 20 < D^* \leq 150 \\ \tau_c^* &= 0.055 \quad \text{for } D^* > 150\end{aligned}\tag{3.5}$$

where D^* is calculated using equation 3.4, similarly to the previous method. Since in this work D^* was calculated equal to 62, the following equation would be valid to estimate τ_c^* :

$$\tau_c^* = 0.013D^{*0.29}\tag{3.6}$$

Substituting $D^* = 62$ in this formula, the critical Shields parameter is obtained equal to:

$$\tau_c^* = 0.043$$

It is worth mentioning that the critical Shields parameter proposed by Meyer-Peter and Müller is equal to 0.047, which is in agreement with the values calculated using the Brownlie and the Van Rijn approaches.

The other important parameter in the MPM formula is the Shields parameter, τ^* , which is computed using equation 1.15 (presented in chapter 1.5.1):

$$\tau^* = \frac{\tau}{(\rho_s - \rho)gd}\tag{1.15}$$

where τ is the bed shear stress and is calculated using the following equation:

$$\tau = \rho g R_H S_f \quad 3.7$$

where R_H shows the hydraulic radius and S_f represents the friction slope and can be calculated using equation 1.32.

$$S_f = \frac{n^2 \times U^2}{R_H^{4/3}} \quad 1.32$$

In this formula, U is the velocity of the flow, and $n = 0.015 \text{ s/m}^{1/3}$ is the Manning's coefficient, obtained experimentally by Unigarro Villota (2017) with performing multiple tests in uniform flow.

Having the values of the critical Shields parameter and calculation of the Shields parameter, now the non-dimensional solid discharge (Φ) can be calculated applying the MPM formula (equation 3.2). By obtaining Φ , the initial sediment transport capacity of the channel (Q_{s0}) can be computed using equation 3.8.

$$Q_{s0,MPM} = B q_{s0} \quad 3.8$$

where:

B = the width of the channel, equal to 0.3 m in this work

q_{s0} = sediment transport capacity per unit width, which is calculated as follows:

$$q_{s0} = \Phi \sqrt{g \left(\frac{\rho_s - \rho}{\rho} \right) d^3} \quad 3.9$$

As an example, the results of the calculations of the initial sediment transport capacity for the experiments with $Q = 7 \text{ l/s}$ are presented in Table 3.1.

Table 3.1. The results of the estimation of the initial sediment transport capacity for experiment series with $Q = 7 \text{ l/s}$, using Brownlie and Van Rijn approaches and applying MPM formula.

Approach	D^*	τ_c^*	τ (N/m)	τ^*	Φ	$q_{s0,MPM}$ (m²/s)	$Q_{s0,MPM}$ (m³/s)
Brownlie	62	0.0486	3.3074	0.2003	0.473	2.31E-04	6.92E-05
Van Rijn	62	0.0430	3.3074	0.2003	0.499	2.44E-04	7.31E-05

All estimations of the initial sediment transport capacity for all experiments are presented in a summary table (Table 3.5) in chapter 3.2.5.

3.2.2. SC experiments

This type of experiment is designed based on the concept of the hydrodynamic equilibrium. As previously mentioned, there is neither aggradation nor degradation in the equilibrium condition, which means that the sediment inflow discharge is equal to the sediment transport capacity of the channel (whatever gets into the channel from the upstream, gets out from the downstream). Because of the reason mentioned above, this method's main goal is to find a sediment feeding rate that does not cause aggradation or degradation in the channel. As a result, this sediment feeding rate can be considered the channel's sediment transport capacity. The procedure of this method is explained below.

First of all, the hopper's vibration level is set to an initial value with a fixed opening height; then, the experiment is run with a specific water inflow discharge. One of the following conditions will happen:

- 1. Aggradation**

The occurrence of this condition means that the sediment inflow discharge is higher than the sediment transport capacity; as a result, the vibration level must be set to a lower value for the next step.

- 2. Degradation**

The occurrence of this condition means that the sediment inflow discharge is lower than the sediment transport capacity; as a result, the vibration level must be set to a higher value for the next step.

- 3. No aggradation or degradation (equilibrium condition)**

The occurrence of this condition means that the sediment inflow discharge is equal to the sediment transport capacity; as a result, there is no need to change the vibration level anymore, but this does not mean that the experiment is finished right after this observation since some time is needed to assess the possible variation of the bed elevation.

One should pay attention that none of the above-mentioned conditions occurs immediately, and some time is needed to be passed for being able to assess the condition of the channel correctly.

In the next step of the experiment, the hopper's vibration level is changed based on the above-mentioned conditions, then the channel bed is checked again for the occurrence of these conditions. This procedure goes on until the equilibrium condition is reached, which means that the bed elevation remains constant. The sediment inflow discharge related to the vibration level coincident with the equilibrium condition is obtained through the PIV method (explained in [chapter 2.2.1.1](#)) and reported as the channel's sediment transport capacity.

Estimation of the initial sediment transport capacity

As an example, in Table 3.2, the results of the experiment SC3 (related to $Q = 7 \text{ l/s}$) are presented. Also, in Figure 3.1, the $Q_{sin} - \text{time}$ graph obtained from the PIV process, and in Figure 3.2, the temporal evolutions of the bed corresponding to this experiment are shown.

Table 3.2. The results of experiment SC3, obtained from the PIV process.

<i>Vibration levels</i>	<i>Time (s)</i>	$Q_{sin} \text{ (m}^3\text{/s)}$
7.7	50	1.22E-04
8	142	2.00E-04
7.85	146	1.40E-04

Vibration levels

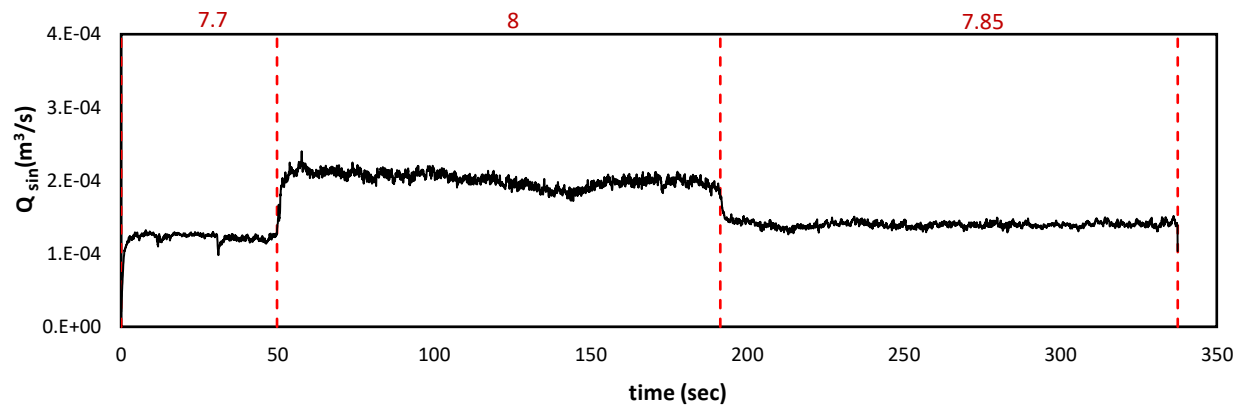


Figure 3.1. Temporal evolution of sediment inflow discharge for experiment SC3, obtained from PIV process.

INITIAL SEDIMENT TRANSPORT CAPACITY AND INCIPIENT MOTION

Vibration levels

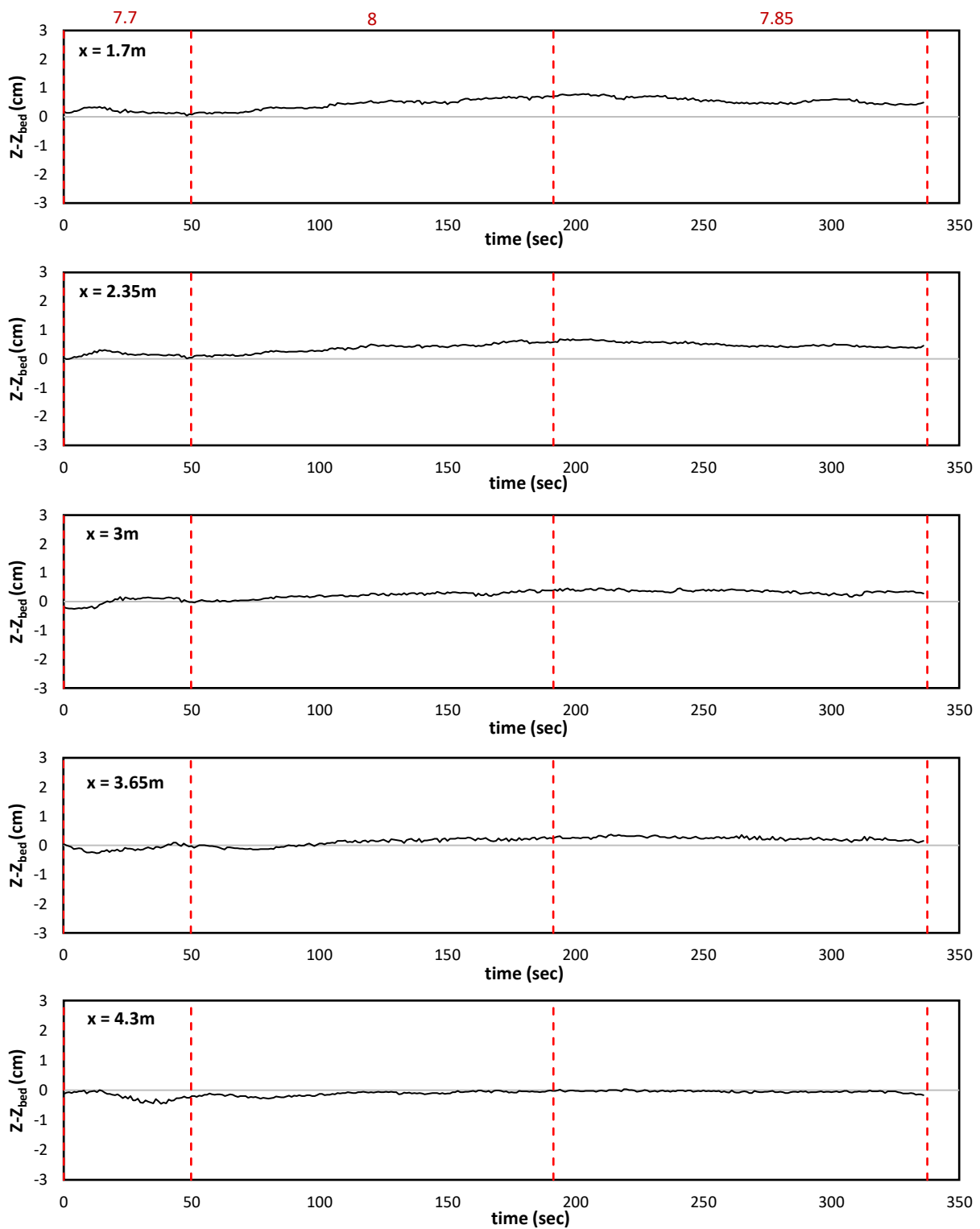


Figure 3.2. Temporal evolution of the bed for experiment SC3, obtained from the bed detection process.

From the above graphs, it is recognized that the equilibrium condition happens in vibration level between 7.7 and 7.85. Therefore, according to PIV results, the average of sediment feeding rates corresponding to these vibration levels is considered as the initial sediment transport capacity of the channel for $Q = 7 \text{ l/s}$, which is equal to $1.31 \times 10^{-4} \text{ m}^3/\text{s}$.

3.2.3. Collector method

The collector method is applied to the AE experiments, and it is derived from the fact that almost all sediments transported through the channel are trapped into the collector; as a result, the amount of sediment inside the collector can be used to calculate the sediment transport capacity of the channel. Indeed, the method is based on measuring the volume of the accumulated sediments in the downstream collector at different times. First of all, the total volume of sediment inside the collector ($V_{measured_collector}$) is measured with the method mentioned in [chapter 2.2.4](#) at different times, then the sediment volume ($V_{sediment_collector}$) can be calculated by multiplying the total measured volume by $(1 - p)$. In the next step, one can obtain the sediment transport capacity ($Q_{s,collector}$) with the following formula:

$$Q_{s,collector} = \frac{V(t)_{measured_collector} \times (1 - p)}{t} = \frac{V(t)_{sediment_collector}}{t} \quad 3.10$$

where p is the porosity of the sediments and t is the time at which the volume accumulated in the collector is measured.

The initial sediment transport capacity of the channel ($Q_{s0,collector}$) would be the average of sediment transport capacities obtained from the above equation at the initial time instants, where the values of $Q_{s,collector}$ are almost constant, and the bed is not changed significantly by the aggradation phenomenon.

It is worth mentioning that the calculations are done at every 5-sec time interval for the initial part of the experiments (almost the initial 100 sec), and then it increases to 10 seconds or more.

Here, as an example, the procedure and results of this method are shown for experiment AE6 with $Q = 7 \text{ l/s}$.

The calculated $V_{sediment_collector}$ and $Q_{s,collector}$ at different times are shown in [Figures 3.3](#) and [3.4](#), respectively.

INITIAL SEDIMENT TRANSPORT CAPACITY AND INCIPIENT MOTION

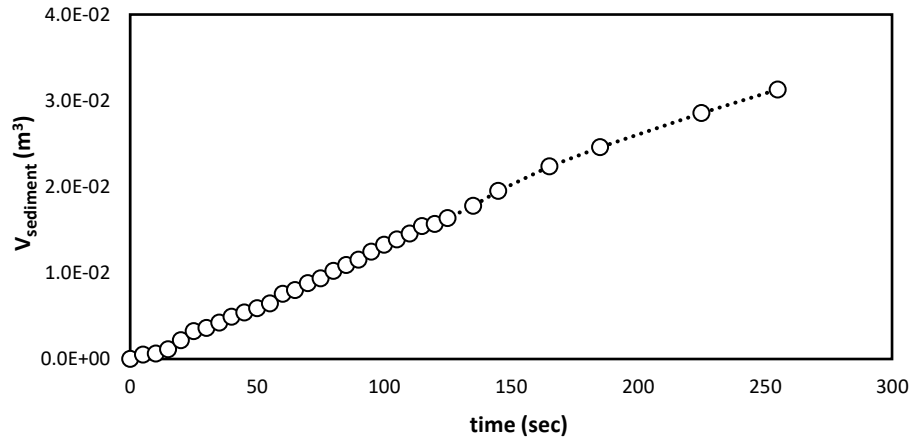


Figure 3.3. The sediment volume inside the collector at different times for experiment AE6.

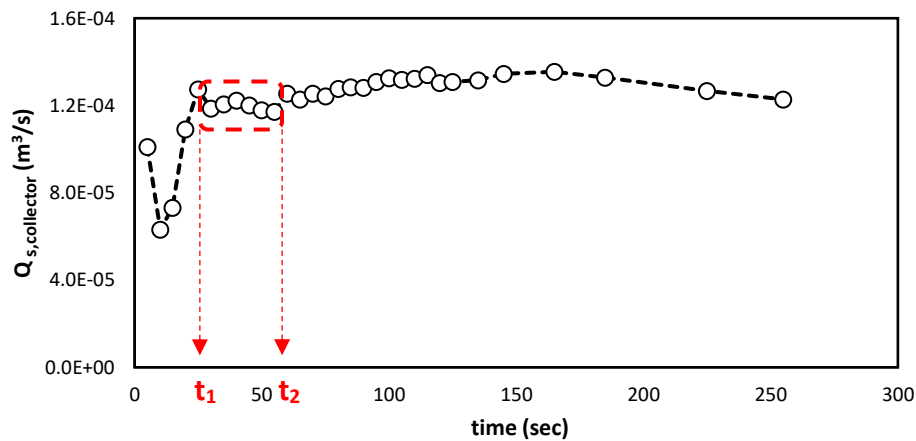


Figure 3.4. The sediment transport capacity for experiment AE6, calculated with the collector method.

According to what explained before, the initial sediment transport capacity of the channel, $Q_{s0,collector}$, would be the average of the calculated $Q_{s,collector}$ between time t_1 and t_2 (red rectangle), where the values of the $Q_{s,collector}$ are almost constant in this time interval. The final result for experiment AE6 is reported in [Table 3.3](#).

Table 3.3. The estimation of initial sediment transport capacity of the channel derived from the experiment AE6 (with $Q = 7 \text{ l/s}$) and using the collector method.

<i>Experiment</i>	<i>t₁ (sec)</i>	<i>t₂ (sec)</i>	<i>Q_{s0,collector} (m³/s)</i>
AE6	30	55	1.19E-04

As it is observed, the initial part of the measurement, between 0 and 30 seconds, is not considered in the calculations. The reason refers to the fact that the initial data before the time t_1 are not reliable for two causes:

1. They are related to the initial bed adjustment that happens at the beginning of every experiment.

2. In the beginning, the amount of sediment inside the collector is not enough to be measured correctly.

It is worth restating that the data corresponding to the times after t_2 are not related to the initial sediment transport capacity of the channel because the bed slope is increasing due to the aggradation phenomenon, therefore as can be seen from [Figure 3.4](#), the sediment transport capacity ($Q_{s,collector}$) is increasing over time. Also, the reason that $Q_{s,collector}$ is decreasing at the final part of the Figure (time > 165 sec) is the fact that the collector has a limited capacity, so when it gets close to its capacity, the existing turbulence inside the collector causes most of the sediments to get out from the monitored collector to the second collector, resulting in obtaining a lower value for transport capacity ([Figure 3.5](#)).



Figure 3.5. Turbulent flow inside the monitored collector.

The above-mentioned turbulence is also a source of error in the estimation of the initial sediment transport capacity from the beginning of the experiments; this is because the turbulence causes some of the sediments to be floating instead of settling at the bottom of the collector; as a result, it leads to an underestimation of the sediment volume measured at each time and consequently underestimation of the sediment transport capacity. Due to this reason, by comparing this method with the SC method, it is observed that this method reports lower values for the initial sediment transport capacity with respect to the other method.

3.2.4. Monitoring method

This method is based on the mass conservation law. In the aggradation experiments, some of the inflow sediment material that gets into the channel will be deposited inside the channel, and the remaining sediments will be transported through the channel. The discharge of the transported sediments through the channel would be the sediment transport capacity, and this discharge at the initial times of the experiment, when the bed is not changed yet, would be the initial sediment transport capacity of the channel. This method was used in previous campaigns (Zanchi 2018; Zucchi 2018; Heydari 2020), and it is also used in this study with some amendments. The procedure to obtain Q_{s0} with this method is explained below.

First, the volume of the deposited material in the channel, called $V_{measured_bed}$ in this work, is calculated with respect to the reference (position of black tapes) at different times (equation 3.11).

$$V(t)_{measured_bed} = A(t)_{bed} \times B \quad 3.11$$

where, $A(t)_{bed}$ is the area under the bed profile in a specific time, t is the time instant at which the deposited material in the channel is measured, and B is the width of the channel, which is equal to 0.3 m . The above calculations are done at every 5-sec time interval from the beginning of the experiment.

One main problem with the measuring deposited material is that the sediment feeding occurs in the location $x = 25 \text{ cm}$ from the upstream of the channel, while the bed profiles are monitored from $x = 136 \text{ cm}$, so the bed profiles between these two coordinates are not monitored in the data acquisition. Consequently, the sediment volume deposited in this part cannot be calculated. If one does not consider the sediment volume of the missing area in the calculations, it leads to an overestimation of the Q_{s0} ; to solve this problem, two scenarios are considered to simulate the non-monitored upstream bed:

1. Constant upstream scenario (CU) (Zucchi 2018): in this scenario, it is assumed that the profile of the missing area is a constant profile with a constant elevation equal to the bed level in the location of $x = 136 \text{ cm}$ (first monitored point in the upstream), see Figure 3.6.

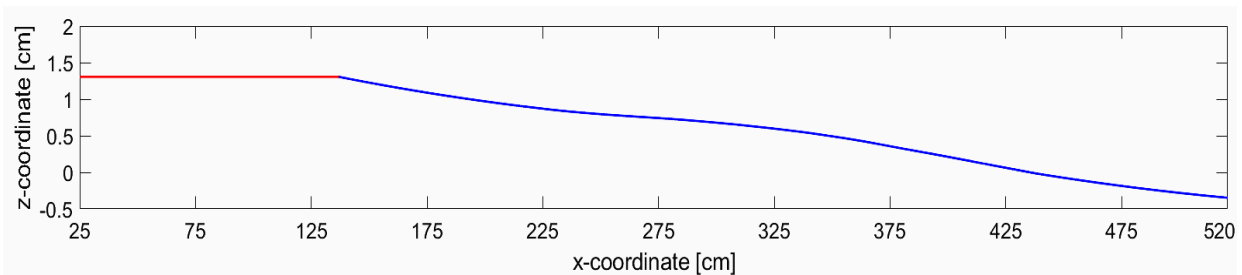


Figure 3.6. The monitored bed profile is shown in blue, and the constantly extended part is shown in red. Experiment: AE6, time: 100 sec . The area under the whole profile is considered as the $A(t = 100 \text{ sec})_{bed}$.

- Inclined upstream scenario (IU): in this scenario, it is assumed that the profile of the missing area is a linear profile with the same slope between the points in $x = 136 \text{ cm}$ and $x = 247 \text{ cm}$ (Figure 3.7). The reason for choosing the slope between these points is the fact that the distance between them is the same as the length of the non-monitored section of the bed.

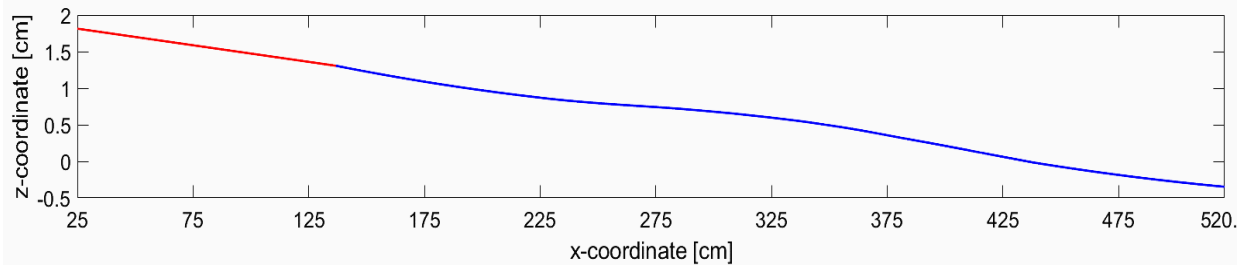


Figure 3.7. The monitored bed profile is shown in blue, and the linearly extended part is shown in red.

Experiment: AE6, time: 100 sec. The area under the whole profile is considered as the $A(t = 100 \text{ sec})_{bed}$.

In Figure 3.8, the comparison between the calculated volume of sediment deposited in the bed using these two scenarios for experiment AE6 is shown.

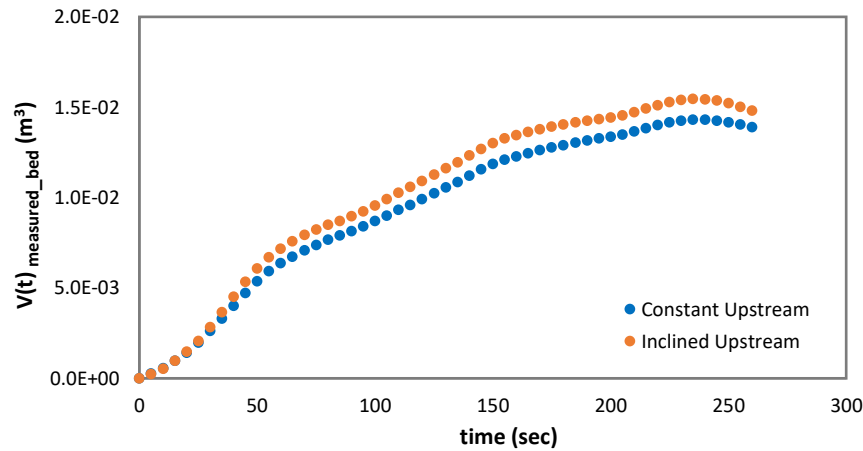


Figure 3.8. The measured volume of the sediment deposited in the bed with respect to the reference using two scenarios for experiment AE6. The calculations of the $V(t)_{measured_bed}$ is done at every 5-sec time interval.

By having the measured volume of the sediment deposited in the bed ($V(t)_{measured_bed}$) at different times, sediment inflow discharge (Q_{sin}) obtained from the PIV process and using transfer function (explained in chapter 2.2.1.1), and porosity (p), one can estimate the Q_{s0} with the following formula:

$$Q_{s0,monitoring} = Q_{sin} - m \times (1 - p) \quad 3.12$$

where:

$$m = \frac{dV_{measured_bed}}{dt} \quad 3.13$$

INITIAL SEDIMENT TRANSPORT CAPACITY AND INCIPIENT MOTION

In this formulation, m represents the slope of a linear function which is fitted to the values of $V(t)_{measured_bed}$ in time. In this regard, one important issue is the time, meaning that in order to estimate the initial sediment transport capacity, only the values of $V(t)_{measured_bed}$ corresponding to the initial times of the experiment should be considered in the calculations; because, at the initial times, the bed in the downstream part of the flume is not affected by the aggradation phenomenon. Based on this concept, two different scenarios to obtain m and evaluate the initial sediment transport capacity of the channel are considered:

1. Fitting a line to the values of $V(t)_{measured_bed}$ in the time interval between $t = 0$ and $t = t_2$ (Zanchi 2018).
2. Fitting a line to the values of $V(t)_{measured_bed}$ in the time interval between $t = t_1$ and $t = t_2$.

where t_1 and t_2 are the bounds of the time interval selected for the collector method ($t_1 < t_2$).

By considering the two scenarios related to the upstream profile and the two related to the time interval, in total, there are four cases:

1. CU1: Constant Upstream with the time interval between $t = 0$ and $t = t_2$
2. CU2: Constant Upstream with the time interval between $t = t_1$ and $t = t_2$
3. IU1: Inclined Upstream with the time interval between $t = 0$ and $t = t_2$
4. IU2: Inclined Upstream with the time interval between $t = t_1$ and $t = t_2$

For all these cases, the initial sediment transport capacity of the channel is calculated using equation 3.12. Here, the graphs of $V(t)_{measured_bed} - time$ and the results of calculation of m and $Q_{s0,monitoring}$ for the experiment AE6 are presented in Figures 3.9 to 3.12, and summarized in Table 3.4.

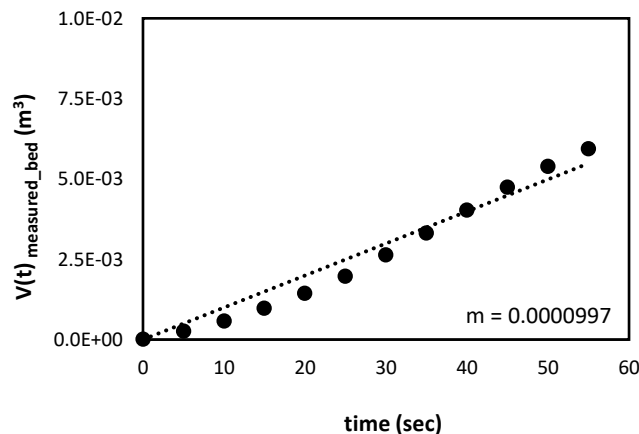


Figure 3.9. The linear line fitted to the measured volume of sediment deposited in the bed, experiment AE6. Case CU1, $t = 0$ and $t_2 = 55$ sec.

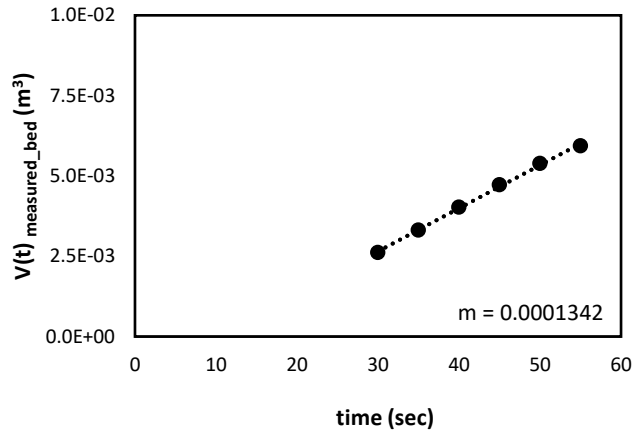


Figure 3.10. The linear line fitted to the measured volume of sediment deposited in the bed, experiment AE6.
Case CU2, $t_1 = 30 \text{ sec}$ and $t_2 = 55 \text{ sec}$.

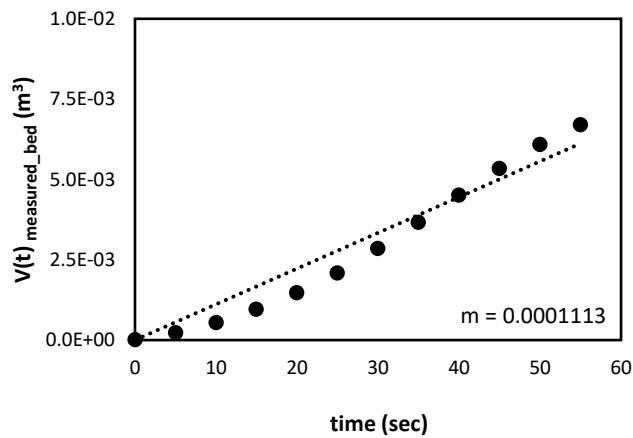


Figure 3.11. The linear line fitted to the measured volume of sediment deposited in the bed, experiment AE6.
Case IU1, $t = 0$ and $t_2 = 55 \text{ sec}$.

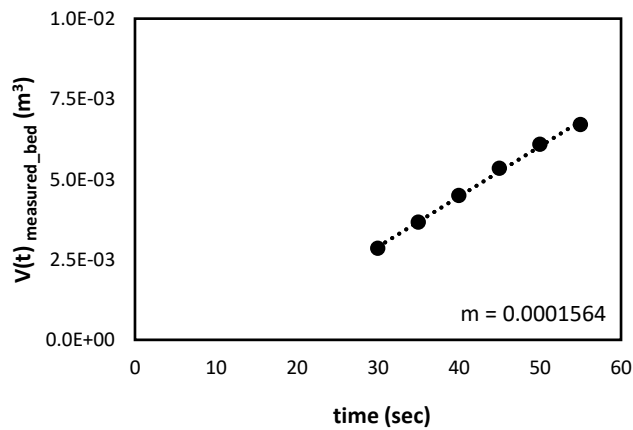


Figure 3.12. The linear line fitted to the measured volume of sediment deposited in the bed, experiment AE6.
Case IU2, $t_1 = 30 \text{ sec}$ and $t_2 = 55 \text{ sec}$.

INITIAL SEDIMENT TRANSPORT CAPACITY AND INCIPIENT MOTION

Table 3.4. The initial sediment transport capacity of the channel obtained with different scenarios in the monitoring method, derived from experiment AE6.

<i>Experiment</i>	$Q_{sin} (m^3/s)$	$Q_{s0,CU1} (m^3/s)$	$Q_{s0,CU2} (m^3/s)$	$Q_{s0,IU1} (m^3/s)$	$Q_{s0,IU2} (m^3/s)$
AE6	2.28E-04	1.73E-04	1.54E-04	1.67E-04	1.42E-04

It is worth mentioning that this method is so sensitive to small errors in bed detection. A sensitivity analysis can help to understand the susceptibility of the method to small errors. For this analysis, the error related to the volume change rate is needed. This error can be calculated with equation 3.14.

$$\varepsilon_{dV/dt} = \frac{L \times B \times \varepsilon_z \times (1 - p)}{dt} \quad 3.14$$

where L is the bed length, B is the channel width, ε_z is the error related to the bed surface detection, and $\varepsilon_{dV/dt}$ is the error related to the volume change rate.

For the studied channel ($L = 4.95 \text{ m}$, $B = 0.3 \text{ m}$, and $p = 0.45$), by considering the ε_z equal to $\pm 10^{-3} \text{ m}$ (less than one-third of the sediment particle size) in 10 seconds, the error related to the volume change rate would be equal to:

$$\varepsilon_{dV/dt} = \frac{4.95 \times 0.3 \times (\pm 10^{-3}) \times (1 - 0.45)}{10} = \pm 8.17 \times 10^{-5} \text{ (m}^3/\text{s)}$$

Such an error for dV/dt , can cause about 51 % relative error with respect to the average values of Q_{s0} reported for the AE6 in Table 3.4, which is a relatively high error.

Another source of error for this method is the error related to the measurement of sediment inflow discharge (Q_{sin}). For example, in the experiment AE6, 10 % error in the measurement of Q_{sin} ($\varepsilon_{Q_{sin}} = 2.28 \times 10^{-5}$) can cause about 14 % relative error with respect to the average values of Q_{s0} reported in Table 3.4.

3.2.5. Comparison of the estimations

The methods to estimate the initial sediment transport capacity of the channel, explained above, were performed for all experiments, AE1 – AE8. The results are presented in Table 3.5 and Figure 3.13.

Estimation of the initial sediment transport capacity

Table 3.5. The initial sediment transport capacity of the channel obtained using different methods.

Experiment	Water discharge (l/s)	$Q_{s0,MPM_Brownlie}$ [$10^{-5} m^3/s$]	$Q_{s0,MPM_Van Rijn}$ [$10^{-5} m^3/s$]	$Q_{s0,SC}$ [$10^{-5} m^3/s$]	$Q_{s0,Collectpr}$ [$10^{-5} m^3/s$]	$Q_{s0,Monitoring_CU1}$ [$10^{-5} m^3/s$]	$Q_{s0,Monitoring_CU2}$ [$10^{-5} m^3/s$]	$Q_{s0,Monitoring_IU1}$ [$10^{-5} m^3/s$]	$Q_{s0,Monitoring_IU2}$ [$10^{-5} m^3/s$]
AE1	5	4.80	5.14	8.46	7.31	8.38	8.80	8.15	8.55
AE2	5	4.80	5.14	8.46	7.20	8.49	8.66	9.58	8.82
AE3	5	4.80	5.14	8.46	8.22	9.15	8.61	9.76	8.69
AE4	5	4.80	5.14	8.46	8.20	8.75	8.96	8.57	9.02
AE5	5	4.80	5.14	8.46	8.30	8.35	13.6	7.02	13.0
AE6	7	6.92	7.31	13.1	11.9	17.3	15.4	16.7	14.2
AE7	7	6.92	7.31	13.1	11.8	13.6	13.6	13.5	13.6
AE8	7	6.92	7.31	13.1	11.7	13.7	15.1	11.9	13.8

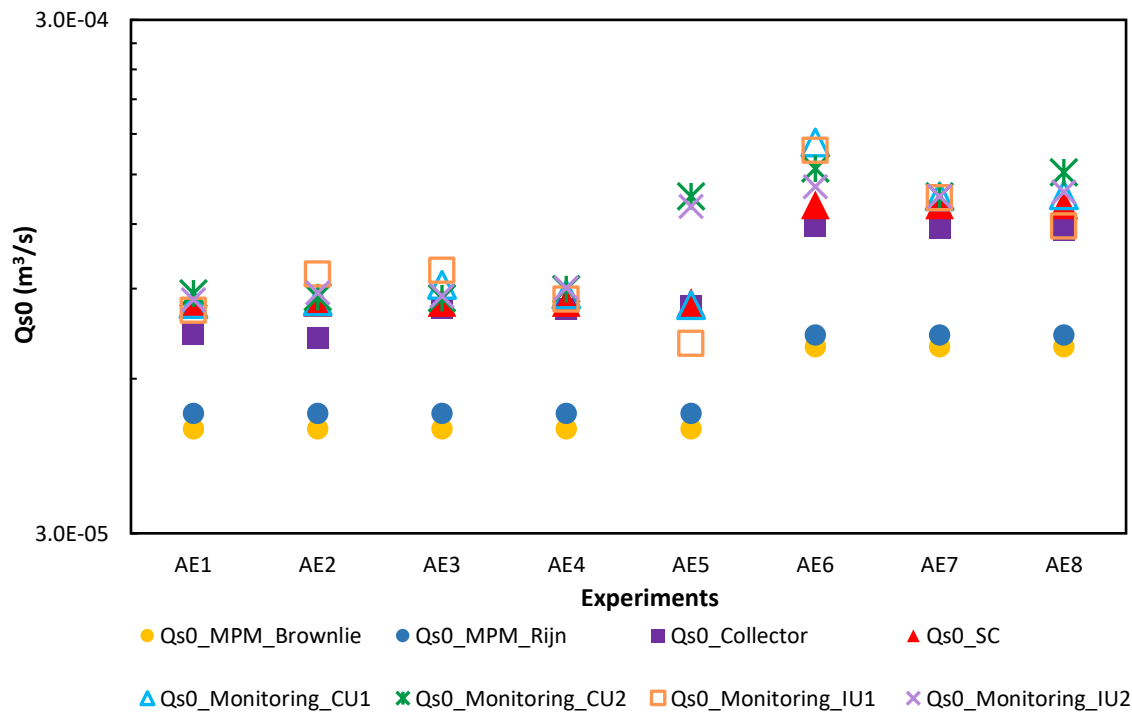


Figure 3.13. Comparison between the initial sediment transport capacities obtained from the different methods.

From the above comparison, some points are identified:

- As it was mentioned since in this thesis work the properties of the channel for all experiments remained constant, the initial sediment transport capacity of the channel should theoretically be a function of water discharge; as a result, It is expected to have only two values for Q_{s0} , one for $Q = 5 \text{ l/s}$ and another for $Q = 7 \text{ l/s}$. This is while by looking at the results, a dispersion among the values is identified. The reason refers to the methods used to estimate Q_{s0} and the related error sources, which may be due to the presence of uncertainty in the methods. For instance, as it was explained in the monitoring method, due to the existing uncertainties, four scenarios are considered to estimate the upstream profile and the time at which the bed is not changed dramatically; clearly, these scenarios may not be coincident with the reality, resulting in errors in the estimation of the initial sediment transport capacity. Also, it was observed that a small error in bed detection could lead to a significant error in the final estimation of Q_{s0} . For the collector method, the other sources of error could be imagined; as it was discussed, one likely error is due to the presence of turbulent flow at the upper part of the collector, which causes sediment not to be settled in the bottom part and cannot be measured in this method. The other disadvantage of this method refers to the fact that it is a user-dependent method which itself can result in errors in the estimation of Q_{s0} .
- The Meyer-Peter and Müller formula, applying both the Brownlie approach and Van Rijn approach, underestimates the sediment transport capacity of the channel and should be calibrated. The calibration process will be explained in [chapter 5.4](#).
- The method of SC experiment is a specific method that is not performed separately for each experiment; rather it is carried out in two specific conditions with $Q = 5 \text{ l/s}$ and $Q = 7 \text{ l/s}$. Therefore, the outcome of this method is two values for two different water discharges. This method can be considered as the most reliable method because the sources of the errors, existing in the other methods, decrease in this method as much as possible. Also, by using this method during the experiment and before performing the data analysis, a range of initial sediment transport capacity can be obtained.
- As it was expected, in all methods, increasing the water discharge has resulted in an increase in the initial sediment transport capacity of the channel.
- Despite the presence of dispersion among the values of Q_{s0} , looking carefully at the results, it is recognized that there is a satisfactory consistency between the SC, monitoring_CU1, and collector methods ([Figure 3.14](#)).

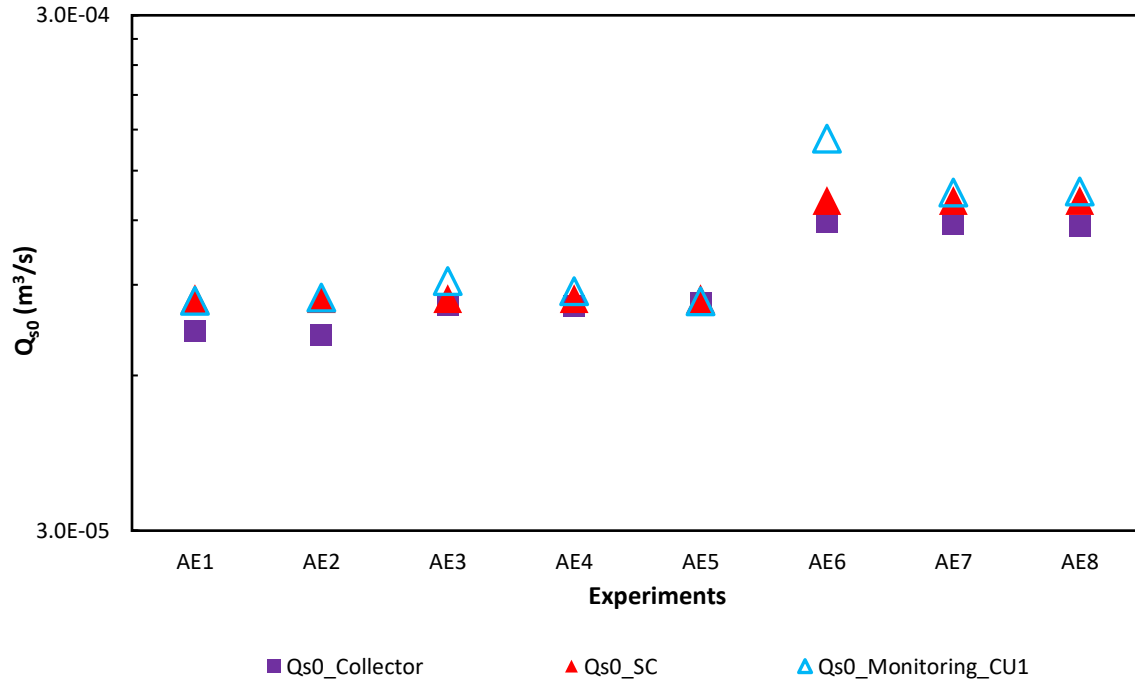


Figure 3.14. Comparison between the results of SC, monitoring_CU1, and collector methods.

It is observed that the only anomaly refers to the estimation of Q_{s0} using the monitoring_CU1 method and derived from experiment AE6. However, the final value for the initial sediment transport capacity of the channel in this study is obtained by averaging the results of these three methods. In Tables 3.6 and 3.7, the final results related to the experiments with $Q = 5 \text{ l/s}$ and $Q = 7 \text{ l/s}$ are shown.

Table 3.6. The final value of Q_{s0} for the experiments with $Q = 5 \text{ l/s}$. The results of the SC, monitoring_CU1, and collector methods are averaged.

Experiments	$Q \text{ (l/s)}$	$Q_{s0} \text{ (m}^3\text{/s)}$
AE1 – AE5	5	8.31E-05

Table 3.7. The final value of Q_{s0} for the experiments with $Q = 7 \text{ l/s}$. The results of the SC, monitoring_CU1, and collector methods are averaged.

Experiments	$Q \text{ (l/s)}$	$Q_{s0} \text{ (m}^3\text{/s)}$
AE6 – AE8	7	1.33E-04

However, depending on the bed definition, the estimated values for Q_{s0} may also change. Comparing the defined bed in this work with the one applied in Heydari’s work (2020), it is observed that the previous definition of the bed results in a higher bed elevation and, consequently, a lower water depth (see chapter 2.2.2.3). This can affect the results of the

different methods which are used to estimate Q_{s0} . For instance, in the monitoring method, using the previous approach for bed detection may result in a different value for deposition rate (m in equation 3.12) and consequently, a different estimation for Q_{s0} . In SC experiments, considering a higher bed, finally would result in a lower Q_{s0} with respect to the one obtained in this work. It is worth mentioning that the bed definition does not affect the collector method.

3.3. Incipient motion, estimation of the critical water discharge

In chapter 1.5, it was discussed that the threshold of the sediment motion could be evaluated by balancing the destabilizing force and the stabilizing resistance. In this regard, the parameter of the critical Shields number, τ_c^* (dimensionless critical shear stress), was introduced as the indicator of the incipient motion of the sediment. In chapter 3.2.1, in order to obtain τ_c^* , two approaches were used, the Brownlie (1981) formula and Van Rijn (1984) formula; using these approaches, the value of τ_c^* was obtained as follows:

$$\text{Brownlie: } \tau_c^* = 0.0486$$

$$\text{Van Rijn: } \tau_c^* = 0.0430$$

The motion of the sediment would happen if $\tau^* \geq \tau_c^*$, where τ^* is the dimensionless shear stress and can be computed using the equation 1.15 (explained in chapter 3.2.1).

Instead of expressing the incipient motion condition in terms of the shear stress, it is more perceptible to represent it in terms of water discharge so that if $Q \geq Q_c$ the motion of the sediment would occur. Q_c is called the critical water discharge, corresponded to the incipient motion condition. By having τ_c^* and knowing the following relationship, the critical water discharge can be estimated as follows:

$$\tau_c^* = \frac{R_{H0c} S_0}{(s - 1)d} \quad 3.15$$

where:

R_{H0c} = the critical hydraulic radius

S_0 = the slope of the channel, which is equal to 0.012 in this work

d = the diameter of the sediment material

$s = \rho_s / \rho_w$, the relative sediment density

Using the above formula, the critical hydraulic radius is calculated, and finally, by applying the Gauckler-Strickler formula (equation 3.16), the value of critical water discharge can be estimated.

$$Q_c = \frac{1}{n} \times A_c \times R_{H0c}^{2/3} \times \sqrt{S_0} \quad 3.16$$

As it was mentioned before, $n = 0.015 \text{ s/m}^{1/3}$ is the Manning's coefficient, obtained experimentally by Unigarro Villota (2017).

In [Table 3.8](#), the results of the estimation of Q_c corresponding to Brownlie and Van Rijn's approaches are presented.

Table 3.8. Estimation of the critical water discharge using Brownlie (1981) and Van Rijn (1984) formulae.

Approach	τ_c^*	R_{H0c} (m)	Q_c (l/s)
Brownlie	0.0486	6.82E-03	0.563
Van Rijn	0.043	6.03E-03	0.456

As it is observed, the estimated Q_c is very small and around 0.5 l/s. With this small value for water discharge, the submergence ratio (water depth/sediment diameter) would also be small so that using the Gauckler-Strickler formula (equation 3.16), it is finally obtained equal to 1.88 for $Q_c = 0.563 \text{ l/s}$ and 1.65 for $Q_c = 0.456 \text{ l/s}$. Knowing that the value of the submergence ratio is small, one may question the validity of the above calculation because this calculation is valid when dealing with a regime that has a relatively high submergence ratio (larger than six). Indeed, the Shields diagram has been provided, assuming that the water depth is at least six times larger than the size of the sediment. In the cases at which the submergence ratio does not satisfy the assumption of the Shields work, different values may be obtained for the critical Shields parameter compared to the values proposed by the Shields diagram. For instance, Armanini and Scotton propose the following equation in order to modify the critical Shields parameter when the submergence ratio is low.

$$\tau_c^* = \tau_{c0}^* \left(1 + 0.67 \sqrt{\frac{d_s}{d}} \right) \quad 3.17$$

where:

τ_c^* = modified critical Shields parameter

τ_{c0}^* = critical Shields parameter obtained from the Shields diagram (equal to 0.0486 and 0.043 in this work using the Brownlie and the Van Rijn approaches, respectively)

$$\frac{d_s}{d} = \frac{1}{\text{submergence ratio}}$$

By substituting the values of the submergence ratio in equation 3.17, the modified critical Shields parameters are computed; having this parameter, the new values for Q_c can be calculated using equations 3.15 and 3.16 ([Table 3.9](#)).

INITIAL SEDIMENT TRANSPORT CAPACITY AND INCIPIENT MOTION

Table 3.9. Estimation of the modified critical Shields parameter using Armanini and Scotton formula.

Approach	τ_{c0}^*	d/d_s	τ_c^*	τ_c^*/τ_{c0}^*	Q_c (l/s)
Brownlie	0.0486	1.88	0.0723	1.49	1.117
Van Rijn	0.0430	1.65	0.0654	1.52	0.938

From the above table, it is understood that having a low submergence ratio has caused the critical Shields parameter to increase about 1.5 times, compared to the ones obtained from the Shields diagram. The reason for this increase in the critical Shields parameter against the submergence ratio is that the velocity of the flow close to the bed becomes less than the value obtained from the logarithmic profile (Armanini and Gregoretti 2005). Indeed, when the submergence ratio is not low, the assumption of the logarithmic velocity distribution across the entire flow depth can be used; consequently, the hydrodynamic forces (drag and lift forces) can be expressed in terms of the square of the velocity (Armanini and Gregoretti 2005). On the other hand, when the submergence ratio is low, the velocity profile would tend to become more uniform in the area close to the bed rather than follow a logarithmic law (Nakagawa, Tsujimoto, and Shimizu 1991). Also, it has been observed that in such a condition, the velocity values close to the bed is less than the one corresponding to the logarithmic profile; as a result, representing the hydrodynamic forces in terms of the square of the velocity cannot be considered as an appropriate assumption in the regime with a small submergence ratio (Armanini and Gregoretti 2005). Since in the Shields work, the velocity profile is assumed to have a logarithmic distribution, using it for a condition with a small submergence ratio, may not guarantee the correct calculation of the critical water discharge.

In order to control the result of the theoretical calculation, performing a preliminary campaign is needed to obtain the value of Q_c experimentally, like the one carried out by Zanchi (2018) and Zucchi (2018) in subcritical condition. They performed an experimental campaign similar to the one used for the aggradation experiments. The only difference was three metallic plates with the dimensions of 8.8×4.3 cm which were located at 1.95 m, 3.25 m, and 4.55 m along the channel (Figure 3.15). These plates were used to measure the sediment transport rate during an incipient motion experiment. The experiments were started with a low water discharge so that no sediment passed through the metallic plates; then, the flow rate is increased progressively until the condition of incipient motion for which a relatively intense transport of the sediment occurred so that a number of sediments passed through the plates. By counting the grains that passed through the plates in a given time period, the sediment transport rate (q_{s0}) for each experiment was measured using the following formula:

$$q_{s0} = \frac{n_{grains} W_{grain}}{T_{PT} W_{plate}} \quad 3.18$$

where:

n_{grains} = the number of grains passing through the plates during the experiment

W_{grain} = the volume of a single grain which in this work is equal to 28.7 mm^3

T_{PT} = the duration of the experiment

W_{plate} = the width of the plate (8.8 cm)



Figure 3.15. Positions of the three metallic plates along the channel (Zucchi 2018).

Having q_{s0} for different experiments with different water discharges, in order to estimate the critical water discharge, Zucchi (2018) and Zanchi (2018) applied a criterion suggested by Radice and Ballio (2008), where the incipient motion condition corresponds to $\Phi = 5.6 \times 10^{-5}$ and computed using the following formula:

$$\Phi = \frac{q_{s0}}{\sqrt{g(s-1)d^3}} \quad 3.19$$

Finally, the critical water discharge for each slope was chosen by aligning the experimental results and data obtained from the previous experimental campaigns in the Politecnico di Milano. In [Table 3.10](#), the final results of Zucchi's work for the estimation of Q_c are shown.

INITIAL SEDIMENT TRANSPORT CAPACITY AND INCIPIENT MOTION

Table 3.10. The critical water discharge obtained experimentally by Zucchi (2018).

	$S_0 = 0.14\%$	$S_0 = 0.2\%$	$S_0 = 0.4\%$
Q_c (l/s)	4.55	4.00	1.66

As it is observed from the results, increasing the slope of the channel has resulted in the decrease in the critical water discharge corresponding to the incipient motion condition.

However, since the aggradation experiments in the presented work are performed in supercritical conditions with a slope of 1.2 %, the establishment of a campaign similar to the previous one needs to adjust the slope of the channel to 1.2 %. If the trend of [Table 3.10](#) and the results of the theoretical calculation is considered, it is expected that for a slope of 1.2 %, a very small value to be obtained for the critical water discharge. Therefore, by considering the results of the preliminary calculations ([Table 3.8](#)), the incipient motion experiments should be started with a water discharge, less than 0.5 l/s. Heydari (2020) tried to perform the incipient motion experiment for a slope of 1.2 %, but it was impossible due to two reasons:

1. The flowmeter used in the laboratory cannot measure water discharges lower than 1 l/s ([Figure 3.16](#)).

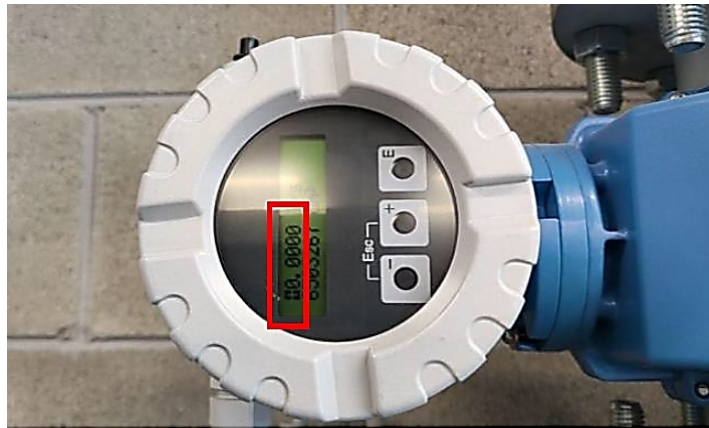


Figure 3.16. Flowmeter is not able to measure very low water discharge and shows zero value (Heydari 2020).

2. Also, it was observed that despite a very low water discharge, an erosion phenomenon at the lateral sides of the channel was happening so that the sediment particles were passing close to the lateral sides rather than through the located plate ([Figure 3.17](#)), resulting in the performance of an incipient motion experiment with such a low water discharge is almost infeasible.

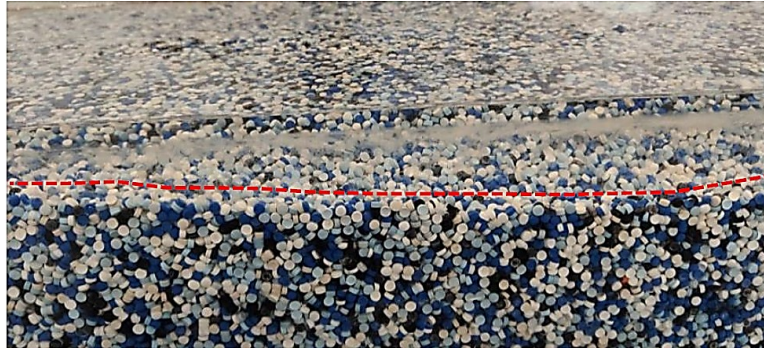


Figure 3.17. The erosion phenomenon at the lateral sides of the channel during a trial incipient motion experiment with a low water discharge (Heydari 2020).

The other trial to estimate the critical water discharge is to use the experimental data coming from the previous campaigns performed in the Politecnico di Milano (Figure 3.18).

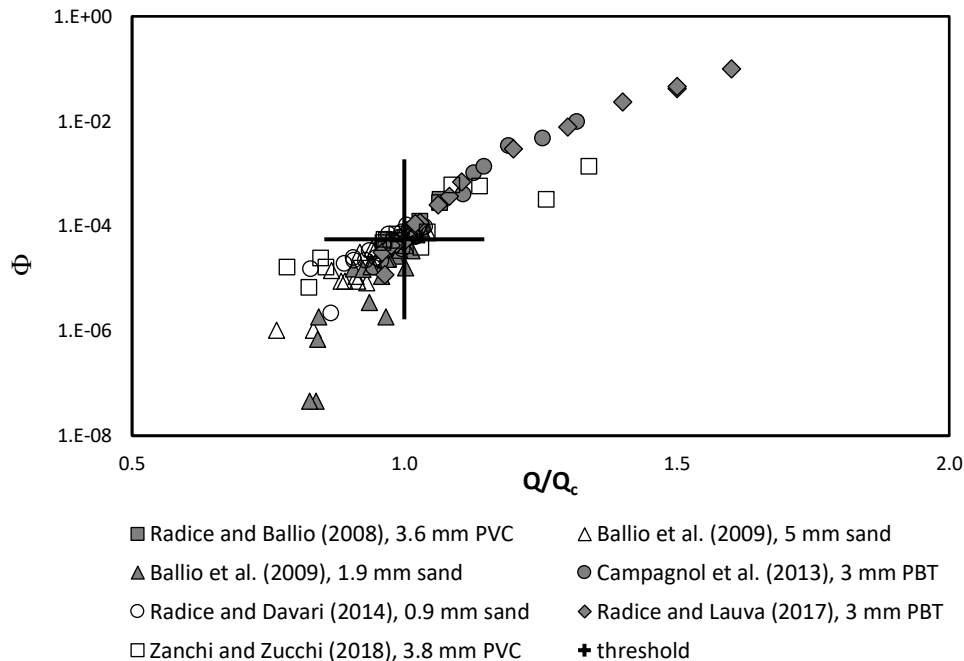


Figure 3.18. Experimental results from previous studies, performed in the Politecnico di Milano.

These results have been obtained by performing different experiments in different situations like different geometry of the channel, different roughness, and different sediment material.

In order to exploit these results to estimate Q_c , the initial sediment transport capacity of the channel obtained in the previous part is used. In this regard, first, the dimensionless sediment transport capacity of the channel per unit width (Φ) should be computed using the following formula:

$$\Phi = \frac{Q_{s0}}{B\sqrt{g(s-1)d_s^3}} \quad 3.20$$

INITIAL SEDIMENT TRANSPORT CAPACITY AND INCIPIENT MOTION

Substituting $B = 0.3 \text{ m}$, $s = 1.443$, $d_s = 0.0038 \text{ m}$ and the values of Q_{s0} , presented in Tables 3.6 and 3.7, in the above equation, the values of Φ are computed (Table 3.11).

Table 3.11. The dimensionless sediment transport capacity of the channel per unit width.

Experiments	$Q \text{ (l/s)}$	$Q_{s0} \text{ (m}^3\text{/s)}$	Φ
AE1 – AE5	5	8.31E-05	5.68E-01
AE6 – AE8	7	1.33E-04	9.09E-01

Now, having the values of Φ , it is enough to put them in the graph obtained from the previous campaigns (Figure 3.18) and align them with the previous data to estimate the value of Q/Q_c . In this regard, one main problem is that the previous experiments have been performed near the threshold condition of the sediment motion ($Q/Q_c = 1$), where the values of Φ is small and close to the criterion suggested by Radice and Ballio (2008) ($\Phi = 5.6 \times 10^{-5}$). This is while the values of Φ , estimated from the initial sediment transport capacity of the channel (Table 3.11), are significantly higher than the threshold criterion so that they are notably far from the previous experimental results. In order to solve this problem and estimate Q_c corresponding to this work, an extrapolation operation from the previous data can be done. In this regard, some trials were carried out. Here, the scenarios corresponding to each trial and the obtained results are presented:

- Trial 1: since the values of Φ , obtained from Q_{s0} are significantly far from the threshold condition, in this trial, the experimental data smaller than the threshold criterion ($Q/Q_c = 1$ and $\Phi = 5.6 \times 10^{-5}$) are neglected, and a polynomial of order two is selected for the extrapolation function. In Figure 3.19 and Table 3.12, the results of this scenario are shown.

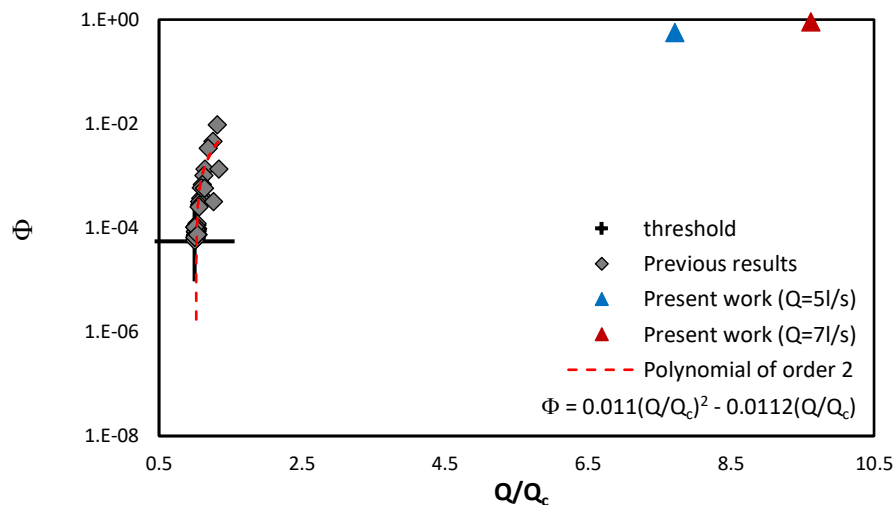


Figure 3.19. Extrapolation from previous data to estimate Q_c , using a polynomial of order 2 (trial 1).

Incipient motion, estimation of the critical water discharge

Table 3.12. The critical water discharge is obtained from an extrapolation operation (trial 1).

<i>Experiments</i>	Φ	Q/Q_c	Q (l/s)	Q_c (l/s)
AE1 – AE5	5.68E-01	7.712	5	0.648
AE6 – AE8	9.09E-01	9.613	7	0.728

- Trial 2: this trial is similar to the previous one. The only difference is the order of the polynomial so that a polynomial of order three is used for extrapolation. In [Figure 3.20](#) and [Table 3.13](#), the results of this scenario are shown.

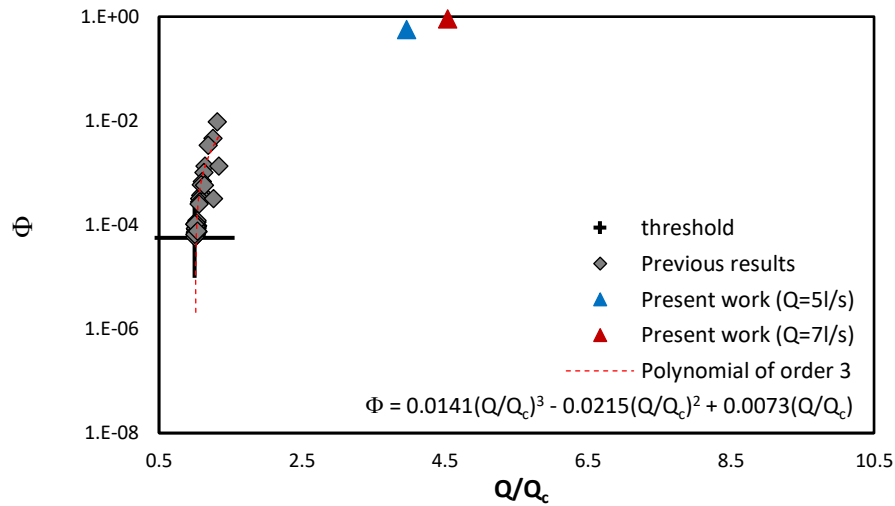


Figure 3.20. Extrapolation from previous data to estimate Q_c , using a polynomial of order 3 (trial 2).

Table 3.13. The critical water discharge is obtained from an extrapolation operation (trial 3).

<i>Experiments</i>	Φ	Q/Q_c	Q (l/s)	Q_c (l/s)
AE1 – AE5	5.68E-01	3.961	5	1.262
AE6 – AE8	9.09E-01	4.539	7	1.542

Here, all values estimated for the critical water discharge with different methods are shown in [Table 3.14](#).

Table 3.14. All values related to the critical water discharge, estimated by different methods.

<i>Experiments</i>	Q (l/s)	Q_c (l/s)				<i>trial 1</i>	<i>trial 2</i>
		<i>Theory (Brownlie)</i>	<i>Theory (Van Rijn)</i>	<i>Modified (Armanini-Brownlie)</i>	<i>Modified (Armanini-Van Rijn)</i>		
AE1 – AE5	5	0.563	0.456	1.117	0.938	0.648	1.262
AE6 – AE8	7					0.728	1.542

INITIAL SEDIMENT TRANSPORT CAPACITY AND INCIPIENT MOTION

Looking at the table, it is realized that applying different approaches does not result in a unique value for the critical water discharge, and it varies between 0.456 l/s and 1.542 l/s. Obviously, this range for Q_c is considered as a significant uncertainty; in this work, the average of the above values would be considered as the critical water discharge, which is equal to 0.907 l/s. It is worth restating that this value is an uncertain value for the critical water discharge in this work. However, the discussion presented in this part ([chapter 3.3](#)) provides some views of the issue and can be helpful for future works.

CHAPTER 4

RESULTS OF AGGRADATION EXPERIMENTS

4.1. Aggradation experiments, parameters

For the purposes of this thesis, eight aggradation experiments are performed with the name of AE1 to AE8. The characteristics of the channel (slope, length, and width) and the sediment material characteristics remain constant in all the experiments. The only parameters changed for each experiment are water discharge (Q) and sediment inflow discharge (Q_{sin}). A water discharge is set, then for each water discharge, different experiments are performed with different sediment inflow discharges. The water discharges equal to 5 l/s and 7 l/s are chosen for the experiments AE1 to AE5, and the experiments AE6 to AE8, respectively. In order to have aggradation, the sediment inflow discharges are chosen in a way that the loading ratio be more than one ($Lr > 1$). The value of Q_{sin} depends on the chosen vibration level, and it is obtained from the PIV process and transfer function (explained in [chapter 2.2.1](#)). The Initial sediment transport capacity of the channel (Q_{s0}) for different water discharges were estimated in [chapter 3.2](#).

It should be mentioned that the first three experiments (AE1 to AE3) were performed in the previous thesis (Heydari 2020). As it was concluded by Heydari, some of the previous methods for data extraction from the movies are not reliable for supercritical experiments, so these three experiments are reanalyzed with the updated methods in this study. This is why these three experiments are also included in the current thesis. The parameters and details of the aggradation experiments are listed in [Table 4.1](#).

Table 4.1. The parameters of experiments AE1 -AE8.

<i>Experiment</i>	<i>T</i> (s)	<i>S₀</i> (%)	<i>Q</i> (l/s)	<i>Q_c</i> (l/s)	<i>Q/Q_c</i> (-)	<i>h₀</i> (cm)	<i>Fr</i> (-)	<i>Q_{sin}</i> (m ³ /s)	<i>Q_{s0}</i> (m ³ /s)	<i>Lr</i> (-)
AE1	490	1.2	5	0.907	5.51	2.78	1.14	1.42E-04	8.31E-05	1.7
AE2	560	1.2	5	0.907	5.51	2.78	1.14	1.01E-04	8.31E-05	1.21
AE3	380	1.2	5	0.907	5.51	2.78	1.14	8.67E-05	8.31E-05	1.04
AE4	350	1.2	5	0.907	5.51	2.78	1.14	8.70E-05	8.31E-05	1.05
AE5	340	1.2	5	0.907	5.51	2.78	1.14	2.43E-04	8.31E-05	2.92
AE6	259	1.2	7	0.907	7.71	3.46	1.16	2.30E-04	1.33E-04	1.73
AE7	364	1.2	7	0.907	7.71	3.46	1.16	1.43E-04	1.33E-04	1.075
AE8	233	1.2	7	0.907	7.71	3.46	1.16	2.55E-04	1.33E-04	1.92

Where T is the duration of the experiment, S_0 is the channel's slope, Q is the water discharge, Q_c is the critical water discharge, h_0 is the normal depth, Fr is the Froude number, Q_{sin} is the sediment inflow discharge, Q_{s0} is the initial sediment transport capacity of the channel, and Lr is the loading ratio (Q_{sin}/Q_{s0}).

As it was mentioned in [chapter 3.3](#), the value of critical water discharge (Q_c) is estimated by averaging the values obtained from the theoretical calculations and the ones obtained from applying the extrapolation operations on the previous experimental data. The reported value for the Q_c is not reliable due to the high uncertainties.

It should be mentioned that in order to calculate the Froude number, it is assumed that the flow in the channel is uniform and the corresponding water depth, h_0 , is computed applying the Gauckler-Strickler formula:

$$Q = \frac{1}{n} \times A_0 \times R_{H0}^{2/3} \times \sqrt{S_0} \quad 4.1$$

where:

$A_0 = B \times h_0$ is the flow area

$n = 0.015 \text{ s/m}^{1/3}$ is the Manning's coefficient, obtained experimentally by Unigarro Villota (2017)

R_{H0} = the hydraulic radius

S_0 = the slope of the channel, which is equal to 0.012 in this work

Having h_0 , the Froude number is calculated as follows:

$$Fr = \frac{Q}{B \times h_0 \times \sqrt{g \times h_0}} \quad 4.2$$

4.2. Experimental results

4.2.1. Spatial and temporal evolution of the bed and water

The spatial evolution profiles show the bed and water surface elevation along the channel in a specific time instant, while the temporal evolution profiles indicate the position of the bed and water surface during the experiment in a specific section of the channel. The profiles are obtained with the data acquisition methods (explained in [chapter 2.2.2.2](#) and [2.2.3.2](#)) with a temporal resolution of 1 second. Here, as an example, the bed and water profiles of the experiments AE5 with $Q = 5 \text{ l/s}$ and AE7 with $Q = 7 \text{ l/s}$ are presented ([Figures 4.1 to 4.4](#)).

RESULTS OF AGGRADATION EXPERIMENTS

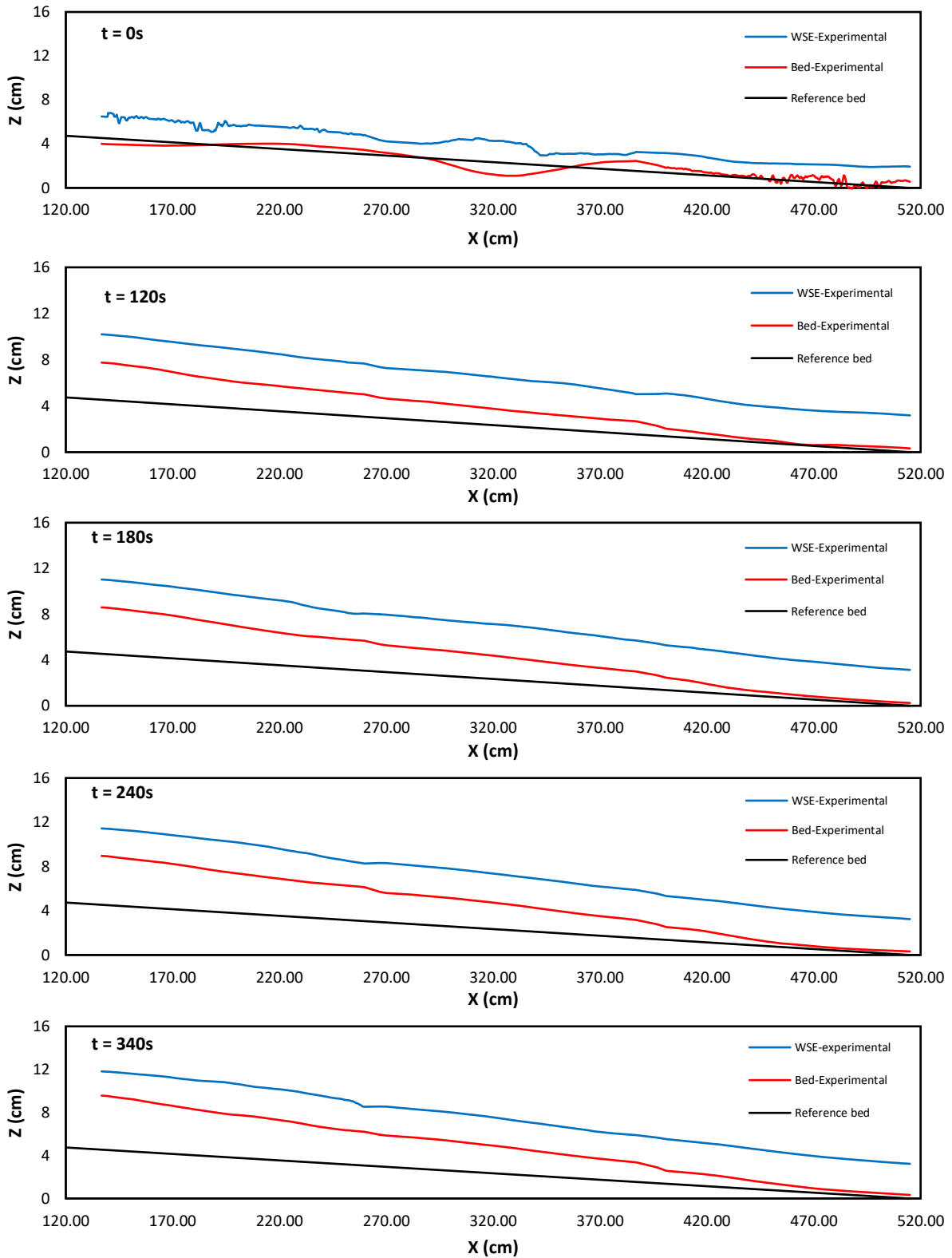


Figure 4.1. Spatial evolution of bed and water at the selected times for experiment AE5 with overloading ratio equal to 2.92 and water discharge equal to 5 l/s.

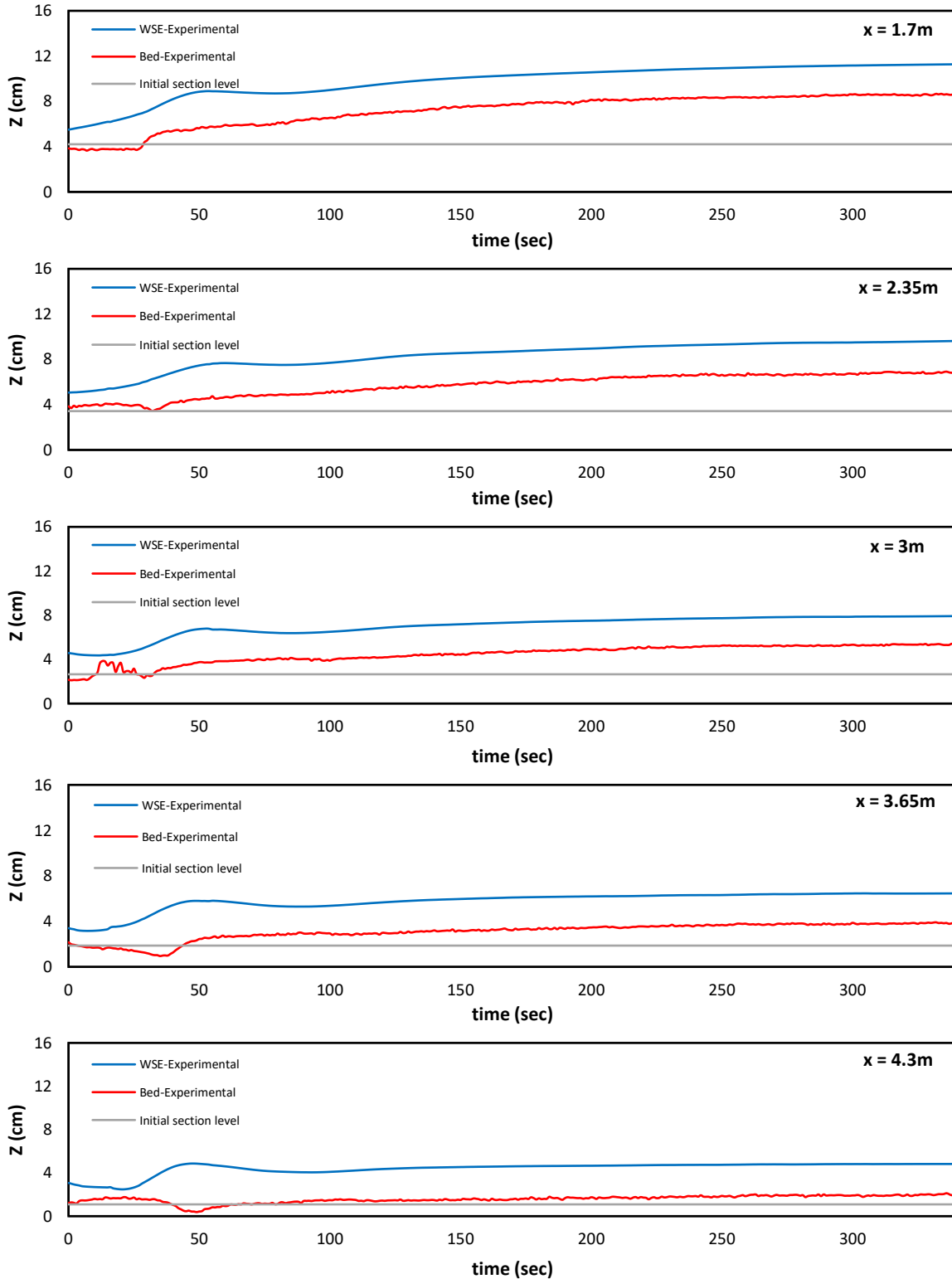


Figure 4.2. Temporal evolution of bed and water at the selected sections for experiment AE5 with overloading ratio equal to 2.92 and water discharge equal to 5 l/s.

RESULTS OF AGGRADATION EXPERIMENTS

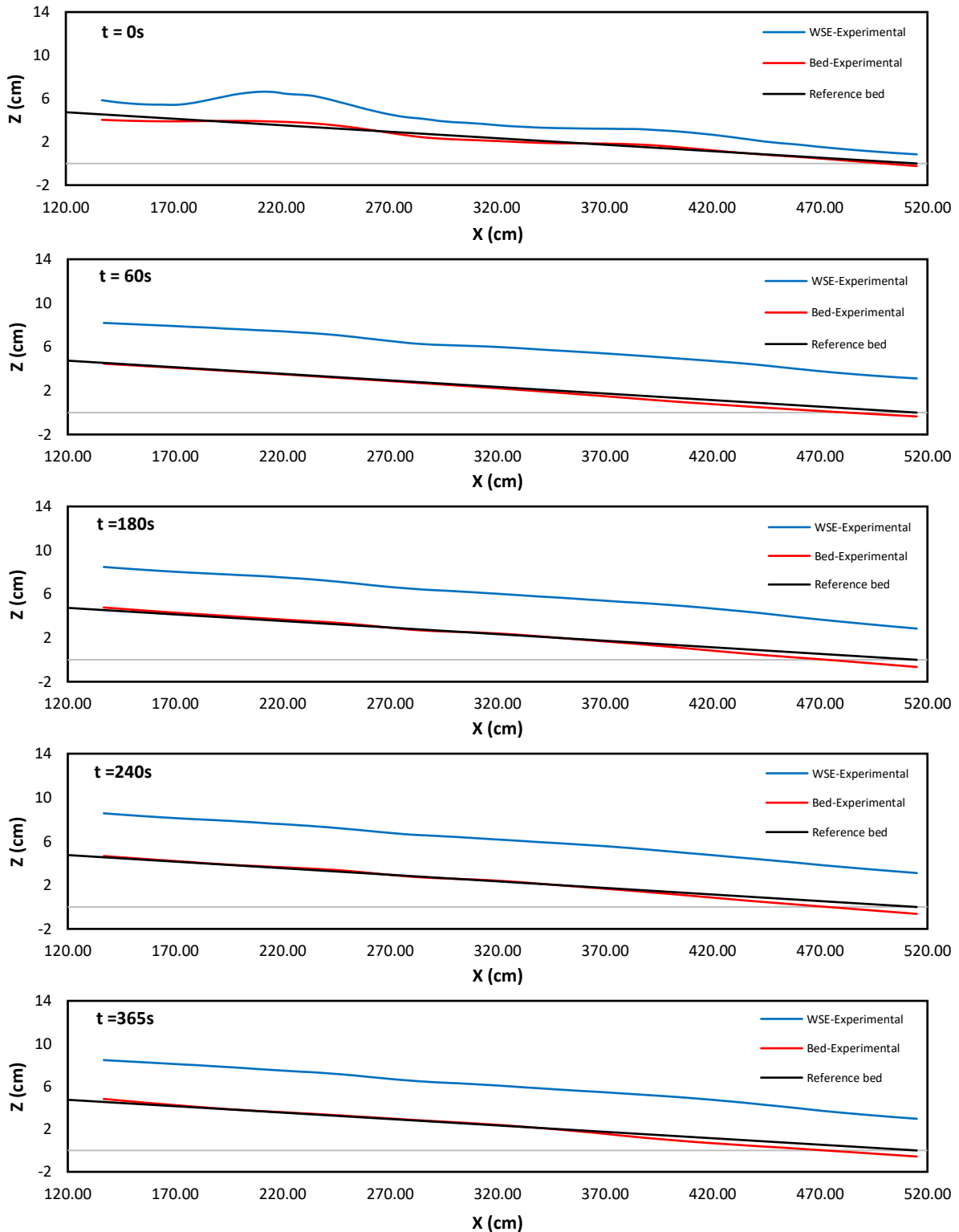


Figure 4.3. Spatial evolution of bed and water at the selected times for experiment AE7 with overloading ratio equal to 1.075 and water discharge equal to 7 l/s.

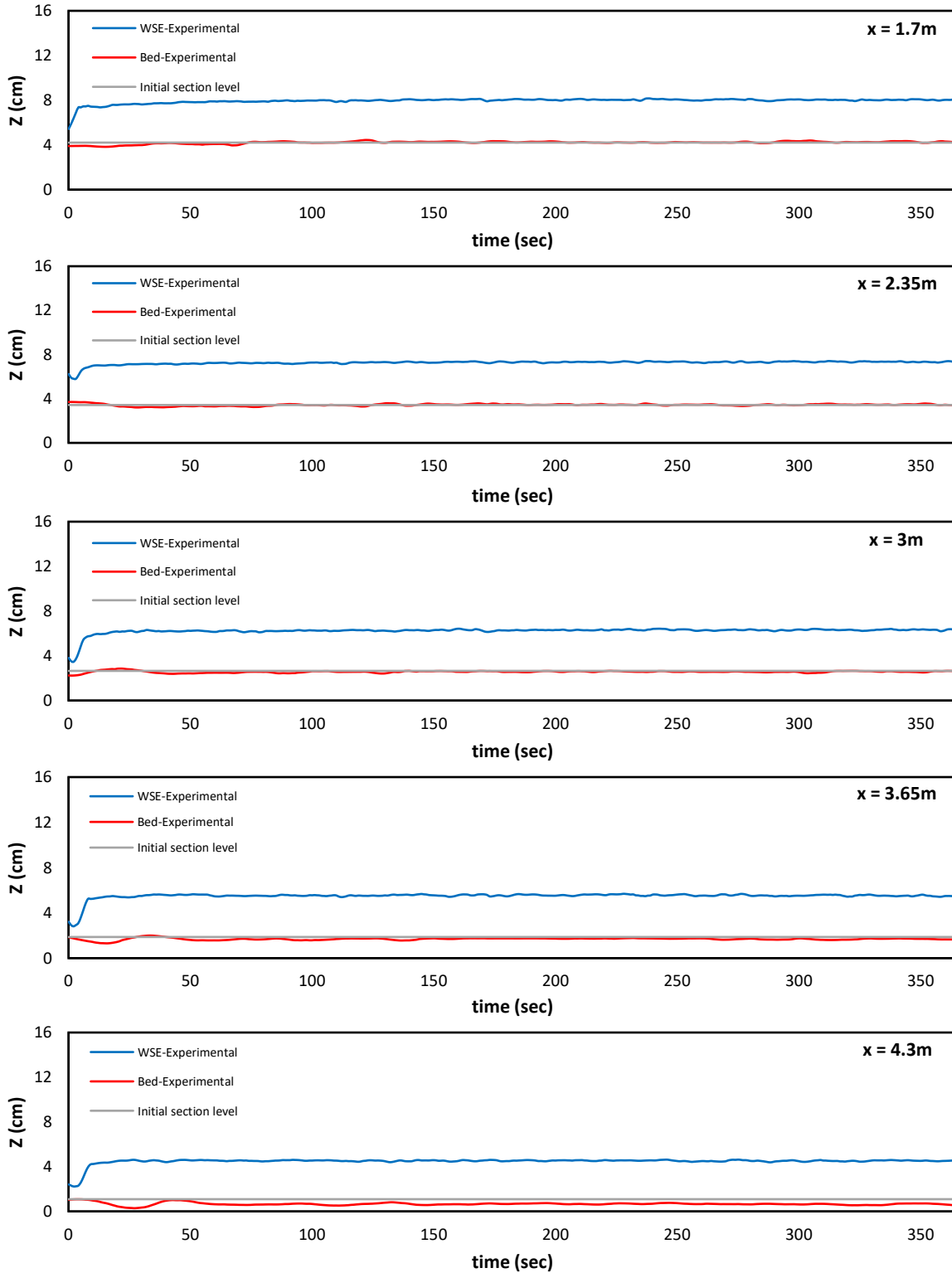


Figure 4.4. Temporal evolution of bed and water at the selected sections for experiment AE7 with overloading ratio equal to 1.075 and water discharge equal to 7 l/s.

RESULTS OF AGGRADATION EXPERIMENTS

As it can be seen from Figures 4.1 and 4.2, the ones corresponding to experiment AE5, the bed elevation is increasing progressively with time. The increase in the bed elevation is more in the upstream than the downstream, leading to an increase in the bed's slope. The rise in the bed's slope causes the sediment transport capacity to increase until it becomes close to the sediment feeding rate; in other words, the channel reaches the equilibrium condition. For this reason, the bed slope rises faster at the beginning of the experiments compared to the final times of the experiments. More precisely, in the aggradation process, since the bed tends to the equilibrium condition, its elevation increases at the beginning, and then it slows down and tends to reach a specific value. This trend cannot be observed in Figures 4.3 and 4.4 related to experiment AE7 so that during the experiment, the bed and water profiles remain almost unchanged and constant. The reason refers to the fact that the loading ratio for this experiment is close to one ($Lr = 1.075$), so in this experiment, the bed is in the equilibrium condition almost from the beginning. It should be mentioned that in the experiments with the same water discharge, a higher loading ratio results in higher aggradation, which is consistent with the theory.

By looking carefully at the spatial and temporal evolution profiles of the experiments, it is realized that a degradation phenomenon happens in the downstream part of the channel close to the outlet. In Figure 4.5, this phenomenon is shown for all of the experiments at their final times.

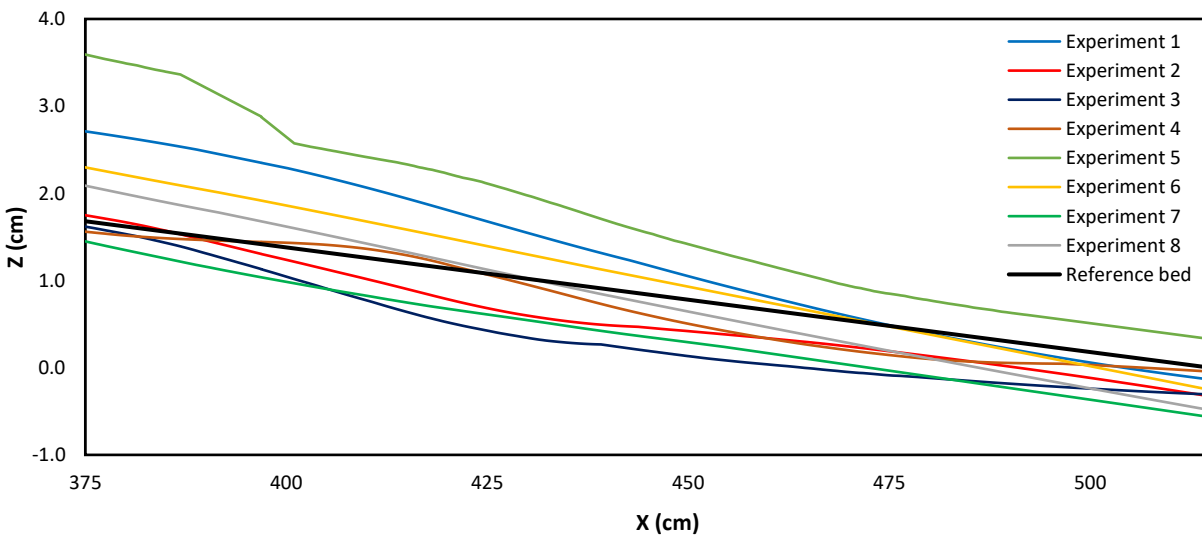


Figure 4.5. Degradation phenomenon at the downstream of the channel.
Experiments AE1-8, time: end of the experiments.

From the Figure, it is observed that this degradation behavior is occurred in all of the experiments except for experiment AE5. The reason for this behavior is the fact that a transverse wooden sill is located at the outlet of the channel, imposing the bed elevation to remain constant. This transverse sill blocks the movement of water in the main direction in the porous medium of the bed close to the outlet, so the water tends to move upwards; consequently, the lifting force increases; as a result, the sediment transport capacity in the area where it is affected by the

transverse sill increases. The increase in sediment transport capacity causes erosion in this area. In [Figure 4.6](#), a sketch of the explained phenomenon is presented.

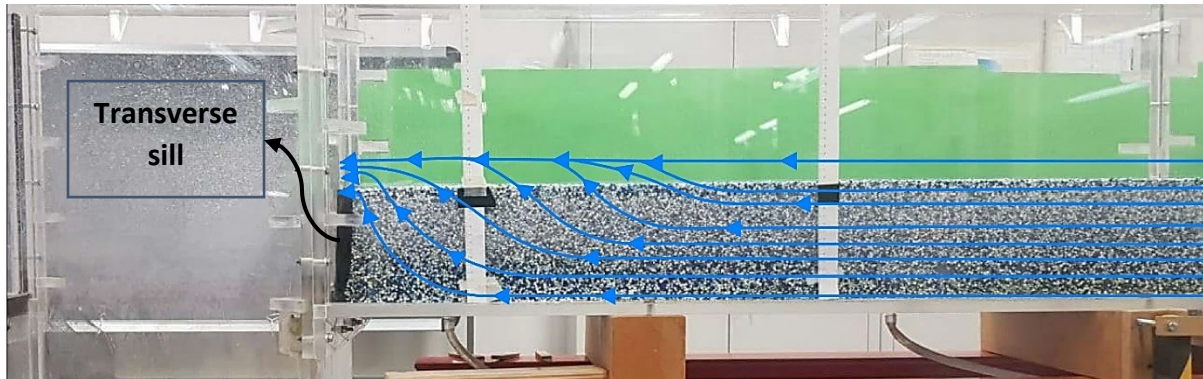


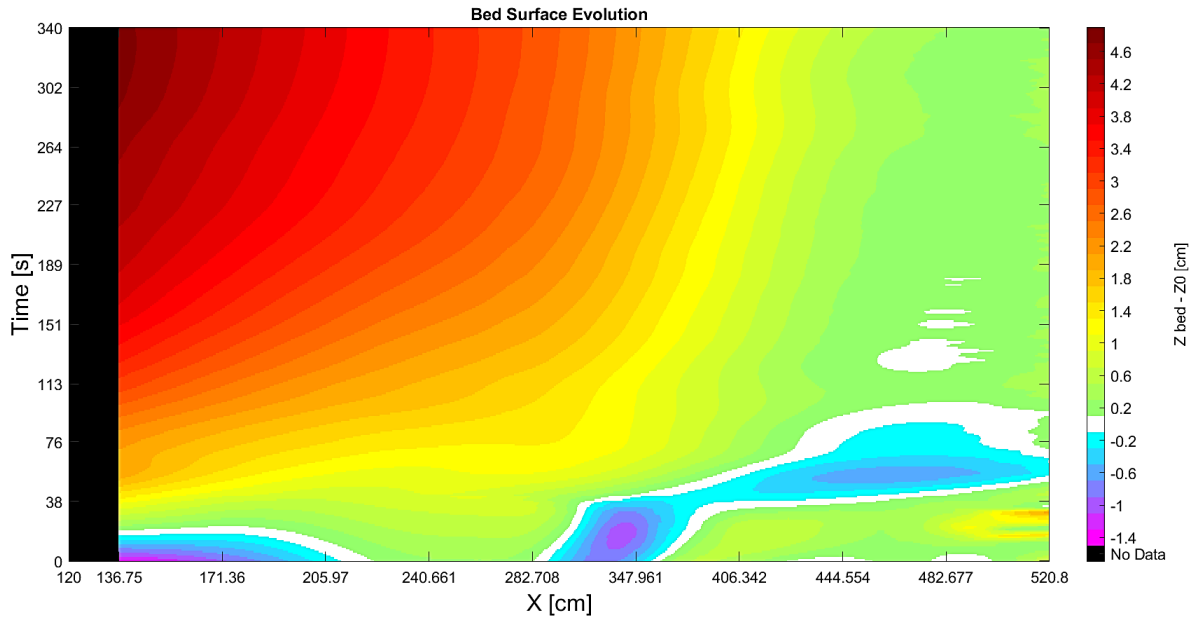
Figure 4.6. The sketch of the degradation procedure in the downstream part of the channel.

As mentioned, this effect cannot be observed in experiment AE5. This is because, in this experiment, the overloading ratio is very high ($Lr = 2.92$) compared to the other experiments; as a result, this high ratio overcomes the effect of the transverse sill.

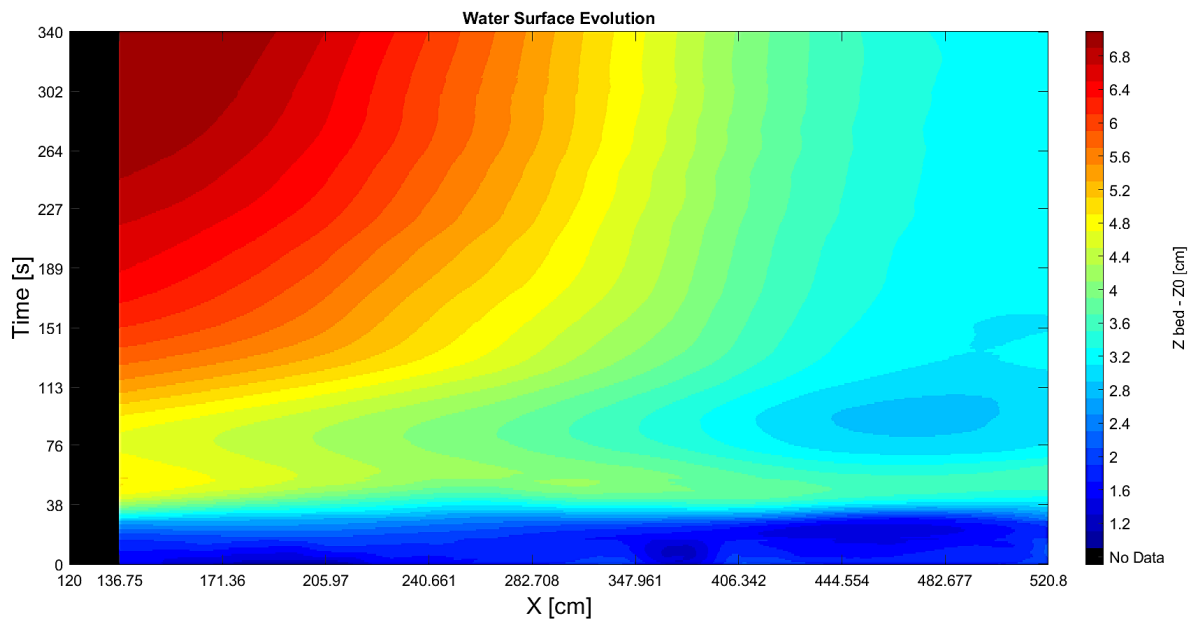
In order to see the whole process in one frame, it is needed to put the data together; to do so, a matrix is created so that each array of it shows the elevation of the profile in a specific section and time. The rows of the matrix show the time, and the columns represent the location of the sections. To perceive the results in a better way, the matrices of the profiles are shown with color gradient graphs. These graphs represent the evolution of the profiles in all sections during the experiments in one frame. To be more precise, the horizontal axis of these graphs shows the x -coordinate of the profiles, which increases from upstream to downstream of the channel, and the vertical axis shows the time. These graphs are built up in a way that each pixel's intensity represents the elevation of the profile in a specific section and a specific time, and these values are shown with different colors. They are also handy for finding the celerity of the aggradation wave (will be explained in detail in [chapter 4.2.3](#)).

Here, the color gradient graphs for the bed and water profiles, related to the experiment AE5 and AE7, are shown in [Figures 4.7](#) and [4.8](#).

RESULTS OF AGGRADATION EXPERIMENTS

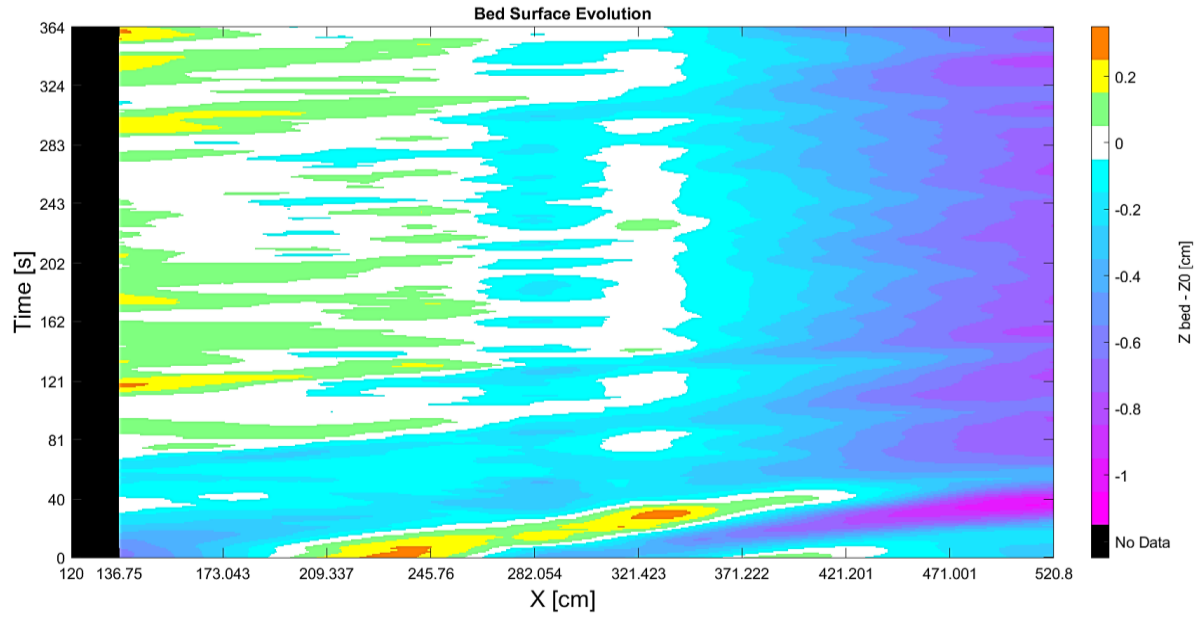


(a)

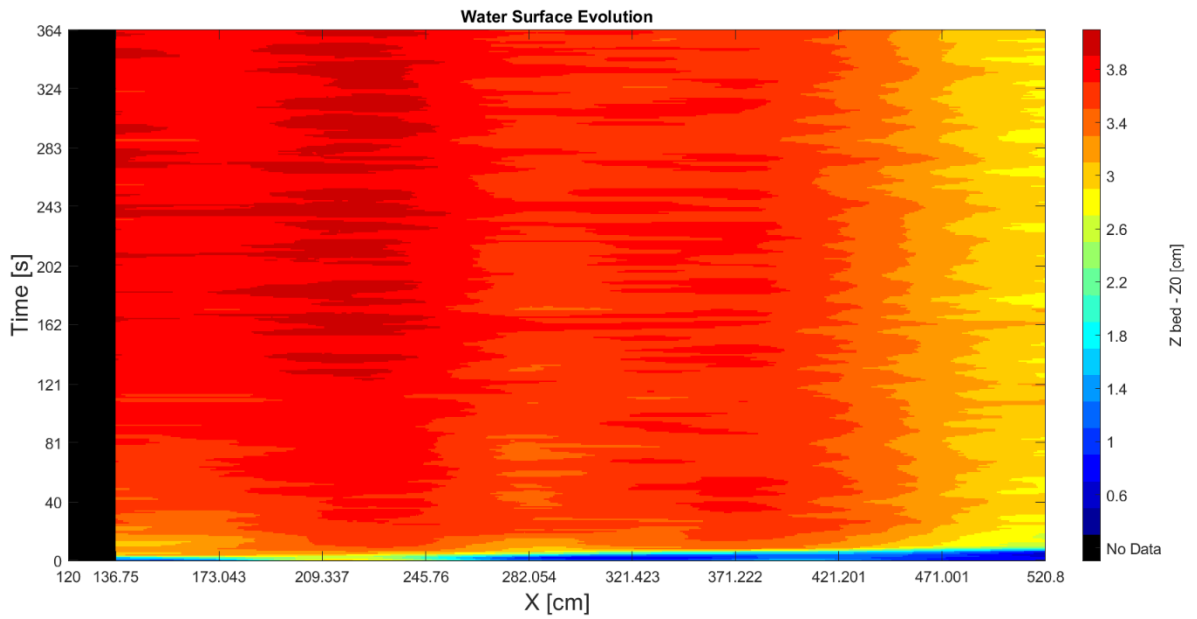


(b)

Figure 4.7. Color gradient graphs for experiment AE5. (a) bed evolution in space and time
(b) water evolution in space and time.



(a)



(b)

Figure 4.8. Color gradient graphs for experiment AE7. (a) bed evolution in space and time (b) water evolution in space and time.

RESULTS OF AGGRADATION EXPERIMENTS

Now, from these kinds of graphs, the evolution of bed and water in time and space is more perceptible so that the aggradation pattern during the time can be clearly seen in the upstream part of the channel in experiment AE5 (Figure 4.7). When the slope of the borders between different colors becomes vertical, it means that the bed elevation does not change anymore; as a result, an equilibrium condition has been reached. This behavior can be observed in the graphs since the slope of the borders is increasing over time and tends to be vertical at the final times. Also, from Figure 4.8, corresponding to the experiment AE7, an equilibrium condition is easily recognizable since the changes in the bed elevation values in the upstream part of the channel are very low (almost in the range of one sediment particle size). It should be mentioned that the changes in the downstream part are not low due to the effect of the transverse sill, explained before.

By looking carefully at the graphs, strange behavior can be recognized at the early times of the experiments. The bed and water surface elevations are not reliable (especially the water surface) at these times due to the errors in the bed and water surface detection. These errors happen at the early times since the movements of water and sediment particles are not stable yet; as a result, the motion is not in a way to be detectable. It should be mentioned that one can increase the threshold value mentioned in chapter 2.2.2.2 to increase the sensitivity of the algorithm to the motion, but it would not help since it also causes the noises to increase.

4.2.2. Spatial and temporal evolution of the Froude number

The color gradient graphs can be produced for the evolution of the Froude number by using the Froude number matrix. This matrix can be derived by applying the following formula on the data related to each section of the channel in each time instant:

$$Fr = \frac{U}{\sqrt{g \times h}} \quad 4.3$$

where Fr is the Froude number, U is the flow velocity, h is the water depth, and g is the gravitational acceleration.

To derive the water depth, one can subtract the bed elevation from the water elevation. The velocity can be derived from the following formula:

$$U = \frac{Q}{B \times h} \quad 4.4$$

where Q is the water discharge, and B is the channel width.

The color gradient graphs for the Froude number related to experiments AE1, AE5, and AE8 are shown in Figures 4.9 to 4.11.

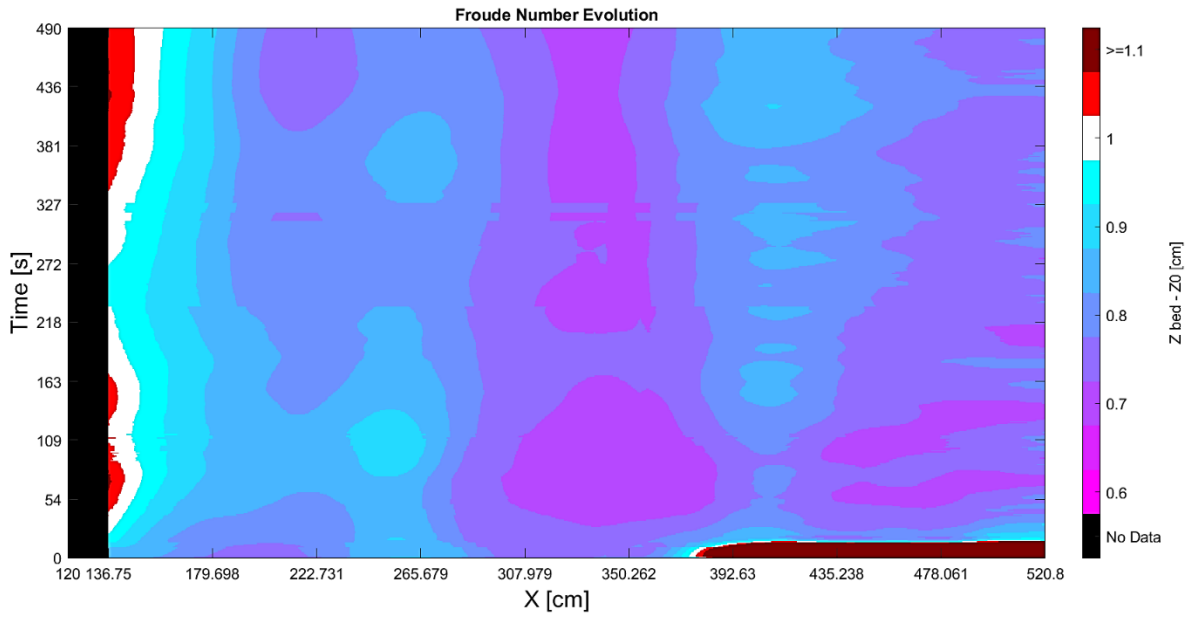


Figure 4.9. Color gradient graph for Froude number, experiment AE1.

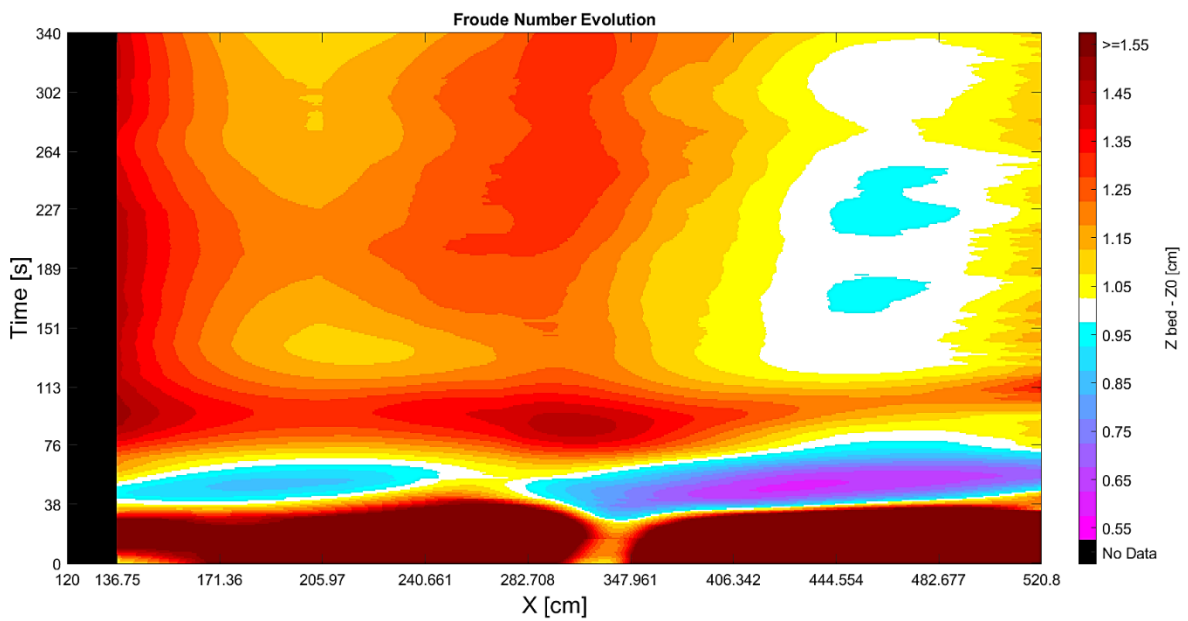


Figure 4.10. Color gradient graph for Froude number, experiment AE5.

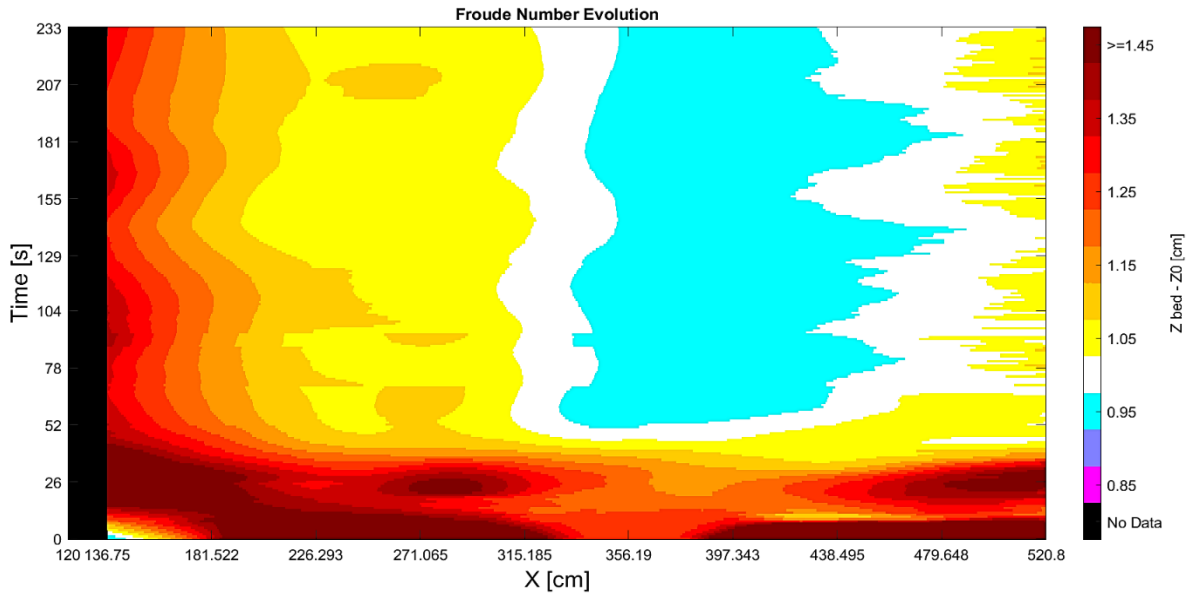


Figure 4.11. Color gradient graph for Froude number, experiment AE8.

As it can be seen in [Figure 4.9](#), the flow regime in experiment AE1 is subcritical; all the experiments with water discharge equal to 5 l/s are in a subcritical regime except experiment AE5 ([Figure 4.10](#)). In contrast, the flow regimes of the experiments AE1 to AE3 were reported supercritical in the previous study (Heydari 2020); this contradiction is due to the fact that a different method for bed detection is used in the current study compared to the previous one. In this study, the bed surface is considered the border between the bedload layer and the stationary bed, while in the previous one, the bed is considered the surface of the bedload layer. As a result, the bed surface level in the previous study is higher than the current one, which leads to obtaining a lower water depth. With the same water discharge and the same channel width, lower water depth means higher velocity, consequently higher Froude number. Also, this contradiction can be observed between the experimental results related to the experiments with $Q = 5 \text{ l/s}$ and the theoretical values reported in [Table 4.1](#). The reason refers to the fact that in the calculation of the Froude number using theory, in order to obtain h_0 (water depth in uniform condition) the Manning's coefficient is selected equal to $0.015 \text{ s/m}^{1/3}$, the one obtained by Unigarro Villota experimentally. As it will be explained in [chapter 5](#), Unigarro Villota derived this coefficient with the clear-water flow over the fixed bed; this is while in this study, there is an upstream sediment feed on a mobile bed; as a result, the presence of the sediment transport may result in an increase in the Manning's coefficient (see [chapter 5.5](#)).

Also, from [Figure 4.10](#), it is recognized that the Froude number at the beginning is very high compared to other times. As mentioned at the end of [chapter 4.2.1](#), there are errors in the detection of water surface elevation at the beginning of all experiments, but these errors last longer (about 35 seconds) in experiment AE5. The reason for such a prolonged duration of initial errors in this experiment is that a dam is created in the upstream part of the channel due to starting the sediment feeding before the water discharge reaches 5 l/s . When the water

discharge reach 5 l/s, the dam's effect is removed, and the situation become normal. These errors cause the water depth to be underestimated, resulting in higher Froude numbers. After the first 35 seconds, the results are reliable since the water flow becomes stable. It can be seen that the flow regime is subcritical after the first 35 seconds like the experiments AE1 to AE4, but it changes to supercritical after the time equal to approximately 75 seconds; this is because the overloading ratio in this experiment is very high, so the bed slope increases significantly and rapidly; as a result, the flow regime becomes supercritical.

The experiments with water discharge equal to 7 l/s are in supercritical condition because of the higher water discharge (Figure 4.11).

4.2.3. Analysis of the aggradation wave celerity

In the aggradation process, the deposition happens by moving a sediment front along the channel. The sediment front velocity is known as celerity. In the flows with lower velocities (mostly in subcritical flows), the sediment front is of a translating type; on the other hand, in the flows with higher velocities (mostly in supercritical flows), the sediment front is dispersive. The schematic representation of these two types of sediment front is shown in Figure 4.12.

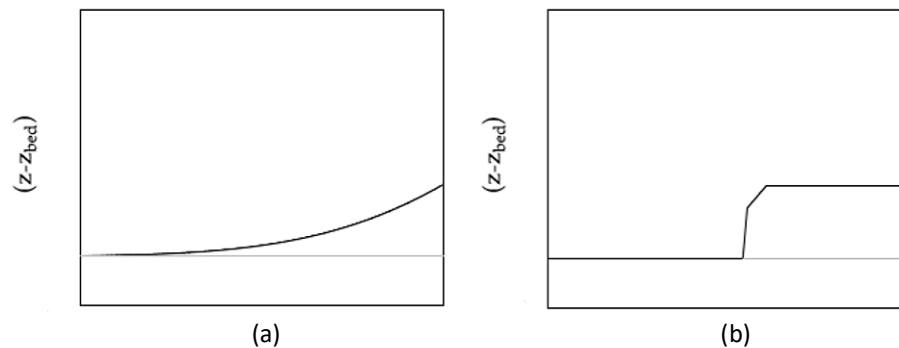


Figure 4.12. Schematic representation of the two types of sediment front: a) dispersive type, b) translating type (Zanchi 2018).

When dealing with a translating sediment front, one can trace the front in different time instants to find its celerity. In the subcritical campaign (Unigarro Villota 2017; Zanchi 2018; Zucchi 2018), the method of tracing the sediment front was used to find the celerity. As mentioned before, the aggradation process in supercritical flows is highly dispersive. In the previous study (Heydari 2020), it was tried to use the method of tracing the sediment front to find the celerity in supercritical flows, but since the aggradation was dispersive, it was not possible to detect a sediment front. For this reason, Heydari suggested that a new method should be developed to find the celerity when dealing with dispersive aggradation. In the current study, a new method is implemented for the analysis of celerity. As previously mentioned in chapter 4.2.1, the color gradient graphs and their related matrices are handy for finding the celerity of aggradation wave since the slope of the borders between the colors can be interpreted as the inverse of the celerity because this slope shows dt/dx , while celerity is dx/dt (Figure 4.13).

RESULTS OF AGGRADATION EXPERIMENTS

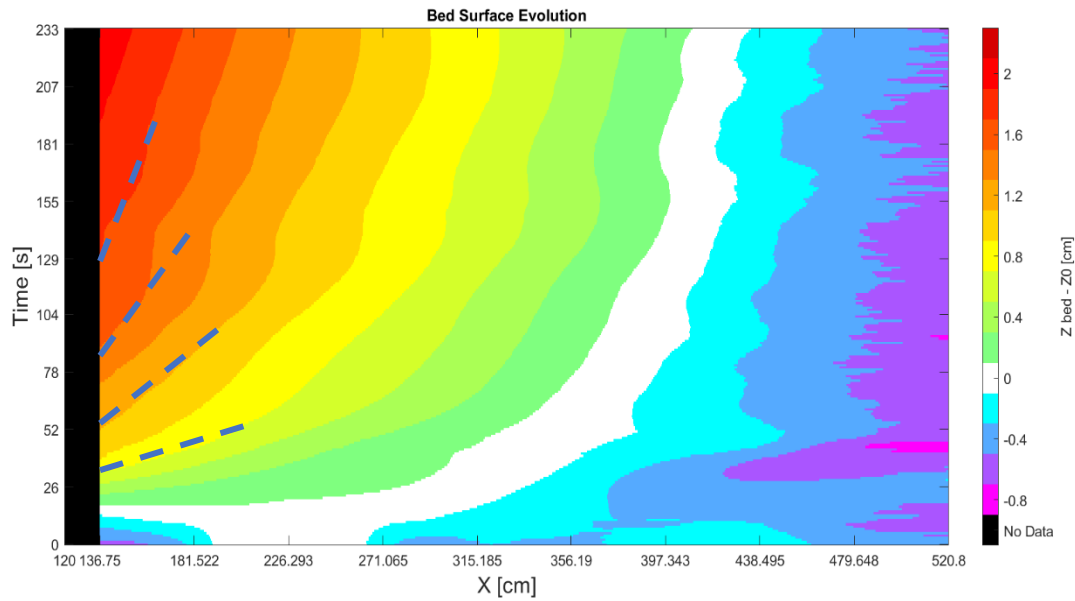


Figure 4.13. Lines fitted to the borders between the colors of the color gradient graphs in the upstream part, experiment AE8.

The procedure for finding the celerity is explained below.

An aggradation height is chosen, then the coordinates of the channel in the x -direction in which the aggradation height is equal to the chosen one, and their corresponding times are extracted from the matrices used for the color gradient graphs. These data are plotted in a way that the y -axis and x -axis represent the coordinates and their corresponding times, respectively. Now by fitting a linear function to the data, one can find the celerity of the chosen aggradation height since the slope of the fitted line is equal to the celerity. It should be mentioned that these lines are fitted to the initial times of each aggradation height, which happens in the upstream part of the channel. In this thesis, different aggradation heights are chosen based on the sediment particle size (0.38 cm). The fitted lines for different aggradation heights of experiment AE8 are shown in Figure 4.14.

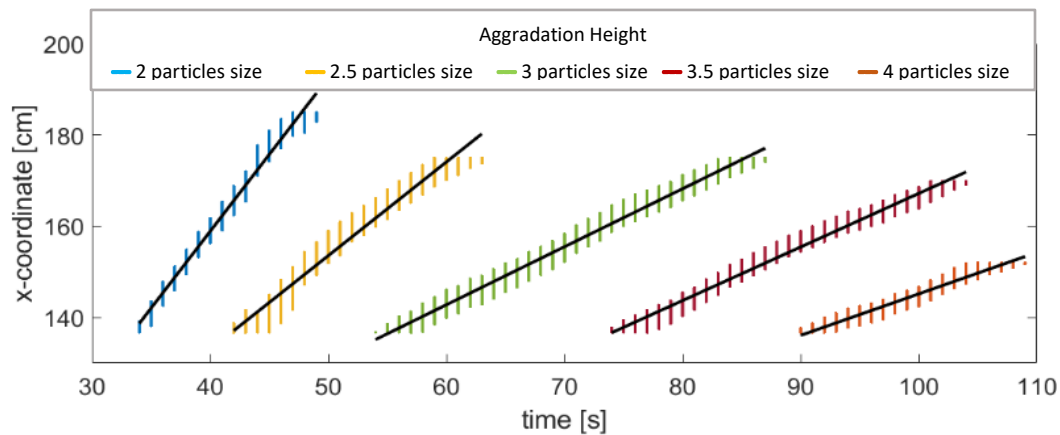


Figure 4.14. The plot of the x -coordinate of aggradation heights and their corresponding time and the fitted linear lines, experiment EA8.

The celerity corresponding to the chosen aggradation heights are reported for the experiments AE1, AE5, AE6, and AE8 in Table 4.2 and Figure 4.15. The reason for choosing these experiments is the fact that their overloading ratio and consequently their aggradation were higher compared to other experiments.

Table 4.2. Celerity of aggradation wave for different aggradation heights in different experiments.

<i>Celerity of aggradation wave (cm/s)</i>					
<i>Experiment</i>	<i>Aggradation height</i>				
	<i>2 particles size (0.76 cm)</i>	<i>2.5 particles size (0.95 cm)</i>	<i>3 particles size (1.14 cm)</i>	<i>3.5 particles size (1.33 cm)</i>	<i>4 particles size (1.52 cm)</i>
AE1	0.78	0.72	0.60	0.49	0.48
AE5	4.41	4.04	3.86	3.14	2.84
AE6	2.65	1.89	0.74	0.71	0.64
AE8	3.37	2.05	1.27	1.17	0.91

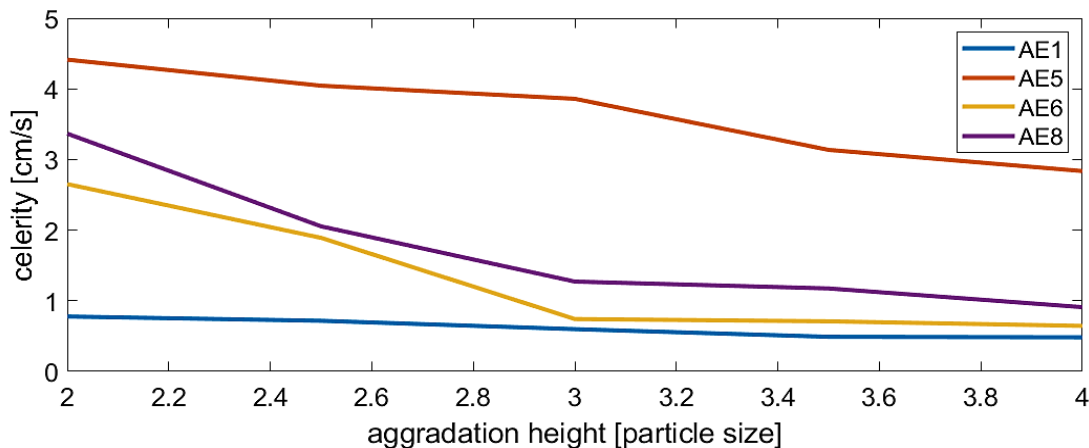


Figure 4.15. The plot of aggradation wave celerity for different aggradation heights in different experiments.

Some points can be concluded from the results:

- Different heights in the aggradation wave travel at different celerity (the lower, the faster).
- For the same aggradation heights, a higher loading ratio causes a higher celerity.
- The overloading ratio in the experiments AE1 and AE6 are almost equal, but the celerity for the same aggradation heights is higher in the AE6 compared to the AE1. This might be due to the fact that the water discharge in the AE6 is higher than the water discharge in the AE1.

RESULTS OF AGGRADATION EXPERIMENTS

- For each experiment, the aggradation heights and celerity are normalized with respect to the minimum aggradation height and its corresponding celerity, respectively. By plotting the normalized data for different experiments (Figure 4.16), one can conclude that the gradient of normalized celerity with respect to the normalized aggradation height depends on the water discharge. The experiments with the same water discharge show similar trends, and the gradient of the normalized celerity with respect to the normalized aggradation height is larger for experiments with higher water discharge. It means that in the experiments with the same water discharges and different overloading ratios, by a relative increase in the aggradation height, their celerity decreases with the same proportion. This relative decrease in the celerity is more for experiments with higher water discharges.

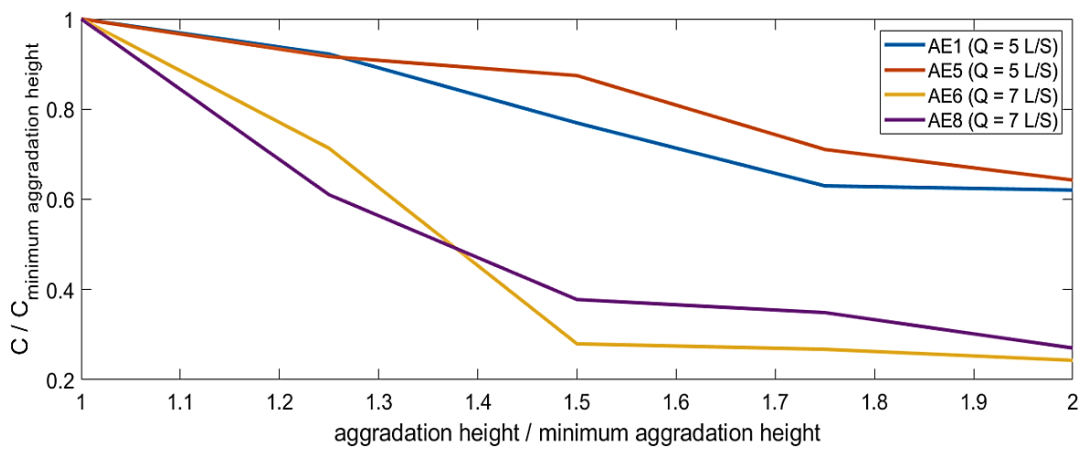


Figure 4.16. The plot of normalized aggradation wave celerity for different normalized aggradation heights in different experiments.

In conclusion, this study finds that the loading ratio, water discharge, and aggradation height are three effective parameters for the celerity of the aggradation wave. More experiments should be performed to validate the above-mentioned points and to see if any other parameters are involved in changing the celerity.

4.2.4. Analysis of mass conservation

Based on the mass conservation law, in the aggradation experiments, the sum of the sediment mass deposited inside the channel and trapped inside the collectors must be equal to the inflow sediment mass, which is the amounts of sediments entering the channel by the hopper during the experiments. The inflow mass (M_{inflow}) for each experiment is computed through the formula:

$$M_{inflow} = Q_{sin} \times T \times \rho_s \quad 4.5$$

where Q_{sin} is the sediment inflow discharge, T shows the duration of the experiment, and ρ_s represents the sediment density (1443 kg/m^3).

After each experiment, the sediments trapped inside the collectors and the ones deposited inside the channel are collected, dried, and their mass is measured ($M_{collected}$). According to the mass conservation law, M_{inflow} and $M_{collected}$ must be equal, but due to some errors in the measurements, these two values are not exactly the same. One should compute the relative error of mass conservation for each experiment to check the validity of the measurement of inflow sediments. The results of mass conservation error for all experiments performed in this campaign (AE4 to AE8) are reported in Table 4.3.

Table 4.3. Results of mass conservation analysis.

Experiment	Q_{sin} (m^3/s)	T (s)	M_{inflow} (kg)	$M_{collected}$ (kg)	Relative Error (%)
AE4	8.70E-05	350	43.94	45.52	-3.59
AE5	24.30E-05	340	119.22	114.05	4.33
AE6	23.00E-05	260	86.29	82.80	4.04
AE7	14.30E-05	365	75.32	80.30	-6.62
AE8	25.50E-05	234	86.10	83.10	3.48

4.3. Summary

Eight aggradation experiments were performed in the supercritical campaign (AE1 to AE8). The first three experiments were run in the previous study (Heydari 2020), and they were reanalyzed in the current study with the updated methods for the detection of bed and water surface elevations. Out of these eight experiments, only four of them were actually in the overloading conditions (AE1, AE5, AE6, and AE8). The experiments AE1 to AE5 and AE6 to AE8 were run with water discharge (Q) of 5 l/s and 7 l/s, respectively. The channels and sediment particles characteristics remained constant for all of the experiments, and for the experiments with the same water discharge, the only factor that was changed is the sediment inflow discharge (Q_{sin}). The sediment inflow discharge was obtained with the PIV method, and the temporal evolution of the bed and water was obtained by the motion detection algorithm. The initial sediment transport capacity (Q_{s0}) for the aggradation experiments were calculated, and the loading ratio (Lr) for each experiment was obtained by dividing the Q_{sin} by Q_{s0} . For the occurrence of aggradation, Lr must be greater than one, so for each experiment, the vibration level is set in a way that the Lr be greater than one. After analyzing the results, a clear consistency was observed between the results since the temporal evolution of the bed showed an equilibrium condition almost from the beginning for experiments with a loading ratio close to one; also, for experiments with a higher loading ratio, aggradation was observed during the experiment. The aggradation

RESULTS OF AGGRADATION EXPERIMENTS

height in the upstream part of the channel was higher compared to the downstream part; this causes the bed slope to increase because the channel tends to an equilibrium condition.

In all of the experiments except AE5, degradation happened in the downstream part of the channel close to the outlet because of the effect of the transverse sill located at the outlet. The reason that this degradation did not happen in AE5 is because of its higher loading ratio that overcomes the effect of the transverse sill.

For better analysis of the data, two matrices were created, which contain the data related to the bed and water surface elevations in a way that each array of them shows the surface elevation in a specific time and coordinate. The rows and columns represent the time and coordinate, respectively.

The matrices related to the bed and water profiles in each experiment were used to obtain the matrix for the Froude number. By visualization of these matrices through color gradient graphs, it was observed that the experiments with water discharge of 5 l/s are in subcritical regime except the experiment AE5, and the experiments with water discharge of 7 l/s are in the supercritical regime. In the previous study, the experiments AE1 to AE3 were reported to be in the supercritical regime, which contradicts with the current study. The reason for this contradiction refers to the fact that different methods were used for bed detection; in the previous thesis, the surface of the bedload layer was detected as the bed surface, while in the current study, the surface of the stationary bed is considered as the bed surface. As a result, the water depth with the previous method is calculated lower than the new one; consequently, the velocity and Froude number are obtained higher compared to the current study. The results show that the experiment AE5 is in a subcritical regime at the beginning, but due to the high loading ratio, the bed slope increases rapidly, so it causes the flow regime to change from subcritical to supercritical.

Since the aggradation phenomenon in these experiments was dispersive, it was not possible to detect the sediment front for finding the front celerity by the method that was used in the subcritical campaign, so in the current study, a new method is introduced by using the bed surface elevation matrix mentioned before. The data (time and coordinate) corresponding to the initial time of several aggradation heights (2, 2.5, 3, 3.5, and 4 *particles size*) are extracted and mapped in a way that the x -axis and y -axis represent the time and coordinate, respectively. The celerity of each aggradation height is the slope of the line, which is fitted to the data related to each aggradation height. The values of celerity were obtained for the experiments AE1, AE5, AE6, and AE8 since their loading ratios are higher compared to the other experiments. The results of the current study show that the celerity depends on the loading ratio, water discharge, and aggradation height in a way that higher loading ratio and water discharge result in higher celerity, while higher aggradation height travels with a lower celerity. Another conclusion is that in the experiments with the same water discharges and different overloading ratios, by a relative

increase in the aggradation height, their celerity decreases with the same proportion. This relative decrease in the celerity is more for experiments with higher water discharge.

In the subcritical campaign, it was concluded by Zucchi (2018) that the normalized celerity (c/\sqrt{gh}) increases with the increase in Froude number or, in other words, the celerity increases with the increase in flow velocity. This dependency can be in conformity with one of the conclusions of the current study, which is the dependency between the celerity and water discharge; because flows with higher water discharge have higher velocity compared to those with lower water discharge. Another conclusion of the subcritical campaign was that the sediment front celerity is independent of the loading ratio, while the current study shows a dependency between these two parameters.

There are some issues related to this work and some points that should be considered in future works:

- In this study, the number of experiments was low because of difficulties related to running these types of experiments, and they are very time-consuming; Therefore, more experiments should be performed to validate the results and to see if any other parameters are involved in changing the celerity.
- Although the cameras for monitoring the bed were changed with higher quality ones, there are still some problems related to the referencing of the profiles because of the distortion. The problem is that when regrouping the profiles detected with different cameras, there is a difference between the elevation of the profiles at the common borders of the photos; sometimes, this difference is up to 0.5 cm, which can be considered significant. If the referencing improves, this difference decreases; Thus, some solution must be introduced to solve the issue of referencing the data.
- Another issue is the difficulty of performing experiments with higher water discharges and higher loading ratios. The water discharge should gradually increase to reach the desired discharge before the sediment feeder starts working, so because of the lack of sediment feeding in this duration, high water discharge can significantly erode the bed. This issue might be solved by starting the hopper earlier to avoid the erosion of the bed.
- Since the higher loading ratios can cause the formation of a dam, in the future works, an upper bound for Lr might be found in a way that for loading ratios lower than the founded bound, the process takes place in the form of migrating aggradation front rather than the formation of a dam.
- The effect of transverse sill causes the bed to behave differently in the downstream part of the channel compared to the upstream part, while in this work, it is assumed that the behavior of the channel is uniform in every section; thus, this issue might be handled by using a permeable transverse sill.

CHAPTER 5

NUMERICAL SIMULATION

5.1. Introduction

The theory corresponding to the morphological processes tries to model the reality, which in this study, it is the performed experiments, but it does not yield any quantitative results. This is while the investigation about the consistency of the experiments and theory needs a quantitative comparison. Therefore, in order to make a connection between the experimental results and theoretical concepts, performing a numerical simulation of flow and bed behavior is required, which in the end leads to the quantitative results. In the presence of an appropriate adaptation between the experimental and numerical results, numerical modeling can be used to simulate the condition at which physical modeling is not conceivable. However, in the absence of a suitable adaption between the two results, in order to make a correlation between them, some calibration on the numerical model would be required. This chapter will consider the correspondence between the performed experiments and numerical simulations run with the same boundary conditions.

5.2. Hydro-morphologic model and numerical solver used

The hydro-morphologic evolution of the bed and water is by definition unsteady, and due to this reason, the governing flow equations used in the 1-D modeling are Saint-Venant equations (SVEs), including continuity (mass balance) and momentum equations in unsteady conditions. While the water motion is described by SVEs, the sediment continuity is represented by the Exner equation. Therefore, the hydro-morphologic evolution in one-dimensional conditions is depicted by a system of partial differential equations, including two SVEs and one Exner equation (equation 1.34).

$$\begin{cases} \frac{\partial h}{\partial t} + \frac{\partial q}{\partial x} = 0 \\ \frac{\partial q}{\partial t} + \frac{\partial}{\partial x} \left(\frac{q^2}{h} \right) + gh \left(\frac{\partial h}{\partial x} + \frac{\partial z_b}{\partial x} \right) = -ghS_f \\ (1-p) \frac{\partial z_b}{\partial t} + \frac{\partial q_s}{\partial x} = 0 \end{cases} \quad 1.34$$

In addition, to estimate the sediment discharge, a closure equation should be used; in this work, among different equations, the Meyer-Peter and Müller (1948) formula has been chosen (equation 3.2).

$$\Phi = 8(\tau^* - \tau_c^*)^{1.5} \quad 3.2$$

Another closure equation to solve the problem is the Manning-Strickler equation, which is used to obtain the friction slope (equation 1.32).

$$S_f = \frac{n^2 \times U^2}{R_H^{4/3}} \quad 1.32$$

In the presented work, the numerical solver used to solve the above-mentioned hydro-morphologic system of PDEs is BASEMENT software (BASIC SIMULATION ENVIRONMENT FOR COMPUTATION OF ENVIRONMENTAL FLOW AND NATURAL HAZARD SIMULATION), provided by ETH Zurich / Laboratory of Hydraulics, Glaciology, and Hydrology (VAW). Since the most often governing equations for flow cannot be solved analytically for general boundary conditions, BASEMENT uses time and space discretization methods to solve the system of PDEs so that, for space discretization, it uses the Finite Volume method (FV) and for time discretization it applies the Finite Difference method (FD) with Explicit Euler scheme. The applied approach follows a line already established by previous works on the subject (Zanchi 2018; Zucchi 2018).

5.2.1. Model parameterization

In order to make the model in the BASEMENT, it is essential to define different parameters as the input of the model. The geometrical and hydro-morphological parameters used in this work are as follows.

5.2.1.1. Geometry

- Section

As it was mentioned in [chapter 2.1.1](#), the rectangular section of the experimental channel in the presented thesis is characterized by the width and overall bank height equal to 0.3 m and 0.45 m, respectively; therefore, in order to reproduce this channel, the same characteristics are used in the numerical model ([Figure 5.1](#)).

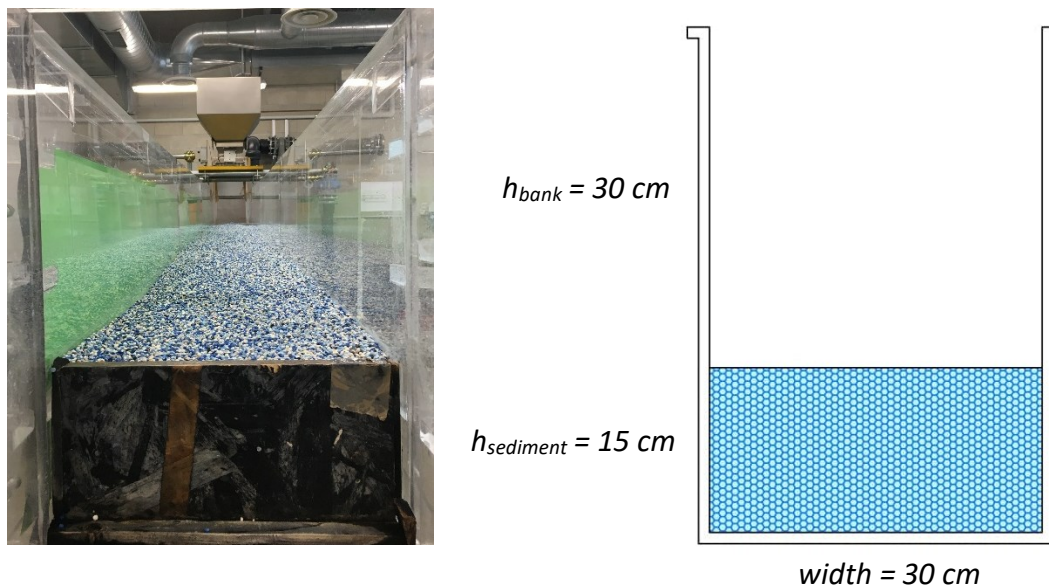


Figure 5.1. Characteristics of the channel section.

NUMERICAL SIMULATION

- Length

The sediment inflow location is chosen as the upstream section of the simulated channel, which is 0.25 m far from the upstream section of the experimental channel, while the downstream section is selected a fixed point at the downstream, 5.15 m far from the upstream section of the experimental channel. Therefore, the length of the simulated channel is equal to 4.9 m whereas the length of the experimental channel is 5.2 m . In order to produce the numerical channel, this 4.9 m length is subdivided into 98 reaches with the length of 5 cm , resulting in 99 sections with the above-mentioned characteristics (Figure 5.1). Also, the slope of the channel is considered equal to the experimental one, 1.2% . The scheme of the simulated channel is represented in Figure 5.2.

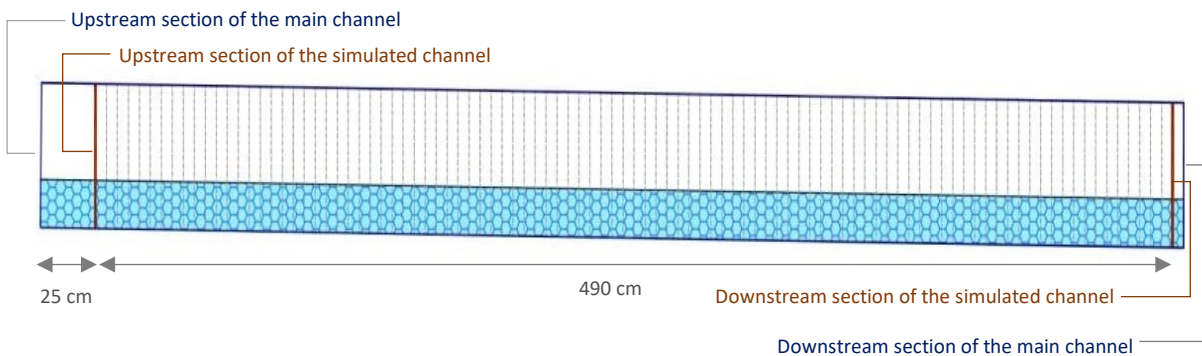


Figure 5.2. The scheme of the experimental and simulated channel.

5.2.1.2. Hydraulics

- Manning's coefficient

The Manning's coefficient used in the simulation is the one obtained experimentally by Unigarro Villota (2017), which is equal to $0.015\text{ s}/\text{m}^{1/3}$. It should be mentioned that this value is a reference one, but it will be an object of the final calibration (will be explained in chapter 5.4).

- Upstream boundary condition

A flow hydrograph corresponding to each experiment is imposed at the upstream section of the simulated channel as the boundary condition of the hydraulics part. Since in the experiments AE1-AE5, the inflow water discharge has a constant value and equal to $5\text{ l}/\text{s}$, the hydrograph has a constant value with a duration of the experiment duration. Similarly, for experiment AE6-AE8, the hydrograph has a constant value but equal to $7\text{ l}/\text{s}$.

- Downstream boundary condition

The water elevation (h) is assigned to the downstream section as the downstream boundary condition of the hydraulics part. Since the value of the water elevation at the downstream is not known during the experiment, in order to define it, the option of "hqrelation" in BASEMENT

would be used. By using this option as the downstream boundary condition, the water elevation is computed, applying the relationship between water depth and discharge in uniform condition.

- Initial condition

A steady water profile obtained from a clear-water, fixed-bed model is introduced to the software in this part as the initial condition. Indeed, according to what occurs in the experimental work, it is assumed that before supplying the channel with sediment, there is a steady flow in the channel; this water profile is created using a preliminary fictitious model at which there is no sediment inflow discharge, the bed is assumed to be non-erodible, and the time of simulation is long enough to achieve a steady profile starting from a dry condition.

5.2.1.3. Morphology

- Sediment material properties

By referring to [chapter 2.1.3](#), the sediment particles used in the experimental works are cylindrical PVC grains with the characteristics represented in [Table 5.1](#); in the numerical simulations, the same properties are used for both bed and inflow sediment material.

Table 5.1. Material properties used in the experimental and numerical models.

<i>Material properties (cylindrical PVC)</i>		
<i>Diameter (mm)</i>	<i>Porosity (%)</i>	<i>Density (kg/m³)</i>
3.8	45	1443

- Sediment transport formula

As it was discussed before, in order to evaluate the sediment transport rate in each section, a closure equation is needed. BASEMENT software proposes different equations in this regard, and among those, in the presented thesis, the Meyer-Peter and Müller formula (equation 3.2) is chosen, which is a suitable one for single grain simulations.

$$\Phi = 8(\tau^* - \tau_c^*)^{1.5} \tag{3.2}$$

The critical Shields parameter (τ_c^*) is an important factor in this formula that can be specified either by the user or the software; in this work, it is computed by the software and according to the transformed Shields diagram. It is worth mentioning that the BASEMENT offers two approaches to transform the Shields diagram and calculate τ_c^* , Van Rijn (1984) and Yalin and Silva (2001) approach; in this thesis, the Van Rijn approach is used, which was explained in [chapter 3.2.1](#).

- Upstream boundary condition

In the morphology part, for the upstream boundary condition, a sediment graph is imposed at the upstream section of the simulated channel. The duration of this graph matches with the

NUMERICAL SIMULATION

experiment duration, and its value is assumed to be constant and equal to the sediment inflow discharge (Q_{sin}) obtained from the PIV process and transfer function explained in [chapter 2.2.1](#).

However, the assumption of a constant value for the sediment inflow discharge can be considered as an appropriate assumption when the behavior of the hopper during the experiment is uniform. In the cases in which the hopper does not work uniformly, like experiment AE2, the sediment graph obtained from the PIV process is assigned as the upstream boundary condition in the numerical channel ([Figure 5.3](#)).

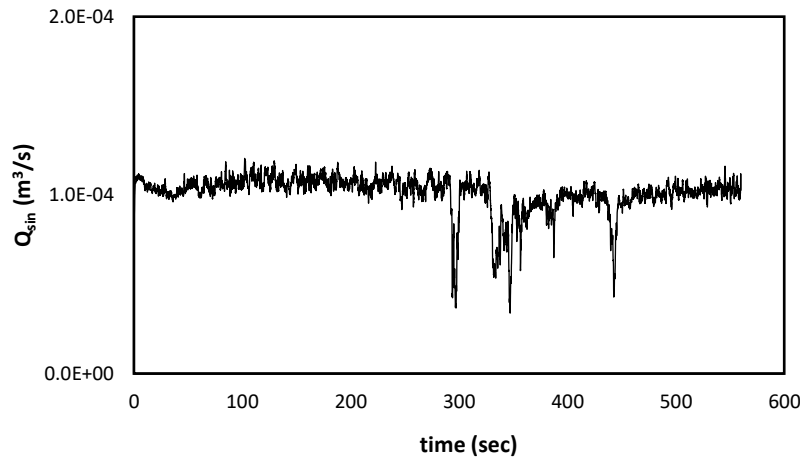


Figure 5.3. The sediment graph corresponding to the experiment AE2, used as the upstream boundary condition in the simulated channel.

- Downstream boundary condition

The “IODown” option is the only downstream boundary condition available for sediment transport in BASEMENT, which somehow coincides with the structure of the experimental channel. Using this option, all sediment entering the last computational section leaves the section through the downstream boundary. It is worth mentioning that if no boundary condition is defined in this part, a wall is assumed at the boundary, and sediment transport will not occur.

As it is observed, the total number of boundary conditions needed to be introduced to the software is four, two for the hydraulics part and two for the morphology part. This is while looking at equation 1.34, it is easily understood that from the theoretical point of view, in order to solve a PDEs system with three equations, three boundary conditions are required. In this regard, according to what is explained in [chapter 1.8.1.1](#), two boundary conditions must be introduced at the upstream and one at the downstream; these boundary conditions will depend on the Froude number of the flow. In [Table 5.2](#), the combinations of boundary conditions required to solve equation 1.34 are shown.

Table 5.2. The required boundary conditions according to the theory to solve the SVE and Exner equations.

<i>Froude number</i>	<i>Upstream BC</i>	<i>Downstream BC</i>
<i>Fr < 1 (subcritical flow)</i>	Q, Z_{bed}	h
<i>Fr > 1 (supercritical flow)</i>	Q, h	Z_{bed}

Therefore, from the theoretical point of view, for a supercritical regime, two boundary conditions which should be assigned to the upstream are Q and h (water elevation), and the one assigned to the downstream, is Z_{bed} . Comparing these boundary conditions with the ones introduced to the software, some points are identified:

- According to the theoretical solution, the water discharge (Q) is correctly introduced to the software at the upstream boundary.
- There is an inconsistency between the theoretical solution and software requirement in the definition of the water level as the boundary condition. While, according to the theory, the water level in a supercritical flow should be imposed at the upstream boundary, it is required by the software in the downstream part. Indeed, from the theory, it is known that in the supercritical flows, no information arrives from the downstream, and two boundary conditions related to the SVEs (Q and h) should be defined at the upstream; as a result, imposing the water level as the boundary condition at the downstream in the software, will lead to a useless boundary condition in computation, because it cannot influence the flow within the computational domain. Therefore, in the supercritical flows, the given useful value at the upstream boundary to solve the SVEs is usually Q . In this regard, the second boundary condition, h , is determined by introducing the slope at the upstream and using a flow resistance law for a uniform flow. Indeed, the software calculates the value of h , assuming that the flow at the upstream is uniform. This is while in the experimental work because of the change of the slope and backwater induced by sediment feeding, there is some transition through the critical depth at the upstream; as a result, in contrast with the software assumption, the flow is not uniform at the upstream in the experimental work.
- Assignment of the bed elevation (Z_{bed}) in the software as a downstream boundary condition is consistent with the theory solution in the supercritical flows.
- The sediment inflow discharge, which is imposed as an upstream boundary condition in the software, is not required by the theoretical solution. Although this boundary condition is not needed to solve the problem mathematically, it is a real upstream boundary condition that is imposed in the experiments and influences the evolution of the bed from upstream towards downstream.

NUMERICAL SIMULATION

In conclusion, the only useless boundary condition required by the software is the water level at the downstream. This boundary condition is considered only in the downstream section and would be neglected in the evolution of the water because it does not influence the flow in a supercritical regime.

- Initial condition

The initial bed topography, introduced in the geometry part, is used as the initial condition of the morphology part.

5.3. Comparison between numerical and experimental results

After creating the model, simulation is performed, and results are obtained. In the presented work, the numerical simulation is done for all experiments except AE3 and AE4. The numerical parameters used for each experiment are reported in [Table 5.3](#).

Table 5.3. Numerical parameters corresponding to each experiment.

<i>Experiment</i>	<i>Duration of the simulation, T (s)</i>	<i>Water discharge, Q (l/s)</i>	<i>Sediment inflow discharge, Q_{sin} (m^3/s)</i>
AE1	490	5	1.42E-04
AE2	560	5	Sediment graph obtained from PIV process with a mean value equal to 1.01E-04
AE5	340	5	2.43E-04
AE6	259	7	2.3E-04
AE7	364	7	1.43E-04
AE8	233	7	2.55E-04

In order to investigate the consistency of the numerical and experimental results, a comparison between the two is needed. Here, the comparison between the profiles for the experiments AE5 and AE7 is presented ([Figures 5.4 to 5.7](#)).

Comparison between numerical and experimental results

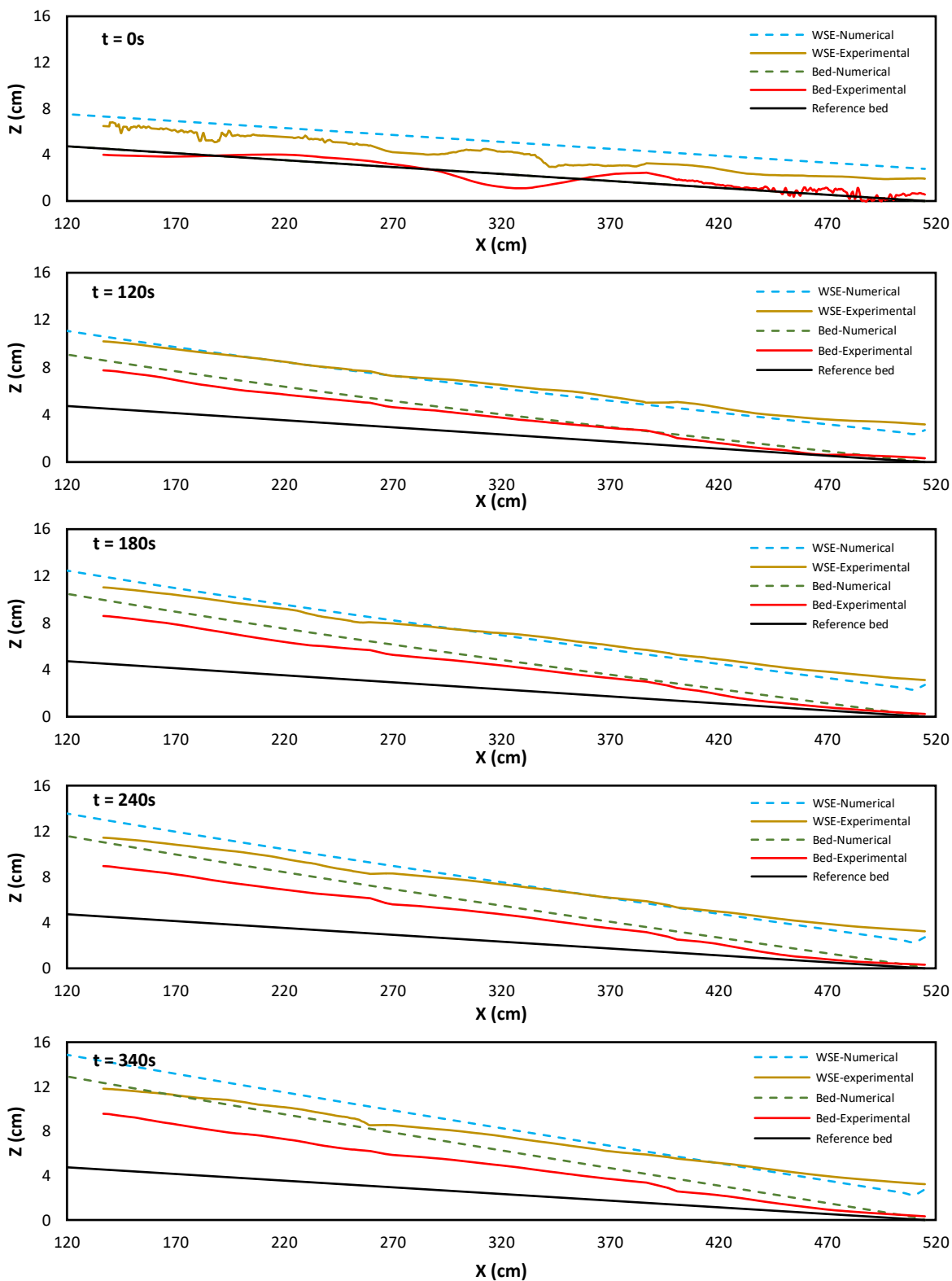


Figure 5.4. Spatial evolution of bed and water at the selected times for experiment AE5 with overloading ratio equal to 2.92. The experimental results are compared to the numerical ones.

NUMERICAL SIMULATION

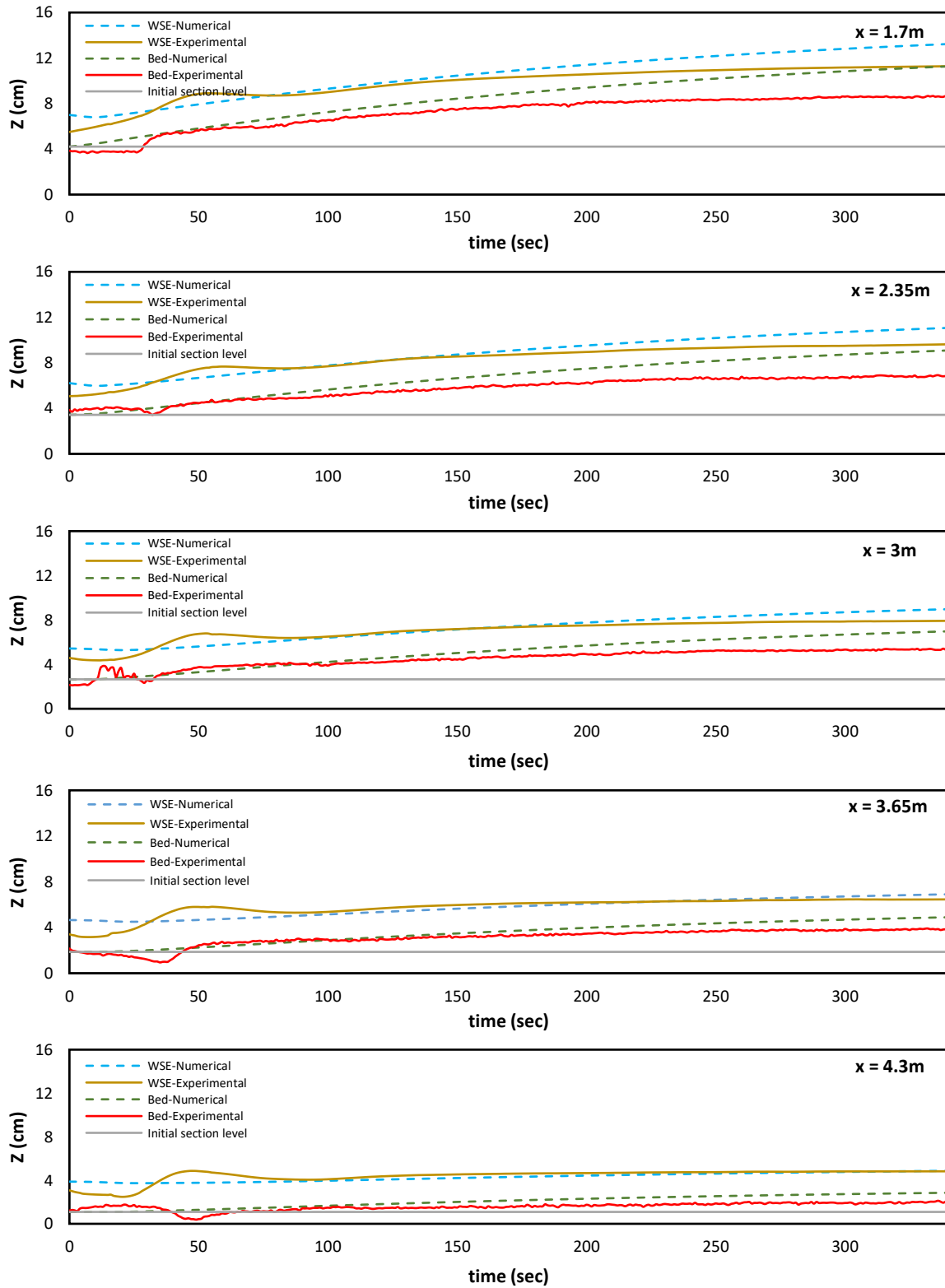


Figure 5.5. Temporal evolution of bed and water at the selected points for experiment AE5 with overloading ratio equal to 2.92. The experimental results are compared to the numerical ones.

Comparison between numerical and experimental results

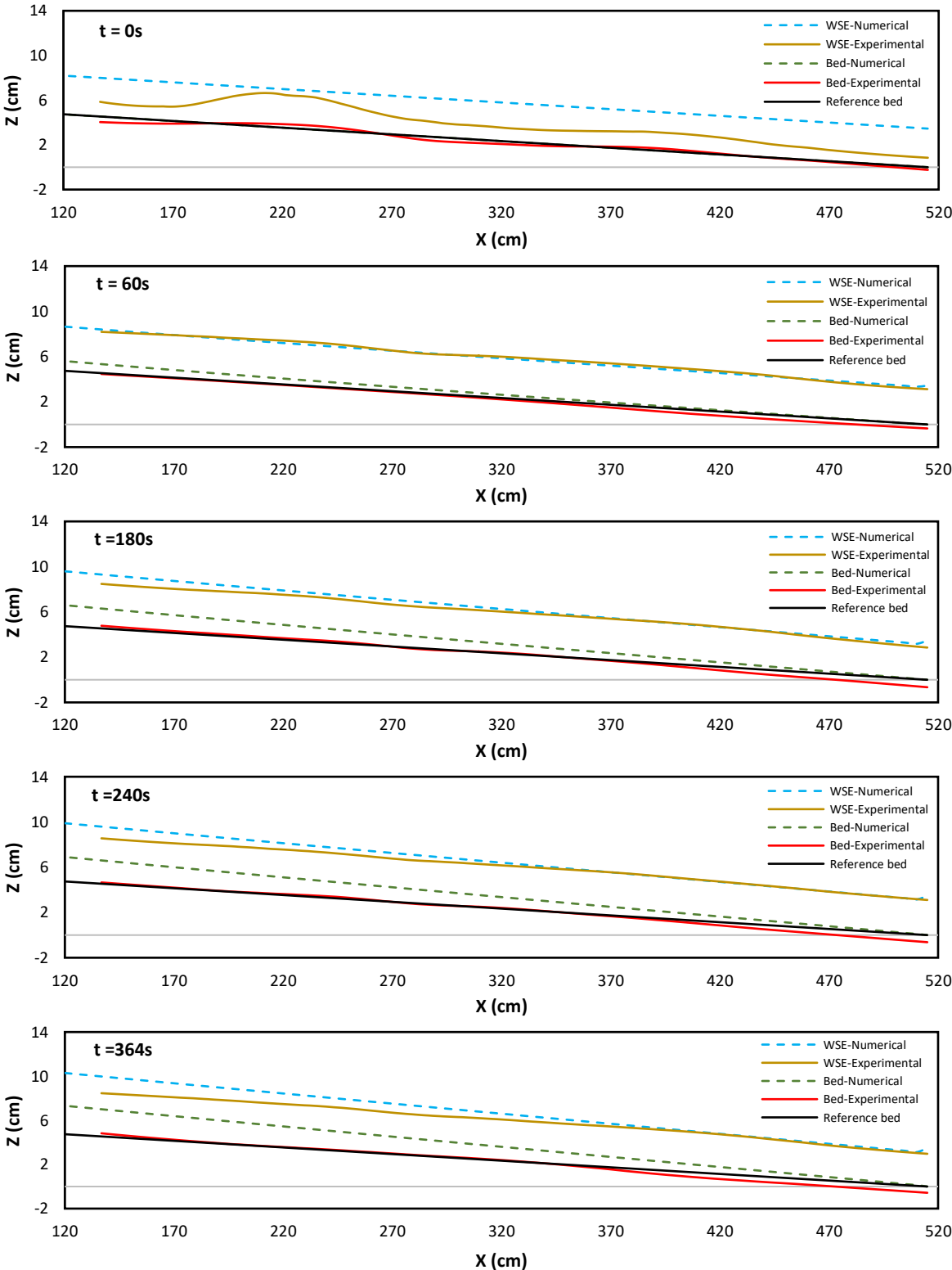


Figure 5.6. Spatial evolution of bed and water at the selected times for experiment AE7 with overloading ratio equal to 1.075. The experimental results are compared to the numerical ones.

NUMERICAL SIMULATION

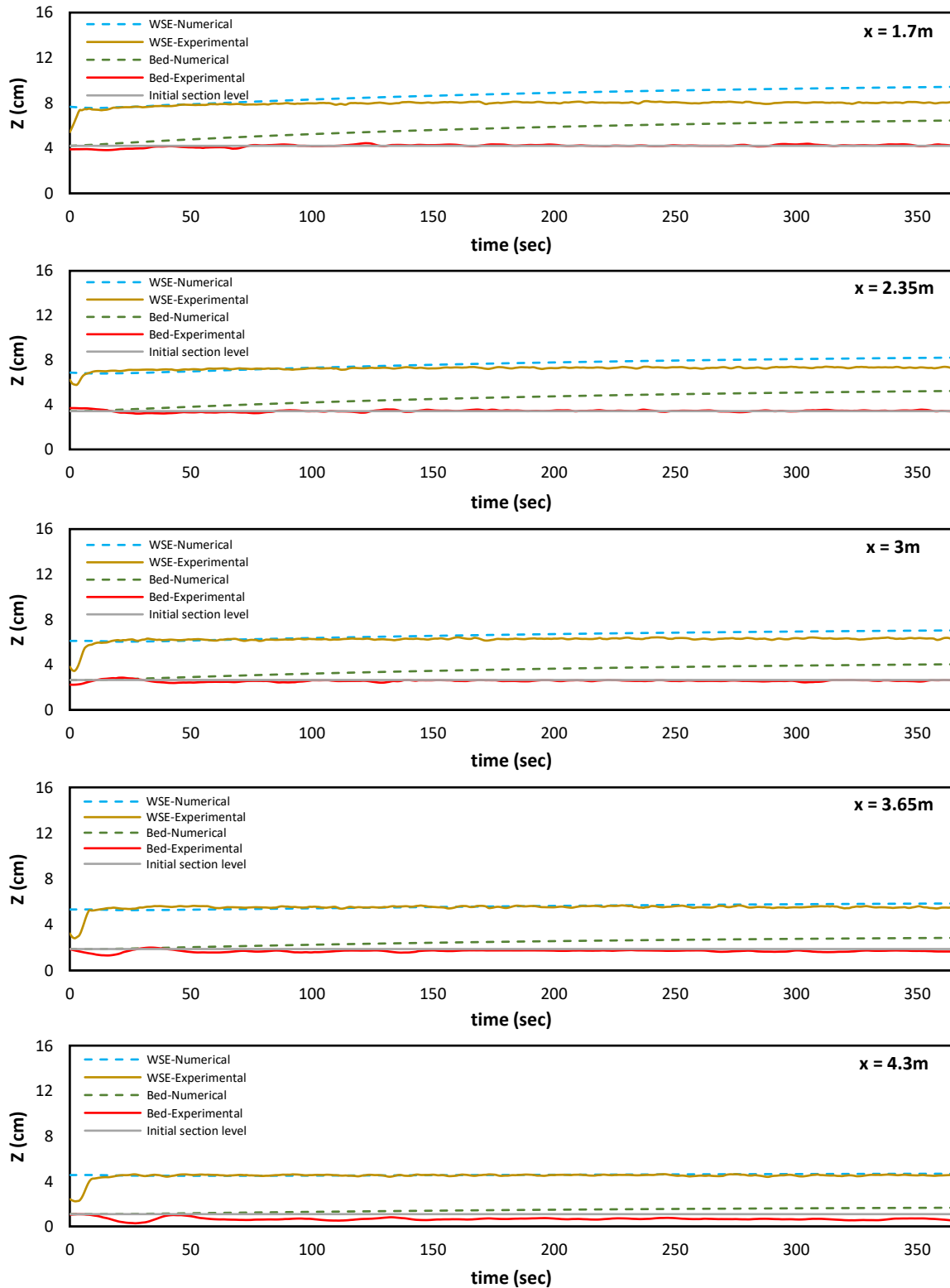


Figure 5.7. Temporal evolution of bed and water at the selected points for experiment AE7 with overloading ratio equal to 1.075. The experimental results are compared to the numerical ones.

From the morphological evolution point of view, in some experiments, there is a similar behavior between the results so that when the overloading ratio (Q_{sin}/Q_{s0}) is significant, like experiment AE5 with the ratio equal to 2.92, the bed tends to have a rapid evolution and creates a new configuration with a higher slope; however, with the increase in the slope, the rate of the deposition of the sediment material decreases and it tends to stop in the equilibrium condition, where the sediment inflow discharge (Q_{sin}) is close to the sediment transport capacity of the new bed. This consistency is not observed in the experiments like Experiment AE7 in which the overloading ratio is near to 1; while in the experimental results, an equilibrium condition from the beginning of the experiment is visible (the bed remains almost unchanged during the experiment), the numerical results show a considerable deposition of the sediment material in the bed with the time.

However, from the bed and water elevation point of view, in all experiments, there is no consistency between experimental and numerical results. In all cases, even in experiments like AE5, at which the general trend of the results is similar, the numerical results represent a bed elevation higher than the experimental ones. The reason refers to the fact that the numerical simulation underestimates the sediment transport capacity of the bed with respect to the experimental one, resulting in more deposition of the sediment material in the bed. For example, according to [chapter 3.2.5](#), in the experiment AE5, while the initial sediment transport capacity from the experimental work has been estimated $Q_{s0} = 8.31 \times 10^{-5} \text{ m}^3/\text{s}$, using the numerical simulation (the Meyer-Peter and Müller formula and Van Rijn approach), it is computed equal to $5.14 \times 10^{-5} \text{ m}^3/\text{s}$ which is 1.6 times less than the experimental one.

Also, looking carefully at the graphs, it is observed that as time goes on, the difference between numerical profiles and experimental ones increases so that the maximum discrepancy can be identified at the end of the experiments.

However, since the inconsistency between the numerical and experimental results is evident, in order to decrease the difference between the results, a calibration of the numerical model is needed.

5.4. Calibration of the model

5.4.1. Modification of the bedload factor (the multiplier coefficient of the Meyer-Peter and Müller formula)

As it was explained, one reason causing the numerical bed to become higher than the experimental one is that using the Meyer-Peter and Müller formula, the numerical model underestimates the sediment transport capacity with respect to the experimental one. Therefore, in order to make the consistency between the results, one way could be increasing the sediment transport capacity of the channel estimated by the software. To do this, it is enough to increase the multiplier coefficient of the Meyer-Peter and Müller formula (α_{MPM}) in the

NUMERICAL SIMULATION

software, which has a default value equal to 1, and it is known as the bedload factor (see equation 5.1).

$$\Phi = \alpha_{MPM} 8(\tau^* - \tau_c^*)^{1.5} \quad 5.1$$

The main issue in this regard is the value of the α_{MPM} and how much it should be increased. For the first estimation, the initial sediment transport capacity (Q_{s0}) obtained from the experimental works is imposed to the Meyer-Peter and Müller formula, and the modified bedload factor is computed as follows:

$$\alpha_{MPM} = \frac{Q_{s0}(\text{experimental work})}{Q_{s0}(\text{Meyer - Peter and Müller formula})} \quad 5.2$$

The values of the initial sediment transport capacity, both experimentally and theoretically, were reported in chapter 3.2.5; by using these values, the modified bedload factor for different experiments can be calculated. The results are shown in Table 5.4.

Table 5.4. Modified bedload factor for different experiments, obtained from making equality between the experimental Q_{s0} and the numerical one.

<i>Experiment</i>	<i>Q (l/s)</i>	<i>Q_{s0} (m³/s) Experimental</i>	<i>Q_{s0} (m³/s) Numerical (MPM formula)</i>	<i>α_{MPM}</i>
AE1-5	5	8.31E-05	5.14E-05	1.61
AE6-8	7	1.33E-04	7.31E-05	1.82

Applying these factors in the software and running the simulation, the new results are obtained. Here the comparison between the numerical and experimental profiles for the experiments AE5 (as the representative of the experiments with $Q = 5$ l/s) and AE7 (as the representative of the experiments with $Q = 7$ l/s) is shown (Figures 5.8 and 5.9).

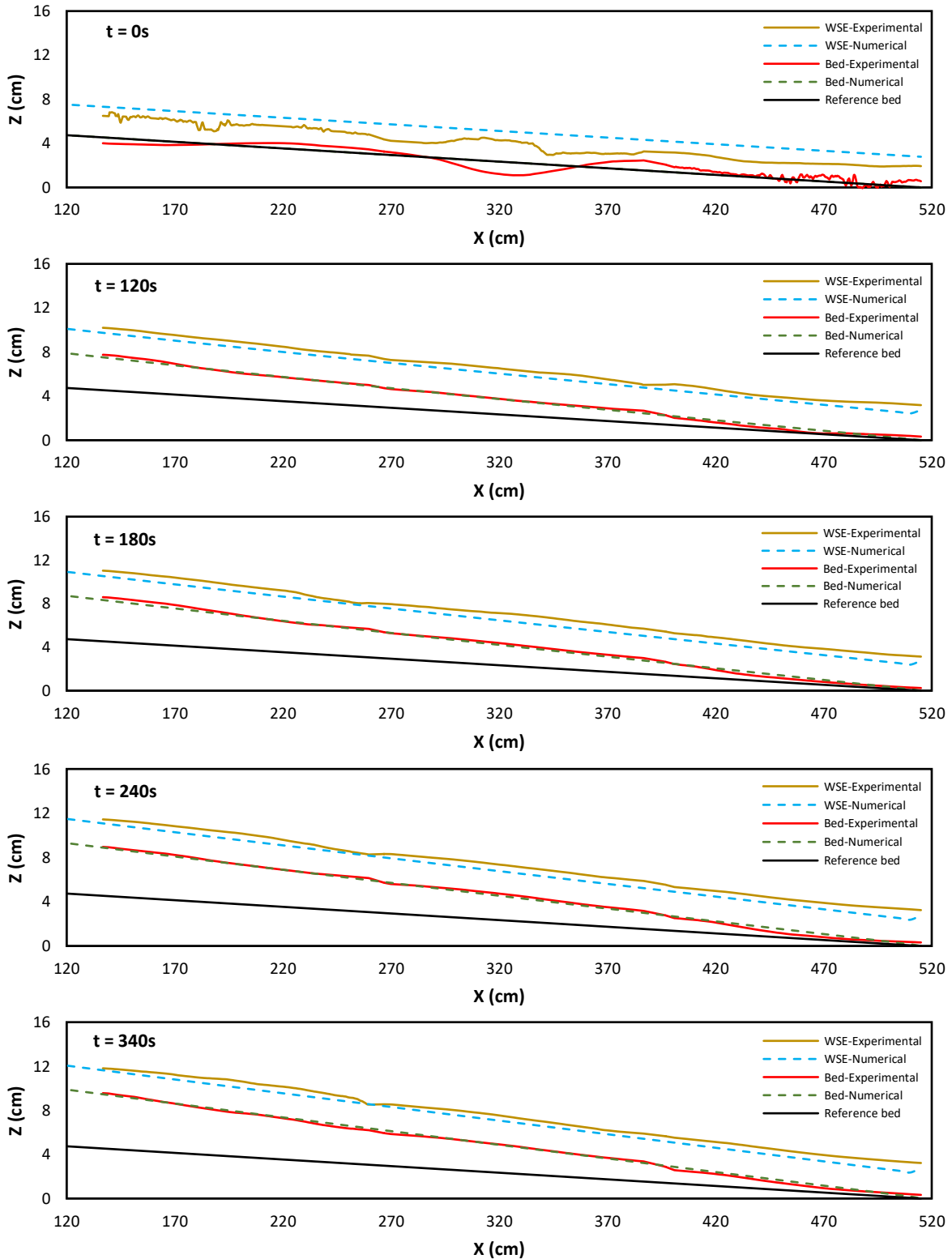


Figure 5.8. Spatial evolution of bed and water at the selected times for experiment AE5. The experimental results are compared to the numerical ones obtained by applying the new modified bedload factor.

NUMERICAL SIMULATION

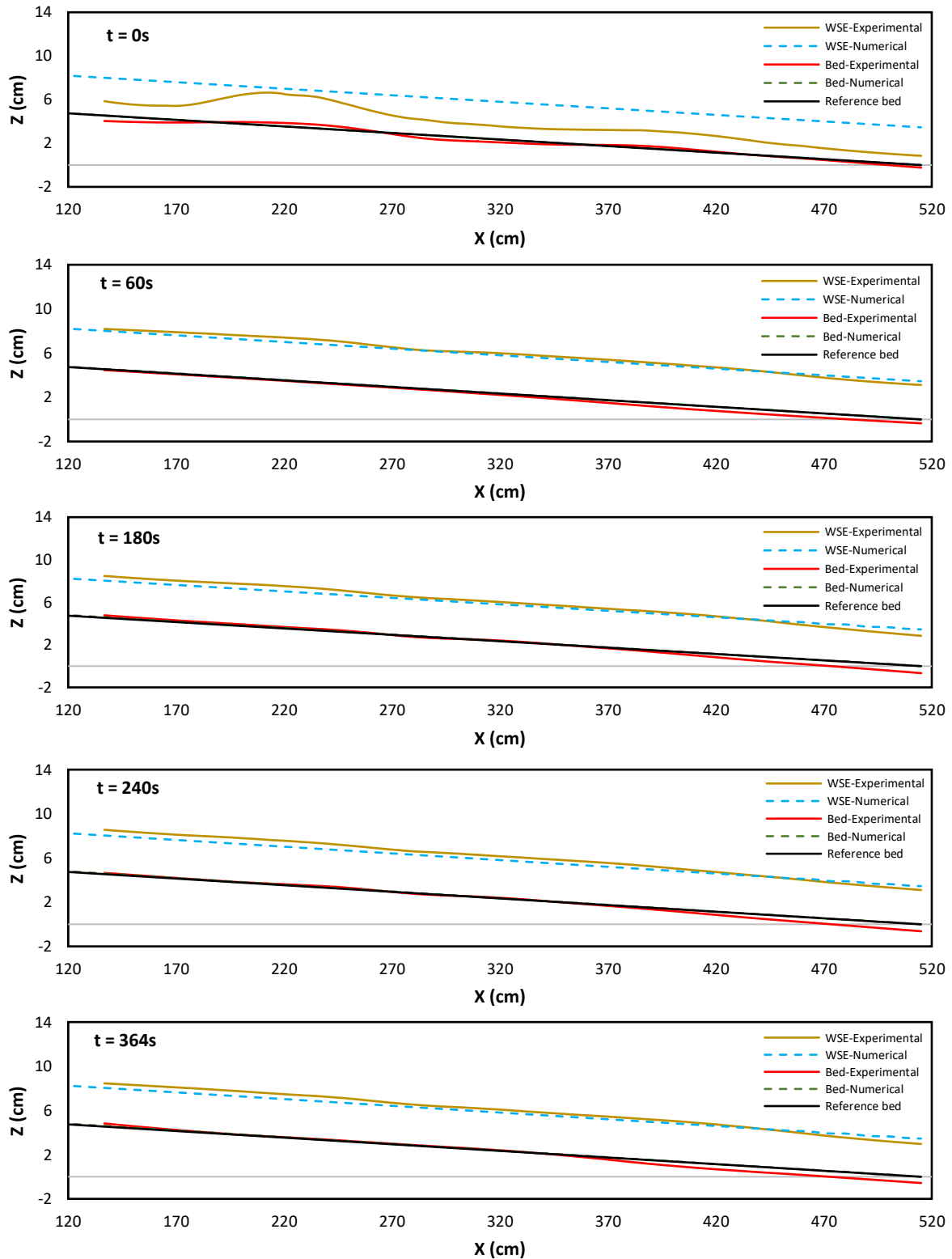


Figure 5.9. Spatial evolution of bed and water at the selected times for experiment AE7. The experimental results are compared to the numerical ones obtained by applying the new modified bedload factor.

The comparison demonstrates that the modification of the bedload factor has resulted in a good match between the experimental and numerical bed. However, despite this convergency between the results for the bed profiles, one can recognize that this modification leads to a drop in the numerical water profile so that in all graphs, the experimental water surface is higher than the numerical one. For instance, in experiment AE5, the average difference between the numerical water surface and the experimental one is about 0.7 *cm*. This is while the experimental water depth is around 2.8 *cm* during the experiment, meaning that there is a 25 % difference between the results with respect to the water depth. These attitudes are also true for all experiments. Therefore, it seems that in order to reduce the difference between the experimental water profile and numerical one, another calibration of the numerical model is needed. The new calibration should be in a direction resulting in an increase in the numerical water surface. One way to do this is to modify Manning's coefficient of the simulated model.

5.4.2. Modification of the Manning's coefficient

As it was explained before, the Manning's coefficient used in the simulation is the one obtained experimentally by Unigarro Villota (2017), which is equal to $0.015 \text{ s/m}^{1/3}$. In order to raise the numerical water surface, it is enough to increase this value in the software. It should be noted that although the increase in the Manning's coefficient leads to the rise of the water elevation, due to the increase in the shear stress in the bed, it can cause the sediment transport capacity of the channel to increase. This issue itself can result in a drop in the numerical bed elevation, meaning that the previous calibration for bed profiles would not work anymore, and some corrections are needed in this regard.

5.4.3. Final calibration of the model

From what is explained up to now, one can conclude that in the case of calibration of the bed profiles, the experimental and numerical water profiles would not be matched with each other. On the other hand, in the case of calibration of the water surfaces, the bed profiles would not be consistent. To solve this problem, a combination of calibrations on the bedload factor and Manning's coefficient is required, meaning that the calibration process should be done on the two parameters simultaneously. In this regard, several trials for each experiment were performed, and the best calibration parameters for which the consistency between the experimental and numerical results is satisfied were selected. The results of the final calibration factors for each experiment are presented in [Table 5.5](#).

NUMERICAL SIMULATION

Table 5.5. Selected calibration parameters for each experiment.

<i>Experiment</i>	<i>Q (l/s)</i>	<i>Modified bedload factor</i>	<i>Modified Manning's coefficient (s/m^{1/3})</i>
AE1	5	1.05	0.022
AE2	5	1.1	0.022
AE5	5	1.2	0.02
AE6	7	1.7	0.016
AE7	7	1.7	0.016
AE8	7	1.75	0.0175

Looking carefully at the table, it is recognized that for the experiments with $Q = 5$ l/s the calibration parameters are almost similar so that the bedload factor is around 1.1 and the Manning's coefficient around 0.021 s/m^{1/3}. This is while for the experiments with $Q = 7$ l/s the other range of the calibration parameters is obtained, the bedload factor around 1.7 and the Manning's coefficient around 0.0165 s/m^{1/3}. Therefore, one may conclude that in order to predict the hydro-morphologic evolution of a channel, depending on the inflow water discharge, different formulations with different calibration factors are required. In other words, using one unique formula for different inflow discharges may result in a wrong model of the experimental works. However, to investigate more in this regard, more experiments with various water discharges should be carried out.

After applying the final calibration parameters, the model is run, and the new results are obtained. The results corresponding to the experiments AE5 and AE7 are shown in [Figures 5.10](#) to [5.13](#). Looking at both kinds of graphs (spatial and temporal evolution graphs), it is observed that there is now a good consistency between the results so that the above-mentioned 25 % difference between the experimental and numerical water surfaces in experiment AE5 has disappeared. This trend is also true for all experiments.

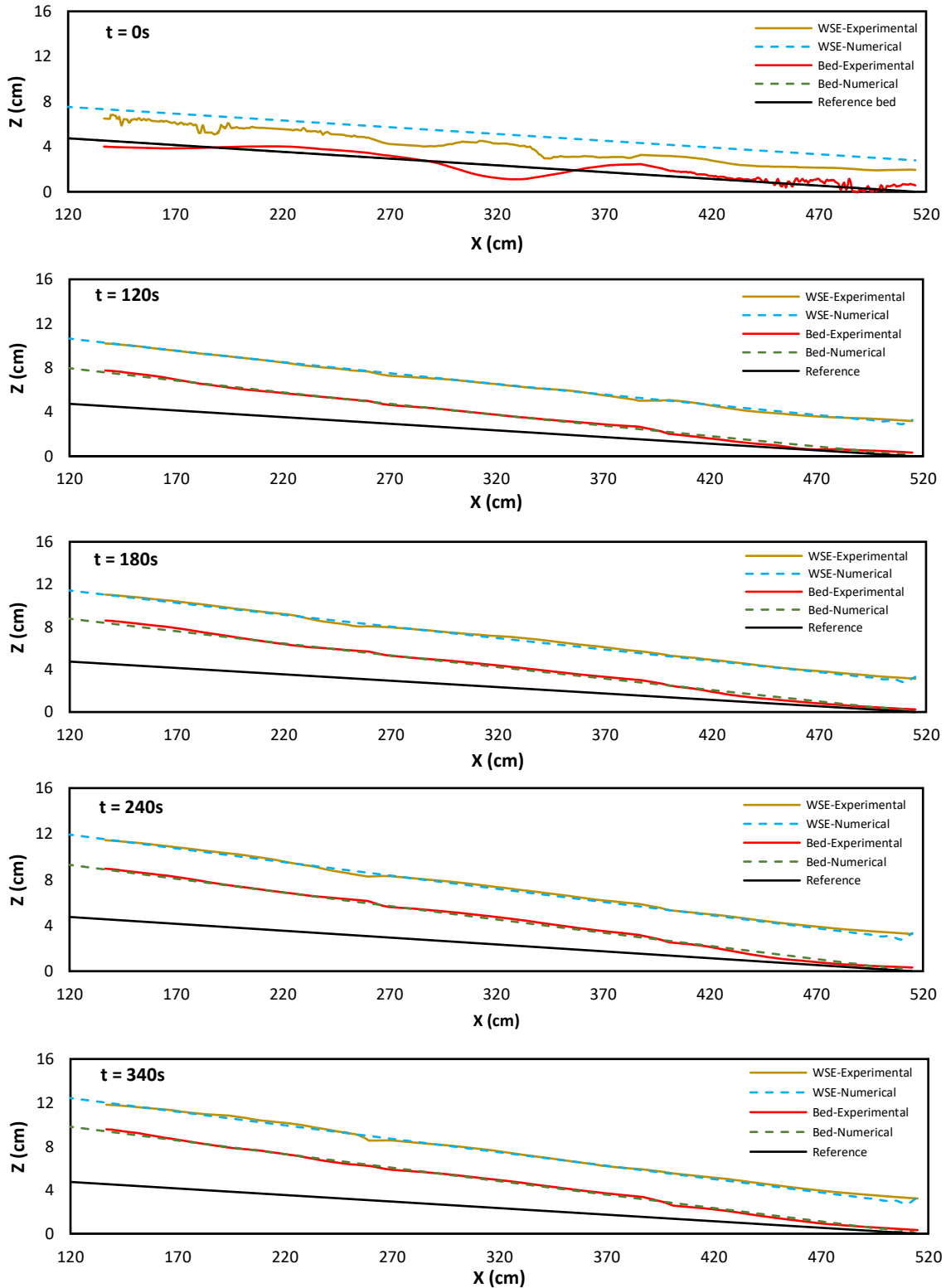


Figure 5.10. Spatial evolution of bed and water at the selected times for experiment AE5. The experimental results are compared to the numerical ones obtained by applying the final calibration parameters.

NUMERICAL SIMULATION

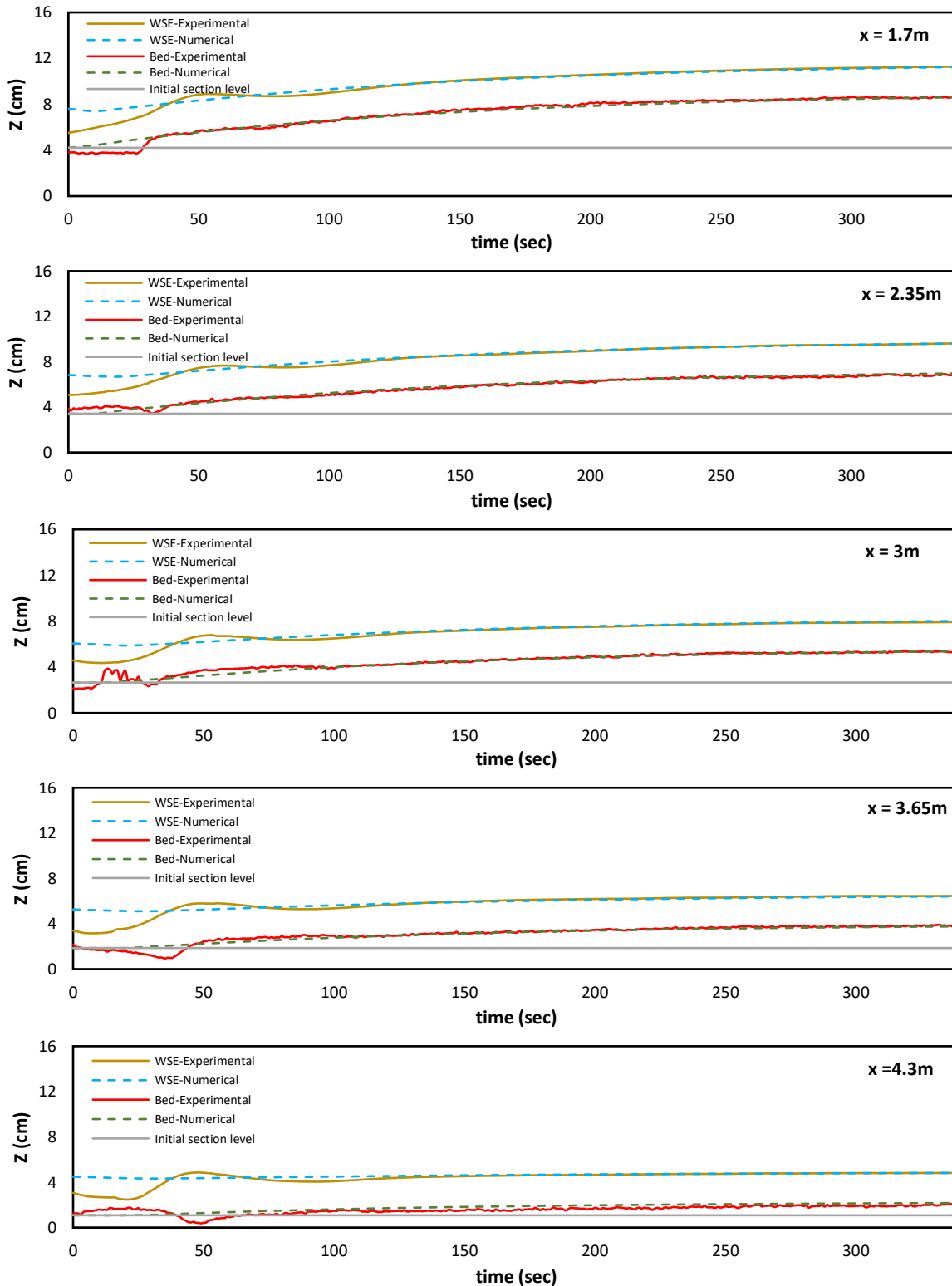


Figure 5.11. Temporal evolution of bed and water at the selected points for experiment AE5. The experimental results are compared to the numerical ones obtained by applying the final calibration parameters.

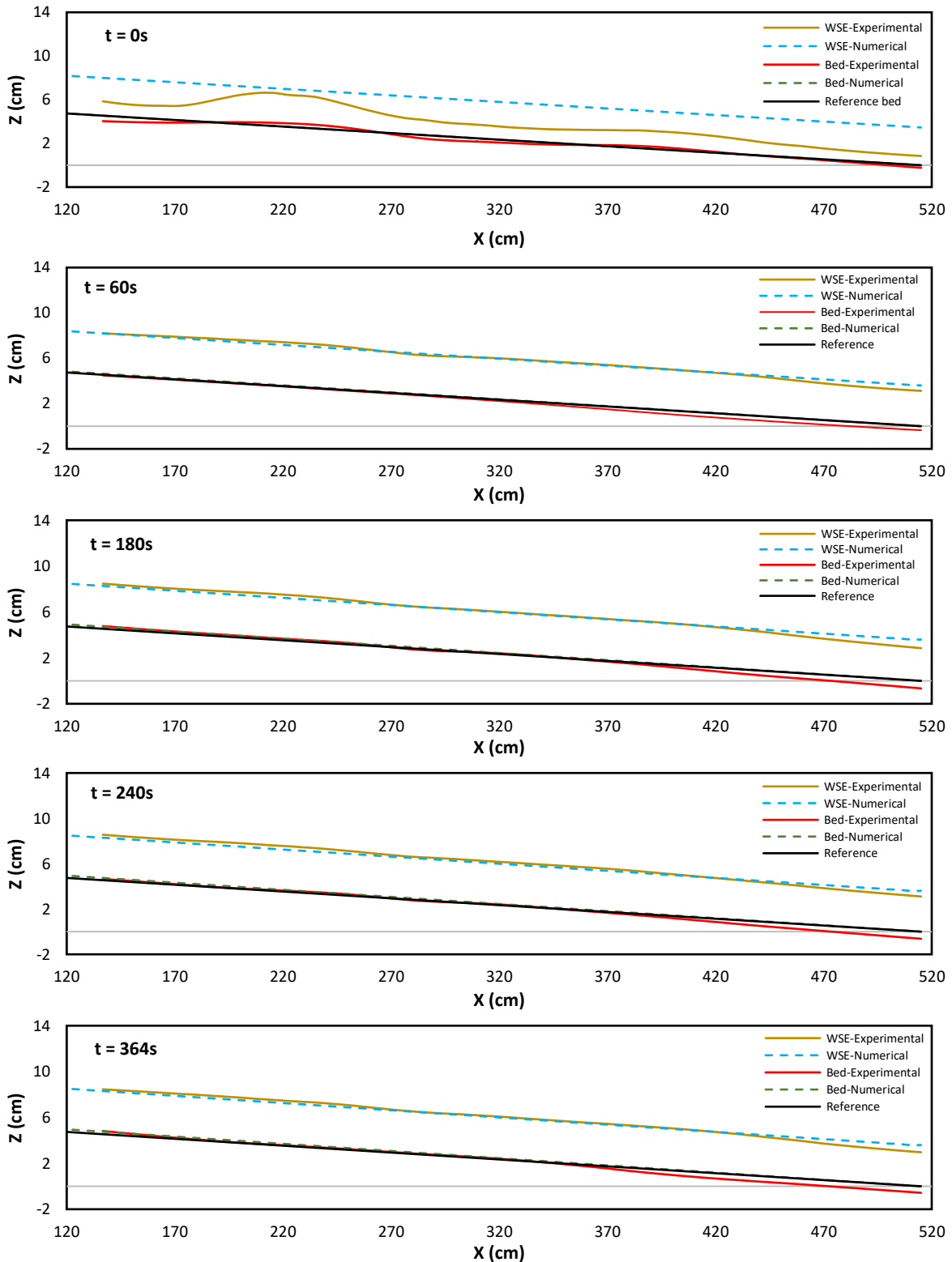


Figure 5.12. Spatial evolution of bed and water at the selected times for experiment AE7. The experimental results are compared to the numerical ones obtained by applying the final calibration parameters.

NUMERICAL SIMULATION

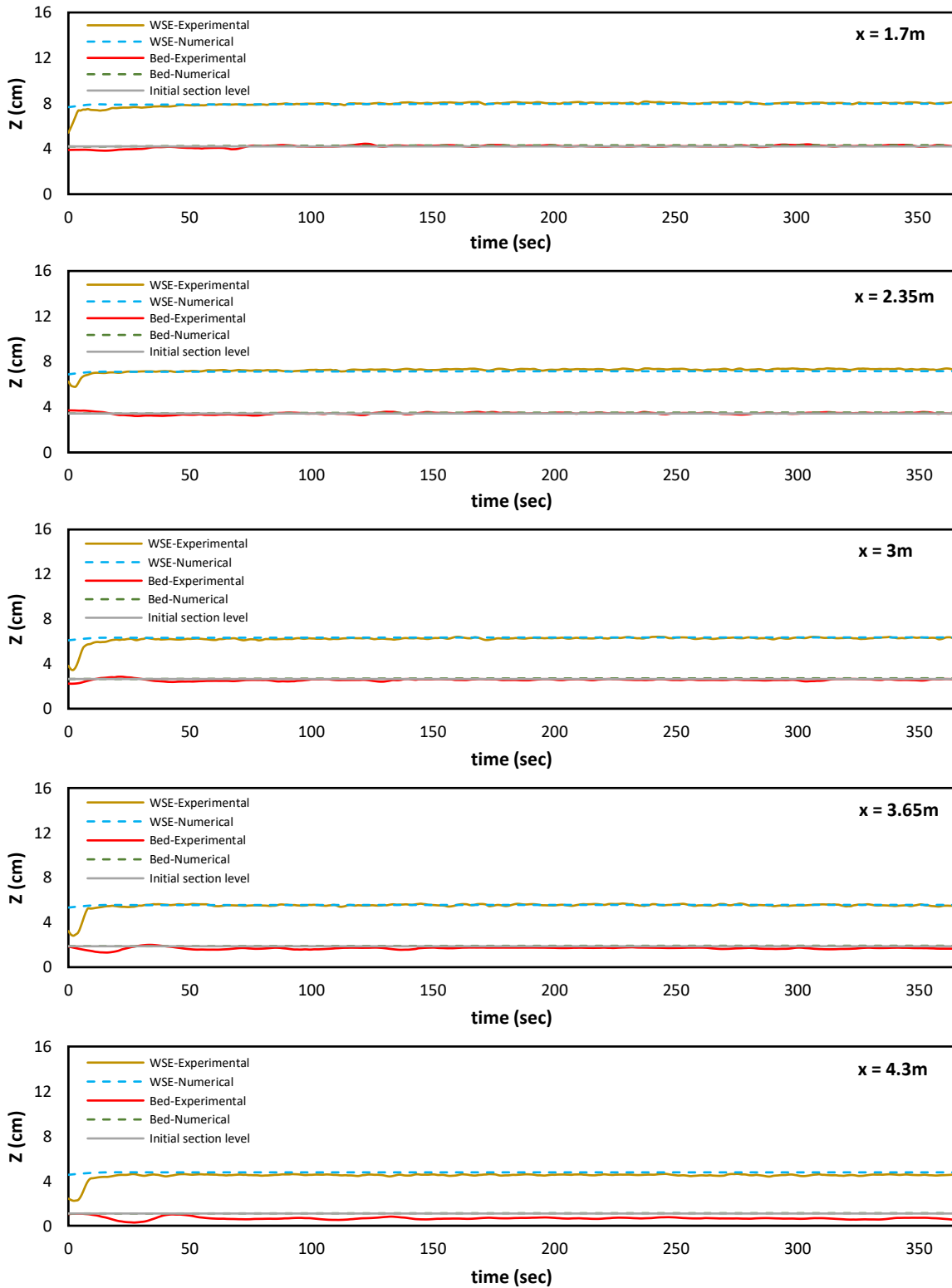


Figure 5.13. Temporal evolution of bed and water at the selected points for experiment AE7. The experimental results are compared to the numerical ones obtained by applying the final calibration parameters.

By investigation of the results, one can understand that even after the final calibration, there is a difference between numerical and experimental bed at the downstream part of the channel. In Figures 5.14 and 5.15, this discrepancy for experiment AE7 is shown.

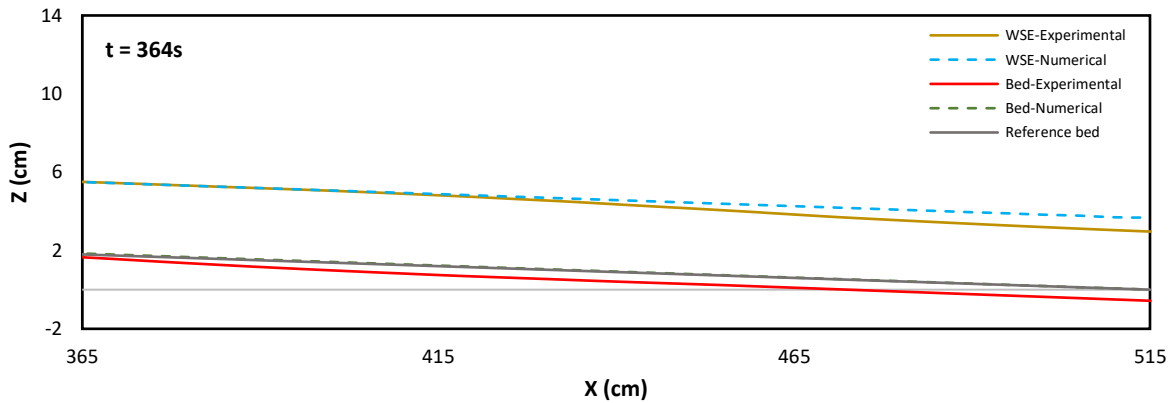


Figure 5.14. Spatial evolution of bed and water at the downstream part for experiment AE7.

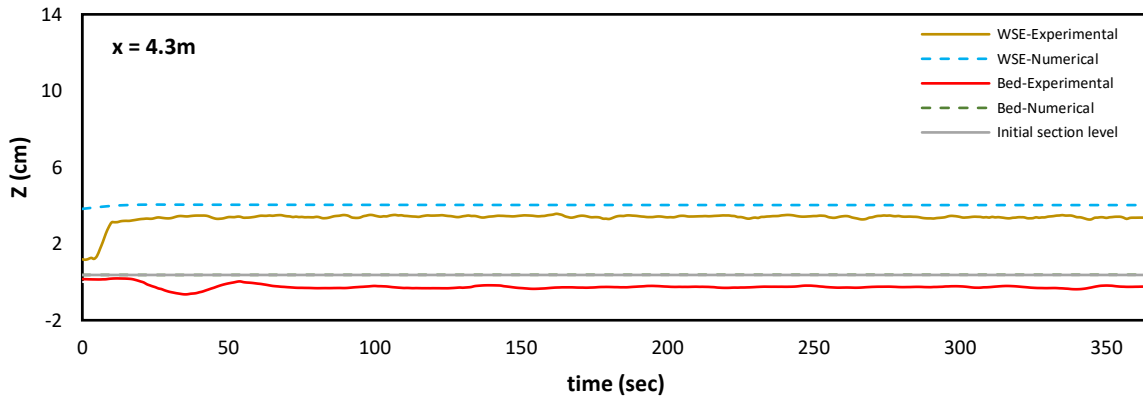


Figure 5.15. Temporal evolution of bed and water at the point 4.3 m far from the upstream, for experiment AE7.

As it is observed, while a degradation phenomenon occurs at the downstream part of the experimental bed, it does not happen in the numerical one. This discrepancy in most experiments is evident. The reason refers to the different downstream boundary conditions defined in the numerical model with respect to the existing one in the experimental work. As it was explained in chapter 4.2.1, the presence of the transverse sill at the outlet of the channel eventually leads to a degradation pattern at the downstream part of the bed. This is while in the numerical model, by applying the “IODown” option, all sediment entering the last computational section leaves the section through the downstream boundary, resulting in the imposition of a fixed bed elevation at the end of the simulated channel. Therefore, the effect of the wooden plate is not considered in the numerical simulations; as a result, different behavior is observed between the numerical and experimental results at the downstream part of the channel.

The other issue which is realized from the graphs (both before calibration and after calibration) is that at $t = 0$ the experimental water profile is much below the numerical one. In addition to

the error in water surface detection, explained in [chapter 4.2.1](#), another reason for this behavior is that at the beginning, the channel was still not in a regime condition, and the water depth was still increasing.

5.5. Discussion on the roughness of the channel

As mentioned in [chapter 5.4.2](#) and shown in [Table 5.5](#), there is a need to increase the Manning's coefficient derived by Unigarro Villota (2017) for the calibration of the numerical model. The reason for this inconsistency between Manning's coefficient values may refer to the bed and sediment condition of the channel. Unigarro Villota derived this coefficient with the clear-water flow over a fixed bed and also with the movable bed, but sediment transport did not occur due to the low water discharge. This is while in this study, there is an upstream sediment feed on a mobile bed, leading to the occurrence of sediment transport in the channel. As a result, one may infer that the same value for the Manning's coefficient obtained in clear-water flow with no sediment transport could not be used when dealing with bed mobility and sediment transport phenomenon; For instance, it was observed that the presence of the sediment transport resulted in a need to a Manning's coefficient equal to $0.02 \text{ s/m}^{1/3}$ in the experiment AE5, while Unigarro Villota proposed a value equal to $0.015 \text{ s/m}^{1/3}$ for this coefficient. Also, there are other researches in conformity with this inference; several studies show that the flow resistance over the mobile bed and in the presence of sediment transport is higher compared to those in clear-water flows and over the fixed bed (Gust and Southard 1983; Z. Wang and Larsen 1994; Best et al. 1997; Song, Chiew, and Chin 1998; Calomino, Gaudio, and Miglio 2004; Gaudio, Miglio, and Calomino 2011). Indeed, the sediments in motion cause more energy loss through the work of drag and lift force; as a result, it leads to higher roughness felt by flow (Owen 1964; Ferreira et al. 2012).

However, looking carefully at [Table 5.5](#), it is observed that the required Manning's coefficient for the experiments with $Q = 7 \text{ l/s}$ is significantly lower than the ones corresponding to the experiments with $Q = 5 \text{ l/s}$. For instance, for experiment AE6, it is observed that the needed Manning's coefficient is equal to $0.016 \text{ s/m}^{1/3}$ which it is somehow close to the Unigarro Villota's value. Therefore, one may conclude that depending on the flow condition, the presence of the sediment transport may not lead to the increase in the Manning's coefficient. Also, there are other studies suggesting that the bedload transport causes a decrease in flow resistance; consequently, the streamwise velocity increases. For example, it was reported by Nikora and Goring (2000) that the weak gravel transport as a bedload in the channel could cause an increase in streamwise velocity.

The other issue in this regard refers to the methods applied for bed detection. Comparing the methods used by the previous thesis work for bed detection (Heydari 2020) with the one corresponding to the present work, it is observed that the previous method returns a higher bed elevation and, consequently, a lower water depth (see [chapter 2.2.2.3](#)). This means that using

the previous method for bed detection may not result in a need to increase the Manning's coefficient proposed by Unigarro Villota. Therefore, from this comparison, one would conclude that there is an interplay between the bed definition and a best-fit roughness coefficient.

In conclusion, as it is observed, the subject of the channel roughness is a complex matter, and it becomes more complicated in the presence of sediment transport. The presence of the sediment transport in the experiments with lower Q resulted in a higher Manning's coefficient compared to the clear-water condition. This is while in experiments with higher Q , the presence of the sediment transport does not lead to a significant change in the Manning's coefficient obtained from the clear-water condition. Also, it was concluded that the selection of the Manning's coefficient, when dealing with sediment transport phenomenon, might depend on the bed definition. However, the purpose of this thesis work is not to solve this problem, but this discussion is an interesting subject stimulating further analyses of the issue.

CHAPTER 6

SUMMARY AND CONCLUSIONS

SUMMARY AND CONCLUSIONS

The hydro-morphologic state of a river depends on many parameters, most importantly on characteristics of the riverbed, for example, the bed slope, cross-section, sediment size, and density, and it is also dependent on the water and sediment inflow discharge. Since a river, as a part of the natural system, tends to reach an equilibrium condition, any perturbation of the above-mentioned parameters can cause the river to adapt itself to the new condition. The sediment transport phenomenon is of high importance in mountain rivers because of the geomorphological characteristics of mountain areas. Higher slopes and the higher rate of precipitation in mountain areas can cause more erosion and landslides, which are some of the important sources of the sediment inflow to the rivers. Life in the mountain areas is not without danger since an erosional reach can undermine the structures, and a depositional reach can increase the flood water levels in the river; as a result, it increases the flood hazard. Therefore, the existence of warning systems and protection measures is essential for the purpose of risk mitigation in the mountain areas. Studying the sediment transport phenomenon can help understand more about this source of hazard, leading to take proper actions and measures in order to mitigate the related existent risk in the area. Some critical factors for introducing hazard warning systems and protection methods in these areas are identification of the amount of precipitation, the quantity of sediment transferred downstream, and the aggradation height. In addition, in hazard studies, the time scales of the aggradation process are another important factor for planning the mitigation measures in case of any adverse events; thus, it is essential to study the celerity of the aggradation wave.

The main goal of this thesis is to analyze the aggradation process in supercritical flow regimes by studying the sediment front characteristics such as sediment front propagation celerity and its corresponding height. This study is done by performing experiments in the Mountain Hydraulics Lab of the Politecnico di Milano, located in the Lecco campus. The current study is the continuation of the previous thesis (Heydari 2020) with updating some of the measurement methods, developing a new method for analyzing the celerity of the aggradation wave, and introducing a new type of experiments for estimation of sediment transport capacity (Q_s) of the channel (SC experiments). In this campaign, eight aggradation experiments (AE experiments) and three SC experiments are performed; the first three AE experiments (AE1 to AE3) were performed in the previous thesis, and they are reanalyzed in the current thesis with the updated methods. In all the experiments, the properties of the channel and sediment material remain constant, and the experiments are performed with different water and sediment inflow discharges.

For performing the experiments, first, the water discharge (Q) is set on a specific value, then the hopper starts feeding the channel with sediment particles at a specific rate. The hopper's vibration channel is monitored with a camera, and its sediment feeding rate is measured by processing the frames of the recorded video through the Particle Image Velocimetry (PIV method) to obtain the temporal evolution of the particle velocity on the vibrating channel. The obtained values of the velocity are translated into sediment inflow discharge (Q_{sin}) through a

transfer function. For obtaining the transfer function, a preliminary campaign is run by performing several experiments to find a relationship between the velocity of the particles on the vibrating channel (u), and their corresponding sediment inflow discharges; then, these data are interpolated with a second-degree polynomial to define the Q_{sin} as a function of u . The channel's bed elevation changes during the experiment because of the aggradation phenomenon; since the bed and water elevation is changing over time, it is needed to detect their surface in different time instants for further analyses. For detection of the bed and water surface, the channel is monitored with several cameras, and the frames of recorded videos are processed with a motion detection algorithm. After detecting the bed and water surface on the photos, they must be referenced to change their coordinates from the pixel scale into a metric scale. Since each section of the channel is monitored by a camera separately, these processes must be done on the recorded frames of each camera; then, the resulted data must be regrouped to produce the bed, and water surface profiles for the whole monitored part of the channel in different time instants. During the experiments, some of the sediments are deposited inside the channel, and the others get out of the channel through the outlet and trapped into the collectors. The first collector is monitored with a camera to measure the amount of sediments trapped into the collector in each instant of time; these data are needed for further analyses of initial sediment transport capacity (Q_{s0}).

In order to have an aggradation phenomenon in the channel, it is needed to feed it with a loading ratio ($Lr = Q_{sin}/Q_{s0}$) higher than one, so the initial sediment transport capacity must be estimated. Since the characteristics of the channel and the sediment particles are similar in all of the experiments, the only factor that can change the Q_{s0} is the water discharge. In this campaign, AE experiments are run with two different water discharges, $Q = 5 \text{ l/s}$, and $Q = 7 \text{ l/s}$; therefore, the Q_{s0} must be estimated for each water discharge by performing SC experiments. To estimate the Q_{s0} related to a specific water discharge, an SC experiment is run with an initial sediment feeding rate by setting the vibration level selector of the hopper on a specific value, and then, based on the evolution of the channel bed, the vibration level is changed to finally find a feeding rate which corresponds to the equilibrium condition. When the channel is in equilibrium condition ($Lr = 1$), whatever gets into the channel, gets out from the outlet; as a result, the feeding rate corresponding to the equilibrium condition shows the initial sediment transport capacity of the channel. Apart from SC experiments, three other methods, the Meyer-Peter and Müller formula, monitoring, and collector method, are used for the estimation of Q_{s0} .

The first method to estimate Q_{s0} is to use one of the most common formulas in this regard, represented by Meyer-Peter and Müller formulae in 1948. The other method is the monitoring method which is based on the mass conservation law. In this method, the initial sediment transport capacity is obtained by subtracting the calculated initial sediment deposition rate from the sediment feeding rate. The last method is the collector method. Based on the concept of the sediment transport capacity, the deposition rate of the sediment particles trapped into the

SUMMARY AND CONCLUSIONS

collector at the initial times of the experiment gives the initial sediment transport capacity. It should be mentioned that the Q_{s0} corresponding to each water discharge is calculated by averaging the results of the monitoring method, collector method, and SC experiments. The values of Q_{s0} related to the water discharges of 5 l/s and 7 l/s are obtained equal to $8.31 \times 10^{-5} \text{ m}^3/\text{s}$ and $1.33 \times 10^{-4} \text{ m}^3/\text{s}$, respectively.

Besides the need for Q_{s0} to estimate the value of Lr , the determination of Q_{s0} provides some values for a $Q - Q_{s0}$ correspondence; even if this is not crucial for the analysis of the AE experiments, it may be used to estimate the value of the critical water discharge (Q_c). In order to determine the critical water discharge corresponding to the threshold condition of the sediment motion, different trials are performed. First, the value of Q_c is estimated by applying the Brownlie and the Van Rijn approaches, obtaining Q_c equal to 0.563 l/s and 0.456 l/s, respectively. Since these values are extremely small, performing a preliminary campaign to estimate Q_c is infeasible. The other trial to estimate the critical water discharge is to use $\Phi - Q/Q_c$ graph, which its data come from the previous experimental campaigns carried out in the Politecnico di Milano. In this regard, the values of Q_{s0} obtained in the previous part are transformed to Φ , the dimensionless sediment transport capacity of the channel per unit width, then it is put on the graph, and finally by an extrapolation operation, the value of Q/Q_c is estimated. Different trials with different extrapolation functions are performed, and the final value of the critical water discharge is estimated as an average of all trials and equal to 0.907 l/s. However, this value is largely uncertain because a large range of values is obtained for Q_c using different trials (between 0.456 l/s and 1.542 l/s).

The experiments AE1 to AE5 and AE6 to AE8 are performed with the water discharges of 5 l/s and 7 l/s, respectively. The only parameter that is changed for the AE experiments with the same water discharges is their sediment inflow discharge, so by having their Q_{s0} , the loading ratio is calculated for each experiment. By analyzing the temporal and spatial evolution of the bed and water surfaces, consistency between the results can be observed since in the experiments with the loading ratio close to one, equilibrium condition can be seen almost from the beginning; also, for the experiments with the same water discharge, more aggradation happens when the loading ratio is higher. Another observation from these results is that the aggradation at the upstream part of the channel is higher compared to the downstream part of the channel leading to an increase in the bed slope over time, which is because of the tendency of the channel to reach an equilibrium condition. In all of the experiments except AE5, degradation can be observed close to the outlet which is because of the effect of the transverse sill located at the outlet. In experiment AE5, degradation did not occur due to its higher loading ratio that overcomes the effect of the transverse sill.

For better analysis of the data related to the bed and water surface elevations, two matrices are created separately for each experiment in a way that each array of them shows the elevation of

the profiles in a specific section and time. The rows of each matrix show the time, and the columns represent the location of the sections.

The Froude number evolution matrix is obtained by using the bed and water surface evolution matrix. By mapping the matrices with color gradient graphs, it is observed that the experiments with water discharge of 5 l/s are in subcritical regime except for the experiment AE5 and the experiments with water discharge of 7 l/s are in the supercritical regime. This is in contradiction with the previous study (Heydari 2020) since the flow regimes in the experiments AE1 to AE3 were reported to be supercritical, while in this study, calculations show they are in the subcritical regime. The reason for this contradiction refers to the fact that in the previous thesis, the bedload layer surface was detected as the bed surface, while in this study, the surface of the stationary part of the bed is considered to be the bed surface. Therefore, the water depth calculated with the previous method is lower than the new one, so the flow velocity and Froude number are calculated higher compared to the current study. The flow in experiment AE5 is subcritical at the beginning, but it changes to supercritical after a while; this is because in this experiment, the loading ratio is very high, so it causes the bed slope to increase significantly; as a result, the flow regime changes from subcritical to supercritical.

Since the aggradation happens in a dispersive way when dealing with higher flow velocities, it gets difficult and almost impossible to detect any aggradation front; therefore, it is not possible to obtain a sediment front celerity by studying the sediment front location in different time instants. To overcome this problem, the bed evolution matrix is used. An aggradation height is chosen, and then the matrix is searched for values almost equal to the chosen aggradation height, and their corresponding times and coordinates are extracted. The extracted data are mapped in a way that the x -axis and y -axis represent the time and the coordinate, respectively. The celerity is obtained by fitting a linear function to the initial part of the graph. In the current study, the mentioned procedure is done for different aggradation heights equal to 2, 2.5, 3, 3.5, and 4 particle sizes (1 *particle size* = 3.8 mm). Because of the higher aggradation in the experiments AE1, AE5, AE6, and AE8, they are chosen for estimation of their celerity. After analyzing the results, it is concluded that the loading ratio, water discharge, and aggradation height are three effective parameters for the celerity of the aggradation wave in a way that by increasing the loading ratio and water discharge, the celerity for the same aggradation height increases, while higher aggradation height travels with a lower celerity. These findings are confirming the translational behavior of the aggradation process. It should be mentioned that water discharge and loading ratio are external controls, while the aggradation height is an operational variable that is part of the process. Another important conclusion from the results is that the gradient of normalized celerity with respect to the normalized aggradation height depends on the water discharge. To elaborate more on this conclusion, let's assume that the celerity values corresponding to the aggradation heights of h_1 and h_2 are C_1 and C_2 , respectively. The ratio

SUMMARY AND CONCLUSIONS

between C_1 and C_2 (C_2/C_1) is almost the same for experiments with the same water discharges and different loading ratios, and by increasing the water discharge, this ratio increases.

The aggradation process investigated experimentally is also studied with a numerical modeling approach. The software used to implement the numerical model is BASEMENT which numerically solves the hydro-morphologic system of PDEs, including two SVEs and one Exner equation. The numerical model simulates the aggradation process with the same characteristics of the experimental channel, such as the same geometry, sediment material, water discharge, etc. The boundary conditions imposed in the numerical model are similar to those existing in the physical one; the water discharge and sediment inflow discharge are assigned to the upstream boundary, while the water and bed elevations are imposed on the downstream boundary. By comparing the imposed boundary condition in the numerical model with the theoretical solution in a supercritical regime, it is concluded that the only useless boundary condition required by the software is the water elevation in the downstream part of the channel; the software calculates the water depth by introducing the slope at the upstream and using a flow resistance law for a uniform flow.

The numerical model is performed for all experiments except AE3 and AE4. By comparing the numerical results with the experimental ones, it can be understood that there is no consistency between the results from the bed and water elevations point of view; thus, some calibrations on the numerical model are needed. The final calibration of the numerical model is done on two parameters simultaneously, bedload factor (the multiplier coefficient of the Meyer-Peter and Müller formula) and the Manning's coefficient of the channel. After several trials, the best calibration parameters are selected so that the consistency between the experimental and numerical results is satisfied. While the reference values of the bedload factor and the Manning's coefficient are equal to 1 and $0.015 \text{ s/m}^{1/3}$, respectively, for experiments with $Q = 5 \text{ l/s}$, these parameters are obtained around 1.1 and $0.021 \text{ s/m}^{1/3}$, respectively, and for experiments with $Q = 7 \text{ l/s}$ are obtained around 1.7 and $0.0165 \text{ s/m}^{1/3}$, respectively. This shows that in order to predict the hydro-morphologic evolution of a channel, using a unique calibrated formula may result in a wrong model, and depending on the water discharge, the calibration factors may vary.

There are some issues related to this work that should be handled somehow within future works. First of all, in order to validate the results of this study and also to see if any other parameters are involved in affecting the celerity of aggradation height, it is necessary to perform more experiments. In this work, the number of experiments is low due to difficulties related to performing them, and also performing this type of experiments and extracting their related data are time-consuming. The second issue is related to referencing the data related to the bed and water surface elevation detection. Despite the cameras for monitoring the channel were changed with higher quality ones, there are still some inconsistencies at the common border of profiles detected with different cameras. The elevation in the common borders must be equal in both profiles, but due to errors in referencing, they are not equal, and in some cases, the difference is

up to 0.5 *cm*. Third, In the experiments with higher water discharges, the bed is eroded significantly at the beginning before the hopper starts working; as a result, it does not let to perform experiments with higher water discharges. Also, higher loading ratios can cause problems in performing the experiments because of the possibility of the creation of a dam at the feeding point. Fourth, In these experiments, it is assumed that the channel is acting as a single reach with a uniform behavior all along the flume, while because of the transverse sill effect, the behavior of the channel is different between upstream and downstream parts. Fifth, despite performing different trials to estimate the critical water discharge, it is obtained with notable uncertainty. In order to estimate critical water discharge using the data related to the previous preliminary campaigns, it is essential to carry out different experiments with different water discharges. In this study, only two series of experiments from the water discharge point of view are performed. The last issue is Manning's coefficient issue; it is observed that there is an inconsistency between the Manning's coefficient obtained experimentally with no sediment transport condition and the ones coming from the calibration of the numerical model. In this regard, it is seen that in the experiments with the lower water discharge, the presence of the sediment transport results in a higher Manning's coefficient compared to the clear-water condition. By contrast, the presence of sediment transport in the experiments with the higher water discharge leads to a negligible change in the Manning's coefficient with respect to the clear-water condition.

BIBLIOGRAPHY

BIBLIOGRAPHY

- Alves, E, and A H Cardoso. 1999. "Experimental Study on Aggradation." *International Journal of Sediment Research* 14 (1): 1–15.
- An, Chenge, Xudong Fu, Guangqian Wang, and Gary Parker. 2017. "Effect of Grain Sorting on Gravel Bed River Evolution Subject to Cycled Hydrographs: Bed Load Sheets and Breakdown of the Hydrograph Boundary Layer." *Journal of Geophysical Research: Earth Surface* 122 (8): 1513–33.
- Armanini, Aronne, and Carlo Gregoretti. 2005. "Incipient Sediment Motion at High Slopes in Uniform Flow Condition." *Water Resources Research* 41 (12).
- Bareš, Vojtěch, Štěpán Zrostlík, Tomáš Pícek, Jan Krupička, and Václav Matoušek. 2016. "On Local Velocity Measurement in Gravity-Driven Flows with Intense Bedload of Coarse Lightweight Particles." *Flow Measurement and Instrumentation* 51 (October): 68–78.
- Bellal, Mourad. 2012. "Fluvial Morphodynamics in Super and Transcritical Flows: Experimental and Analytical Approaches." Ph. D. Thesis, University College London, London, UK.
- Best, Jim, Sean Bennett, John Bridge, and Mike Leeder. 1997. "Turbulence Modulation and Particle Velocities over Flat Sand Beds at Low Transport Rates." *Journal of Hydraulic Engineering* 123 (12): 1118–29.
- Calomino, F, R Gaudio, and A Miglio. 2004. "Effect of Bed-Load Concentration on Friction Factor in Narrow Channels." *IAHR, Editor. River Flow. IAHR, Napples*, 279–85.
- Campisano, A, P Cutore, and C Modica. 2013. "Modelling Sediment Deposit Evolution Upstream of Slit-Check Dams in Mountain Streams." In *World Environmental and Water Resources Congress 2013: Showcasing the Future*, 1757–68.
- Chanson, Hubert. 2004. *Hydraulics of Open Channel Flow*. Elsevier.
- Chaudhry, M. Hanif. 2007. *Open-Channel Flow*. Springer Science & Business Media.
- Czuba, Jonathan A, Christopher S Magirl, Christiana R Czuba, Eric E Grossman, Christopher A Curran, Andrew S Gendaszek, and Richard S Dinicola. 2011. *Sediment Load from Major Rivers into Puget Sound and Its Adjacent Waters. USGS Science for a Changing World*. US Department of the Interior, US Geological Survey.
- Dey, Subhasish. 2014. *Fluvial Hydrodynamics. Sciences-New York*. GeoPlanet: Earth and Planetary Sciences. Berlin, Heidelberg: Springer Berlin Heidelberg.
- Dey, Subhasish, Ratul Das, Roberto Gaudio, and Sujit K. Bose. 2012. "Turbulence in Mobile-Bed Streams." *Acta Geophysica* 60 (6): 1547–88.
- Ferreira, Rui M L, Mário J Franca, João G A B Leal, and António H Cardoso. 2012. "Flow over Rough Mobile Beds: Friction Factor and Vertical Distribution of the Longitudinal Mean Velocity." *Water Resources Research* 48 (5).
- Fondriest Environmental. 2014. "Sediment Transport and Deposition." *Fundamentals of Environmental Measurements*. 2014.

-
- Gaudio, Roberto, Antonio Miglio, and Francesco Calomino. 2011. "Friction Factor and von Kármán's κ in Open Channels with Bed-Load." *Journal of Hydraulic Research* 49 (2): 239–47.
- Goutière, Laurent, Sandra Soares-Frazão, C. Savary, T. Laraichi, and Yves Zech. 2008. "One-Dimensional Model for Transient Flows Involving Bed-Load Sediment Transport and Changes in Flow Regimes." *Journal of Hydraulic Engineering* 134 (6): 726–35.
- Gust, Giselher, and John B Southard. 1983. "Effects of Weak Bed Load on the Universal Law of the Wall." *Journal of Geophysical Research: Oceans* 88 (C10): 5939–52.
- Gyr, Albert, and Klaus Hoyer. 2006. *Sediment Transport: A Geophysical Phenomenon*. *Sediment Transport: A Geophysical Phenomenon*. Vol. 82. Springer Netherlands.
- Haan, C.T., B.J. Barfield, and J.C. Hayes. 1994. "Sediment Properties and Transport." In *Design Hydrology and Sedimentology for Small Catchments*, 204–37. Elsevier.
- Heydari, Ehsan. 2020. "Experimental Analysis of Channel Overloading in Supercritical Condition."
- Jain, Subhash C. 1981. "River Bed Aggradation Due to Overloading." In *Journal of the Hydraulics Division, Proceedings of the American Society of Civil Engineers*. Vol. 107.
- Krumbein, William Christian. 1941. "Measurement and Geological Significance of Shape and Roundness of Sedimentary Particles." *Journal of Sedimentary Research* 11 (2): 64–72.
- Langmaak, Kai Rainer. 2013. "INCIPIENT MOTION OF RIPRAP ON STEEP SLOPES."
- Lyn, Dennis A., and M. Altinakar. 2002. "St. Venant–Exner Equations for Near-Critical and Transcritical Flows." *Journal of Hydraulic Engineering* 128 (6): 579–87.
- Lyn, Dennis A. 1987. "Unsteady Sediment-Transport Modeling." *Journal of Hydraulic Engineering* 113 (1): 1–15.
- McNally, W H, and A J Mehta. 2009. "Sediment Transport in Estuaries." In . EOLSS Publications Oxford.
- Miglio, A, R Gaudio, and F Calomino. 2009. "Mobile-Bed Aggradation and Degradation in a Narrow Flume: Laboratory Experiments and Numerical Simulations." *Journal of Hydro-Environment Research* 3 (1): 9–19.
- Nakagawa, Hiroji, Tetsuro Tsujimoto, and Yoshihiko Shimizu. 1991. "Turbulent Flow with Small Relative Submergence." In *Fluvial Hydraulics of Mountain Regions*, 33–44. Springer.
- Nikora, Vladimir, and Derek Goring. 2000. "Flow Turbulence over Fixed and Weakly Mobile Gravel Beds." *Journal of Hydraulic Engineering* 126 (9): 679–90.
- Owen, P Rr. 1964. "Saltation of Uniform Grains in Air." *Journal of Fluid Mechanics* 20 (2): 225–42.
- Pfeiffer, Allison, Katherine Barnhart, Jonathan Czuba, and Eric Hutton. 2020. "NetworkSedimentTransporter: A Landlab Component for Bed Material Transport through River Networks." *Journal of Open Source Software* 5 (53): 2341.
- Radice, Alessio, and Francesco Ballio. 2008. "Double-Average Characteristics of Sediment Motion
-

BIBLIOGRAPHY

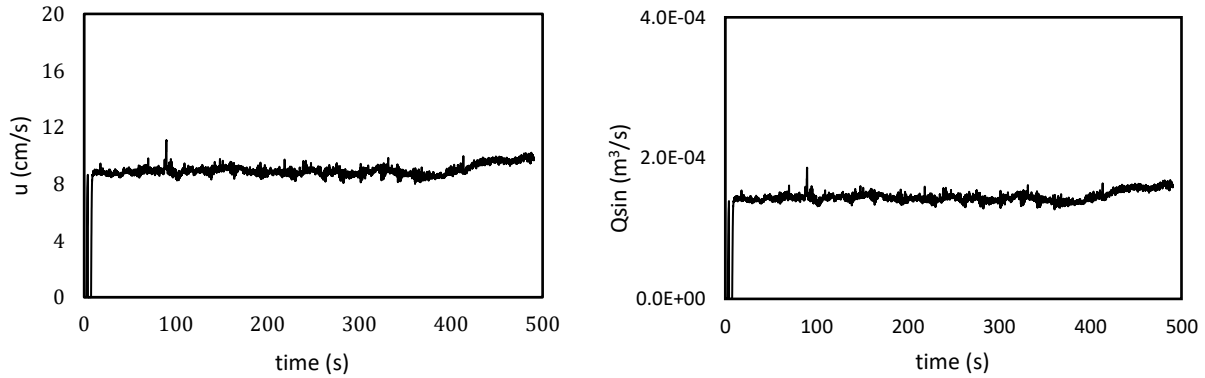
- in One-Dimensional Bed Load." *Acta Geophysica* 56 (3): 654–68.
- Shields, Albert. 1936. "Application of Similarity Principles and Turbulence Research to Bed-Load Movement."
- Simões, Francisco J.M. M. 2014. "Shear Velocity Criterion for Incipient Motion of Sediment." *Water Science and Engineering* 7 (2): 183–93.
- Song, T, Y M Chiew, and C O Chin. 1998. "Effect of Bed-Load Movement on Flow Friction Factor." *Journal of Hydraulic Engineering* 124 (2): 165–75.
- Soni, J P. 1975. "Aggradation in Streams Due to Increase in Sediment Load." Ph. D., Thesis, University of Roorkee, Roorke (UP).
- Southard, J.B. 2019. *Introduction to Fluid Motions and Sediment Transport. Book.*
- Switzer, Adam D. A.D. 2013. "Measuring and Analyzing Particle Size in a Geomorphic Context." *Treatise on Geomorphology* 14 (March 2013): 224–42.
- Unigarro Villota, Stefania. 2017. "Laboratory Study of Channel Aggradation Due to Overloading."
- Wadell, Hakon. 1932. "Volume, Shape, and Roundness of Rock Particles." *The Journal of Geology* 40 (5): 443–51.
- Wang, Yu Hai, and Guo Hua Yu. 2007. "Velocity and Concentration Profiles of Particle Movement in Sheet Flows." *Advances in Water Resources* 30 (5): 1355–59.
- Wang, Zhaoyin, and Peter Larsen. 1994. "Turbulent Structure of Water and Clay Suspensions with Bed Load." *Journal of Hydraulic Engineering* 120 (5): 577–600.
- Wu, Weiming, Wolfgang Rodi, and Thomas Wenka. 2000. "3D Numerical Modeling of Flow and Sediment Transport in Open Channels." *Journal of Hydraulic Engineering* 126 (1): 4–15.
- Yen, Chin-lien, Shou-young Chang, and Hong-Yuan Lee. 1992. "Aggradation-Degradation Process in Alluvial Channels." *Journal of Hydraulic Engineering* 118 (12): 1651–69.
- Zanchi, Barbara. 2018. "Indagine Sperimentale Sul Fenomeno Di Deposito in Un Canale a Fondo Mobile Sovralimentato."
- Ziegler, Alan D., R.C. Sidle, Valerie X.H. Phang, Spencer H. Wood, and Chatchai Tantasirin. 2014. "Bedload Transport in SE Asian Streams—Uncertainties and Implications for Reservoir Management." *Geomorphology* 227 (December): 31–48.
- Zucchi, Matteo. 2018. "Experimental and Numerical Study of Channel Aggradation," January.

APPENDIX

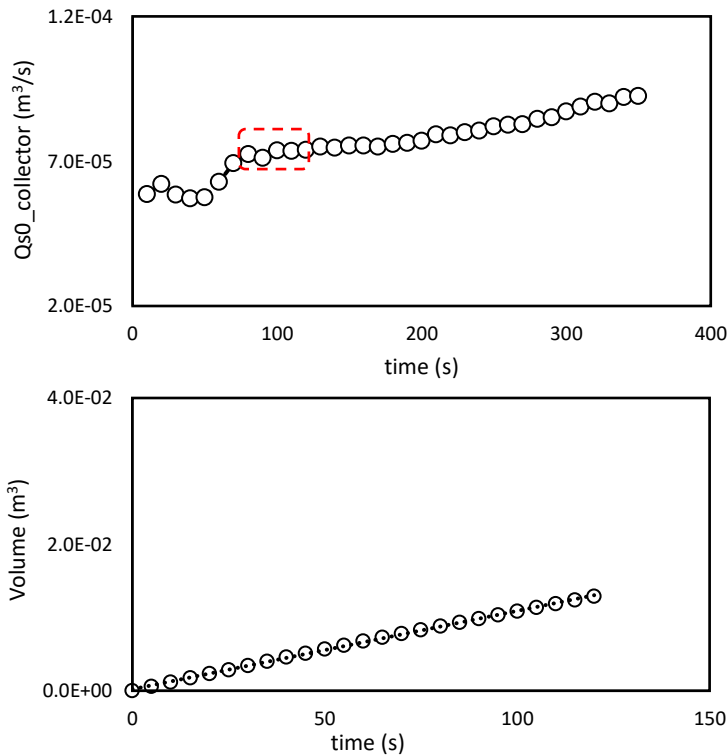
Experiment AE1

T (s)	S ₀ (%)	Q (l/s)	h ₀ (cm)	Fr	Vibration level	Q _{sin} (m ³ /s)	Q _{s0} (m ³ /s)	Q _{sin} /Q _{s0}
490	1.2	5	2.78	1.14	8	1.42E-04	8.31E-05	1.7

AE1.1. Experimental parameters

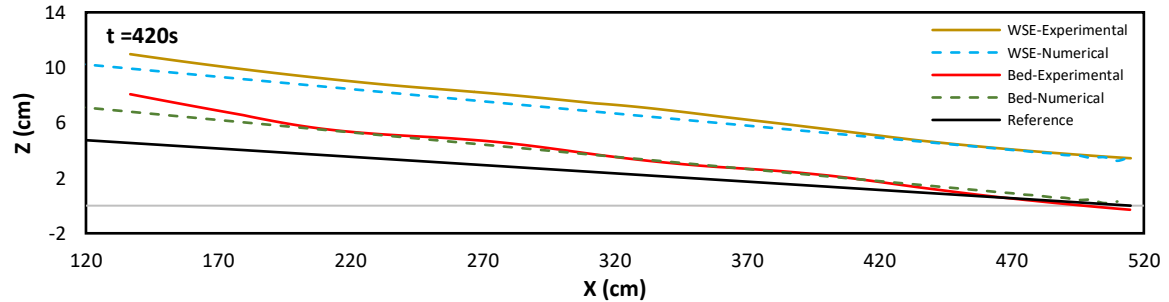
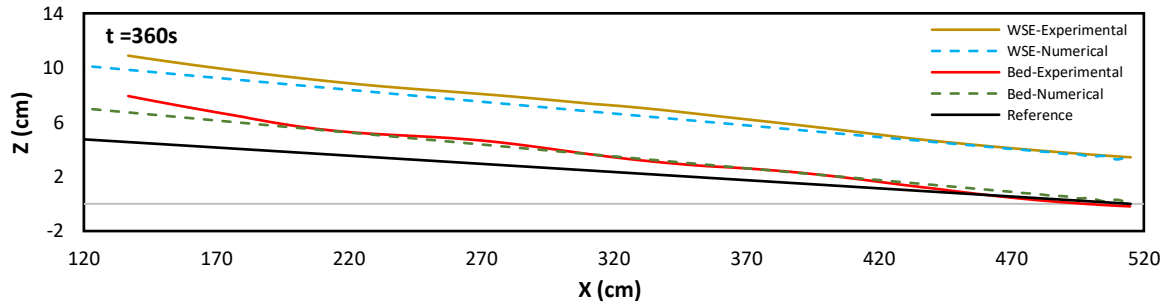
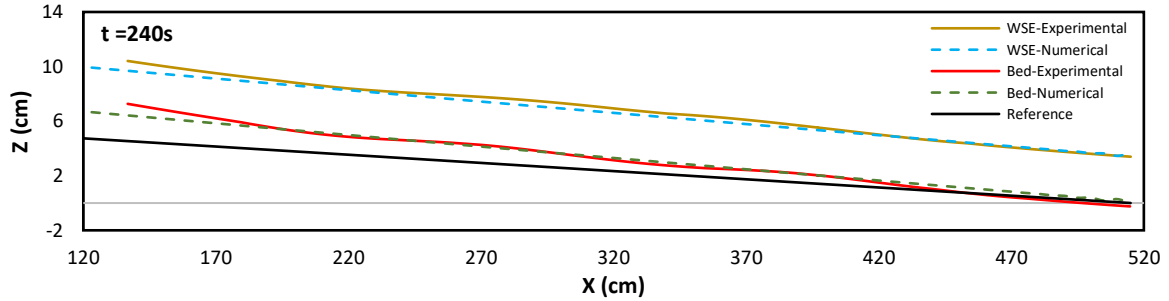
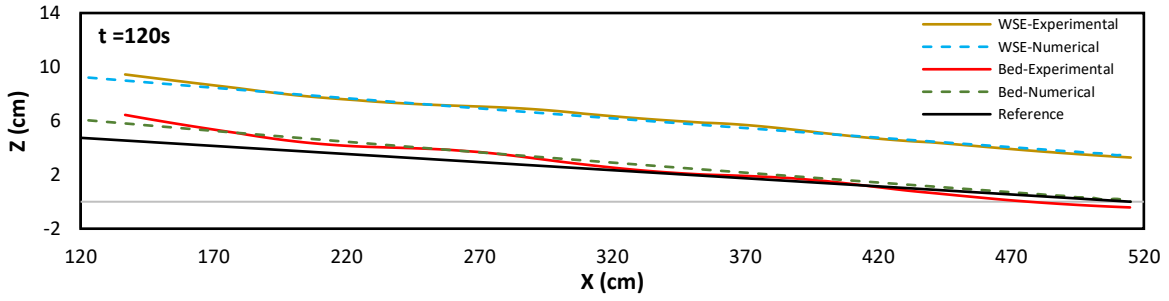
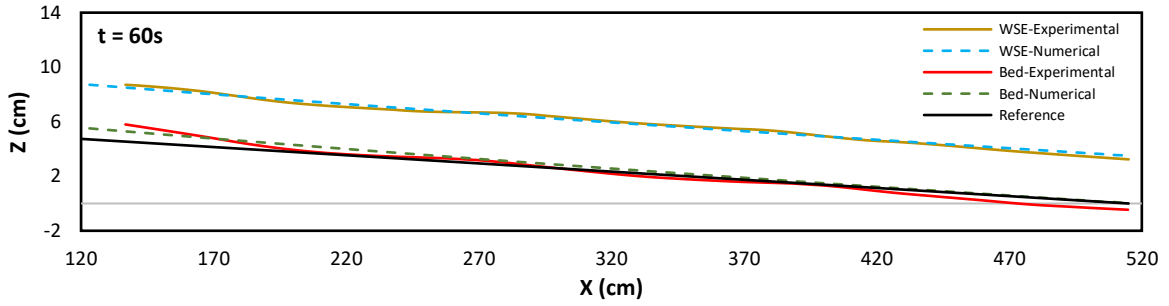


AE1.2. Temporal evolution of velocity and sediment discharge for the inflow material



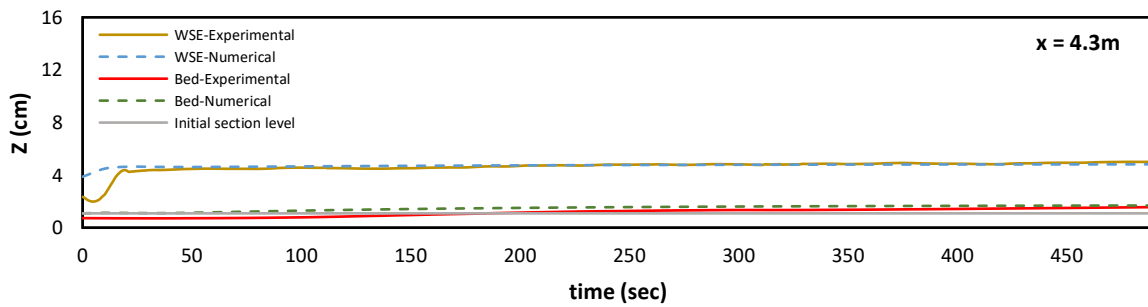
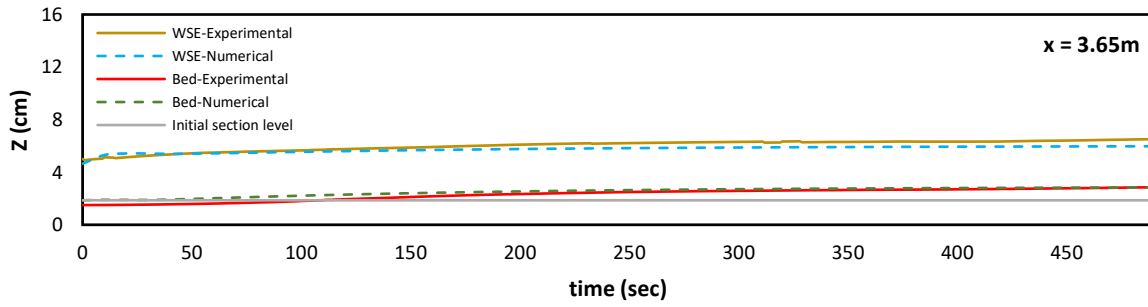
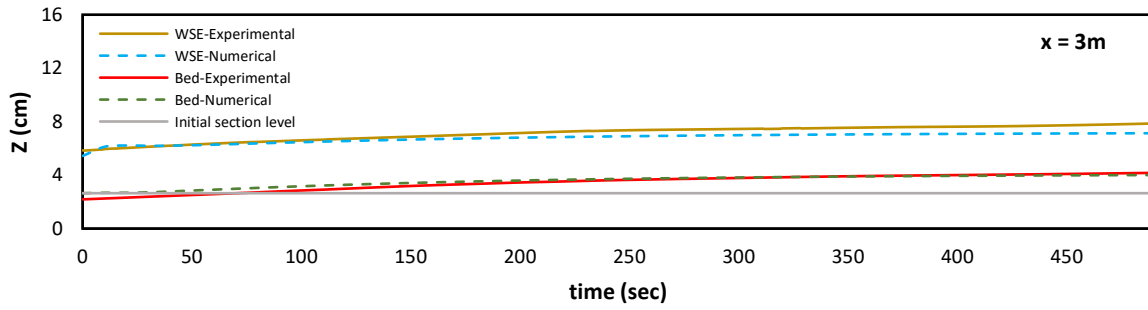
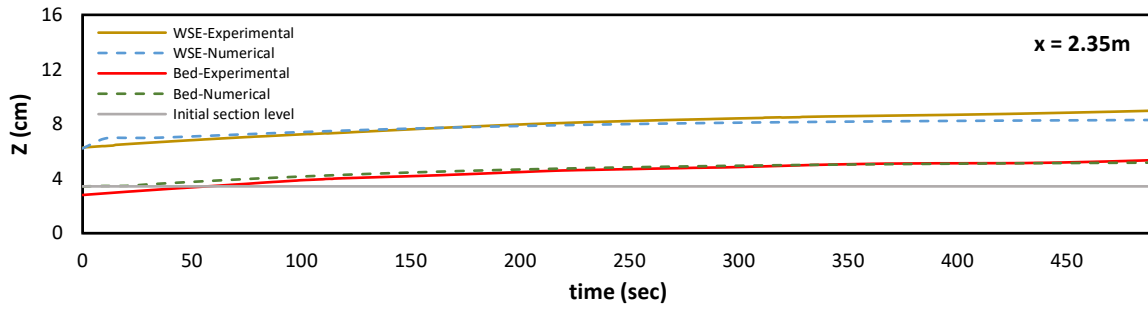
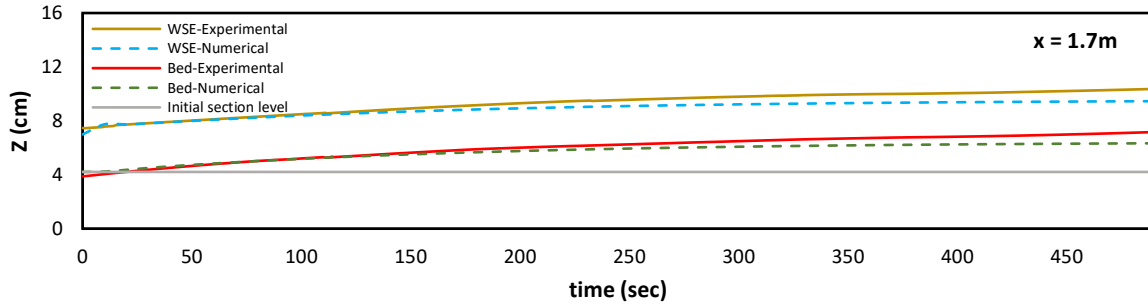
AE1.3. $t - Q_{s0, collector}$ graph, presenting the sediment transport capacity over time, computed using collector method. The average of the constant values of Q_{s0} is considered as the $Q_{s0, collector}$.

AE1.4. t - volume graph, presenting the volume of sediment deposited in the channel with the assumption of constant profile at the upstream. The slope of the interpolating line is used to calculate $Q_{s0, monitored}$.

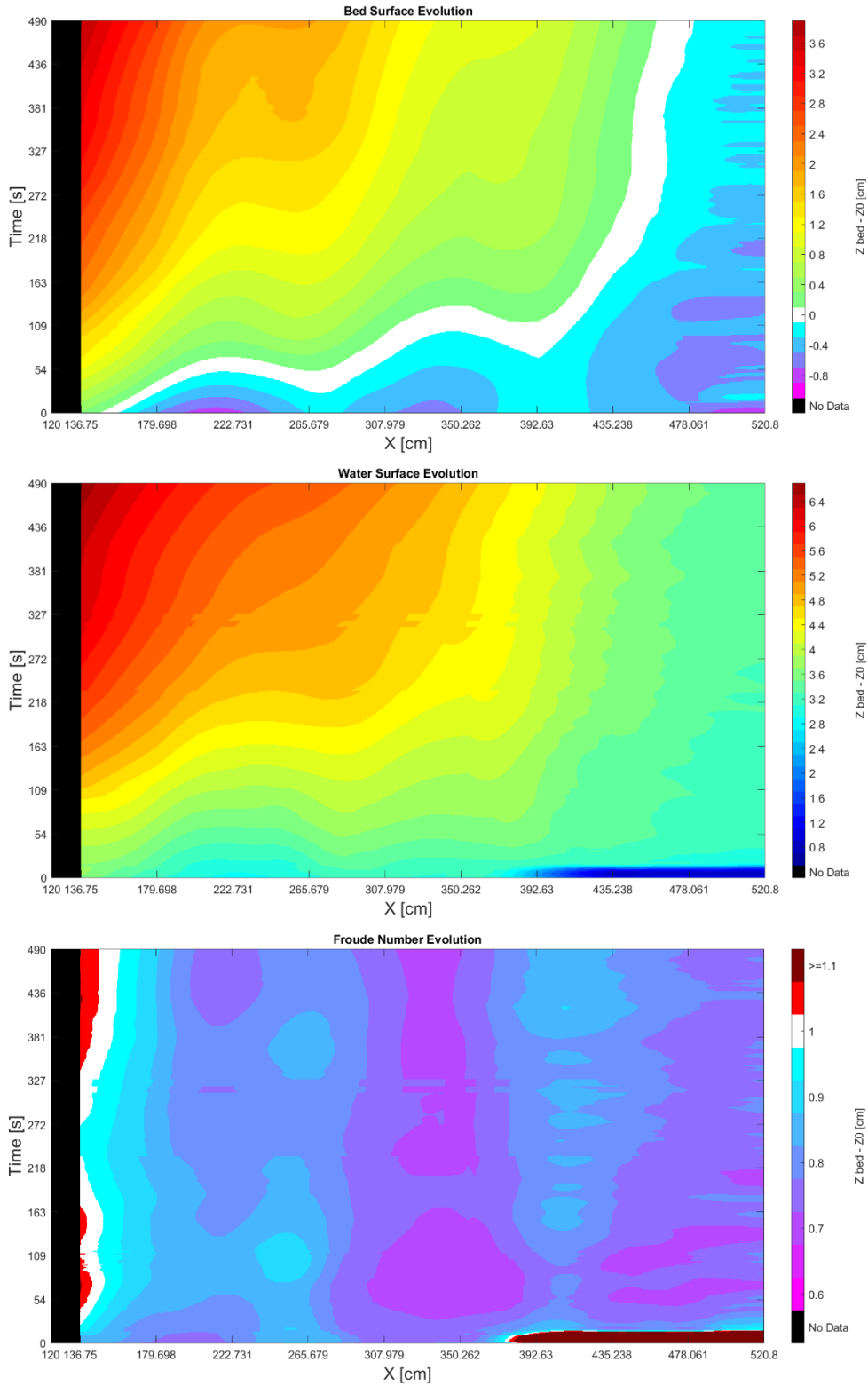


AE1.5. Spatial evolution of bed and water

APPENDIX - RESULTS



AE1.6. Temporal evolution of bed and water in the selected points

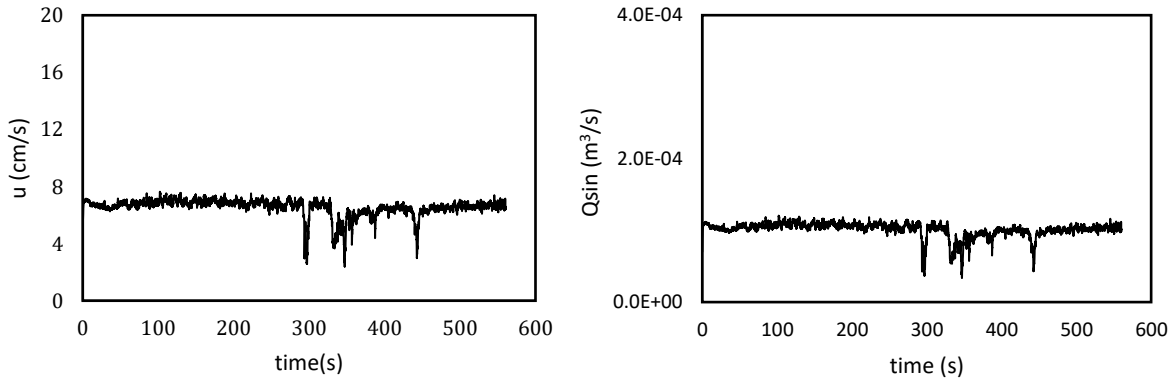


AE1.7. Color gradient graphs for bed, water and Froude number evolution in space and time

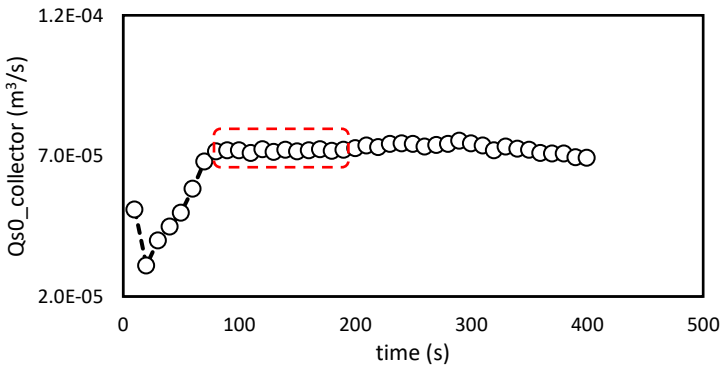
Experiment AE2

T (s)	S ₀ (%)	Q (l/s)	h ₀ (cm)	Fr	Vibration level	Q _{sin} (m ³ /s)	Q _{s0} (m ³ /s)	Q _{sin} /Q _{s0}
560	1.2	5	2.78	1.14	7.5	1.01E-04	8.31E-05	1.21

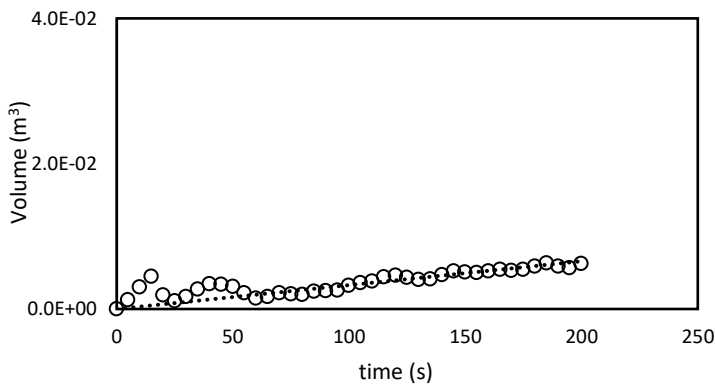
AE2.1. Experimental parameters



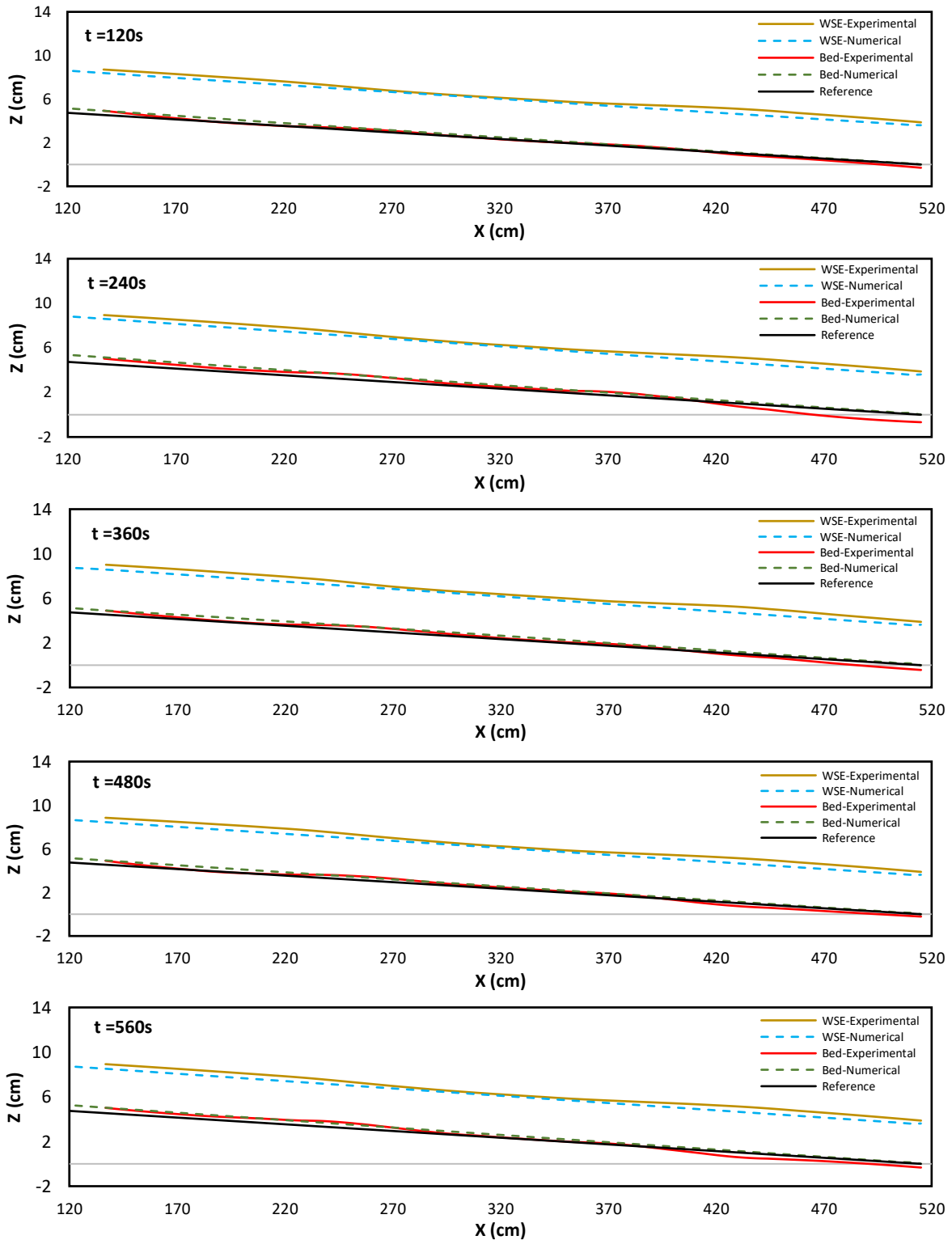
AE2.2. Temporal evolution of velocity and sediment discharge for the inflow material



AE2.3. $t - Q_{s0_collector}$ graph, presenting the sediment transport capacity over time, computed using collector method. The average of the constant values of Q_{s0} is considered as the $Q_{s0_collector}$.

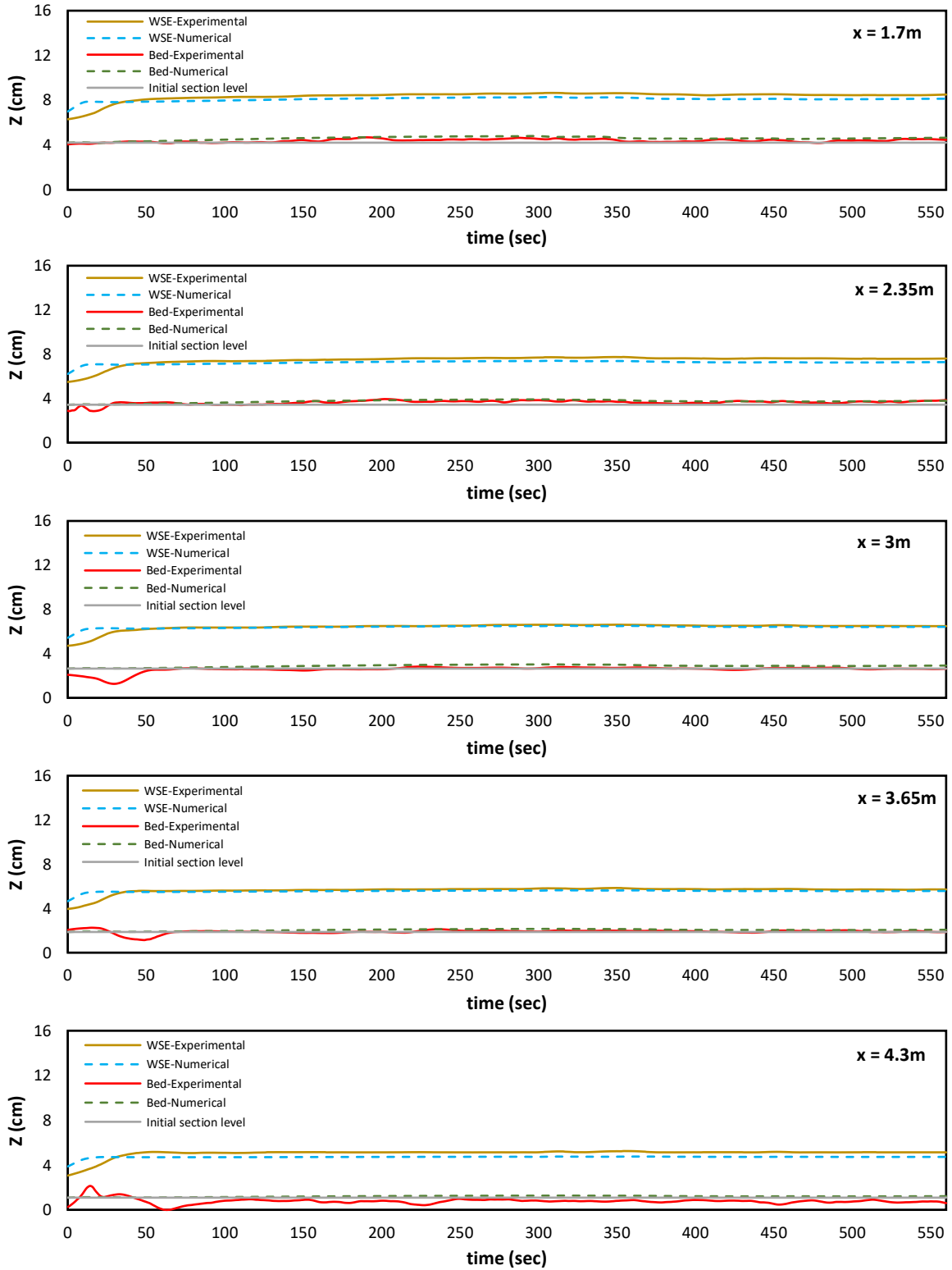


AE2.4. t - volume graph, presenting the volume of sediment deposited in the channel with the assumption of constant profile at the upstream. The slop of the interpolating line is used to calculate Q_{s0} , monitored.

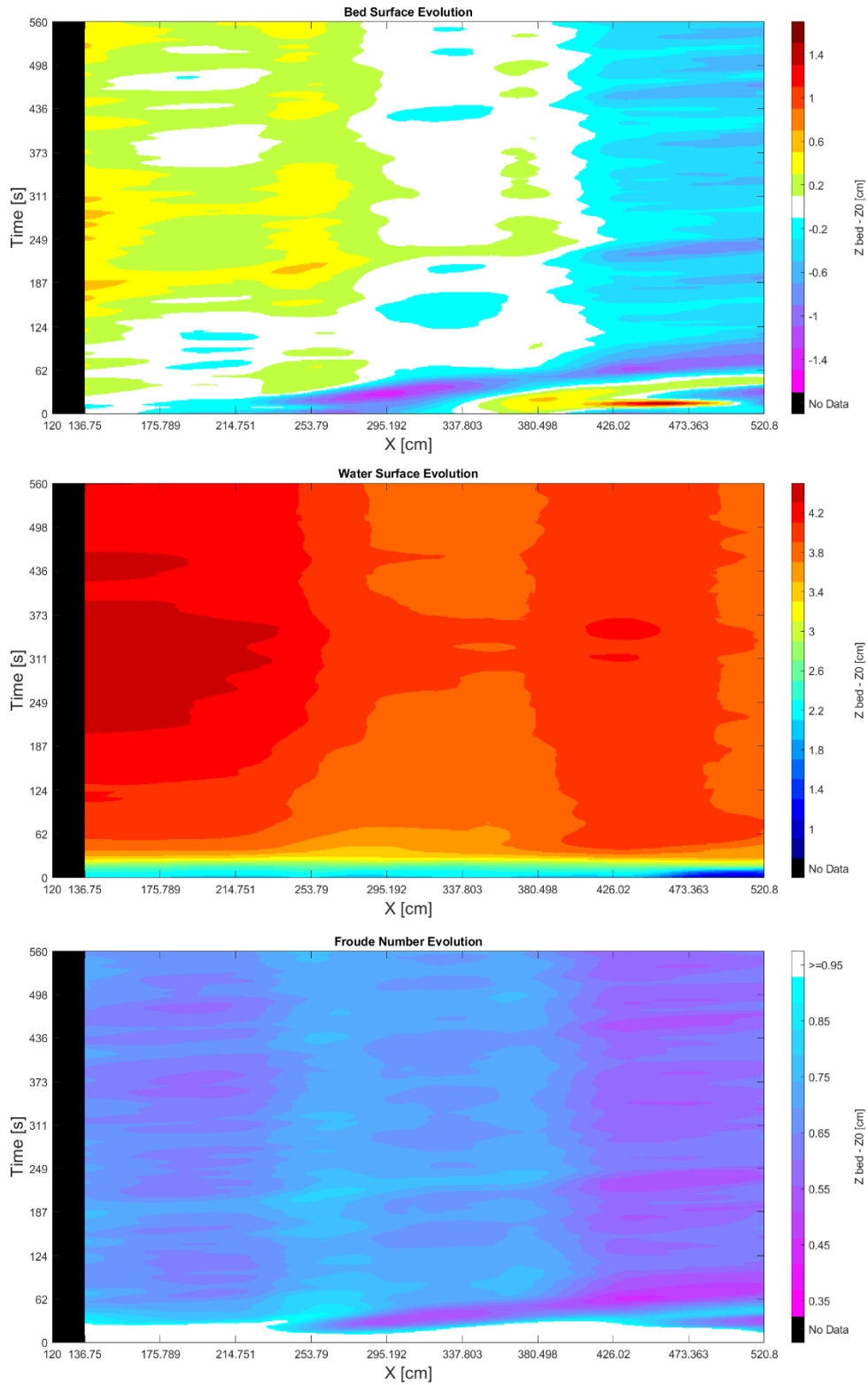


AE2.5. Spatial evolution of bed and water

APPENDIX - RESULTS



AE2.6. Temporal evolution of bed and water in the selected points

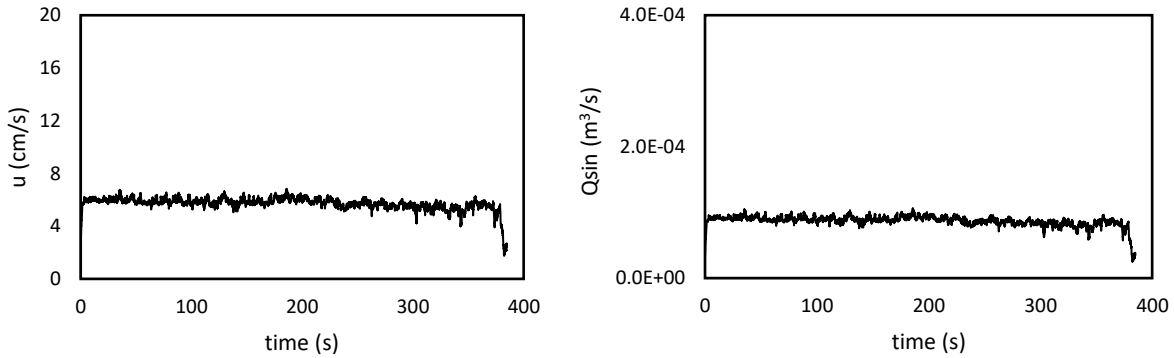


AE2.7. Color gradient graphs for bed, water and Froude number evolution in space and time

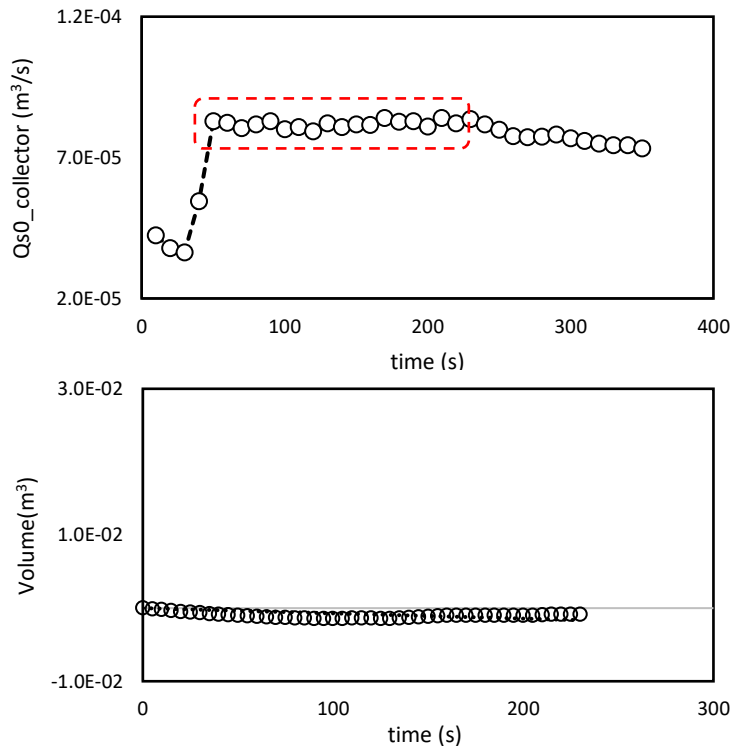
Experiment AE3

T (s)	S ₀ (%)	Q (l/s)	h ₀ (cm)	Fr	Vibration level	Q _{sin} (m ³ /s)	Q _{s0} (m ³ /s)	Q _{sin} /Q _{s0}
380	1.2	5	2.78	1.14	7.3	8.67E-05	8.31E-05	1.04

AE3.1. Experimental parameters

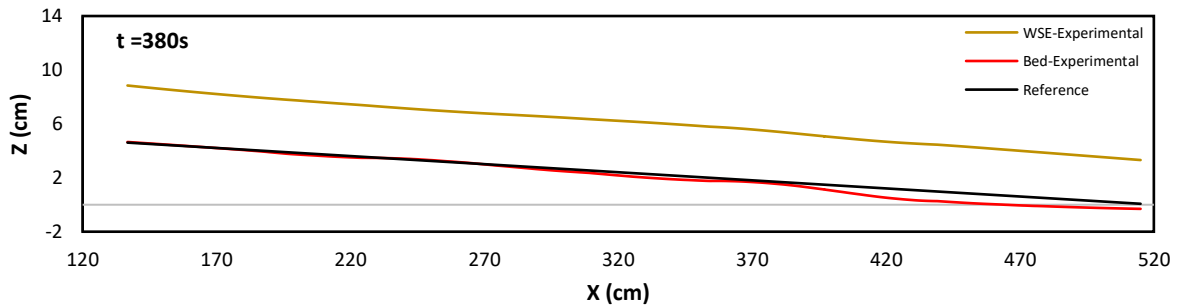
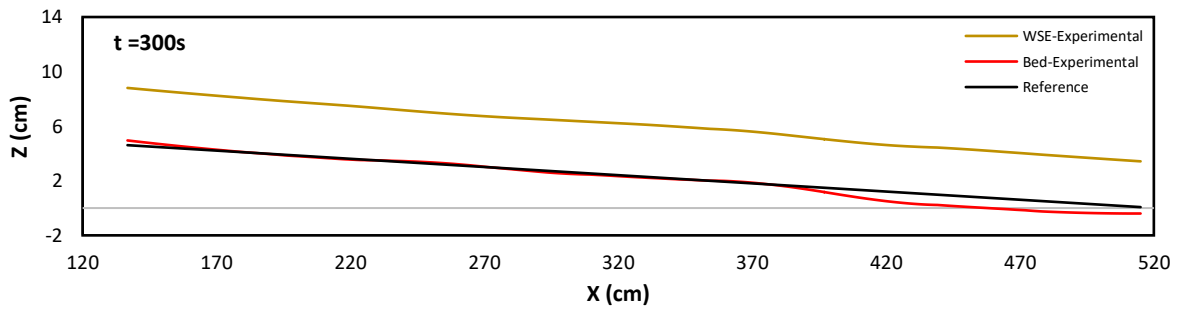
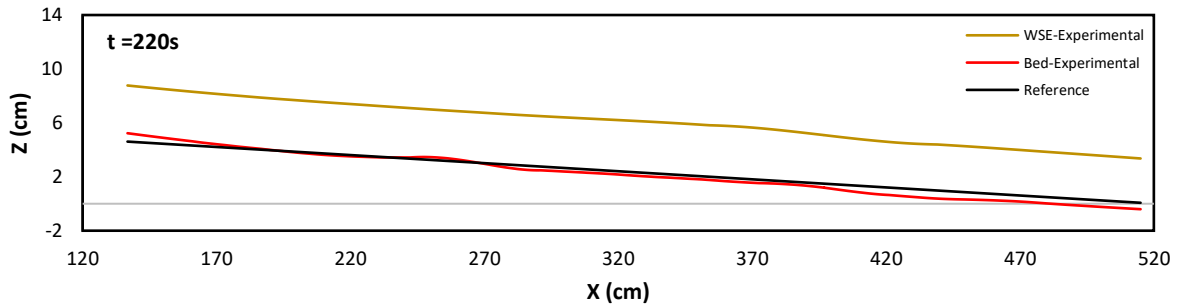
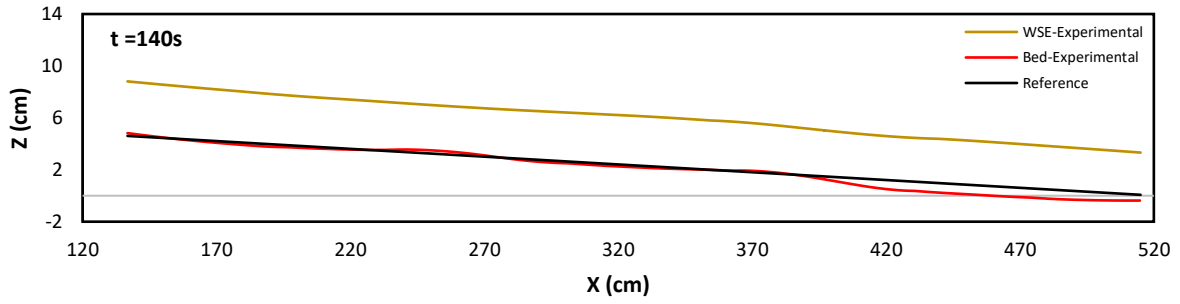
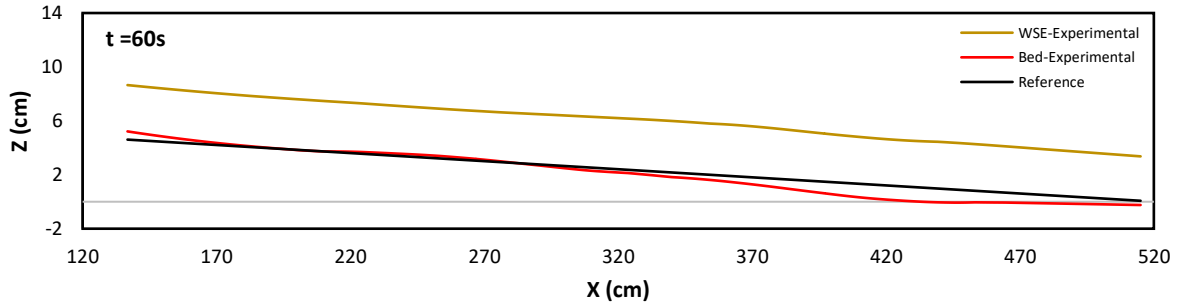


AE3.2. Temporal evolution of velocity and sediment discharge for the inflow material



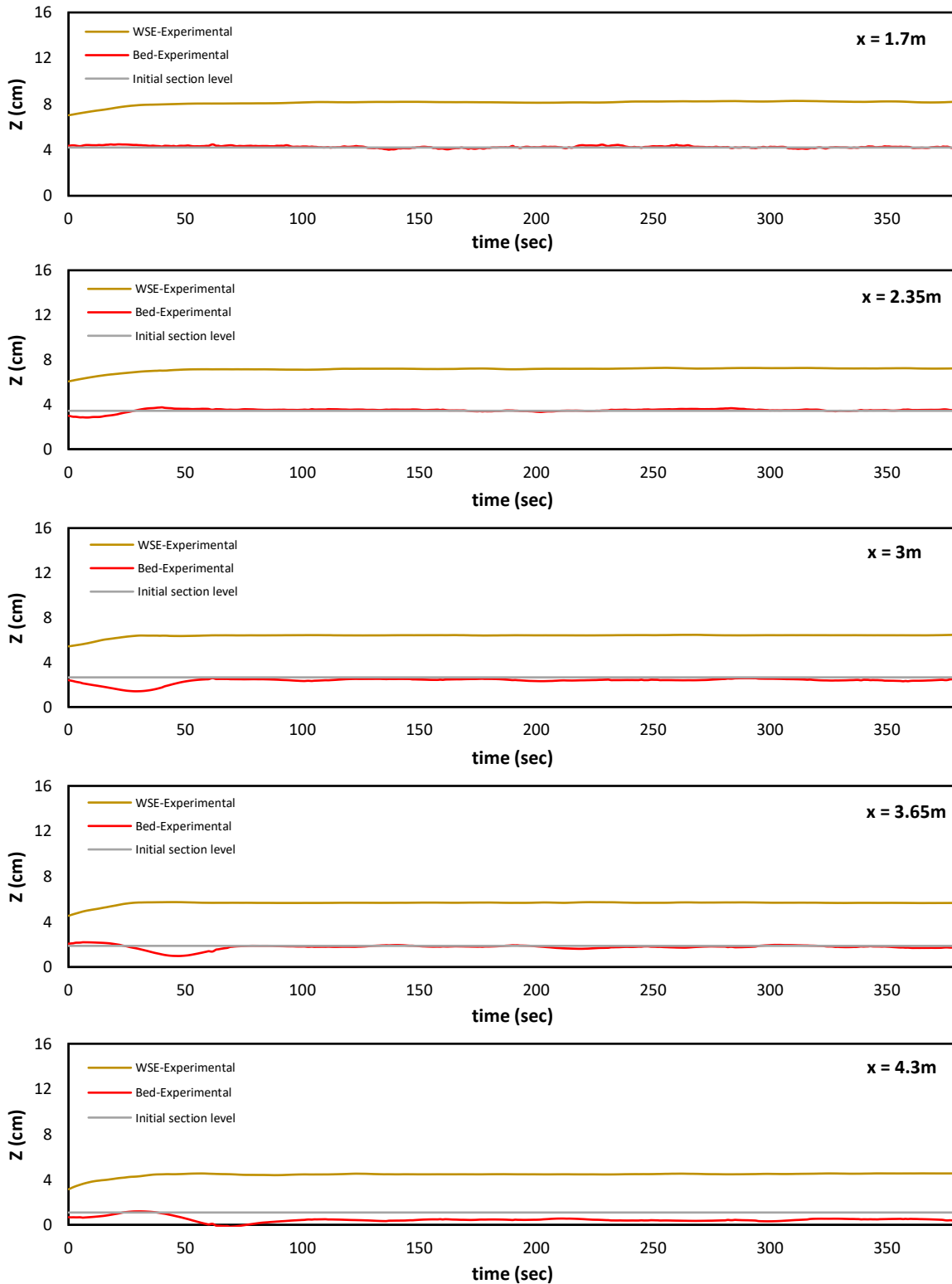
AE3.3. $t - Q_{s0_collector}$ graph, presenting the sediment transport capacity over time, computed using collector method. The average of the constant values of Q_{s0} is considered as the $Q_{s0_collector}$.

AE3.4. t - volume graph, presenting the volume of sediment deposited in the channel with the assumption of constant profile at the upstream. The slop of the interpolating line is used to calculate $Q_{s0_monitored}$.

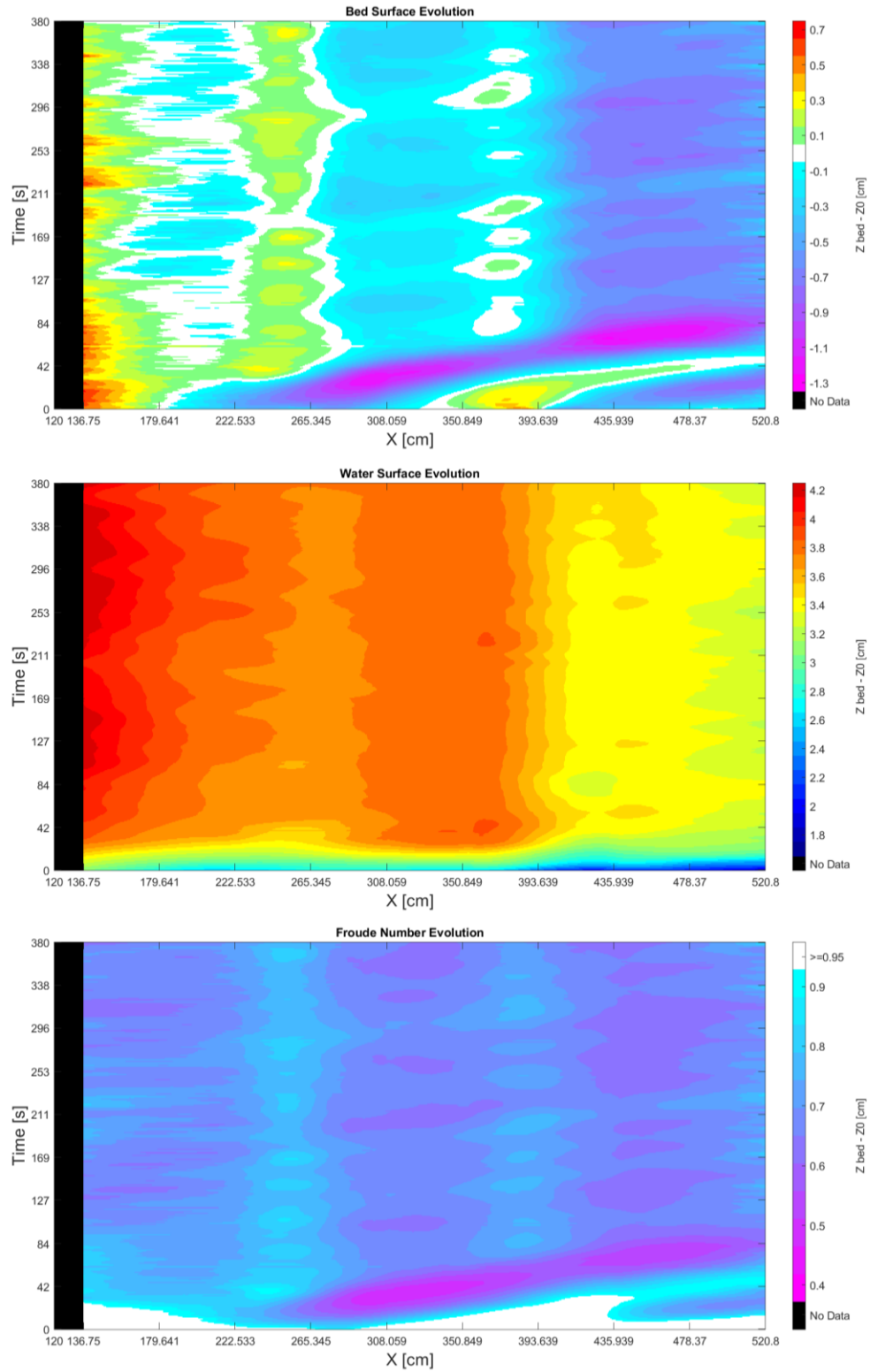


AE3.5. Spatial evolution of bed and water

APPENDIX - RESULTS



AE3.6. Temporal evolution of bed and water in the selected points

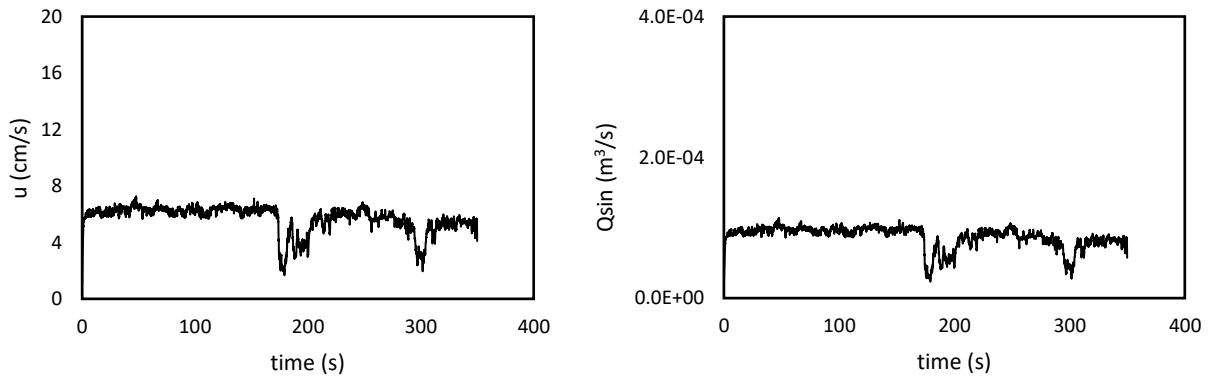


AE3.7. Color gradient graphs for bed, water and Froude number evolution in space and time

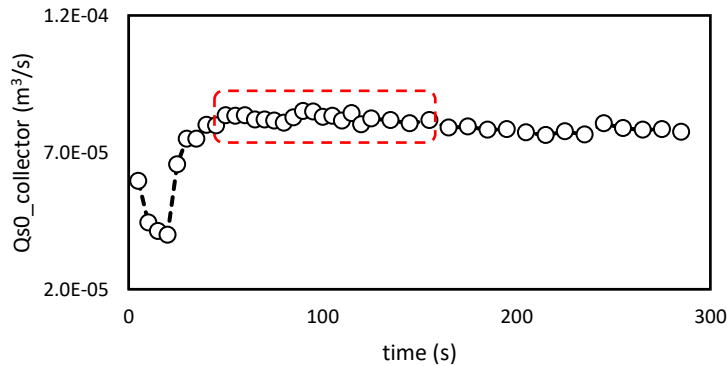
Experiment AE4

T (s)	S ₀ (%)	Q (l/s)	h ₀ (cm)	Fr	Vibration level	Q _{sin} (m ³ /s)	Q _{s0} (m ³ /s)	Q _{sin} /Q _{s0}
350	1.2	5	2.78	1.14	7.5	8.7E-05	8.31E-05	1.05

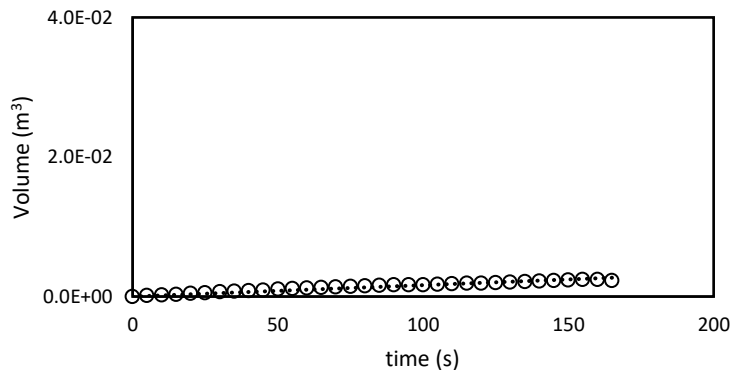
AE4.1. Experimental parameters



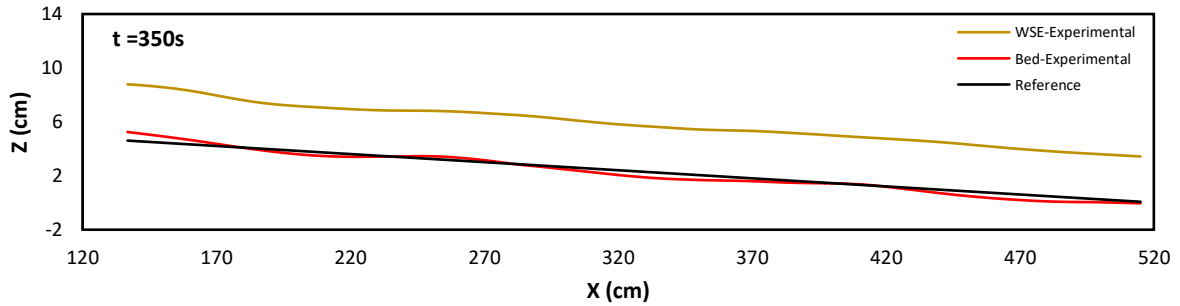
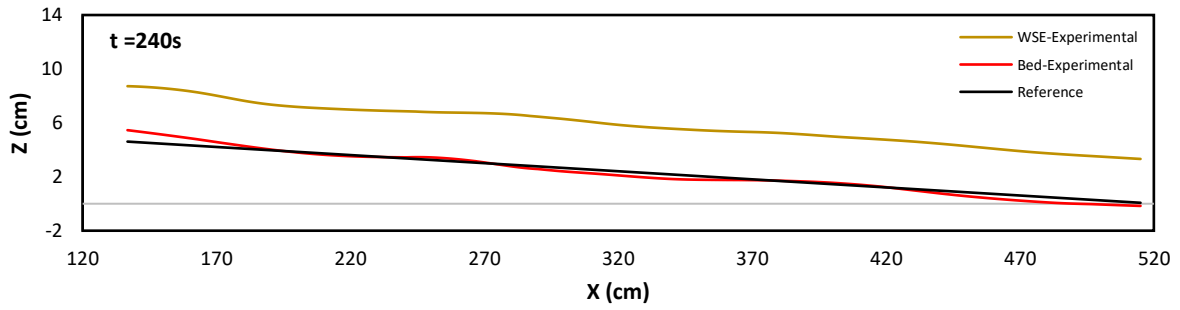
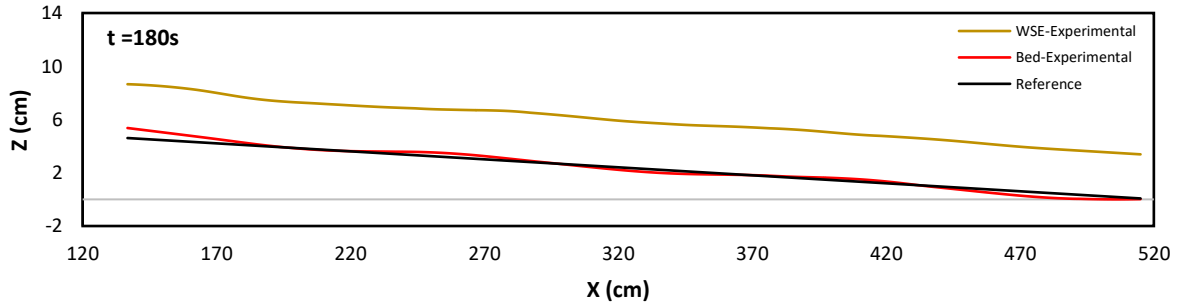
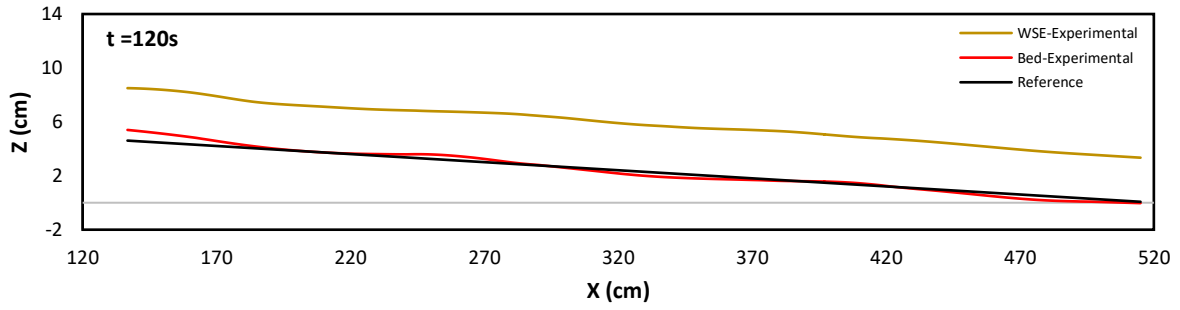
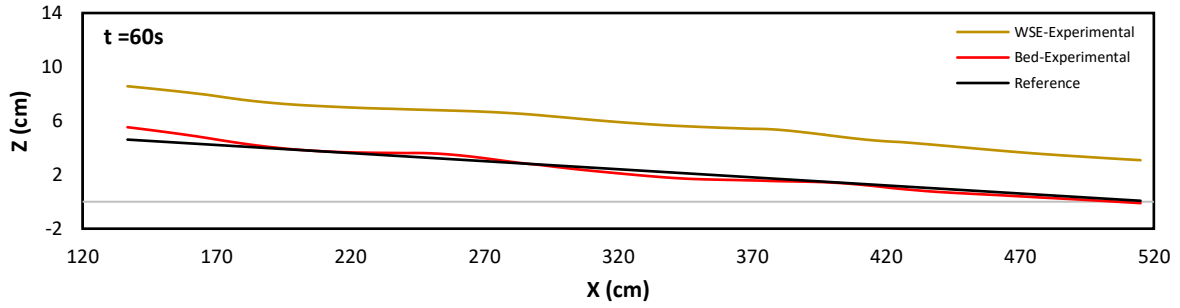
AE4.2. Temporal evolution of velocity and sediment discharge for the inflow material



AE4.3. $t - Q_{s0_collector}$ graph, presenting the sediment transport capacity over time, computed using collector method. The average of the constant values of Q_{s0} is considered as the $Q_{s0_collector}$.

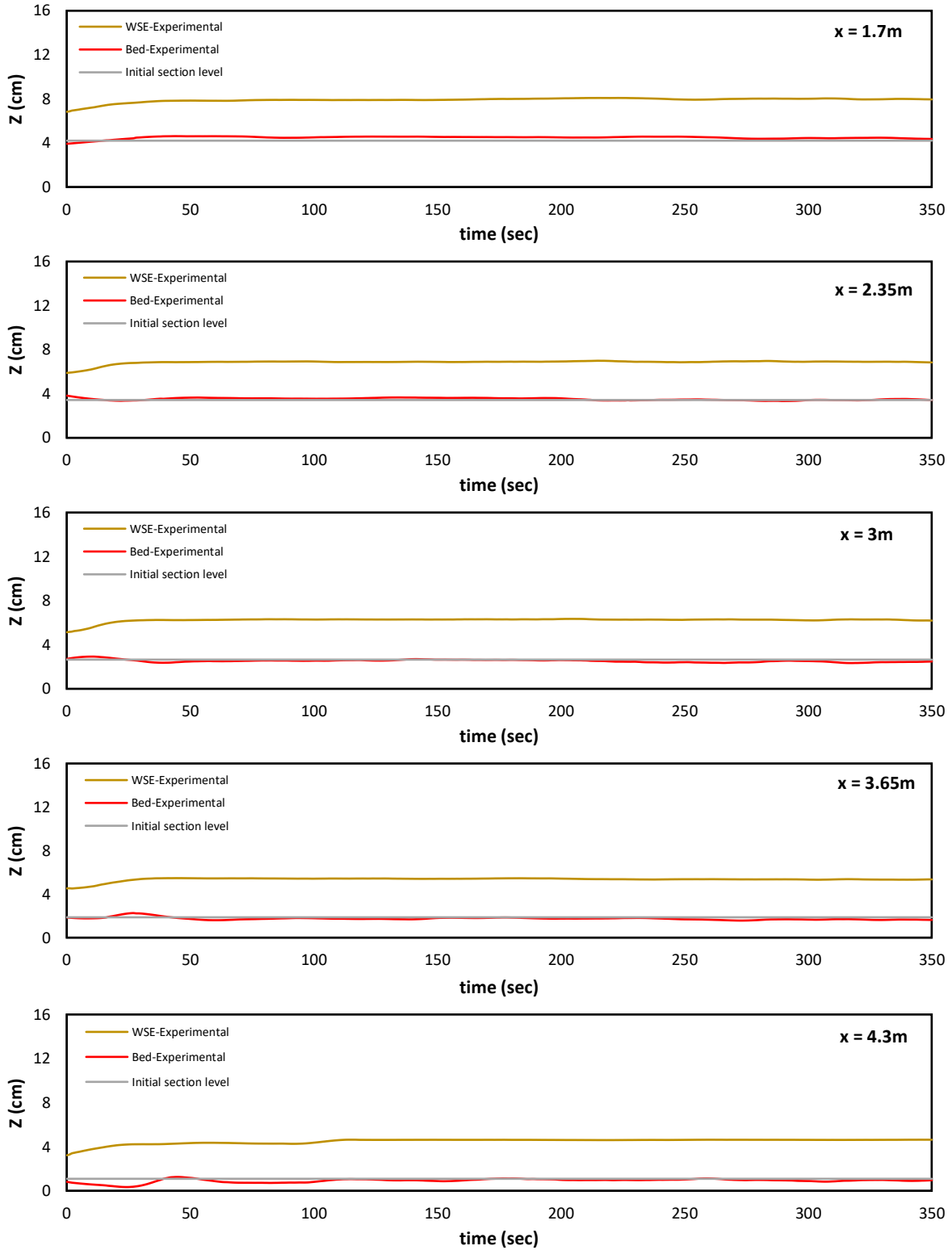


AE4.4. t - volume graph, presenting the volume of sediment deposited in the channel with the assumption of constant profile at the upstream. The slope of the interpolating line is used to calculate Q_{s0} , monitored.

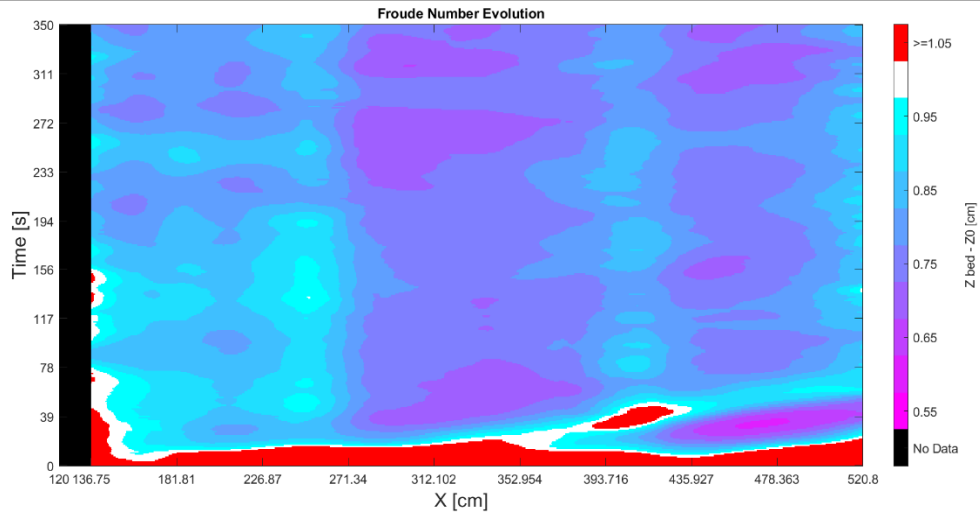
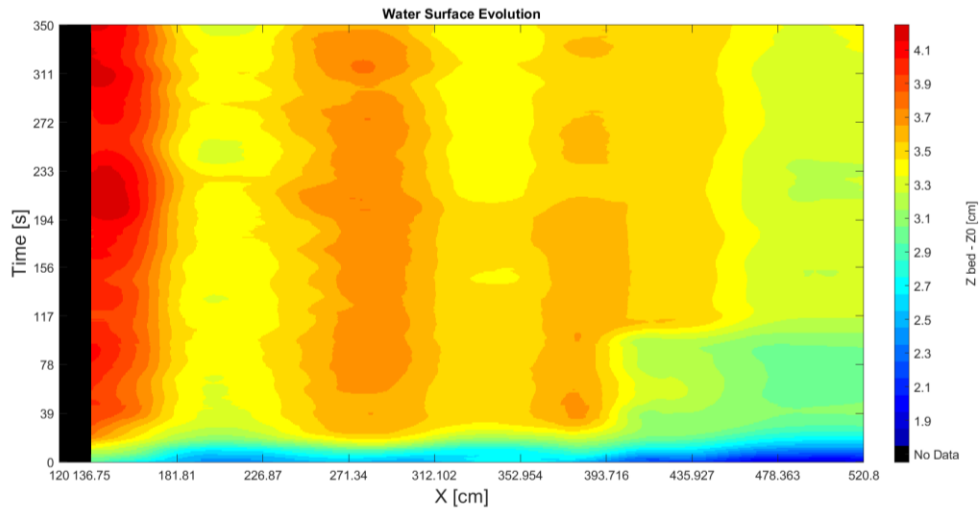
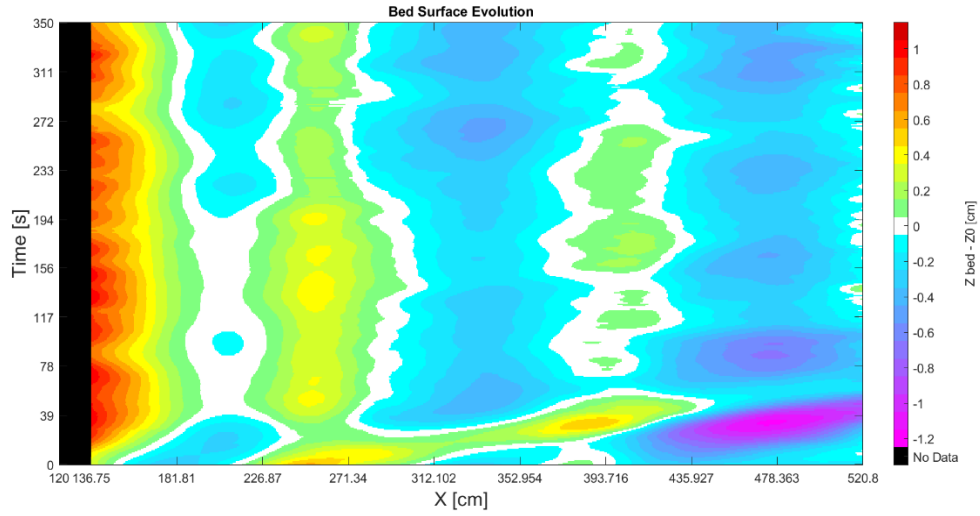


AE4.5. Spatial evolution of bed and water

APPENDIX - RESULTS



AE4.6. Temporal evolution of bed and water in the selected points

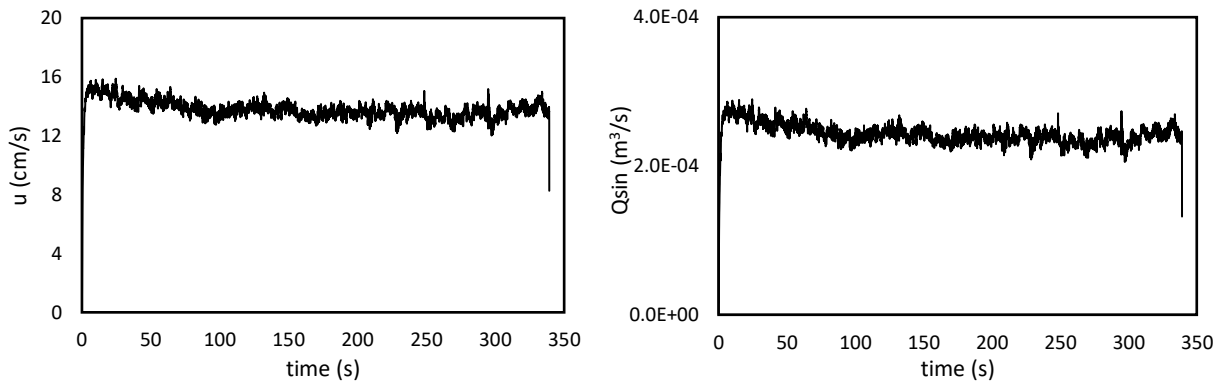


AE4.7. Color gradient graphs for bed, water and Froude number evolution in space and time

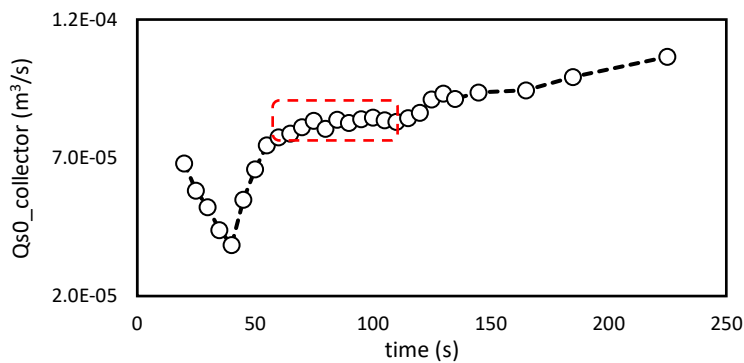
Experiment AE5

T (s)	S ₀ (%)	Q (l/s)	h ₀ (cm)	Fr	Vibration level	Q _{sin} (m ³ /s)	Q _{s0} (m ³ /s)	Q _{sin} /Q _{s0}
340	1.2	5	2.78	1.14	8.3	2.43E-04	8.31E-05	2.92

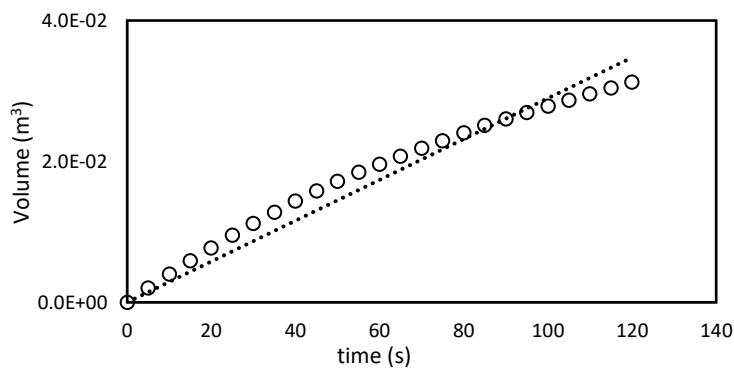
AE5.1. Experimental parameters



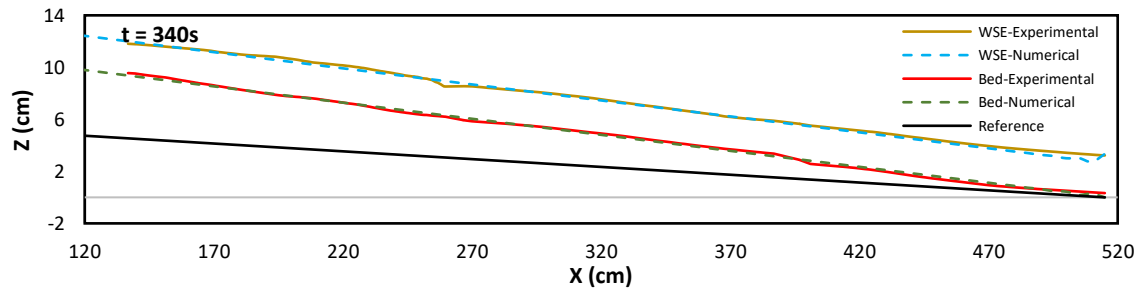
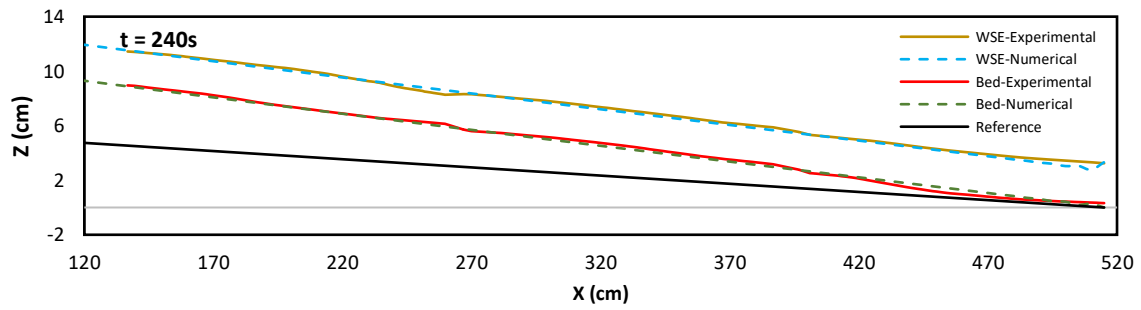
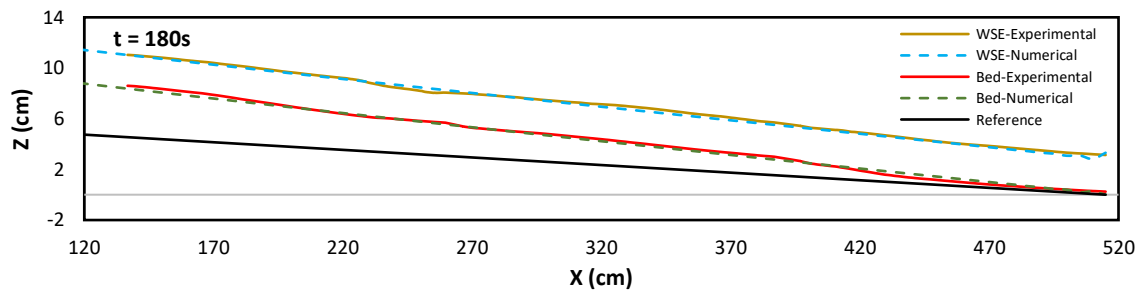
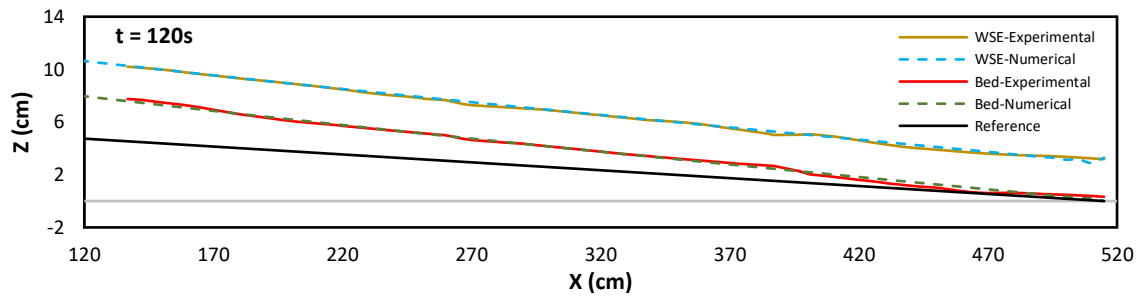
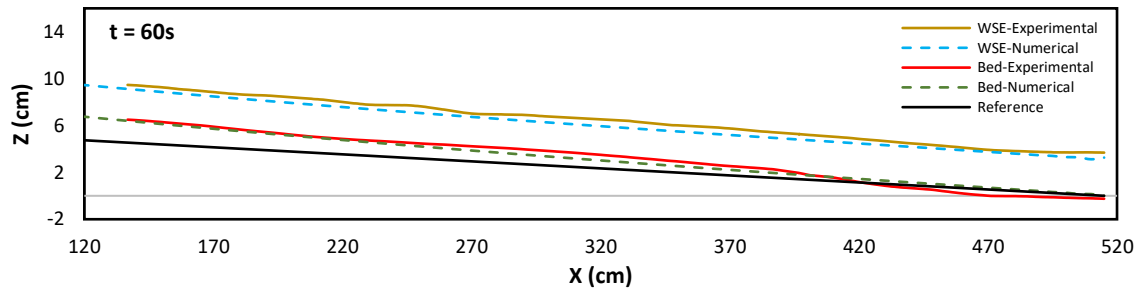
AE5.2. Temporal evolution of velocity and sediment discharge for the inflow material



AE5.3. t – Q_{s0, collector} graph, presenting the sediment transport capacity over time, computed using collector method. The average of the constant values of Q_{s0} is considered as the Q_{s0, collector}.

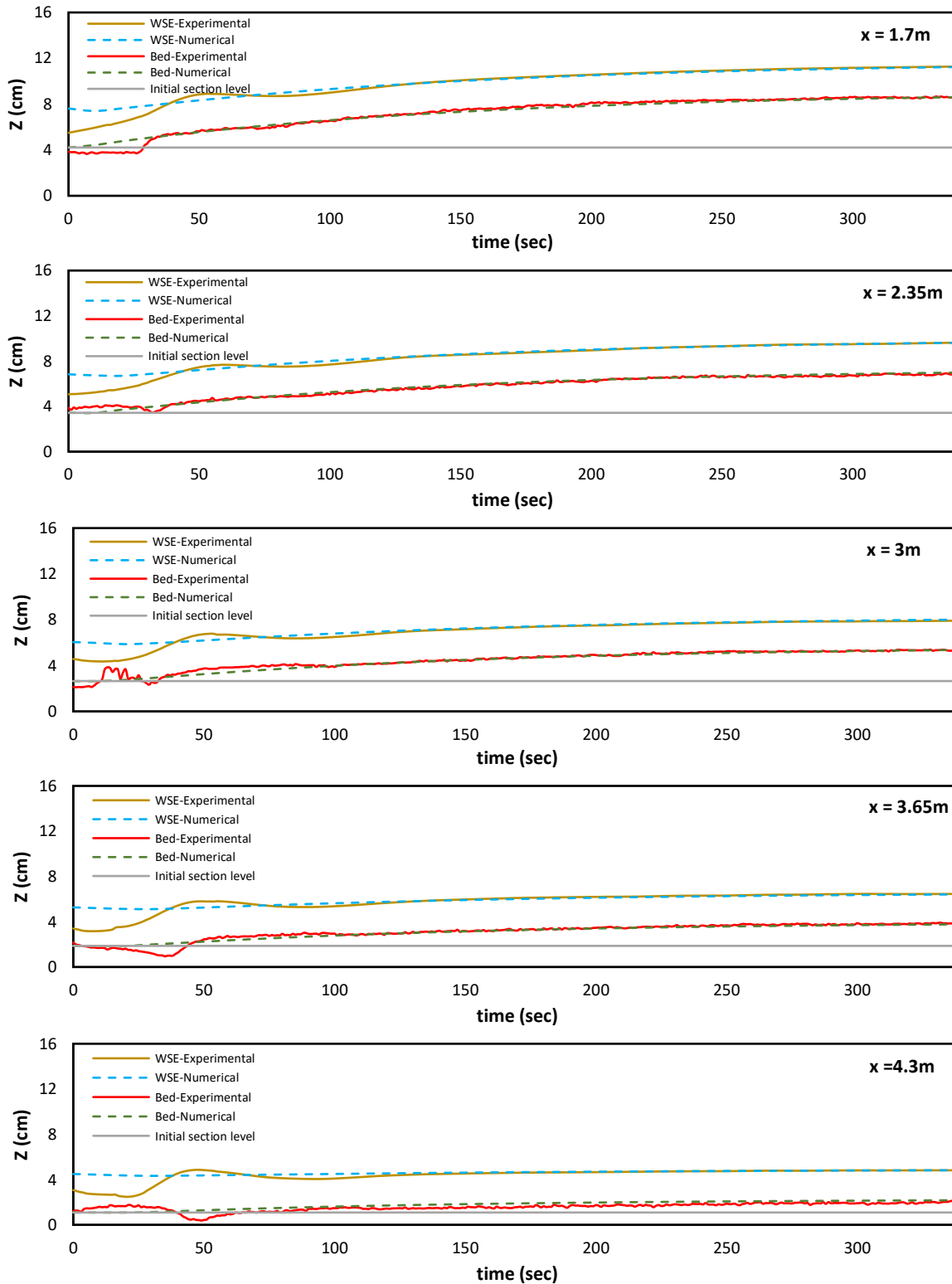


AE5.4. t- volume graph, presenting the volume of sediment deposited in the channel with the assumption of constant profile at the upstream. The slope of the interpolating line is used to calculate Q_{s0, monitored}.

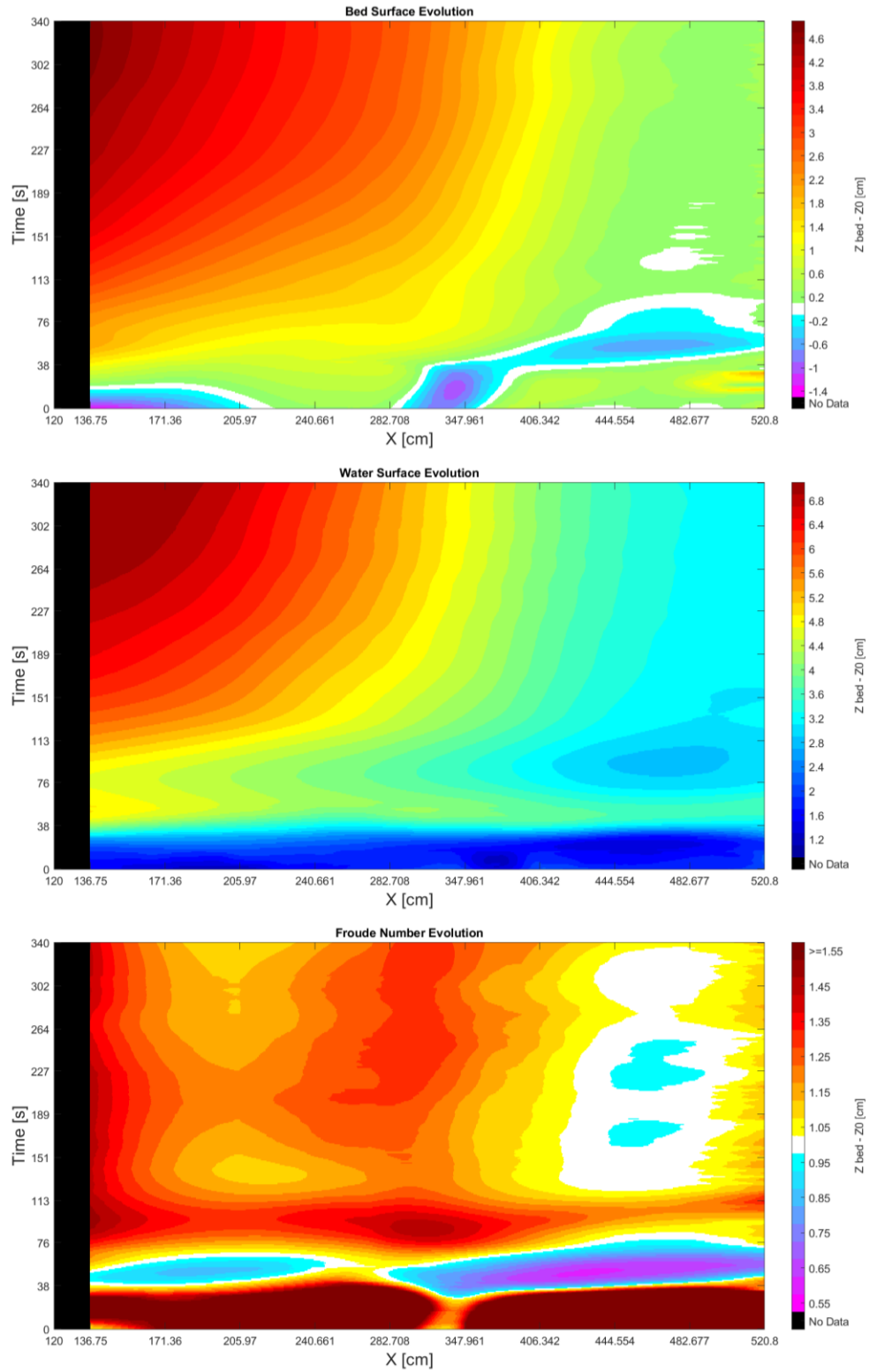


AE5.5. Spatial evolution of bed and water

APPENDIX - RESULTS



AE5.6. Temporal evolution of bed and water in the selected point

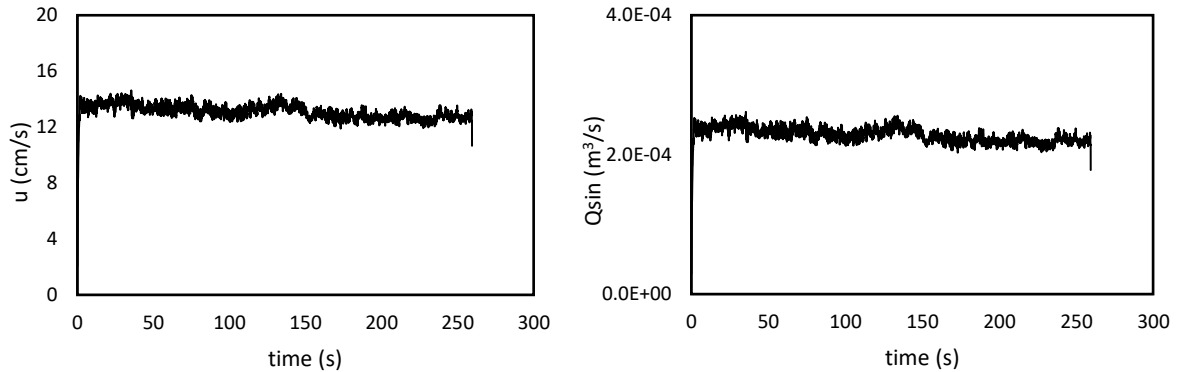


AE5.7. Color gradient graphs for bed, water and Froude number evolution in space and time

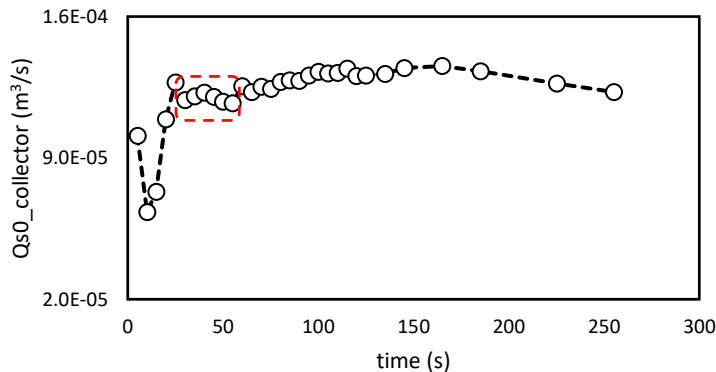
Experiment AE6

T (s)	S ₀ (%)	Q (l/s)	h ₀ (cm)	Fr	Vibration level	Q _{sin} (m ³ /s)	Q _{s0} (m ³ /s)	Q _{sin} /Q _{s0}
259	1.2	7	3.46	1.16	8.3	2.3E-04	1.33E-04	1.73

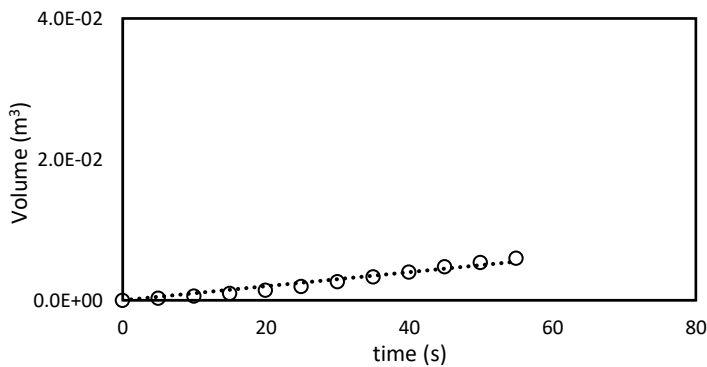
AE6.1. Experimental parameters



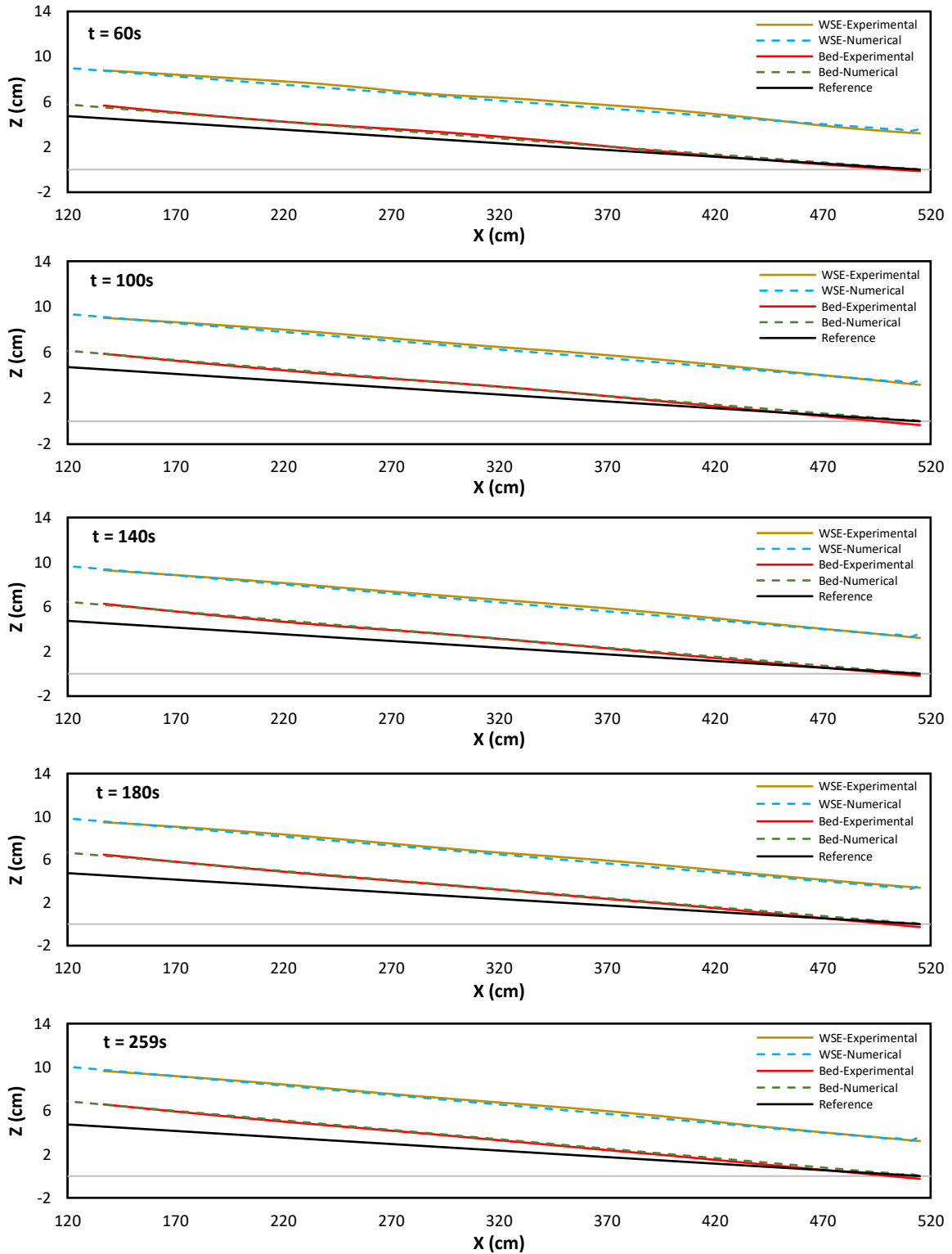
AE6.2. Temporal evolution of velocity and sediment discharge for the inflow material



AE6.3. t – Q_{s0, collector} graph, presenting the sediment transport capacity over time, computed using collector method. The average of the constant values of Q_{s0} is considered as the Q_{s0, collector}.

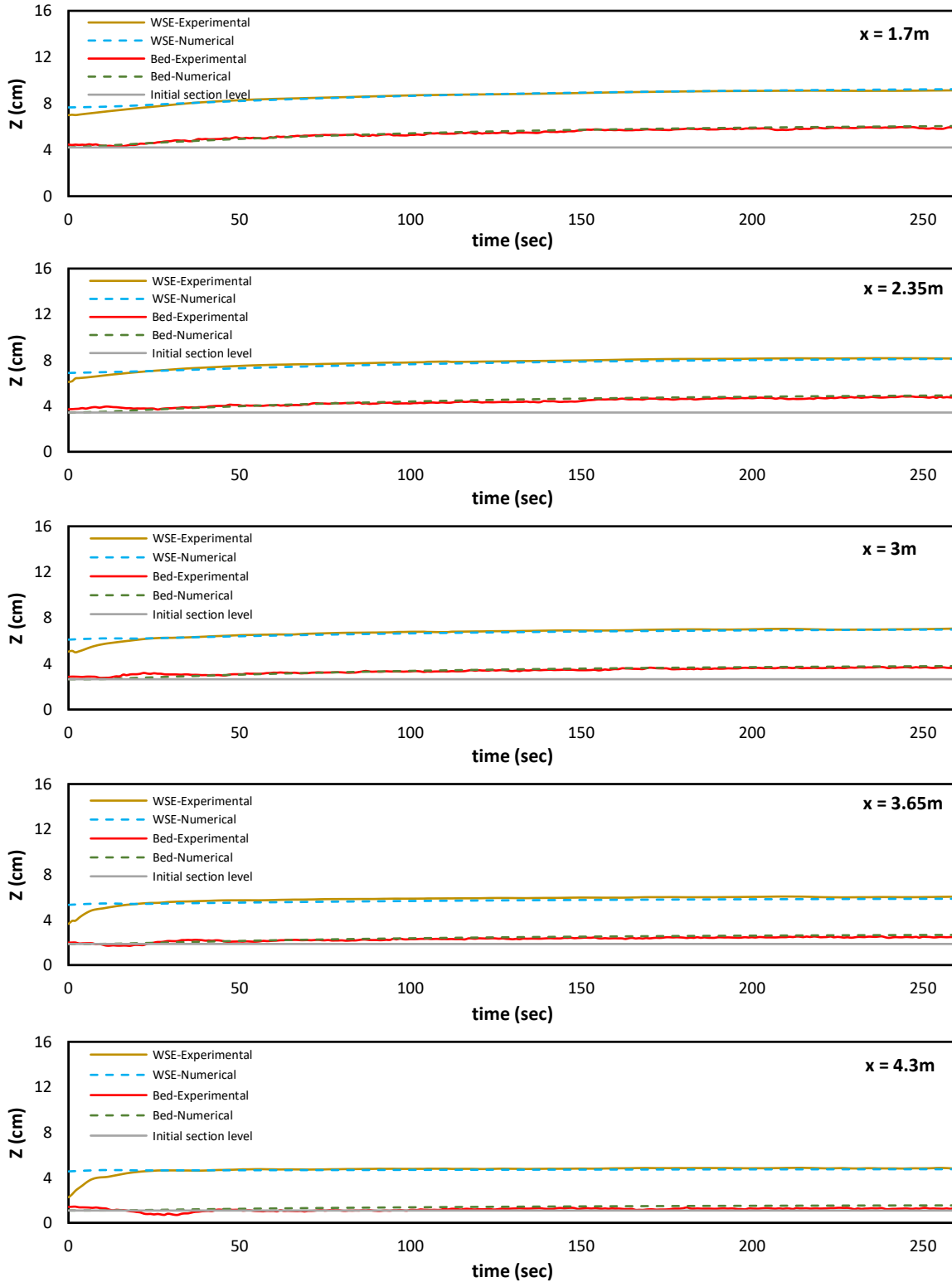


AE6.4. t- volume graph, presenting the volume of sediment deposited in the channel with the assumption of constant profile at the upstream. The slope of the interpolating line is used to calculate Q_{s0, monitored}.

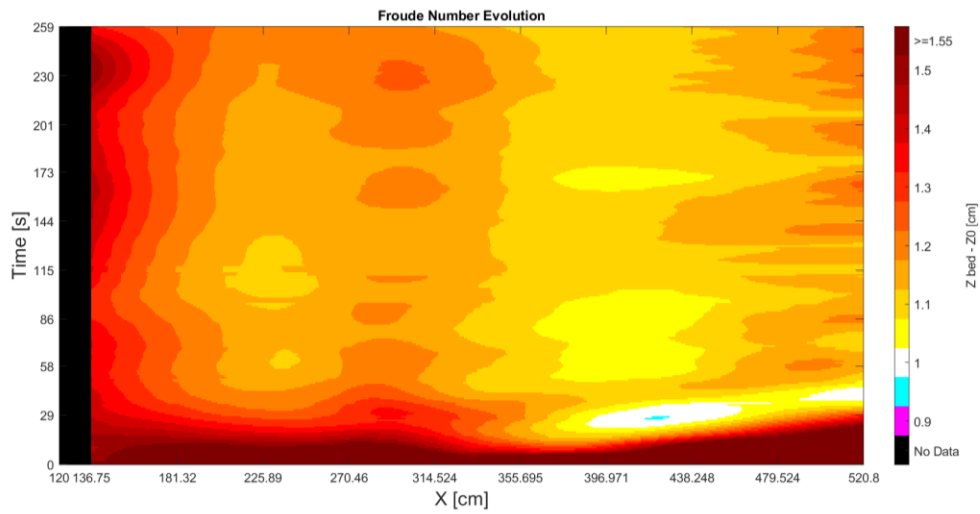
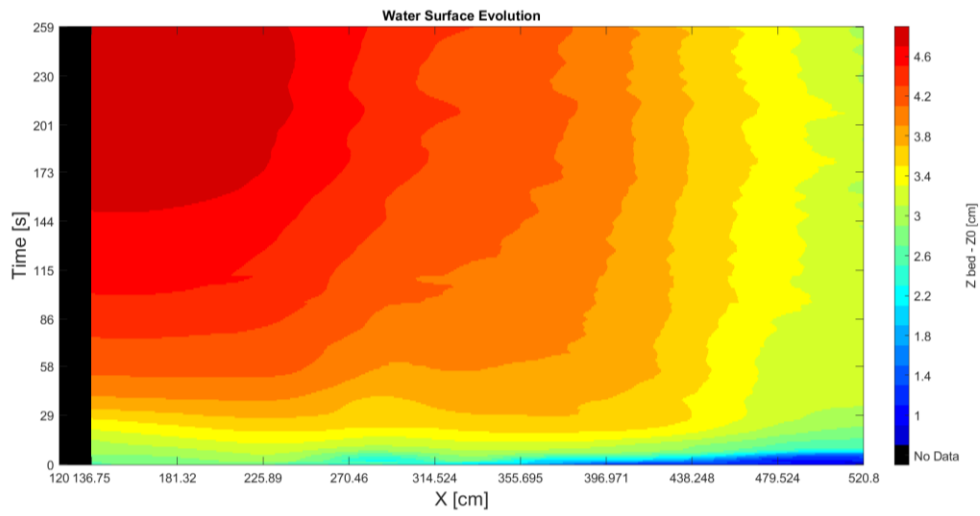
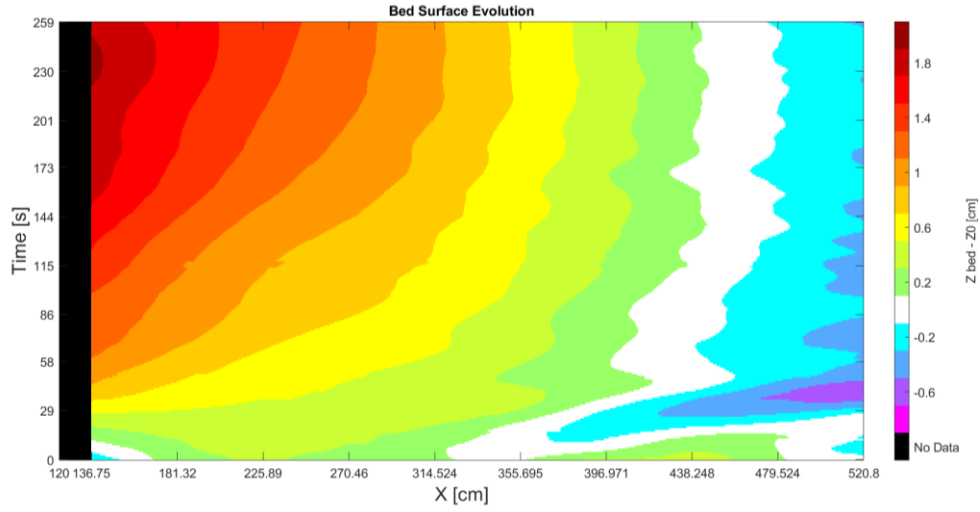


AE6.5. Spatial evolution of bed and water

APPENDIX - RESULTS



AE6.6. Temporal evolution of bed and water in the selected point

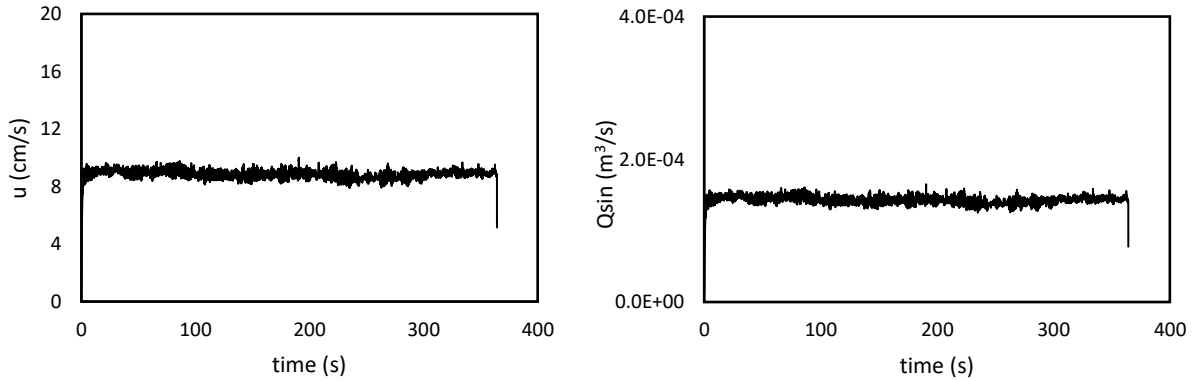


AE6.7. Color gradient graphs for bed, water and Froude number evolution in space and time

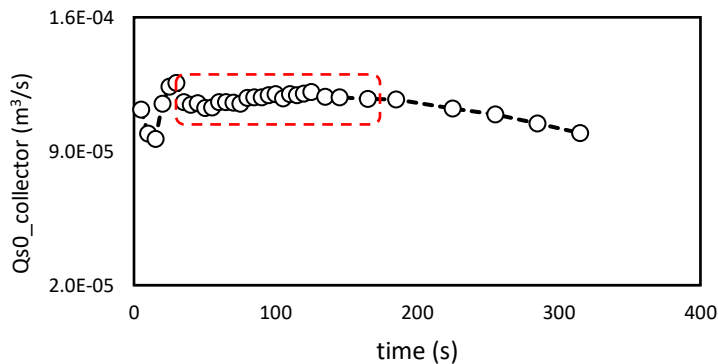
Experiment AE7

T (s)	S ₀ (%)	Q (l/s)	h ₀ (cm)	Fr	Vibration level	Q _{sin} (m ³ /s)	Q _{s0} (m ³ /s)	Q _{sin} /Q _{s0}
364	1.2	7	3.46	1.16	8	1.43E-04	1.33E-04	1.075

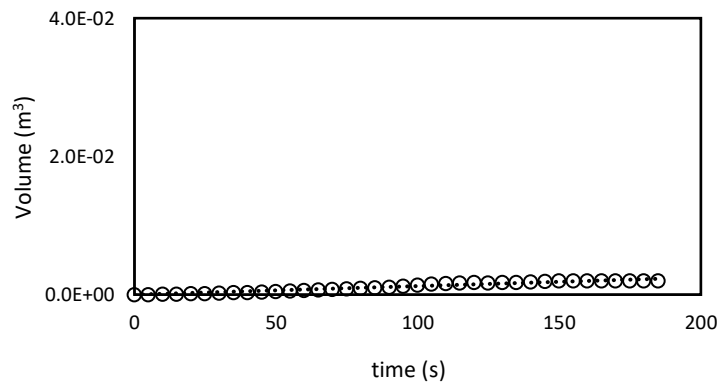
AE7.1. Experimental parameters



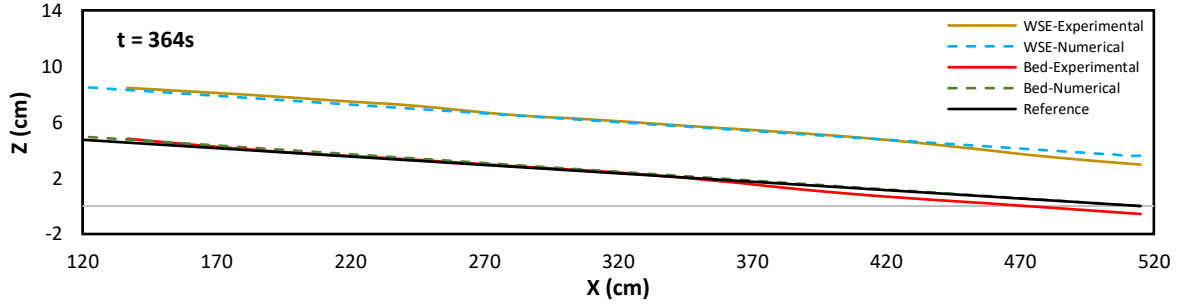
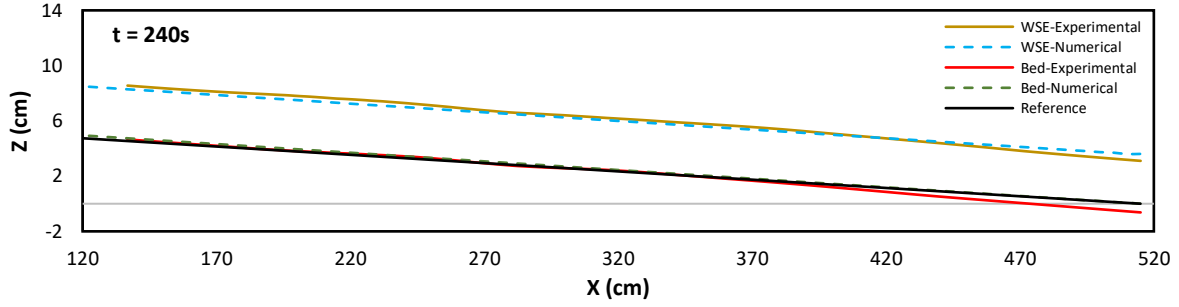
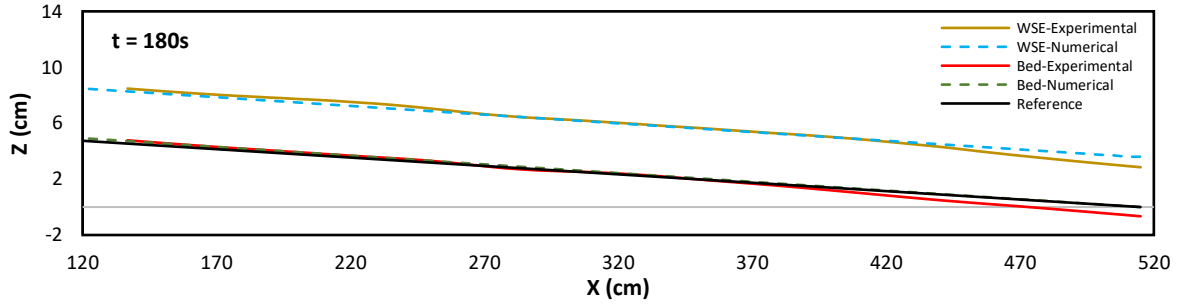
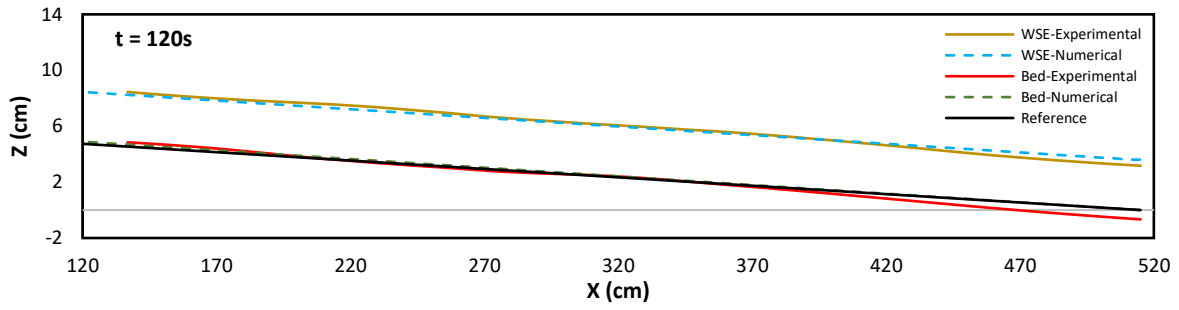
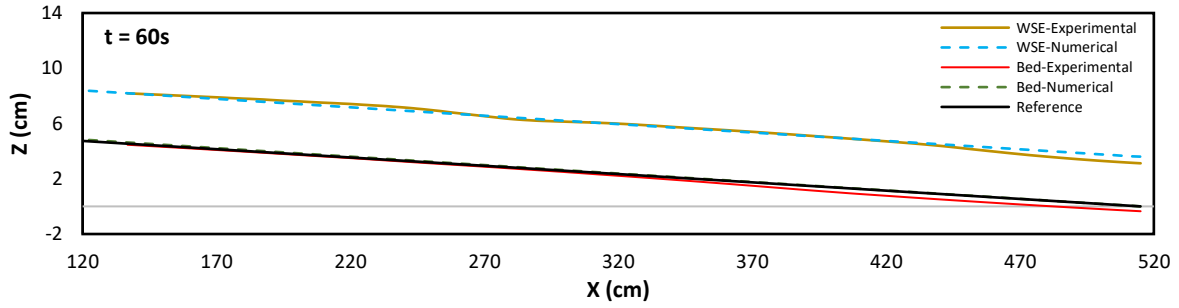
AE7.2. Temporal evolution of velocity and sediment discharge for the inflow material



AE7.3. $t - Q_{s0_collector}$ graph, presenting the sediment transport capacity over time, computed using collector method. The average of the constant values of Q_{s0} is considered as the $Q_{s0_collector}$.

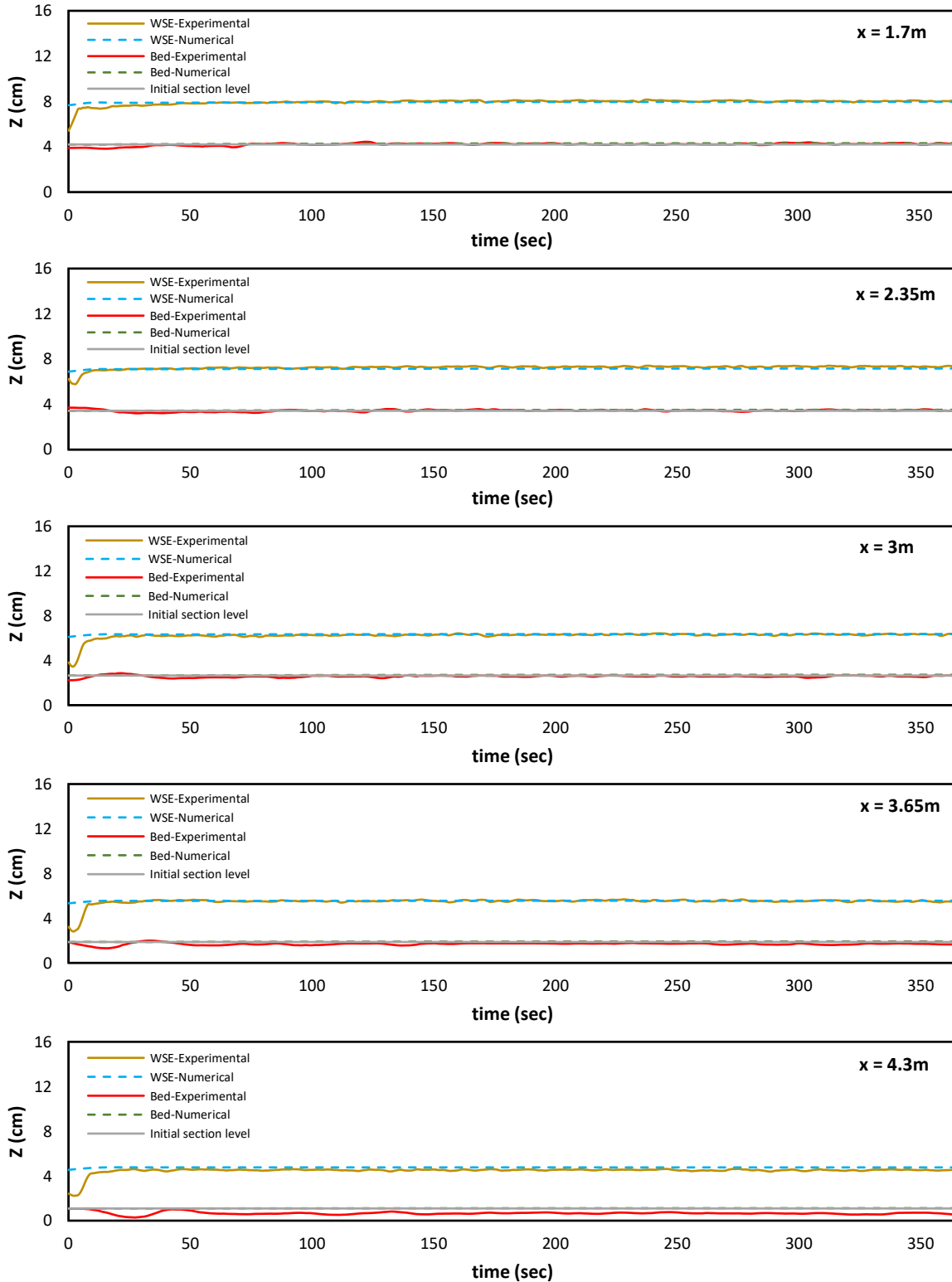


AE7.4. t - volume graph, presenting the volume of sediment deposited in the channel with the assumption of constant profile at the upstream. The slope of the interpolating line is used to calculate $Q_{s0_monitored}$.

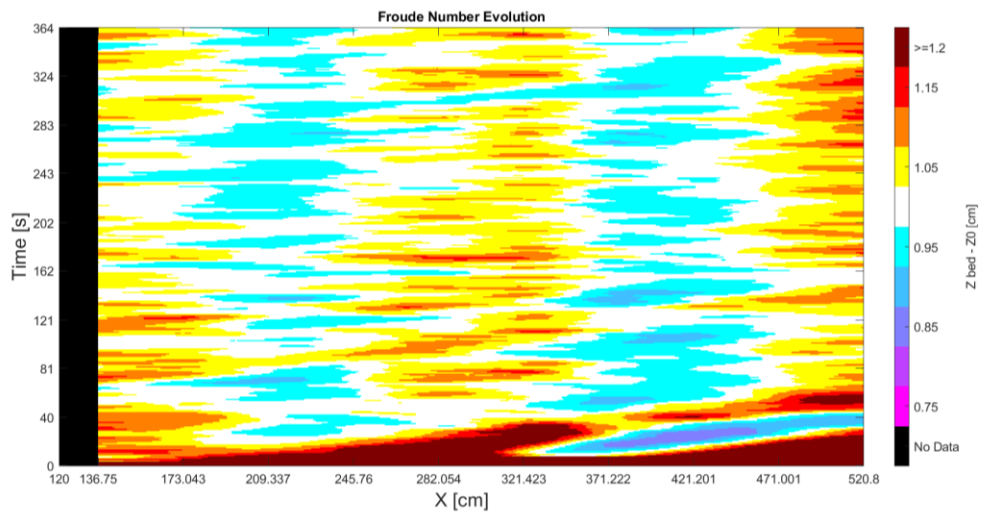
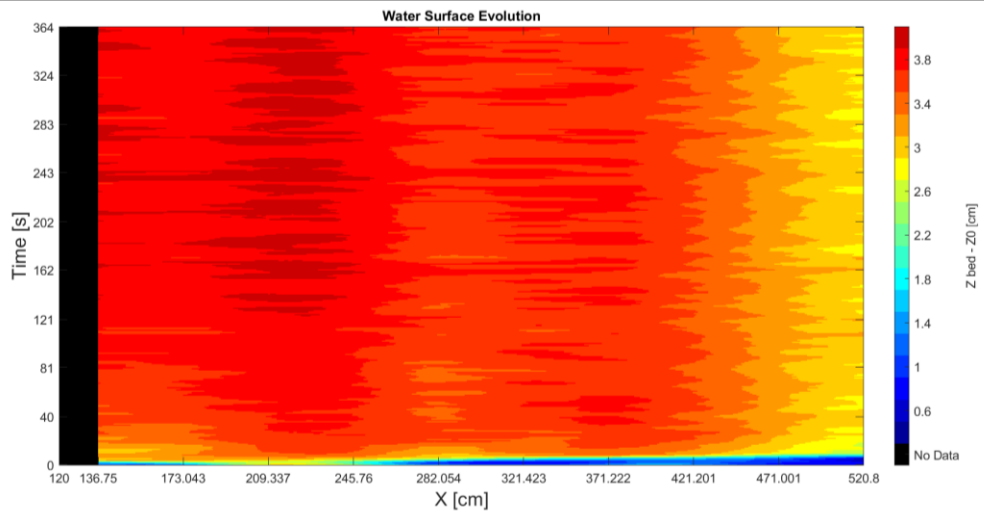
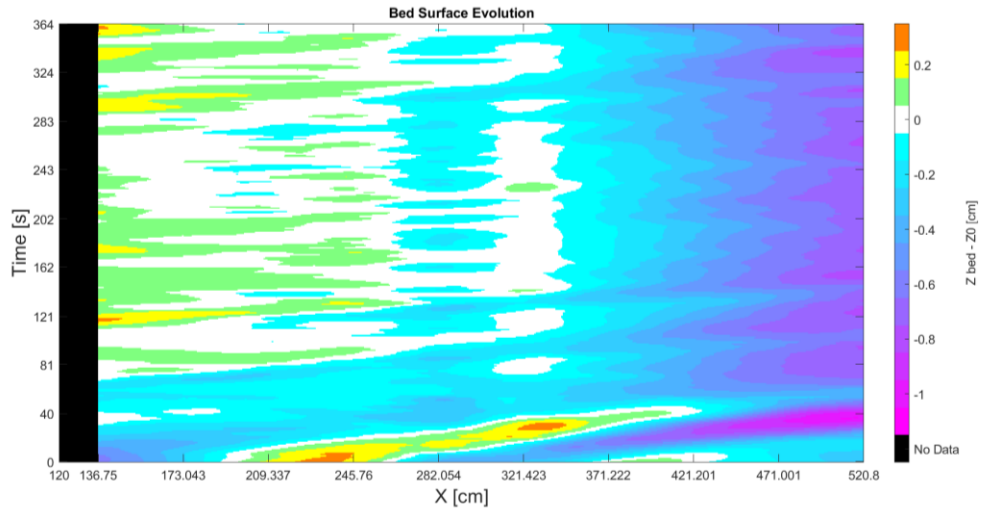


AE7.5. Spatial evolution of bed and water

APPENDIX - RESULTS



AE7.6. Temporal evolution of bed and water in the selected point

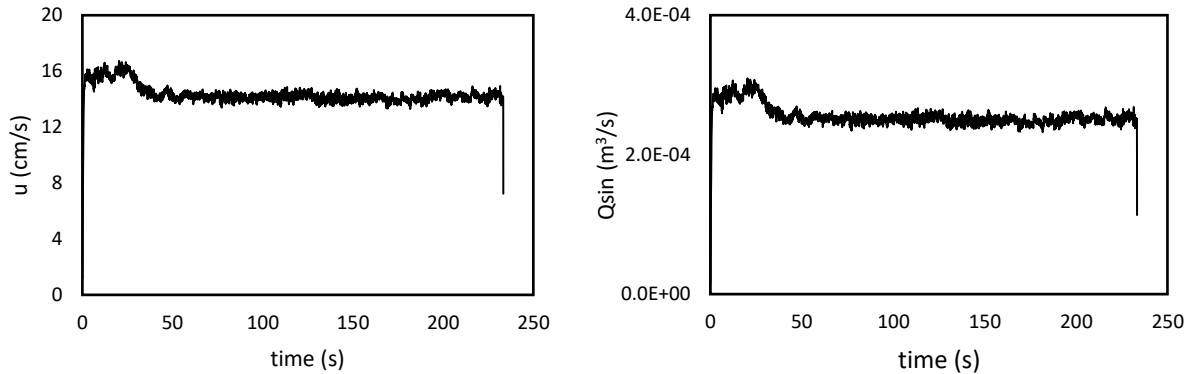


AE7.7. Color gradient graphs for bed, water and Froude number evolution in space and time

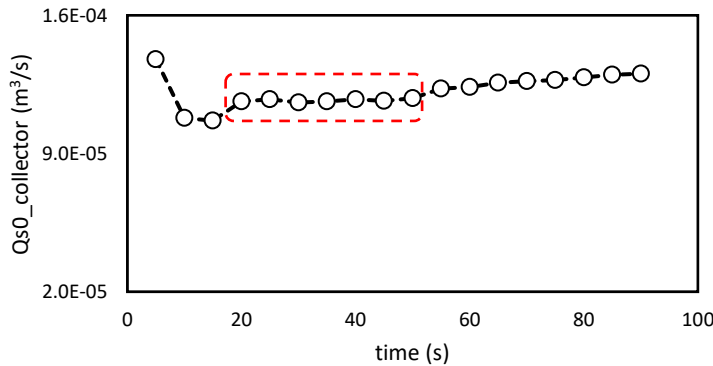
Experiment AE8

T (s)	S ₀ (%)	Q (l/s)	h ₀ (cm)	Fr	Vibration level	Q _{sin} (m ³ /s)	Q _{s0} (m ³ /s)	Q _{sin} /Q _{s0}
233	1.2	7	3.46	1.16	8.75	2.55E-04	1.33E-04	1.92

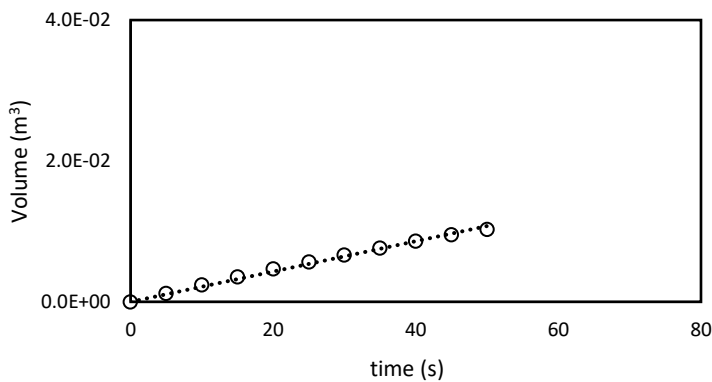
AE8.1. Experimental parameters



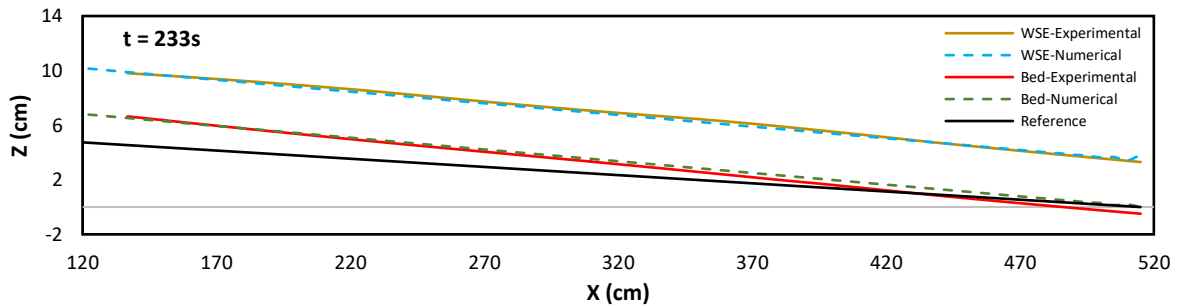
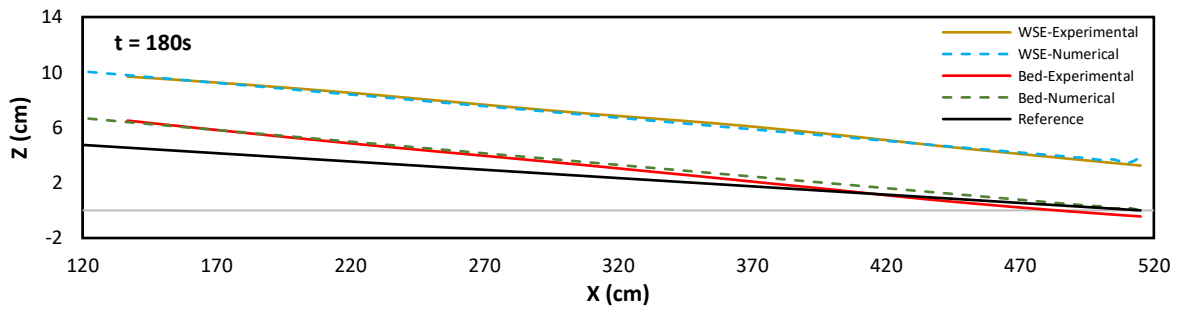
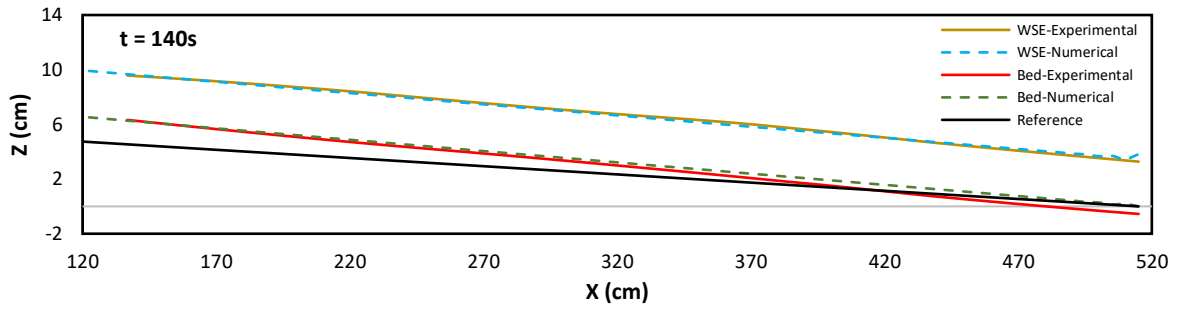
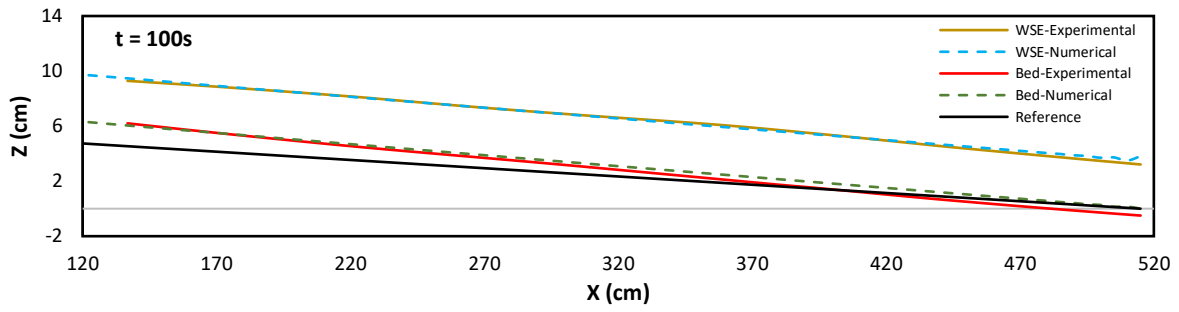
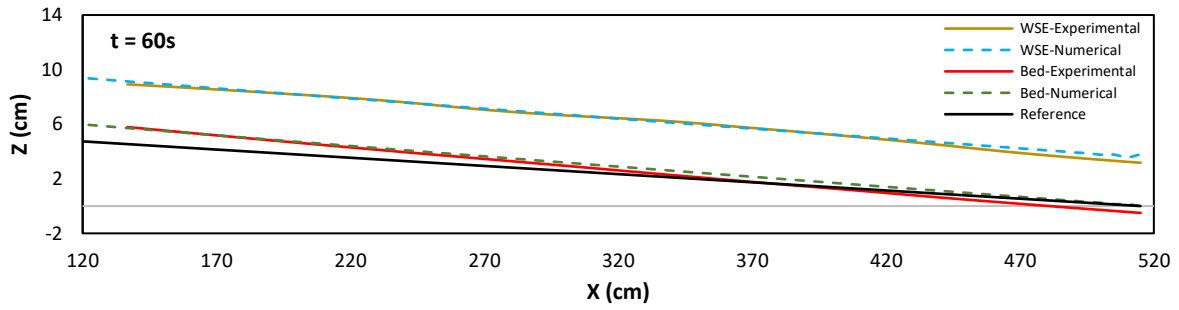
AE8.2. Temporal evolution of velocity and sediment discharge for the inflow material



AE8.3. $t - Q_{s0_collector}$ graph, presenting the sediment transport capacity over time, computed using collector method. The average of the constant values of Q_{s0} is considered as the $Q_{s0_collector}$.

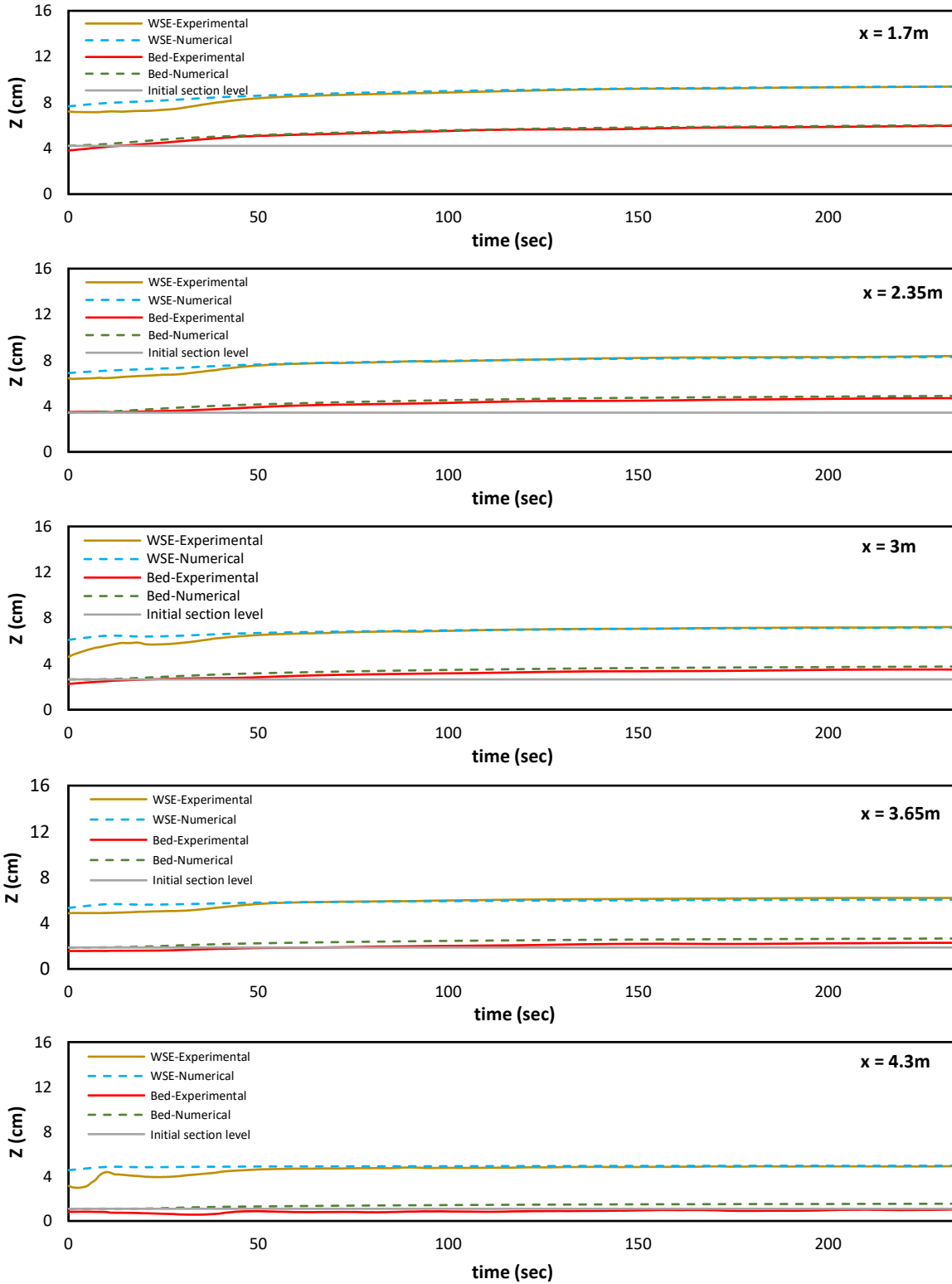


AE8.4. t - volume graph, presenting the volume of sediment deposited in the channel with the assumption of constant profile at the upstream. The slope of the interpolating line is used to calculate Q_{s0} , monitored.

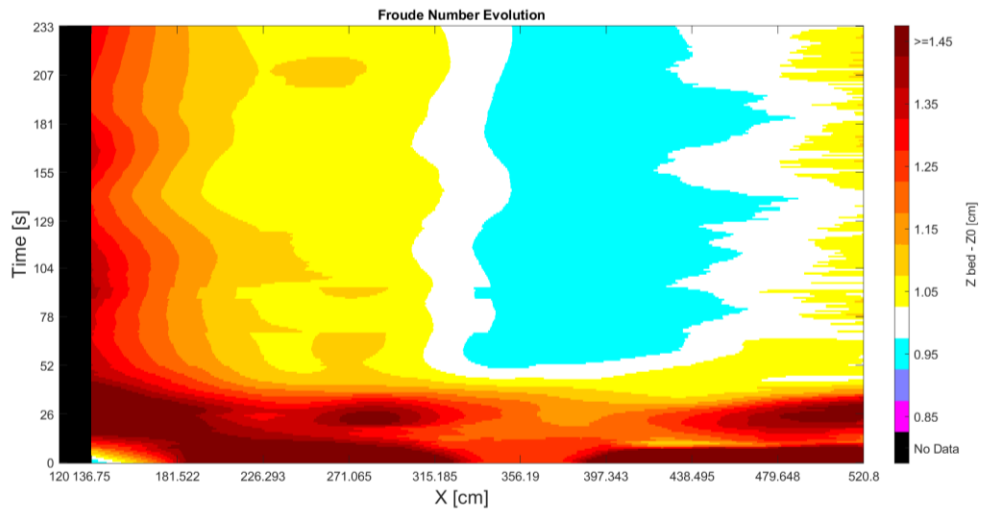
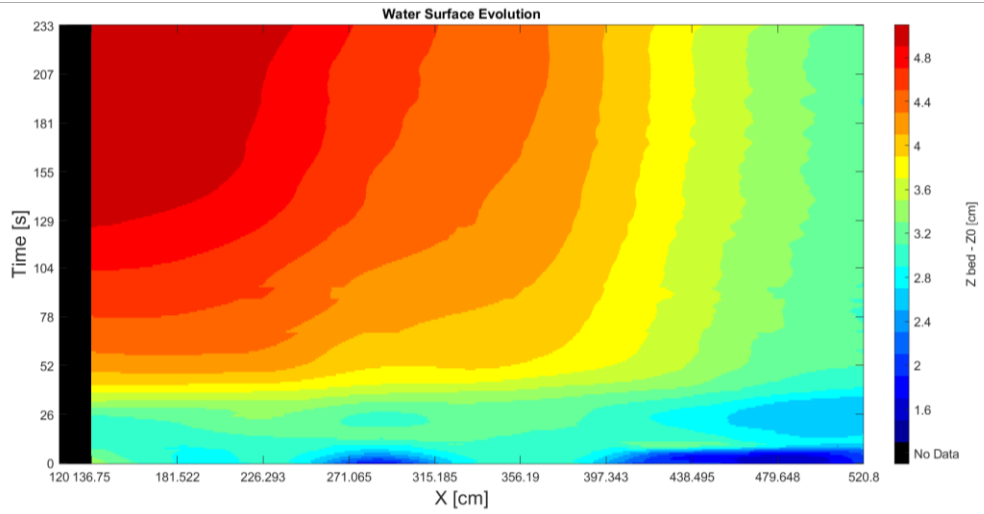
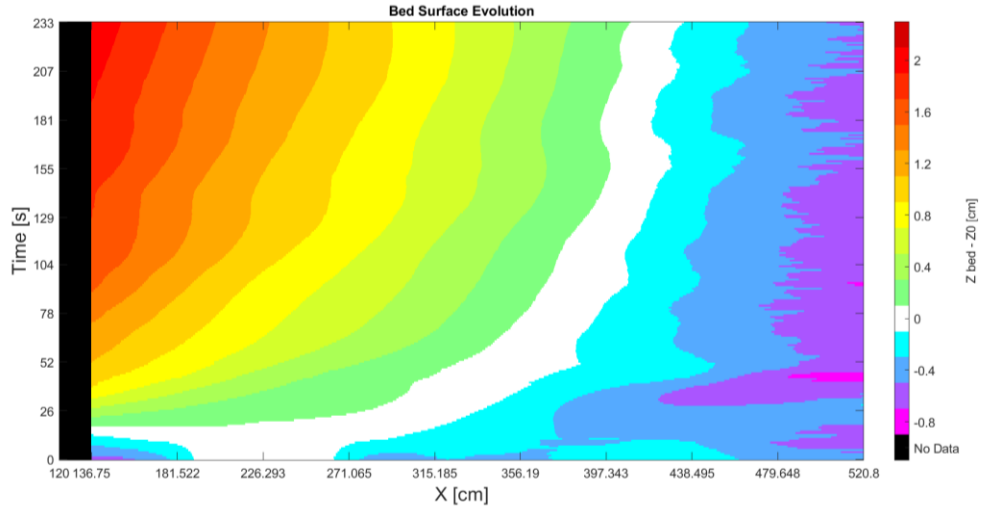


AE8.5. Spatial evolution of bed and water

APPENDIX - RESULTS



AE8.6. Temporal evolution of bed and water in the selected point



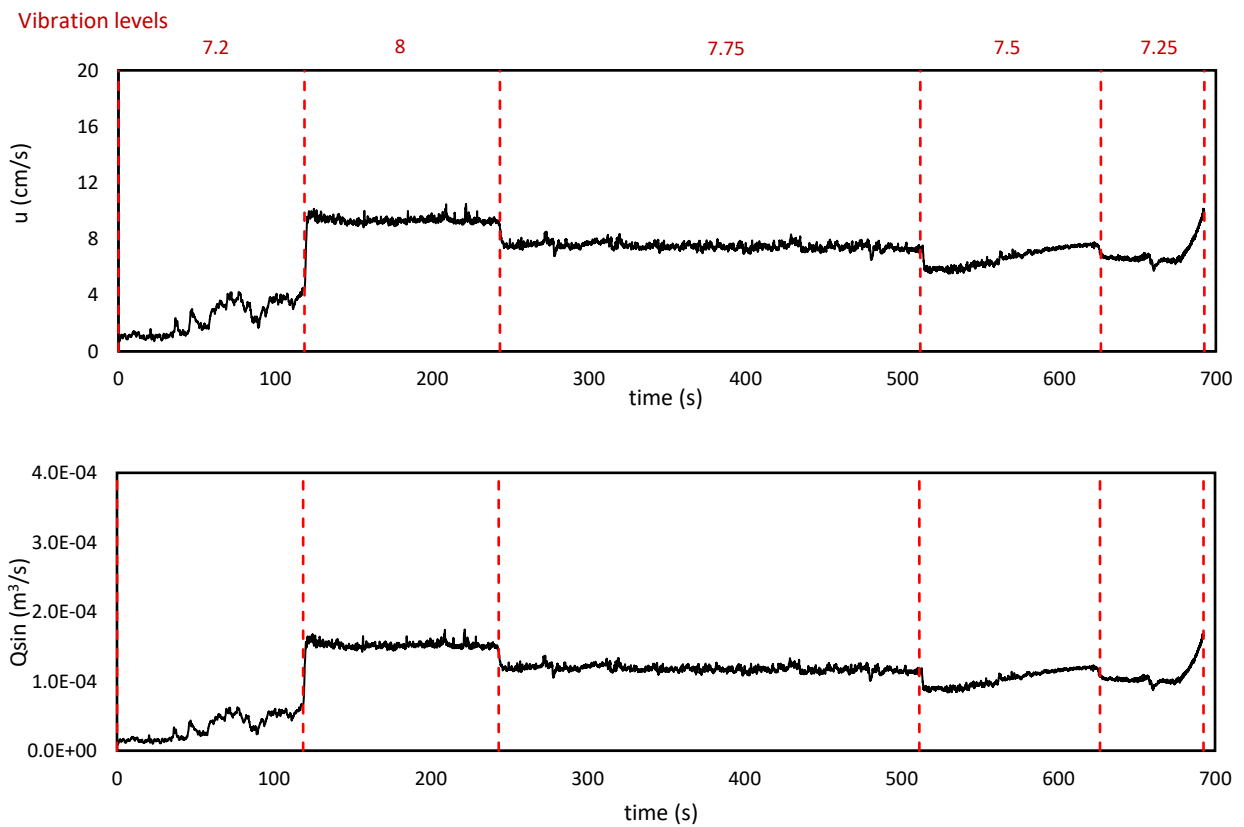
AE8.7. Color gradient graphs for bed, water and Froude number evolution in space and time

Experiment SC1

T (s)	S ₀ (%)	Q (l/s)	Opening height (cm)
693	1.2	5	2

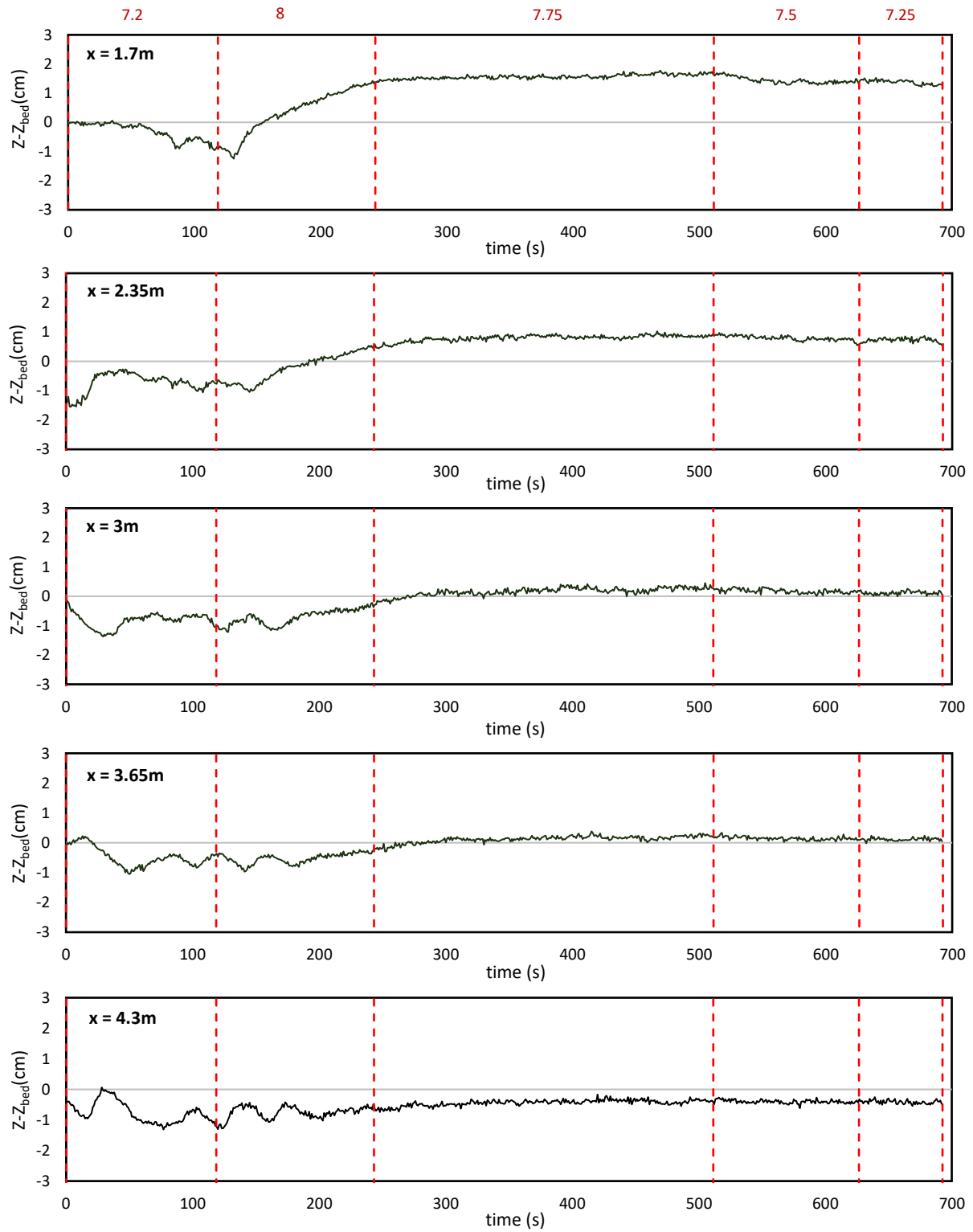
Vibration level	Time (s)	Q _{sin} (m ³ /s)
7.2	119	4.88E-05
8	125	1.52E-04
7.75	268	1.18E-04
7.5	115	9.22E-05
7.25	66	1.02E-04

SC1.1. Experimental parameters



SC1.2. Temporal evolution of velocity and sediment discharge for the inflow material

Vibration levels



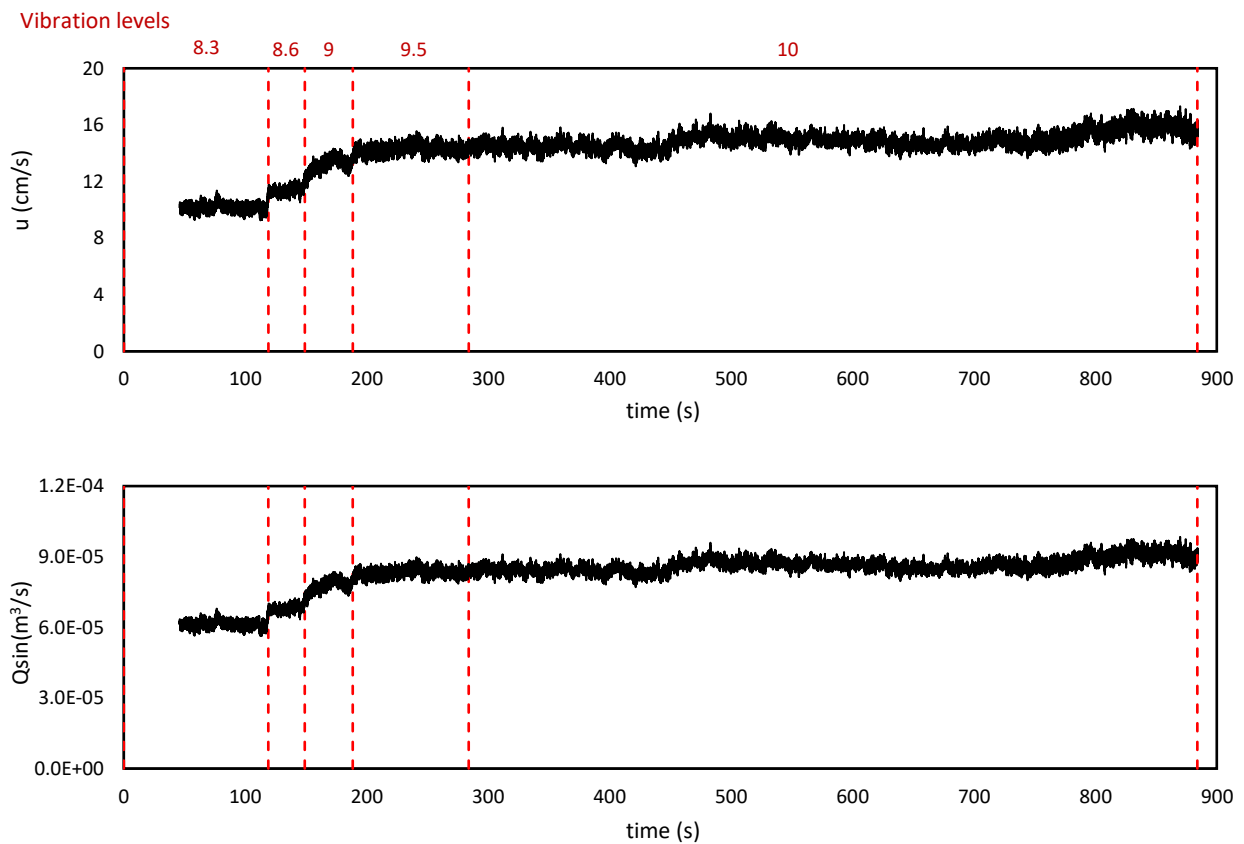
SC1.3. Temporal evolution of bed in the selected points

Experiment SC2

T (s)	S ₀ (%)	Q (l/s)	Opening height (cm)
884	1.2	5	1

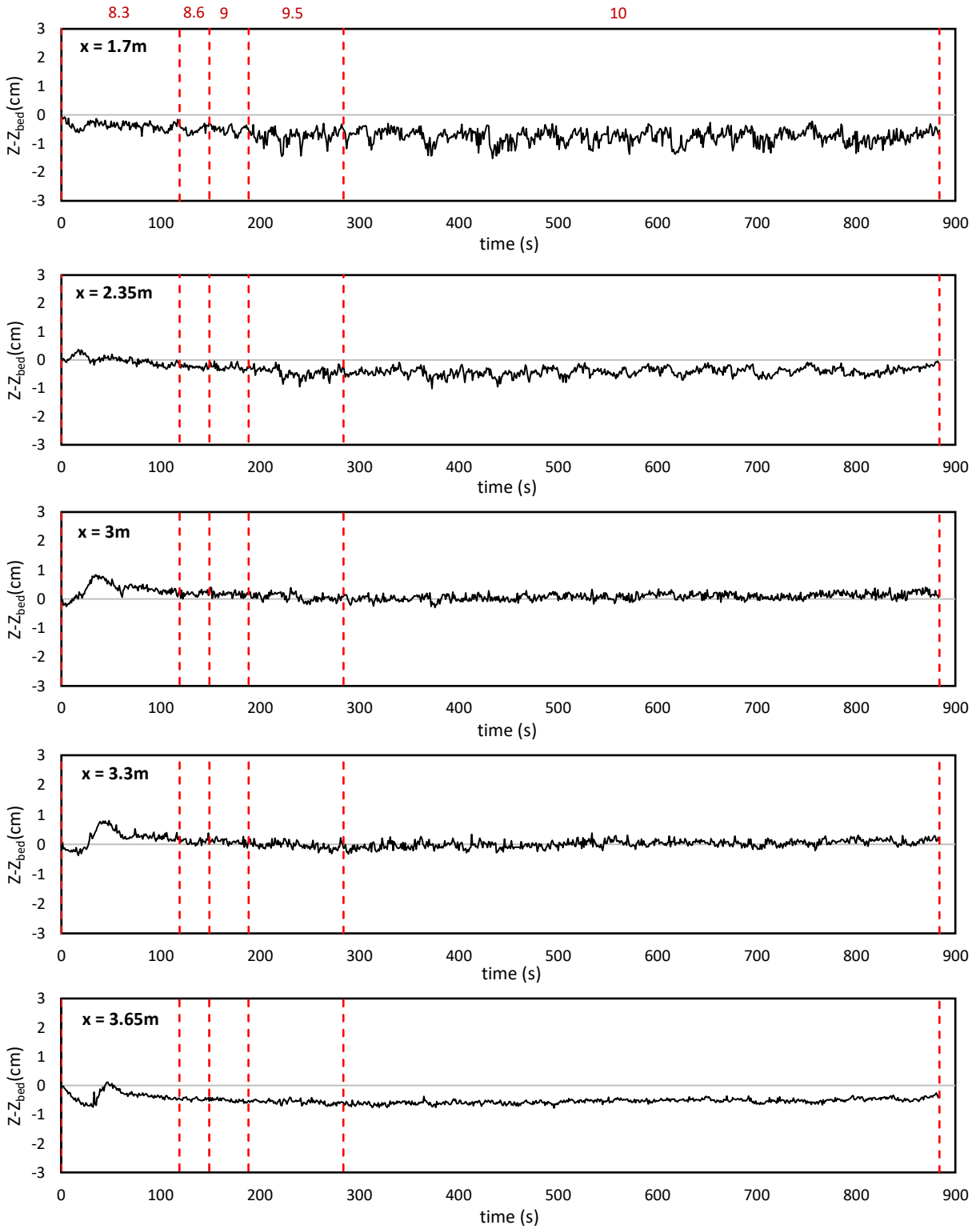
Vibration level	Time (s)	Q _{sin} (m ³ /s)
8.3	119	6.06E-05
8.6	30	6.72E-05
9	39	7.65E-05
9.5	96	8.20E-05
10	600	8.46E-05

SC2.1. Experimental parameters



SC2.2. Temporal evolution of velocity and sediment discharge for the inflow material

Vibration levels



SC2.3. Temporal evolution of bed in the selected points

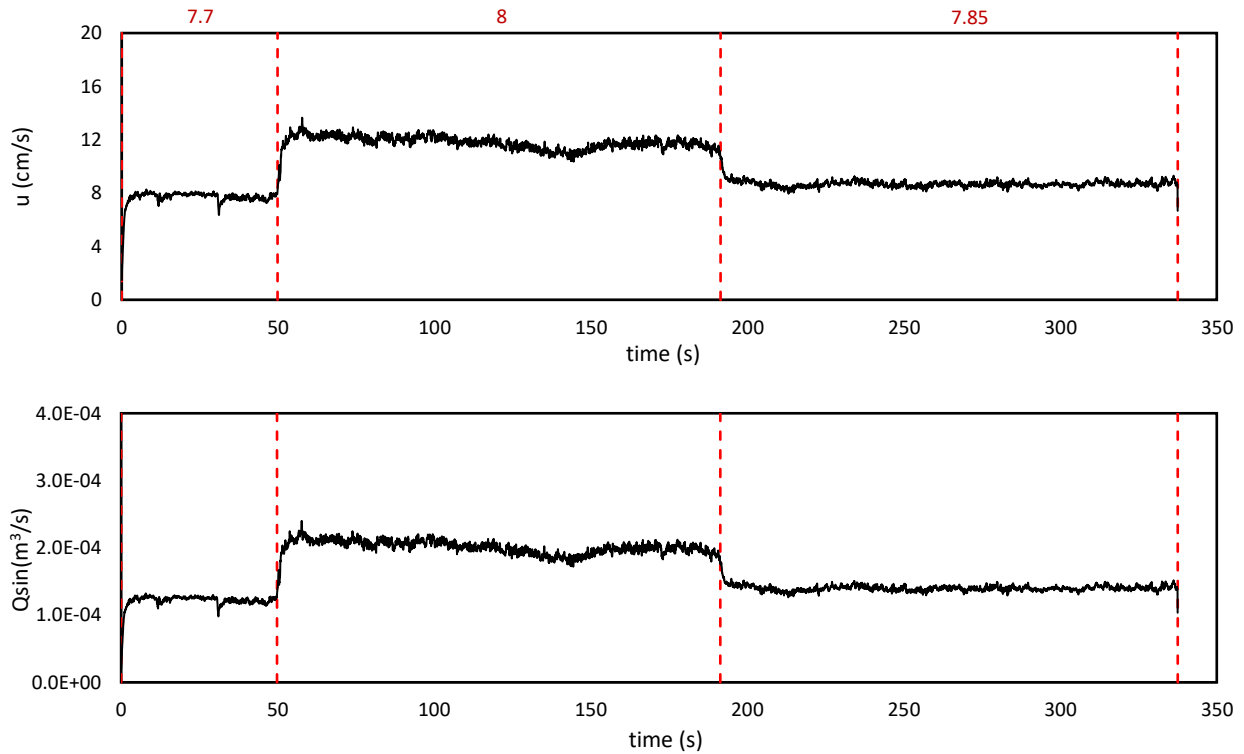
Experiment SC3

T (s)	S ₀ (%)	Q (l/s)	Opening height (cm)
338	1.2	7	2

Vibration level	Time (s)	Q _{sin} (m ³ /s)
7.7	50	1.21E-04
8	142	2.00E-04
7.85	146	1.40E-04

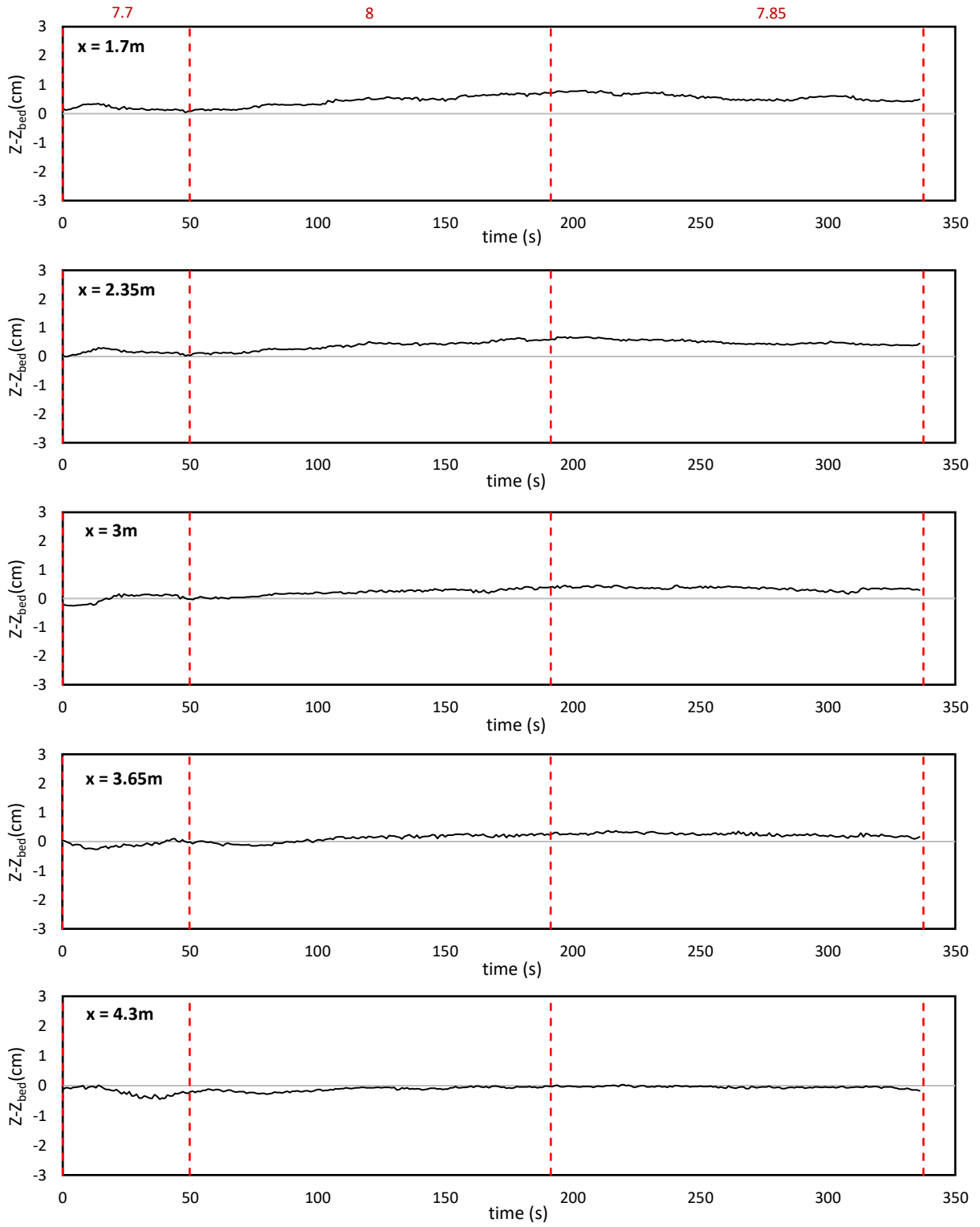
SC3.1. Experimental parameters

Vibration levels



SC3.2. Temporal evolution of velocity and sediment discharge for the inflow material

Vibration levels



SC3.3. Temporal evolution of bed in the selected points